

JOURNAL OF SCIENCE

PART A: ENGINEERING AND INNOVATION



Year | Yıl: 2022

Volume | Cilt: 9

Issue | Sayı: 3

e-ISSN 2147-9542



Owner | Sahibi

on behalf of Gazi University | Gazi Üniversitesi adına

Rector | Rektör

Prof. Dr. | Prof. Dr.

Musa YILDIZ

Publishing Manager

Prof. Dr. | Prof. Dr.

Cevriye GENCER

Gazi University | Gazi Üniversitesi

Chief Editor

Prof. Dr. | Prof. Dr.

Sema Bilge OCAK

Gazi University | Gazi Üniversitesi

Managing Editors

Prof. Dr. | Prof. Dr.

Mustafa Gürhan YALÇIN

Akdeniz University | Akdeniz Üniversitesi

Prof. Dr. | Prof. Dr.

Selim ACAR

Gazi University | Gazi Üniversitesi

Assoc. Prof. Dr. | Doç. Dr.

Uğur GÖKMEN

Gazi University | Gazi Üniversitesi

Assoc. Prof. Dr. | Doç. Dr.

Gürhan İÇÖZ

Gazi University | Gazi Üniversitesi

Associate Editors | Alan Editörleri

- Prof. Dr. | Prof. Dr. Gazi University - Physics
Adem TATAROĞLU Gazi Üniversitesi - Fizik
- Prof. Dr. | Prof. Dr. Gazi University - Energy Systems Engineering
Adnan SÖZEN Gazi Üniversitesi - Enerji Sistemleri Mühendisliği
- Prof. Dr. | Prof. Dr. Çukurova University - Automotive Engineering
Ali KESKİN Çukurova Üniversitesi - Otomotiv Mühendisliği
- Prof. Dr. | Prof. Dr. Ankara University - Chemistry
Ali Osman SOLAK Ankara Üniversitesi - Kimya
- Prof. Dr. | Prof. Dr. Gazi University - Civil Engineering
Alper BÜYÜKKARAGÖZ Gazi Üniversitesi - İnşaat Mühendisliği
- Prof. Dr. | Prof. Dr. Gazi University - Mechanical Engineering
Atilla BIYIKOĞLU Gazi Üniversitesi - Makine Mühendisliği
- Prof. Dr. | Prof. Dr. Bilecik Şeyh Edebali University - Chemical Engineering
Çağlayan AÇIKGÖZ Bilecik Şeyh Edebali Üniversitesi - Kimya Mühendisliği
- Prof. Dr. | Prof. Dr. Ankara University - The Institute of Biotechnology
Demet CANSARAN DUMAN Ankara Üniversitesi - Biyoteknoloji Enstitüsü
- Prof. Dr. | Prof. Dr. Gazi University - Physics
Elif ORHAN Gazi Üniversitesi - Fizik
- Prof. Dr. | Prof. Dr. Gazi University - Electrical-Electronic Engineering
Erdal IRMAK Gazi Üniversitesi - Elektrik-Elektronik Mühendisliği
- Prof. Dr. | Prof. Dr. Atatürk University - Food Engineering
Fatih ÖZ Atatürk Üniversitesi - Gıda Mühendisliği
- Prof. Dr. | Prof. Dr. Gazi University - Metallurgical and Materials Engineering
Hakan ATEŞ Gazi Üniversitesi - Metalurji ve Malzeme Mühendisliği
- Prof. Dr. | Prof. Dr. Gazi University - Automotive Engineering
Hüseyin Serdar YÜCESU Gazi Üniversitesi - Otomotiv Mühendisliği
- Prof. Dr. | Prof. Dr. Gazi University - Chemical Engineering
Meltem DOĞAN Gazi Üniversitesi - Kimya Mühendisliği
- Prof. Dr. | Prof. Dr. Gazi University - Chemical Engineering
Metin GÜRÜ Gazi Üniversitesi - Kimya Mühendisliği
- Prof. Dr. | Prof. Dr. Aksaray University - Biotechnology and Nanotechnology
Murat KAYA Aksaray Üniversitesi - Biyoteknoloji ve Nanoteknoloji



Associate Editors | Alan Editörleri

- Prof. Dr. | Prof. Dr. Ege University - Chemical Engineering
Nalan KABAY Ege Üniversitesi - Kimya Mühendisliği
- Prof. Dr. | Prof. Dr. Ankara Hacı Bayram Veli University - Chemistry
Nazife ASLAN Ankara Hacı Bayram Veli Üniversitesi - Kimya
- Prof. Dr. | Prof. Dr. Eskişehir Technical University - Materials Science and Engineering
Nuran AY Eskişehir Teknik Üniversitesi - Malzeme Bilimi ve Mühendisliği
- Prof. Dr. | Prof. Dr. Gazi University - Electrical-Electronic Engineering
Nursel AKÇAM Gazi Üniversitesi - Elektrik-Elektronik Mühendisliği
- Prof. Dr. | Prof. Dr. İstanbul Technical University - Chemical Engineering
Ömer ŞAHİN İstanbul Teknik Üniversitesi - Kimya Mühendisliği
- Prof. Dr. | Prof. Dr. Konya Technical University - Environmental Engineering
Şükrü DURSUN Konya Teknik Üniversitesi - Çevre Mühendisliği
- Prof. Dr. | Prof. Dr. Ankara Yıldırım Beyazıt University - Mechanical Engineering
Veli ÇELİK Ankara Yıldırım Beyazıt Üniversitesi - Makine Mühendisliği
- Prof. Dr. | Prof. Dr. TOBB University of Economics and Technology - Mechanical Engineering
Yücel ERCAN TOBB Ekonomi ve Teknoloji Üniversitesi - Makine Mühendisliği
- Prof. Dr. | Prof. Dr. Middle East Technical University - Engineering Sciences
Zafer EVİS Orta Doğu Teknik Üniversitesi - Mühendislik Bilimleri
- Assoc. Prof. Dr. | Doç. Dr. Hitit University - Chemical Engineering
Çetin ÇAKANYILDIRIM Hitit Üniversitesi - Kimya Mühendisliği
- Assoc. Prof. Dr. | Doç. Dr. Ankara University - Physics
Defne AKAY Ankara Üniversitesi - Fizik
- Assoc. Prof. Dr. | Doç. Dr. Gazi University - Computer Engineering
Hacer KARACAN Gazi Üniversitesi - Bilgisayar Mühendisliği
- Assoc. Prof. Dr. | Doç. Dr. Gazi University - Biology
Mine TÜRKTAS Gazi Üniversitesi - Biyoloji
- Assist. Prof. Dr. | Dr. Öğr. Üyesi Akdeniz University - Mathematics
Fusun YALÇIN Akdeniz Üniversitesi - Matematik
- Assist. Prof. Dr. | Dr. Öğr. Üyesi Dr. Marmara University - Mechanical Engineering
Senai YALÇINKAYA Marmara Üniversitesi - Makine Mühendisliği



Foreign Editorial Advisory Board | Yabancı Yayın Danışma Kurulu

Prof. Dr.	Istituto Nazionale di Fisica Nucleare (INFN)
Ali Behcet ALPAT	Physics
Prof. Dr.	Université d'Évry Val d'Essonne
Abdelmejid BAYAD	Mathematics
Prof. Dr.	Miami University
Burçin BAYRAM	Physics
Prof. Dr.	The University of Sheffield
Rob DWYER-JOYCE	Mechanical Engineering
Prof. Dr.	Jeonbuk National University
Daeyeoul KIM	Mathematics
Prof. Dr.	Loughborough University
Homer RAHNEJAT	Electrical and Manufacturing Engineering
Prof. Dr.	Vijayanagara Sri Krishnadevaraya University
Loksha VEERABHADRIAH	Mathematics
Assist. Prof. Dr.	University Džemal Bijedić Mostar
Toni NIKOLIC	Geological Engineering

English Language Editors | İngilizce Dil Editörleri

Lecturer Okutman	Gazi University - School of Foreign Languages
Gizem AÇELYA AYKAN	Gazi Üniversitesi - Yabancı Diller Yüksekokulu
Lecturer Okutman	Gazi University - School of Foreign Languages
Tuğçe BÜYÜKBAYRAM	Gazi Üniversitesi - Yabancı Diller Yüksekokulu

Technical Editors | Teknik Editörler

Dr.	Akdeniz University
Fatih UÇAR	Akdeniz Üniversitesi
Dr.	Gazi University
Silver GÜNEŞ	Gazi Üniversitesi
Dr.	Gazi University
Murat AKIN	Gazi Üniversitesi



Correspondence Address

Gazi University Graduate School of Natural and Applied Sciences
Emniyet Neighborhood, Bandırma Avenue, No:6/20B, 06560, Yenimahalle - ANKARA
B Block, Auxiliary Building

Yazışma Adresi

Gazi Üniversitesi Fen Bilimleri Enstitüsü
Emniyet Mahallesi, Bandırma Caddesi, No:6/20B, 06560, Yenimahalle - ANKARA
B Blok, Ek Bina

e-mail | e-posta
gujsa06@gmail.com

web page | web sayfası
<https://dergipark.org.tr/tr/pub/gujsa>

**Gazi University Journal of Science Part A: Engineering and Innovation
is a peer-reviewed journal.**

Gazi Üniversitesi Fen Bilimleri Dergisi Bölüm A: Mühendislik ve İnovasyon
hakemli bir dergidir.

INDEXING | DİZİNLENME

TRDİZİN



ASOS indeks



ACCESSIBILITY | ERİŞİLEBİLİRLİK



DergiPark AKADEMİK



This work are licensed under a Creative Commons Attribution-ShareAlike 4.0 International License.

Bu eser Creative Commons Atıf-AynıLisanslaPaylaş 4.0 Uluslararası Lisansı ile lisanslanmıştır.

CONTENTS | İÇİNDEKİLER

Page | Sayfa Articles | Makaleler

Certain Finite Sums Pertaining to Leibnitz, Harmonic and Other Special Numbers

187-198

N. Kılar 

Research Article

Mathematics

[10.54287/guj.1134534](https://doi.org/10.54287/guj.1134534)

A Hybrid Attention-based LSTM-XGBoost Model for Detection of ECG-based Atrial Fibrillation

199-210

F. Balci 

Research Article

Biomedical Engineering

[10.54287/guj.1128006](https://doi.org/10.54287/guj.1128006)

An Investigation of Benford's Law Divergence and Machine Learning Techniques for Intra-Class Separability of Fingerprint Images

211-224

A. Iorliam  E. Orgem  Y. I. Shehu 

Research Article

Computer Science

[10.54287/guj.1077430](https://doi.org/10.54287/guj.1077430)

The Effect of Nanostructured Titanium Surface on Protein Adsorption

225-232

H. T. Şirin  E. Akdoğan 

Research Article

Bioengineering

[10.54287/guj.1134881](https://doi.org/10.54287/guj.1134881)

Optimal Cutting Conditions of Abrasive Waterjet Cutting for Ti-6Al-2Sn-2Mo Alpha-Beta Alloy Using EDAS and DFA Methods

233-250

U. S. Nwankiti  S. A. Oke 

Research Article

Mechanical Engineering

[10.54287/guj.1135609](https://doi.org/10.54287/guj.1135609)

CONTENTS | İÇİNDEKİLER

Page | Sayfa Articles | Makaleler

In silico* Analyzes of miRNAs Associated with Root and Tuber in *S. commersonii

251-258

A. Ö. Koral^{ID} M. Türктаş^{ID}

Research Article

Biology

[10.54287/gujisa.1142153](https://doi.org/10.54287/gujisa.1142153)

A New Numerical Approach Using Chebyshev Third Kind Polynomial for Solving Integrodifferential Equations of Higher Order

259-266

A. M. Ayinde^{ID} A. A. James^{ID} A. A. Ishaq^{ID} T. Oyedepo^{ID}

Research Article

Mathematics

[10.54287/gujisa.1093536](https://doi.org/10.54287/gujisa.1093536)

The Production of Organic Photodetectors and Determination of Electrical Properties for Optical Sensor Applications

267-275

S. Karadeniz^{ID} B. Barış^{ID} H. Karadeniz^{ID} M. Yıldırım^{ID}

Research Article

Physics

[10.54287/gujisa.1141142](https://doi.org/10.54287/gujisa.1141142)

Effects of Electric Vehicles and Charging Stations on Microgrid Power Quality

276-286

S. Adak^{ID} H. Cangı^{ID} R. Kaya^{ID} A. S. Yılmaz^{ID}

Research Article

Electrical & Electronics Engineering

[10.54287/gujisa.1153313](https://doi.org/10.54287/gujisa.1153313)

The Effect of the Parameters on Al 7075 Coated with MAO Method by Adding Nano Ti-Powder

287-298

M. E. Özcan^{ID} L. Özler^{ID}

Research Article

Mechanical Engineering

[10.54287/gujisa.1148417](https://doi.org/10.54287/gujisa.1148417)

CONTENTS | İÇİNDEKİLER

Page | Sayfa

Articles | Makaleler

299-313	Molecular Docking, HOMO-LUMO, Quantum Chemical Computation and Bioactivity Analysis of vic-Dioxim Derivatives Bearing Hydrazone Group Ligand and Their Ni^{II} and Cu^{II} Complexes Ş. G. Çalışkan ^{ID} O. Genç ^{ID} F. Erol ^{ID} N. Sarıkavaklı ^{ID} Research Article Chemistry	10.54287/gujisa.1160449
314-322	Evaluation of Electromagnetic Field Levels and Student Exposure at Aydın Adnan Menderes University Central Campus Ş. G. Çalışkan ^{ID} M. A. Kılıç ^{ID} D. Bakay İlhan ^{ID} M. Aksel ^{ID} O. Genç ^{ID} M. D. Bilgin ^{ID} Research Article Biophysics	10.54287/gujisa.1151793
323-333	Detecting Turkish Fake News Via Text Mining to Protect Brand Integrity Ö. Doğuç ^{ID} Research Article Information Systems Engineering	10.54287/gujisa.1170640
334-346	Adaptation of the Kantorovich Type Integral to the Dunkl Operator G. İçöz ^{ID} E. Gökmen ^{ID} Research Article Mathematics	10.54287/gujisa.1148199
347-358	Investigation of Organic and Inorganic Contaminants in Water Sources around Elbistan Lignite Beds A. Doğrul Selver ^{ID} Y. Uras ^{ID} Research Article Geological Engineering	10.54287/gujisa.1152444



Gazi University

Journal of Science

PART A: ENGINEERING AND INNOVATION

<http://dergipark.org.tr/gujisa>

Certain Finite Sums Pertaining to Leibnitz, Harmonic and Other Special Numbers

Neslihan KILAR^{1*} ¹Niğde Ömer Halisdemir University, Bor Vocational School, Department of Computer Technologies, Niğde TR-51700 Turkey

Keywords	Abstract
Leibnitz Numbers	The present manuscript deals with some certain finite sums and identities pertaining to some special numbers. Using generating functions methods, some relations and identities involving the Apostol type Euler and combinatorial numbers, and also the Fubini type numbers and polynomials, are given. Then, by using some certain classes of special finite sums involving the following rational sum which is defined by Simsek (2021b): $y(r, \vartheta) = \sum_{b=0}^r \frac{(-1)^r}{(1+b)\vartheta^{b+1}(\vartheta-1)^{r-b+1}},$ many new certain finite sums and formulas related to the Leibnitz, Harmonic, Changhee, and Daehee numbers are obtained. Moreover, some applications of these results are presented.
Harmonic Numbers	
Fubini Type Numbers	
Changhee and Daehee Numbers	
Apostol Type Euler Numbers	

Cite

Kilar, N. (2022). Certain Finite Sums Pertaining to Leibnitz, Harmonic and Other Special Numbers. *GU J Sci, Part A*, 9(3), 187-198.

Author ID (ORCID Number)	Article Process
N. Kilar, 0000-0001-5797-6301	Submission Date 22.06.2022
	Revision Date 22.07.2022
	Accepted Date 25.07.2022
	Published Date 02.08.2022

1. INTRODUCTION

It is well known that certain finite sums including special numbers and special functions have taken their place among the main subjects of the studies of many researchers in recent years. Because these sums contain formulas and relations that are frequently used in mathematics, engineering and other branches of science due to their properties. For this reason, they are frequently used in modeling design and other situations involving many real-world problems.

In present manuscript, we give some certain finite sums and relations covering both the Leibnitz, Harmonic, Changhee, Daehee, and Apostol type Euler numbers, and also the Fubini type numbers and polynomials. In order to obtain these results, let us introduce the following notations and definitions that we will use throughout this manuscript:

Let $\mathbb{N} = \{1, 2, 3, \dots\}$, \mathbb{C} denotes by complex numbers and $\mathbb{N}_0 = \{0, 1, 2, 3, \dots\}$. Let

$$\binom{\omega}{k} k! = (\omega)_k = \omega(\omega-1) \dots (\omega-k+1)$$

with $(\omega)_0 = 1, k \in \mathbb{N}, \omega \in \mathbb{C}$ and

$$0^s = \begin{cases} 1, & s = 0 \\ 0, & s \in \mathbb{N} \end{cases}$$

(Gould, 1972;-;Srivastava & Kızılateş, 2019).

The numbers $E_r^{*(-k)}(\vartheta)$ are defined by

$$\mathcal{Z}_E(t, k, \vartheta) = \left(\frac{\vartheta e^t + \vartheta^{-1} e^{-t}}{2} \right)^k = \sum_{r=0}^{\infty} E_r^{*(-k)}(\vartheta) \frac{t^r}{r!}, \quad (1)$$

where $k \in \mathbb{N}$ and $\vartheta \in \mathbb{C}$. The numbers $E_r^{*(-k)}(\vartheta)$ are called the second kind Apostol type Euler numbers of order $-k$ (Simsek, 2017; 2018; 2022a).

The numbers $W_r^{(-k)}(\vartheta)$ are defined by

$$\mathcal{Z}_W(t, k, \vartheta) = (\vartheta e^t + \vartheta^{-1} e^{-t} + 2)^k = \sum_{r=0}^{\infty} W_r^{(-k)}(\vartheta) \frac{t^r}{r!}, \quad (2)$$

where $k \in \mathbb{N}$ and $\vartheta \in \mathbb{C}$ (Simsek, 2017; 2018; 2022a; see also Kucukoglu & Simsek, 2018; Kucukoglu et al., 2019).

By using (1) and (2), one has

$$W_r^{(-k)}(\vartheta) = 2^k \sum_{j=0}^k \binom{k}{j} E_r^{*(-j)}(\vartheta) \quad (3)$$

(Simsek, 2017; 2018; 2022a).

The Daehee numbers are defined by

$$D_r = (-1)^r \frac{r!}{r+1} \quad (4)$$

(Kim & Kim, 2013; see also Simsek, 2019).

The Changhee numbers are defined by

$$Ch_r = (-1)^r \frac{r!}{2^r} \quad (5)$$

(Kim et al., 2013; see also Simsek, 2019).

The Leibnitz numbers are defined by

$$l(r, b) = \frac{\binom{r}{b}^{-1}}{(r+1)}, \quad (6)$$

where $b = 0, 1, 2, \dots, r$ and $r \in \mathbb{N}_0$ (for detail, see Simsek, 2021a). Recently, Simsek (2021a) has given some results associated with the Leibnitz, Daehee, Changhee and other well-known special numbers.

Simsek (2021a (Theorem 2.9. and Theorem 2.10.)) gave the following formulas

$$2q! \sum_{b=0}^q \mathbf{l}(q, b) - q! \sum_{b=0}^{q-1} \mathbf{l}(q-1, b) = 2(-1)^q D_q \quad (7)$$

and

$$2(1+q) \sum_{b=0}^q \mathbf{l}(q, b) - (1+q) \sum_{b=0}^{q-1} \mathbf{l}(q-1, b) = 2. \quad (8)$$

The Harmonic numbers, H_r , are defined by

$$H_r = \sum_{b=1}^r \frac{1}{b}$$

(for detail, see Simsek, 2021b, 2021c, 2021d; 2022b, 2022c). From the above equation, we have

$$H_{r+1} - H_r = \frac{1}{r+1} \quad (9)$$

(Simsek, 2021b, 2021c; 2022b, 2022c).

Kilar and Simsek (2017) defined the following the Fubini type numbers $a_r^{(n)}$:

$$\frac{2^n}{(2 - e^t)^{2n}} = \sum_{r=0}^{\infty} a_r^{(n)} \frac{t^r}{r!}, \quad (10)$$

where $n \in \mathbb{N}_0$ and $|t| < \ln(2)$ (for detail, see Kilar & Simsek, 2019a, 2019b; 2021a, 2021b; Kilar, 2023a, 2023b).

When $n = 1$ in (10), we get

$$a_r^{(1)} = a_r.$$

Kilar and Simsek (2017) defined the following polynomials $a_r^{(n)}(x)$:

$$\frac{2^n}{(2 - e^t)^{2n}} e^{xt} = \sum_{r=0}^{\infty} a_r^{(n)}(x) \frac{t^r}{r!}. \quad (11)$$

From (10) and (11), we have

$$a_r^{(n)}(x) = \sum_{b=0}^r \binom{r}{b} x^{r-b} a_b^{(n)}$$

(Kilar & Simsek, 2017; 2019a, 2019b; 2021a, 2021b; Kilar, 2023a, 2023b).

Two parametric polynomials $a_r^{(C,n)}(x, y)$ and $a_r^{(S,n)}(x, y)$ are defined, respectively, by

$$Z_{ac}(t, n, x, y) = \frac{2^n e^{xt}}{(2 - e^t)^{2n}} \cos(yt) = \sum_{r=0}^{\infty} a_r^{(C,n)}(x, y) \frac{t^r}{r!} \tag{12}$$

and

$$Z_{as}(t, n, x, y) = \frac{2^n e^{xt}}{(2 - e^t)^{2n}} \sin(yt) = \sum_{r=0}^{\infty} a_r^{(S,n)}(x, y) \frac{t^r}{r!} \tag{13}$$

(Srivastava & Kızılateş, 2019). When $y = 0$ in (12), one can see that

$$a_r^{(C,n)}(x, 0) = a_r^{(n)}(x).$$

Simsek (2021b) defined the following finite sum which is called the numbers $y(r, \vartheta)$:

$$y(r, \vartheta) = \sum_{b=0}^r \frac{(-1)^b}{(1+b)\vartheta^{b+1}(\vartheta-1)^{r+1-b}} \tag{14}$$

(see also Simsek, 2021c, 2021d; 2022b, 2022c).

Simsek (2022b (Equation (59))) gave the following formula

$$y(r-1, \vartheta) + (\vartheta-1)y(r, \vartheta) = \frac{(-1)^r}{(r+1)\vartheta^{r+1}}. \tag{15}$$

When $\vartheta = \frac{1}{2}$ in the above equation, we get

$$2y\left(r-1, \frac{1}{2}\right) - y\left(r, \frac{1}{2}\right) = \frac{(-1)^r 2^{r+2}}{r+1} \tag{16}$$

(Simsek, 2022b (Equation (61))).

2. MAIN RESULTS

Using the generating functions which are introduced previous section, many miscellaneous identities involving the Fubini type numbers, the numbers $E_m^{*(-k)}(\vartheta)$ and the numbers $W_m^{*(-k)}(\vartheta)$, are given. Using derivative and integrate operators, some certain finite sums and formulas pertaining to the Leibnitz, Harmonic, Changhee and Daehee numbers and also the numbers $y(m, \vartheta)$, are presented. Moreover, some applications of the obtained results are given.

Theorem 2.1. For $u \in \mathbb{N}_0$ and $d \in \mathbb{N}$ yields

$$\sum_{b=0}^{\lfloor \frac{u}{2} \rfloor} \binom{u}{2b} (-1)^b y^{2b} (x-d)^{u-2b} + (-1)^{d+1} \sum_{b=0}^u \binom{u}{b} W_{u-b}^{(-d)} \left(-\frac{1}{2}\right) a_b^{(C,d)}(x, y) = 0. \tag{17}$$

Proof. By using (2) and (12), we have

$$e^{(x-d)t} \cos(yt) = (-1)^d Z_W \left(t, d, -\frac{1}{2} \right) Z_{ac}(t, d, x, y).$$

From above equation, we get

$$\sum_{u=0}^{\infty} (x-d)^u \frac{t^u}{u!} \sum_{u=0}^{\infty} \frac{(-1)^u (yt)^{2u}}{(2u)!} = (-1)^d \sum_{u=0}^{\infty} W_u^{(-d)} \left(-\frac{1}{2} \right) \frac{t^u}{u!} \sum_{u=0}^{\infty} a_u^{(c,d)}(x, y) \frac{t^u}{u!}.$$

Thus,

$$\sum_{u=0}^{\infty} \sum_{b=0}^{\lfloor \frac{u}{2} \rfloor} (-1)^b \binom{u}{2b} (x-d)^{u-2b} y^{2b} \frac{t^u}{u!} = \sum_{u=0}^{\infty} \sum_{b=0}^u \binom{u}{b} (-1)^d W_{u-b}^{(-d)} \left(-\frac{1}{2} \right) a_b^{(c,d)}(x, y) \frac{t^u}{u!}.$$

Therefore, Equation (17) is derived.

When $y = 0$ in (17), we get the Corollary 2.2:

Corollary 2.2.

$$(x-d)^u = \sum_{b=0}^u \binom{u}{b} (-1)^d W_{u-b}^{(-d)} \left(-\frac{1}{2} \right) a_b^{(d)}(x). \tag{18}$$

Applying derivative operator $\frac{\partial^u}{\partial x^u}$ to the Equation (18), we get

$$\frac{\partial^u}{\partial x^u} \{(x-d)^u\} = \sum_{b=0}^u (-1)^d \binom{u}{b} W_{u-b}^{(-d)} \left(-\frac{1}{2} \right) \frac{\partial^u}{\partial x^u} \{ a_b^{(d)}(x) \}. \tag{19}$$

Since

$$\frac{\partial^u}{\partial x^u} \{ a_b^{(d)}(x) \} = (u)_b a_{b-u}^{(d)}(x)$$

(Kilar & Simsek, 2017), after some elementary calculations, Equation (19) is derived as follows:

$$u! = (-1)^d u! W_0^{(-d)} \left(-\frac{1}{2} \right) a_0^{(d)}(x). \tag{20}$$

Since

$$a_0^{(d)}(x) = 2^d,$$

Equation (20) reduced to the following special result:

$$W_0^{(-d)}\left(-\frac{1}{2}\right) = \frac{(-1)^d}{2^d}.$$

Theorem 2.3. For $u, d \in \mathbb{N}$ yields

$$\sum_{b=0}^{\lfloor \frac{u-1}{2} \rfloor} \binom{u}{2b+1} (-1)^b (x-d)^{u-2b-1} y^{2b+1} + \sum_{b=0}^u (-1)^{d+1} \binom{u}{b} W_{u-b}^{(-d)}\left(-\frac{1}{2}\right) a_b^{(S,d)}(x, y) = 0. \tag{21}$$

Proof. By (2) and (13), we have

$$e^{(x-d)t} \sin(yt) = (-1)^d Z_W\left(t, d, -\frac{1}{2}\right) Z_{as}(t, d, x, y).$$

Using the above functional equation, we have

$$\begin{aligned} \sum_{u=0}^{\infty} \sum_{b=0}^{\lfloor \frac{u-1}{2} \rfloor} \binom{u}{1+2b} (-1)^b y^{1+2b} (x-d)^{u-2b-1} \frac{t^u}{u!} \\ = \sum_{u=0}^{\infty} \sum_{b=0}^u (-1)^d \binom{u}{b} W_{u-b}^{(-d)}\left(-\frac{1}{2}\right) a_b^{(S,d)}(x, y) \frac{t^u}{u!}. \end{aligned}$$

Thus, Equation (21) is obtained.

Combining (17) with (3), we get the Theorem 2.4:

Theorem 2.4. For $u \in \mathbb{N}_0$ and $d \in \mathbb{N}$ yields

$$\sum_{b=0}^{\lfloor \frac{u}{2} \rfloor} (-1)^b \binom{u}{2b} y^{2b} (x-d)^{u-2b} = (-2)^d \sum_{b=0}^u \binom{u}{b} \sum_{k=0}^d \binom{d}{k} a_b^{(C,d)}(x, y) E_{u-b}^{*(-k)}\left(-\frac{1}{2}\right).$$

By combining (21) with (3), we derive the Theorem 2.5:

Theorem 2.5. For $u, d \in \mathbb{N}$ yields

$$\sum_{b=0}^{\lfloor \frac{u-1}{2} \rfloor} (-1)^b \binom{u}{2b+1} y^{2b+1} (x-d)^{u-2b-1} = (-2)^d \sum_{b=0}^u \binom{u}{b} \sum_{k=0}^d \binom{d}{k} a_b^{(S,d)}(x, y) E_{u-b}^{*(-k)}\left(-\frac{1}{2}\right).$$

Theorem 2.6. For $u \in \mathbb{N}_0$ and $d \in \mathbb{N}$ yields

$$\frac{(1-d)^{u+1} + d(-d)^u}{u+1} = \sum_{b=0}^u \sum_{p=0}^b \binom{u}{b} \binom{b}{p} W_{u-b}^{(-d)}\left(-\frac{1}{2}\right) \frac{(-1)^d a_p^{(d)}}{b-p+1}. \tag{22}$$

Proof. Integrating both sides with respect to x of (18), we obtain

$$\int_0^1 (x - d)^u dx = (-1)^d \sum_{b=0}^u \binom{u}{b} W_{u-b}^{(-d)} \left(-\frac{1}{2}\right) \int_0^1 a_b^{(d)}(x) dx.$$

Hence

$$\frac{(-1)^{u+2} d^{u+1} + (1 - d)^{u+1}}{1 + u} + \sum_{b=0}^u \sum_{p=0}^b \binom{b}{p} \binom{u}{b} W_{u-b}^{(-d)} \left(-\frac{1}{2}\right) \frac{(-1)^{d+1} a_p^{(d)}}{b + 1 - p} = 0.$$

From the above equation, we get the Equation (22).

Gould (1972 (p. 5, Equation (1.37))) gave the combinatorial finite sum:

$$\frac{(x + 1)^{v+1} - 1}{x(1 + v)} = \sum_{s=0}^v \binom{v}{s} \frac{x^s}{1 + s}. \tag{23}$$

Using (23), Equation (22) is reduced to as follows:

Corollary 2.7.

$$\sum_{b=0}^u \binom{u}{b} \frac{(-d)^u (-1)^b}{(b + 1) d^b} = \sum_{b=0}^u \sum_{p=0}^b \binom{u}{b} \binom{b}{p} W_{u-b}^{(-d)} \left(-\frac{1}{2}\right) \frac{(-1)^d a_p^{(d)}}{b - p + 1}. \tag{24}$$

Replacing ϑ by $\frac{1}{d}$ in (15), we have

$$\mathbf{y}(q - 1, d^{-1}) + (d^{-1} - 1)\mathbf{y}(q, d^{-1}) = -\frac{(-d)^{q+1}}{1 + q}. \tag{25}$$

Replacing ϑ by $\frac{1}{d-1}$ in (15), we also have

$$\mathbf{y}(q - 1, (d - 1)^{-1}) + ((d - 1)^{-1} - 1)\mathbf{y}(q, (d - 1)^{-1}) = -\frac{(1 - d)^{q+1}}{q + 1}. \tag{26}$$

Combining (26) and (25) with (22), we get

$$\begin{aligned} &\mathbf{y}(q - 1, d^{-1}) + (d^{-1} - 1)\mathbf{y}(q, d^{-1}) - \mathbf{y}(q - 1, (d - 1)^{-1}) \\ &\quad - ((d - 1)^{-1} - 1)\mathbf{y}(q, (d - 1)^{-1}) \\ &= \sum_{b=0}^q \sum_{p=0}^b \binom{q}{b} \binom{b}{p} W_{q-b}^{(-d)} \left(-\frac{1}{2}\right) \frac{(-1)^d a_p^{(d)}}{b - p + 1}. \end{aligned}$$

From here, we get the Theorem 2.8:

Theorem 2.8. For $d \in \mathbb{N} \setminus \{1,2\}$ and $q \in \mathbb{N}$ yields

$$\begin{aligned} & \mathbf{y}(q-1, d^{-1}) - \mathbf{y}(q-1, (d-1)^{-1}) + \left(\frac{1-d}{d}\right) \mathbf{y}(q, d^{-1}) + \left(\frac{2-d}{1-d}\right) \mathbf{y}(q, (d-1)^{-1}) \\ &= \sum_{b=0}^q \sum_{p=0}^b \binom{q}{b} \binom{b}{p} W_{q-b}^{(-d)} \left(-\frac{1}{2}\right) \frac{(-1)^d a_p^{(d)}}{b-p+1}. \end{aligned} \tag{27}$$

Now it is time to give some interesting applications of Equation (24).

Substituting $x = -1$ into (23), we get

$$\sum_{b=0}^q \frac{\binom{q}{b} (-1)^b}{(b+1)} = \frac{1}{q+1}. \tag{28}$$

When $d = 1$ in (24), and using (28), we get the Corollary 2.9:

Corollary 2.9.

$$1 = (q+1) \sum_{b=0}^q \sum_{p=0}^b \binom{q}{b} \binom{b}{p} W_{q-b}^{(-1)} \left(-\frac{1}{2}\right) \frac{(-1)^{1-q} a_p}{b-p+1}. \tag{29}$$

Moreover, substituting $d = 2$ into (22) we obtain

$$(2^{q+1} - 1)(-1)^q = (q+1) \sum_{b=0}^q \sum_{p=0}^b \binom{b}{p} \binom{q}{b} W_{q-b}^{(-2)} \left(-\frac{1}{2}\right) \frac{a_p^{(2)}}{b-p+1}.$$

When $x = 1$ in (23), and using the previous equation, we also obtain

$$\sum_{b=0}^q \binom{q}{b} \frac{(-1)^q}{b+1} = \sum_{b=0}^q \sum_{p=0}^b \binom{q}{b} \binom{b}{p} W_{q-b}^{(-2)} \left(-\frac{1}{2}\right) \frac{a_p^{(2)}}{b+1-p}. \tag{30}$$

Also, substituting $d = 2$ into (24), we obtain

$$\sum_{b=0}^q \binom{q}{b} \frac{(-1)^{q+b}}{(1+b)2^{b-q}} = \sum_{b=0}^q \sum_{p=0}^b \binom{q}{b} \binom{b}{p} W_{q-b}^{(-2)} \left(-\frac{1}{2}\right) \frac{a_p^{(2)}}{b-p+1}. \tag{31}$$

Combining (30) with (31), we derive the following presumably known result:

Corollary 2.10.

$$\sum_{b=0}^{\varphi} \frac{\binom{\varphi}{b}}{1+b} = \sum_{b=0}^{\varphi} \binom{\varphi}{b} \frac{(-1)^b}{(1+b)2^{b-\varphi}}.$$

By using (22) and (4), we have

$$\frac{(-1)^q}{q!} D_q - \frac{(d-1)^{q+1}}{d^{q+1}(q+1)} = \frac{1}{d^{q+1}} \sum_{b=0}^q \sum_{p=0}^b \binom{q}{b} \binom{b}{p} W_{q-b}^{(-d)} \left(-\frac{1}{2}\right) \frac{(-1)^{d+q} a_p^{(d)}}{b-p+1}.$$

Using (7) and the above equation, we have the Theorem 2.11:

Theorem 2.11. For $q, d \in \mathbb{N}$ yields

$$\begin{aligned} \sum_{b=0}^q l(q, b) - \frac{1}{2} \sum_{b=0}^{q-1} l(q-1, b) \\ = \frac{(1-d^{-1})^{q+1}}{q+1} + \frac{1}{d^{1+q}} \sum_{b=0}^q \sum_{p=0}^b \binom{q}{b} \binom{b}{p} W_{q-b}^{(-d)} \left(-\frac{1}{2}\right) \frac{(-1)^{d+q} a_p^{(d)}}{b-p+1}. \end{aligned} \tag{32}$$

Combining (9) with (8), we derive

$$\sum_{b=0}^q l(q, b) - \frac{1}{2} \sum_{b=0}^{q-1} l(q-1, b) = H_{q+1} - H_q.$$

Using the above equation and (32), we get the Corollary 2.12:

Corollary 2.12.

$$H_{q+1} - H_q - \frac{(1-d^{-1})^{q+1}}{q+1} = \sum_{b=0}^q \sum_{p=0}^b \binom{q}{b} \binom{b}{p} W_{q-b}^{(-d)} \left(-\frac{1}{2}\right) \frac{(-1)^{d+q} a_p^{(d)}}{d^{q+1}(b-p+1)}.$$

Combining (32) with (27), we have the Corollary 2.13:

Corollary 2.13. For $d \in \mathbb{N} \setminus \{1,2\}$ and $q \in \mathbb{N}$ yields

$$\begin{aligned} d(d-1)(y(q-1, d^{-1}) - y(q-1, (d-1)^{-1})) - (d-1)^2 y(q, d^{-1}) + d(d-2)y(q, (d-1)^{-1}) \\ = (d-1)d^{q+2}(-1)^q \left(\sum_{b=0}^q l(q, b) - \frac{1}{2} \sum_{b=0}^{q-1} l(q-1, b) \right) - \frac{d(1-d)^{q+2}}{q+1}. \end{aligned}$$

When $d = 3$ into Corollary 2.13, and using (16), we get the Corollary 2.14:

Corollary 2.14.

$$3y\left(q-1, \frac{1}{3}\right) - 2y\left(q, \frac{1}{3}\right) = (-3)^{q+2} \left(\sum_{b=0}^q I(q, b) - \frac{1}{2} \sum_{b=0}^{q-1} I(q-1, b) \right)$$

or, equivalently,

$$3y\left(q-1, \frac{1}{3}\right) - 2y\left(q, \frac{1}{3}\right) = (-3)^{q+2} (H_{q+1} - H_q).$$

When $d = 2$ in (32), we get

$$\begin{aligned} 2 \sum_{b=0}^q I(q, b) - \sum_{b=0}^{q-1} I(q-1, b) \\ = \frac{2^{-q}}{(q+1)} + 2^{-q} (-1)^q \sum_{b=0}^q \sum_{p=0}^b \binom{q}{b} \binom{b}{p} W_{q-b}^{(-2)} \left(-\frac{1}{2}\right) \frac{a_p^{(2)}}{b+1-p}. \end{aligned}$$

Using (4), (5) and the above equation, we have

$$\begin{aligned} 2 \sum_{b=0}^q I(q, b) - \sum_{b=0}^{q-1} I(q-1, b) \\ = \frac{2Ch_{q+1}}{(2+q)(1+q)D_{q+1}} \left(1 + (1+q)(-1)^q \sum_{b=0}^q \sum_{p=0}^b \binom{q}{b} \binom{b}{p} W_{q-b}^{(-2)} \left(-\frac{1}{2}\right) \frac{a_p^{(2)}}{b-p+1} \right). \end{aligned}$$

Using the previous equation and (30) (or (31)), the following result is derived:

Corollary 2.15.

$$2 \sum_{b=0}^q I(q, b) - \sum_{b=0}^{q-1} I(q-1, b) = \frac{2Ch_{q+1}}{(1+q)(2+q)D_{q+1}} \left(1 + (q+1) \sum_{b=0}^q \frac{\binom{q}{b}}{b+1} \right)$$

or, equivalently,

$$2 \sum_{b=0}^q I(q, b) - \sum_{b=0}^{q-1} I(q-1, b) = \frac{Ch_{q+1}}{(1+q)(2+q)D_{q+1}} \left(2 + \sum_{b=0}^q \binom{q}{b} \frac{(-1)^b (q+1)}{2^{b-q-1} (b+1)} \right).$$

3. CONCLUSION

In this manuscript, some certain finite sums and identities included some special numbers were studied. Using certain special polynomials and numbers with generating functions, and integrating some results, various novel formulas, combinatorial finite sums and identities were given. These various results pertaining to the Leibnitz, Harmonic, Apostol type Euler, Changhee, Daehee, combinatorial and Fubini type numbers, and also the Fubini type polynomials. As a result, the results obtained in present manuscript may be usefulness in related sciences especially engineering and mathematics.

CONFLICT OF INTEREST

The author declares no conflict of interest.

REFERENCES

- Gould, H. W. (1972). *Combinatorial identities*. Morgantown: Morgantown Printing and Binding Co.
- Kilar, N. (2023a). Combinatorial sums and identities associated with functional equations of generating functions for Fubini type polynomials. *Gazi University Journal of Science*, doi:[10.35378/gujs.989270](https://doi.org/10.35378/gujs.989270)
- Kilar, N. (2023b). Formulas for Fubini type numbers and polynomials of negative higher order. *Montes Taurus Journal of Pure and Applied Mathematics*, 5(3), 23-36.
- Kilar, N., & Simsek, Y. (2017). A new family of Fubini numbers and polynomials associated with Apostol-Bernoulli numbers and polynomials. *Journal of the Korean Mathematical Society*, 54(5), 1605-1621. doi:[10.4134/JKMS.j160597](https://doi.org/10.4134/JKMS.j160597)
- Kilar, N., & Simsek, Y. (2019a). Some relationships between Fubini type polynomials and other special numbers and polynomials. *AIP Conference Proceedings*, 2116, 100017-1-100017-4. doi:[10.1063/1.5114093](https://doi.org/10.1063/1.5114093)
- Kilar, N., & Simsek, Y. (2019b). Identities and relations for Fubini type numbers and polynomials via generating functions and p -adic integral approach. *Publications de l'Institut Mathématique*, 106(120), 113-123. doi:[10.2298/PIM1920113K](https://doi.org/10.2298/PIM1920113K)
- Kilar, N., & Simsek, Y. (2021a). Combinatorial sums involving Fubini type numbers and other special numbers and polynomials: Approach trigonometric functions and p -adic integrals. *Advanced Studies in Contemporary Mathematics*, 31(1), 75-87. doi:[10.17777/ascm2021.31.1.75](https://doi.org/10.17777/ascm2021.31.1.75)
- Kilar, N., & Simsek, Y. (2021b). Formulae to Fubini type numbers emerge from application of p -adic integrals. *Gazi University Journal of Science Part A: Engineering and Innovation*, 8(4), 402-410. doi:[10.54287/gujisa.980263](https://doi.org/10.54287/gujisa.980263)
- Kim, D. S., & Kim, T. (2013). Daehee numbers and polynomials. *Applied Mathematical Sciences (Ruse)*, 7(120), 5969-5976. doi:[10.12988/ams.2013.39535](https://doi.org/10.12988/ams.2013.39535)
- Kim, D. S., Kim, T., & Seo, J. (2013). A note on Changhee numbers and polynomials. *Advanced Studies in Theoretical Physics*, 7, 993-1003. doi:[10.12988/astp.2013.39117](https://doi.org/10.12988/astp.2013.39117)
- Kucukoglu, I., & Simsek, Y. (2018). Remarks on recurrence formulas for the Apostol-type numbers and polynomials. *Advanced Studies in Contemporary Mathematics*, 28(4), 643-657. doi:[10.17777/ascm2018.28.4.643](https://doi.org/10.17777/ascm2018.28.4.643)
- Kucukoglu, I., Simsek, Y., & Srivastava, H. M. (2019). A new family of Lerch-type zeta functions interpolating a certain class of higher-order Apostol-type numbers and Apostol-type polynomials. *Quaestiones Mathematicae*, 42(4), 465-478. doi:[10.2989/16073606.2018.1459925](https://doi.org/10.2989/16073606.2018.1459925)
- Simsek, Y. (2017). Computation methods for combinatorial sums and Euler-type numbers related to new families of numbers. *Mathematical Methods in the Applied Sciences*, 40(7), 2347-2361. doi:[10.1002/mma.4143](https://doi.org/10.1002/mma.4143)
- Simsek, Y. (2018). New families of special numbers for computing negative order Euler numbers and related numbers and polynomials. *Applicable Analysis and Discrete Mathematics*, 12, 1-35. doi:[10.2298/AADM1801001S](https://doi.org/10.2298/AADM1801001S)
- Simsek, Y. (2019). Explicit formulas for p -adic integrals: Approach to p -adic distributions and some families of special numbers and polynomials. *Montes Taurus Journal of Pure and Applied Mathematics*, 1(1), 1-76.
- Simsek, Y. (2021a). Construction of generalized Leibnitz type numbers and their properties. *Advanced Studies in Contemporary Mathematics*, 31(3), 311-323. doi:[10.17777/ascm2021.31.3.311](https://doi.org/10.17777/ascm2021.31.3.311)
- Simsek, Y. (2021b). Interpolation functions for new classes special numbers and polynomials via applications of p -adic integrals and derivative operator. *Montes Taurus Journal of Pure and Applied Mathematics*, 3(1), 38-61.

- Simsek, Y. (2021c). New integral formulas and identities involving special numbers and functions derived from certain class of special combinatorial sums. *Revista de la Real Academia de Ciencias Exactas, Físicas y Naturales. Serie A. Matemáticas, (RACSAM)*, 115, 1-14. doi:[10.1007/s13398-021-01006-6](https://doi.org/10.1007/s13398-021-01006-6)
- Simsek, Y. (2021d). Miscellaneous formulae for the certain class of combinatorial sums and special numbers. *Bulletin, Classe des Sciences Mathématiques et Naturelles, Sciences mathématiques*, 46(1), 151-167.
- Simsek, Y. (2022a). Applications of Apostol-type numbers and polynomials: Approach to techniques of computation algorithms in approximation and interpolation functions. In: N. J. Daras & Th. M. Rassias (Eds.) *Approximation and Computation in Science and Engineering*, Springer Optimization and Its Applications 180, (pp. 783-860). doi:[10.1007/978-3-030-84122-5_40](https://doi.org/10.1007/978-3-030-84122-5_40)
- Simsek, Y. (2022b). Derivation of computational formulas for certain class of finite sums: Approach to generating functions arising from p -adic integrals and special functions. *Mathematical Methods in the Applied Sciences*, doi:[10.1002/mma.8321](https://doi.org/10.1002/mma.8321)
- Simsek, Y. (2022c). Some classes of finite sums related to the generalized Harmonic functions and special numbers and polynomials. *Montes Taurus Journal of Pure and Applied Mathematics*, 4(3), 61-79.
- Srivastava, H. M., & Kızılateş, C. (2019). A parametric kind of the Fubini-type polynomials. *Revista de la Real Academia de Ciencias Exactas, Físicas y Naturales. Serie A. Matemáticas (RACSAM)*, 113, 3253-3267. doi:[10.1007/s13398-019-00687-4](https://doi.org/10.1007/s13398-019-00687-4)



Gazi University

Journal of Science

PART A: ENGINEERING AND INNOVATION

<http://dergipark.org.tr/gujisa>

A Hybrid Attention-based LSTM-XGBoost Model for Detection of ECG-based Atrial Fibrillation

Furkan BALCI*

¹Gazi University, Faculty of Technology, Department of Electrical Electronics Engineering, Ankara, Turkey

Keywords	Abstract
LSTM Atrial Fibrillation Classification Deep Learning	Atrial fibrillation (AF) is a frequently encountered heart arrhythmia problem today. In the method followed in the detection of AF, the recording of the Electrocardiogram (ECG) signal for a long time (1-2 days) taken from people who are thought to be sick is analyzed by the clinician. However, this process is not an effective method for clinicians to make decisions. In this article, various artificial intelligence methods are tested for AF detection on long recorded ECG data. Since the ECG data is a time series, a hybrid model has been tried to be created with the Long Short Term Memory (LSTM) algorithm, which gives high results in time series classification and regression, and a hybrid method has been developed with the Extreme Gradient Boosting algorithm, which is derived from the Gradient Boosting algorithm. To improve the accuracy of the LSTM architecture, the architecture has been strengthened with an Attention-based block. To control the performance of the developed hybrid Attention-based LSTM-XGBoost algorithm, a public data set was used. Some preprocessing (filter, feature extraction) has been applied to this data set used. With the removal of these features, the accuracy rate has increased considerably. It has been proven to be a consistent study that can be used as a support system in decision-making by clinicians with an accuracy rate of 98.94%. It also provides a solution to the problem of long ECG record review by facilitating data tracking.

Cite

Balci, F. (2022). A Hybrid Attention-based LSTM-XGBoost Model for Detection of ECG-based Atrial Fibrillation. *GU J Sci, Part A, 9(3)*, 199-210.

Author ID (ORCID Number)	Article Process	
F. Balci, 0000-0002-3160-1517	Submission Date	08.06.2022
	Revision Date	28.07.2022
	Accepted Date	02.08.2022
	Published Date	14.08.2022

1. INTRODUCTION

The incidence of atrial fibrillation (AF) in individuals after childhood is 2.3%. This type of arrhythmia can cause consequences such as stroke and thrombosis. However, the duration of the attack is very short, so it is difficult to diagnose (Hagiwara et al., 2018). According to a report published by the World Health Organization, a total of 8.7 million people in the USA and Europe have a diagnosis of atrial fibrillation. This number is predicted to increase in the calculated future data (Guo et al., 2019; Wang et al., 2020; Shoeibi et al., 2021;). Measures should be taken against this expected increase. Atrial fibrillation, which has a reduction in a human's quality of health, is also an economic burden. Electrocardiogram, which is a noninvasive approach, provides clinicians with various information about atrial activities. It is considered by some experts to be the most understandable biomedical sign. A healthy electrocardiogram sign has three basic parts: P wave, QRS wave, and T wave (Acharya et al., 2017; Shoeibi et al., 2021). There are two main anomalies that clinicians make use of when detecting atrial fibrillation. These anomalies are the alteration of the P wave and the RR interval occurring at different times from the normal range. Classification is made according to the frequency of attacks in atrial fibrillation. These classifications are called paroxysmal atrial fibrillation, which occurs in less than 7 days and can end without any intervention, persistent atrial fibrillation that takes longer than 7 days, and permanent atrial fibrillation, which requires electrical cardioversion to be terminated (Acharya et al., 2017). An accurate and effective diagnosis is a critical issue to prevent people from being in danger.

*Corresponding Author, e-mail: furkanbalci@gazi.edu.tr

However, one of the most important obstacles here is the length of data that clinicians need to examine for diagnosis. Processing and analyzing large ECG data takes quite a long time. For patients with the paroxysmal variant, more than 24 hours of recording is required compared to Holter monitoring. In particular, these problems have led to the development of an artificial intelligence-based approach for the detection of atrial fibrillation. In recent years, very high results have been obtained in studies.

In the field of health, the performance of artificial intelligence-based algorithms that support clinicians in decision-making is increasing. Especially machine learning and deep learning techniques have shown high performance in classification studies in recent years. The parallel processing capability of deep learning methods by taking advantage of the high number of cores in the graphics processing units (GPU) allows them to perform high-performance processing, provided that there is sufficient data. Deep learning methods show high performance in time series data-based classification studies. Therefore, deep learning algorithms are used in the classification of biomedical signals. High accuracy can be achieved by using different methods in the classification of ECG beats and the detection of anomalies. Kiranyaz et al. (2015) performed the classification of ventricular and supraventricular ectopic beats using a CNN-based algorithm. Many artificial intelligence techniques are used to detect different beats like this. Apart from artificial intelligence methods, anomaly detections are also carried out by methods such as entropy (Li et al., 2014), wavelet transform (Sadeghi et al., 2022), and spectrum-based analyzes (Zarei et al., 2016). However, these methods have lower accuracy values. In artificial intelligence-based studies, the accuracy value can reach very high levels with different approaches. Time series such as ECG recording can be used in artificial intelligence-based studies, but due to the abundance of this data, it significantly increases the processing time. Therefore, feature extraction is used. In the attribute step, the data is divided into meaningful small pieces. In this way, systems that support clinicians' decisions and give faster results can be developed. Classification and regression processes can be performed with deep learning and machine learning algorithms. In particular, algorithms based on windowing techniques are used for the detection of arrhythmias. In this type of study, various features are generally extracted. Some of the deep learning and machine learning algorithms are known to show high performance in classifying time series due to their architecture. Examples of these algorithms are CNN, RNN, and LSTM. Pourbabae et al. (2018) detect atrial fibrillation by visualizing time series data using CNN architecture. Pourbabae et al. (2018) used a 4-layer structure in their CNN model. Xiong et al. (2017) detected atrial fibrillation using a 16-layer CNN architecture. Similar studies have been carried out according to the number of layers in the CNN architecture. The advantages of RNN and LSTM architectures in studies using time series data are known. Therefore, various hybrid approaches are implemented with the CNN architecture. Andersen et al. (2019) used a hybrid CNN-LSTM for a classification, taking into account the RR interval. There are many CNN and LSTM-based studies similar to this study (Chen et al., 2020; 2021; Petmezas et al., 2021). Besides hybrid approaches, there are also studies using LSTM and RNN architectures (Pascanu et al., 2012; Zhang et al., 2016; Kim & Cho, 2019; Yao et al., 2020). In addition, some studies have been revealed by combining RNN and LSTM architecture. Faust et al. (2018) used a hybrid RNN-LSTM architecture to perform a classification study between atrial fibrillation and normal sinus rhythm.

In this study, the hybrid LSTM-XGBoost algorithm that detects atrial fibrillation using electrocardiogram data is proposed. A publicly available data set was used to analyze the performance of the algorithm. Various features are extracted before the model directly uses the data. Thanks to these extracted features, the time spent by processing directly on the time series is saved. It is known that the performance of the LSTM architecture in time series is high. However, it is desired that the accuracy of the decision aid systems used by clinicians for detection and diagnosis is quite high. Therefore, in this study, a hybrid method was developed by combining the LSTM architecture with the XGBoost algorithm developed from Gradient boost. This hybrid approach has greatly improved the performance of the LSTM algorithm. First of all, the data is classified by LSTM. Then, the weights of the LSTM architecture are optimized with XGBoost and reclassified. In this way, a model with high accuracy that can be compared with the studies in the literature was obtained.

The remainder of this article consists of 3 parts. In Chapter 2, general information about the data set to be used in this hybrid model and the LSTM and XGBoost architectures to be used in the hybrid model are given. Section 3 shows the results of the proposed hybrid method. It is also discussed by showing the position of the experimental results in the literature. In Chapter 4, the article ends.

2. MATERIAL AND METHOD

A hybrid Attention-based LSTM-XGBoost model that detects atrial fibrillation anomalies is recommended in this study. The flowchart of this model is presented in Figure 1.

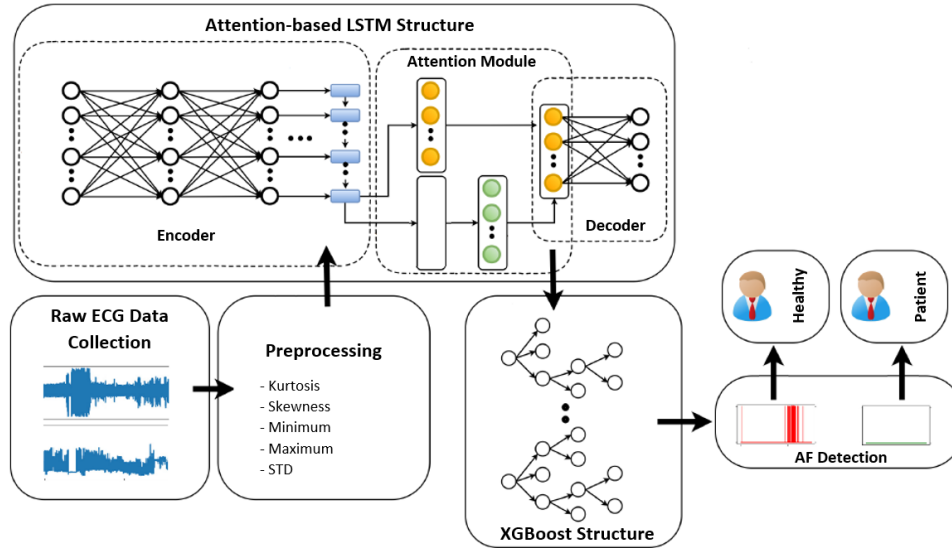


Figure 1. Flowchart of Hybrid Attention-based LSTM-XGBoost Architecture

2.1. Datasets

The data sets used in the study are shared publicly. Dataset from sick individuals MIT-BIH Atrial Fibrillation (AFDB) is a dataset that mostly includes records from patients with paroxysmal atrial fibrillation. In this data set, which consists of long-term recordings, there are ECG signals from 25 subjects. The duration of data from each patient is approximately 10 hours. General features of the recorder; Two-channel ECG electrode sampling at 250 samples per second with the accuracy of the voltage output is ± 10 mV with a 12-bit resolution (Moody & Mark, 1983). There is also a data file about the data from each subject, which was obtained using the R-peak detection algorithm. The average total recording time is approximately 10.2 hours. The number of atrial fibrillations is 291, the duration is 1155.4 seconds. A total of 828000 R-peaks were observed in the data set. MIT-BIH Long-Term ECG dataset was used to classify healthy individuals. There is a recording with the same recording parameters as the AFDB dataset but with a longer duration (14 hours) from 7 subjects. The data set consisting of healthy individuals was used only for educational purposes in the detection of atrial fibrillation. Because deep learning architectures such as LSTM require a lot of data.

2.2. Pre-processing

The AFDB and MIT-BIH Long-term ECG dataset includes data from each patient. For atrial fibrillation detection, the data was first segmented so that it could be processed into windows. Although the data was divided into claws, there was no change in the processing time as there was no reduction in the number of data. Therefore, after windowing the data, meaningful features should be extracted. Five different attributes were extracted for each window. These are Skewness, kurtosis, minimum, maximum, and standard deviation. The general formulas for these attributes are listed in Eq. 1-5. Thanks to the feature extraction together with the windowing process, the processing times can be shortened considerably.

$$Skewness = \frac{1}{N} \frac{\sum_{i=1}^N (x_i - mean)^3}{STD^3} \quad (1)$$

$$Min = \min(x_i) \quad (2)$$

$$Max = \max(x_i) \quad (3)$$

$$Kurtosis = \frac{1}{N} \frac{\sum_{i=1}^N (x_i - mean)^4}{STD^4} \quad (4)$$

$$STD = \sqrt{\frac{1}{N} \sum_{i=1}^N (x_i - mean)^2} \quad (5)$$

2.3. Long Short Term Memory Algorithm Architecture

In this study, a hybrid approach based on deep learning and machine learning is proposed. This deep learning structure is based on the Recurrent Neural Network (RNN) structure. The value to be estimated in RNN structures does not only analyze based on the current value but also based on historical data. Therefore RNN structures are frequently used in time series data (Ciregan et al., 2012; Deng & Yu, 2014). RNN structures do not delete old data, such as the work of the human brain. Classical neural network structures delete after using old data in the weighting setting (Ciregan et al., 2012). RNN structures have been developed to cover this gap. The data used in RNN-based structures are stored in memory units until the cycle is completed. RNN structure has the same structure as classical neural networks (Fukushima & Miyake, 1982). This structure is formed by listing the same networks. The input of each network be attached to the output of the previous RNN cells. There are varieties of RNN structures. Long Short Term Memory (LSTM) structure is used in this study to create hybrid Algorithm for detection of atrial fibrillation. LSTM structure has begun to be used widely in estimation processes based on historical data. RNN structure has a single-layer network structure. The LSTM structure has a four-layer network structure. There are structures called gates in the LSTM structure. These gate structures carry out tasks such as adding and removing information to the neural cell. The sigmoid function used in the neural network layer gives values between 0 and 1. The sigmoid function determines how much of the signal is allowed to pass. This value varying between 0 and 1 is used as a ratio. The first of these gates is called the forget gate. This gate makes an investigation between the prior output and the current input and produces a value between 0 and 1. On the off chance that the produced value is 0, it signifies “forget this state”, assuming the produced value is 1, it signifies “keep this state” (Deng & Yu, 2014). The forget gate is indicated by f_t . Eq. 6 shows the equation of the forget gate result.

$$f_t = \text{sigmoid}(W_f[h_{t-1}, x_t] + b_f) \quad (6)$$

Another gate layer is the input gate. This gate structure decides which new values to keep. In this step, both sigmoid and tanh functions are used. The sigmoid structure produces the value to be updated and the tanh structure produces the intermediate value C_{tx} . Eq. 7 shows the equation of the sigmoid function. Eq. 8 shows the equation of the tanh function. Then these values are combined.

$$i_t = \text{sigmoid}(W_i[h_{t-1}, x_t] + b_i) \quad (7)$$

$$C_{tx} = \text{sigmoid}(W_c[h_{t-1}, x_t] + b_c) \quad (8)$$

Using it and C_{tx} values, C_t is generated that allows the old data to be transferred to the next cell. Eq. 9 shows the current data equation C_t obtained with old data and new entries.

$$C_t = f_t * C_{t-1} + i_t * C_{tx} \quad (9)$$

In the next step, the output of that cell must be calculated. This calculated output is branched to be used in the next cell. It is necessary to decide which data will be used as output from the cell. Sigmoid function is used to make this decision. Eq. 10 shows the equation of the sigmoid function. The tanh function is used to convert the result of the sigmoid function to between -1 and 1. The final cell output is obtained after this transformation. Eq. 11 shows the equation of the final cell output.

$$o_t = \text{sigmoid}(W_o[h_{t-1}, x_t] + b_o) \quad (10)$$

$$h_t = o_t * \tanh(C_t) \quad (11)$$

The Multivariate LSTM structure used in this study is similar to the classical LSTM structure described above. It has 2 differences from the classical LSTM structure. The dependent variable estimation result is estimated with more than one independent variable. LSTM architecture is used in the study carried out in various academic fields such as biomedical data in time series, economic data, and time series data related to the process (Stollenga et al., 2015; Song et al., 2019; Balci & Oralhan, 2020; Yin et al., 2021).

2.4. Extreme Gradient Boosting Architecture

The Extreme Gradient Boosting (XGBoost) algorithm is an application that has become a frequently preferred tool in decision trees and machine learning. It is an algorithm developed by determining the deficiencies of the Gradient Boost algorithm. This developed approach is accepted as an important tool in the field of supervised learning, which provides high performance in classification, regression, and ranking tasks (Jin et al., 2020). Supervised learning refers to a predictive model inference task from a set of labeled training examples. With this predictive model, it is possible to find solutions to problems such as determining whether a manufacturing defect has occurred or predicting temperature or humidity on a particular day. In this context, the XGBoost algorithm can be expressed as a supervised learning algorithm that applies a process called augmentation to produce accurate models (Mitchell & Frank, 2017). Augmented trees in the XGBoost algorithm are divided into regression and classification trees. The essence of this algorithm is based on optimizing the objective function value (Król-Józaga, 2022). The most important point of the XGBoost structure is its scalability in all situations. XGBoost algorithm runs more than 10 times faster than current popular tree-based solutions on a single machine and scales to billions of instances in distributed or memory-limited settings (Mitchell & Frank, 2017). If the dataset is represented by D ; m features, n samples. y_i indicates the value predicted by the model. If the predicted value is shown as in Eq. 12, f_k represents the independent regression tree. The f_k function set in the regression tree model can learn by minimizing the target function (Chen & Guestrin, 2016).

$$y_i = \sum_{k=1}^K f_k(x_i), f_k \in F \quad (12)$$

When defining the XGBoost machine learning algorithm, certain parameters and values need to be entered. Parameter selection can be shaped according to the application to be used. Information about the default parameters and the value ranges of the parameters is shown in Table 1.

Table 1. Parameters of XGBoost Architecture

Parameter	Definition	Range	Default
Nround	Number of trees	[1, ∞]	10
Eta	Learning rate	[0,1]	0.3
Gamma	Lowest partition loss reduction	[0, ∞]	0
max_depth	Highest tree depth	[0, ∞]	6
minimum_child_weight	Minimum observation for new tree	[0, ∞]	1
Subsample	Random sample ratio to be used for training	[0, 1]	1
Lambda	Regulation term in weights	[0, ∞]	1
Alpha	Regulation term in weights	[0, ∞]	0
column_sample_tree	The columns ratio for the training of each tree	[0, 1]	1
column_sample_level	The column ratio for the training of the separation of each tree	[0, 1]	1

2.5. Hybrid Architecture Details

In this study, a hybrid model is proposed for the detection of atrial fibrillation. In this proposed method, the LSTM model, which shows superior performance in time series, and the XGBoost algorithm, which is a developed based on decision tree machine learning method, are combined. If the model is to be summarized in general, first of all, feature extraction was performed on the dataset. Studies in the literature were used to determine these extracted features. Later, these attributes were included in the hybrid LSTM-XGBoost structure. Atrial fibrillation detection has been performed and these points are given as the output of the algorithm.

Since this proposed hybrid method is a classification method, comparison will be made using the most important performance metrics currently used. These metrics are Accuracy (ACC), sensitivity (SEN), and specificity (SPF). General formulas of these metrics are given in Eq. 13-15.

$$ACC = \frac{TP+TN}{TP+TN+FP+FN'} \quad (13)$$

$$SEN = \frac{TP}{TP+FN'} \quad (14)$$

$$SPF = \frac{TN}{TN+FP'} \quad (15)$$

3. RESULTS AND DISCUSSION

A hybrid Attention-based LSTM-XGBoost method is proposed to detect these diseases in individuals with atrial fibrillation in this study. In this context, first of all, two different datasets were combined to perform the detection and classification process. An example graph of these datasets is shown in Figure 2a,b.

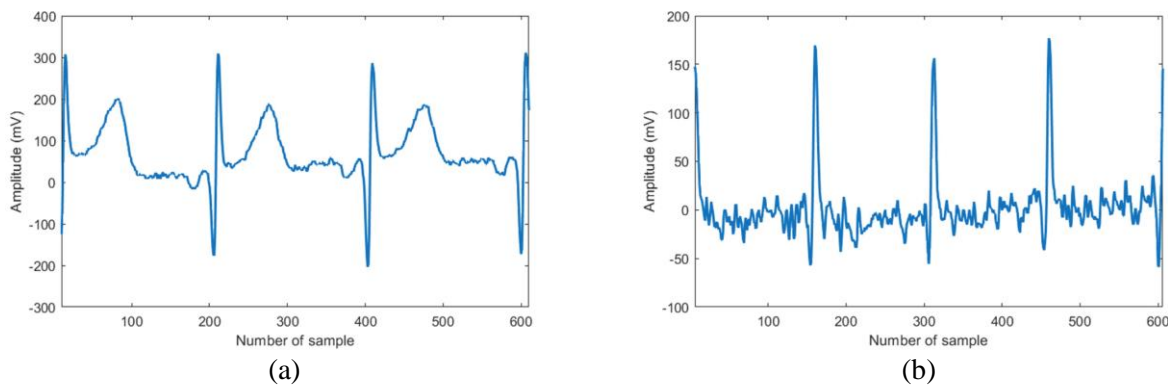


Figure 2. *a) A Sample of Normal Sinus Rhythm Segments, b) A Sample of Atrial Fibrillation Segment*

Each dataset has a column containing ECG data. The average recording time is approximately 10 hours in this dataset, which was obtained using a recorder that takes 250 samples per minute. This situation duplicates the data. Although deep learning architectures such as LSTM are suitable for big data, the large amount of data increases the processing time considerably. Therefore, feature extraction was done under the specified window size. In this way, both the data have been made more meaningful and the processing time has been shortened considerably. The features used were determined by the characteristics of the dataset. These attributes allow reducing the data of each window size to a single data. These attributes are Kurtosis, Skewness, minimum, maximum, and standard deviation. 65% of this dataset was used for training. The remaining 45% is used for testing purposes. For the LSTM structure, the n_{hidden} parameter is set to 30 and the number of layers to 5. Learning rate and lameda parameters were determined as 0.001. An attention-based block is embedded in the LSTM structure. Softmax is used in this block. The weights obtained here are used for detection and classification in the XGBoost machine learning algorithm.

Detection of optimum parameter values is important for maximizing performance in any machine learning algorithm. It involves defining all parameter probabilities and then testing all combinations to select the sets with the best values of the classification results. Grid search means creating grid intervals using parameter values suitable for the algorithm. Random search means randomly selecting different parameter values and testing the results. In this study, the intervals determined by grid search were tested. The most suitable 5 parameters and their values were selected and the other parameters were used with their default values. The values determined for the most suitable parameters selected are given in Table 2. Therefore, the classification model of the XGBoost algorithm was created with these parameter values.

Table 2. Optimized Parameters of XGBoost Algorithm

Parameter	Grid Values	Best
Eta	0.05, 0.2, 0.3, 0.4	0.2
Nrounds	1, 10, 100, 150, 200	170
max_depth	1, 4, 6, 10, 12, 20	12
Subsample	0.5, 0.6, 0.7, 0.9, 1	1
column_sample_level	0, 1	1

Some test results of the proposed method are shown in Figure 3a,b. Figure 3a shows some predicted erroneous points and correctly predicted points during the detected normal sinus rhythm (NSR) of the hybrid Attention-based LSTM-XGBoost algorithm. Noisy data taken during the measurement makes it difficult to detect the R-peaks. Therefore, incorrect classifications may occur on segments. Faulty points are shown in Fig. 3(b) on normal sinus rhythm.

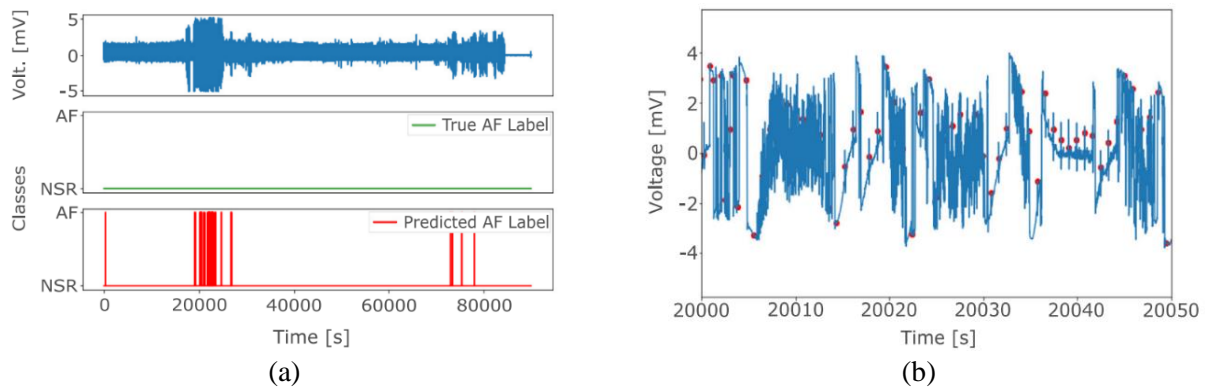


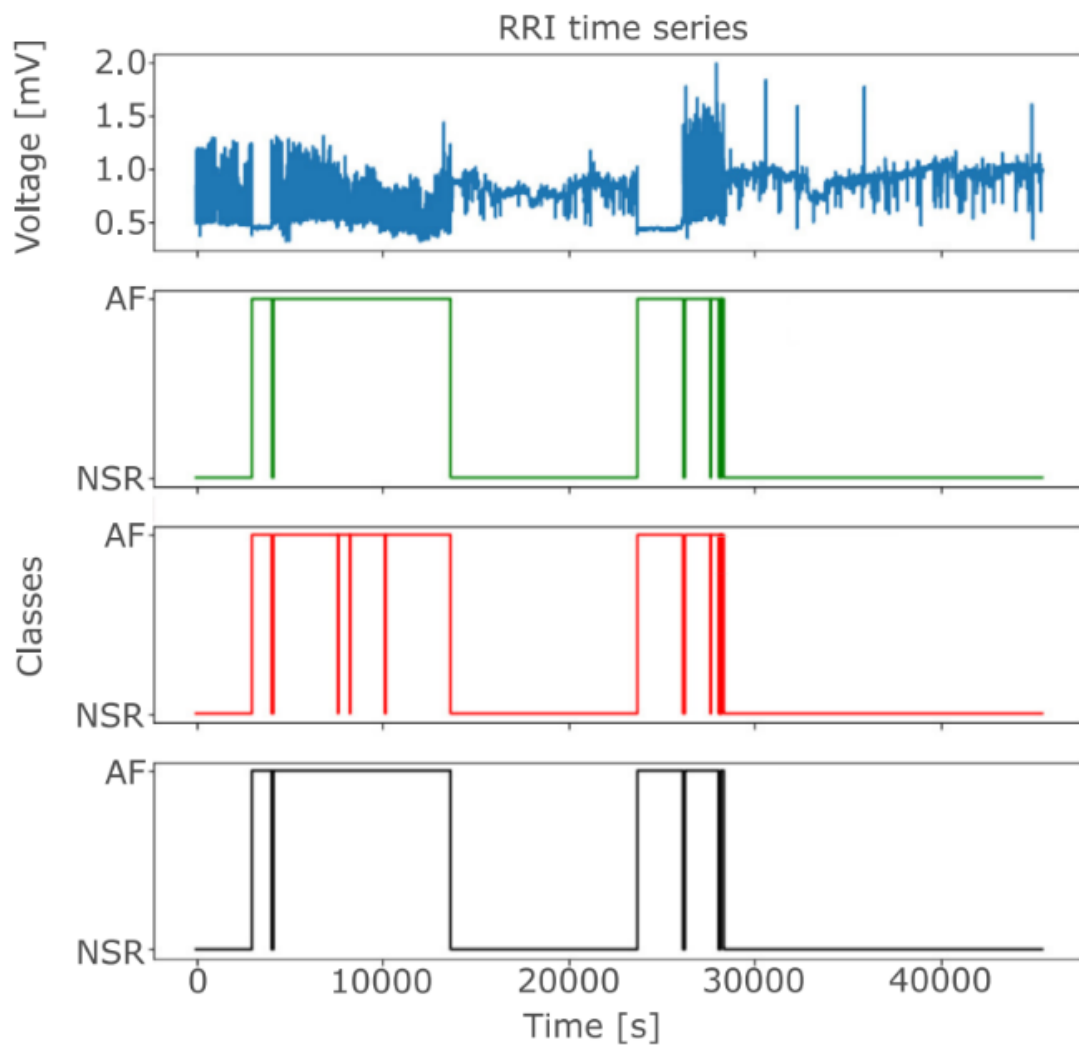
Figure 3. False Prediction Points During Normal Sinus Rhythm

The classification obtained at the output of the XGBoost algorithm has higher accuracy than the classification obtained at the output of LSTM. The result shown in Figure 4 is the blue graph showing the ECG recording. The green graph represents the actual atrial fibrillation points, the red graph represents the atrial fibrillation points obtained from the LSTM result, and the black graph represents the atrial fibrillation points obtained from the XGBoost result. When the graphics are examined, the proposed hybrid Attention-based LSTM-XGBoost method reveals a noticeable improvement compared to the approach determined only according to the LSTM result.

A comparative summary using machine and deep learning methods on the same dataset to compare the superiority of the hybrid Attention-based LSTM-XGBoost algorithm over other algorithms is shown in Table 3. Accuracy, sensitivity and specificity metrics of the algorithms used for comparison are shown in this table.

Table 3. Summary of the Results of Different Deep and Machine Learning Algorithms

Methods	Accuracy	Sensitivity	Specificity
kNN	92.41%	92.19%	92.65%
Decision Tree	89.80%	89.67%	89.56%
LSTM	92.98%	92.23%	92.35%
Random Forest	86.15%	86.11%	86.06%
MLP	95.00%	94.14%	94.76%
SVM	94.14%	94.79%	93.94%
Feature+LSTM+XGBoost	98.90%	98.47%	98.67%

**Figure 4.** Example Prediction Results of the Hybrid Approach

To compare the accuracy and the other performance metrics of the proposed approach, a comparison is made with the results of the studies in the literature. This comparison is shown in Table 4. When this table is examined, it can be seen that the results obtained have higher accuracy values than the “hybrid CNN-LSTM with Feature extraction” method made in 2019 (Kim & Cho, 2019). With these results, it is thought that the proposed method can be used as a mechanism to help clinicians make decisions.

Table 4. Comparison of the Studies in the Literature and Hybrid LSTM-XGBoost Algorithm

Authors	Methods	ACC	SEN	SPF
Xiong et al., 2017	CNN architecture	86.0%	-	-
Zhang et al., 2016	CNN architecture	95.50%	98.09%	-
Pourbabae et al., 2018	CNN architecture with feature extraction	-	76.50%	93.60%
Kim & Cho, 2019	Hybrid CNN-LSTM architecture with feature extraction	98.51%	98.39%	98.67%
Faust et al., 2018	Random forest with entropy-based feature extraction	96.80%	95.80%	-
Andersen et al., 2019	Hybrid CNN-LSTM architecture	97.80%	98.98%	96.95%
Król-Józaga, 2022	Feature extraction and CNN architecture	94.59%	94.28%	-
Kumar et al., 2018	RR features and Discrete state Markov model	-	97.40%	98.60%
Chen et al., 2020	RR features and Hybrid CNN-LSTM architecture	97.15%	97.11%	97.06%
Wei et al., 2019	Feature extraction and SCP architecture	95.00%	-	-
Kalidas & Tamil, 2019	Attention-based LSTM	-	98.14%	98.76%
Petmezas et al., 2021	Hybrid CNN-LSTM architecture	-	97.80%	-
Chen et al., 2021	CNN architecture with multi-feature extraction	98.92%	97.19%	97.04%
Buscema et al., 2020	CNN architecture with spectrogram features extraction	95.00%	-	-
Proposed Method	Hybrid Attention-based LSTM-XGBoost architecture with feature extraction	98.94%	98.47%	98.67%

Some limitations were encountered while carrying out this study. The first of these limitations is that this hybrid algorithm designed is focused only on detecting atrial fibrillation. Therefore, the hybrid LSTM-XGBoost architecture seems to be insufficient when tests are performed with different diseased data. Therefore, by expanding the dataset, classification can be made for the diagnosis of different diseases.

4. CONCLUSION

In this study, hybrid LSTM-XGBoost architecture is proposed for the detection of atrial fibrillation signals with using long or short term ECG data. The data of the patients and healthy individuals on the used dataset were first divided into certain windows. Various feature extraction techniques were applied before these windows were used for testing and training. To improve the accuracy of the detection, LSTM architecture is combined with attention-based structure. In the next step, a hybrid model was obtained by combining it with the XGBoost architecture. Thanks to the windowing technique used, the atrial fibrillation classification, which was the aim of this study, could also be determined locally. Since the designed algorithm has sufficient speed in terms of processing time, it might be used in real-time atrial fibrillation detection applications. Thanks to the features used, the processing time is considerably shortened. It is important for clinicians that it has a high accuracy rate compared to studies in the literature. As a result of the tests performed using the MIT-BIH AF dataset, an accuracy rate of 98.94% was obtained.

A system that supports decision-making for clinicians by directly integrating this system into portable ECG measuring devices may be the subject of future studies. The proposed approach may be insufficient because different diseases are not classified. Therefore, the proposed hybrid method in future studies can be trained with different data and become a more comprehensive study.

CONFLICT OF INTEREST

The authors declare no conflict of interest.

REFERENCES

- Acharya, U. R., Fujita, H., Lih, O. S., Adam, M., Tan, J. H., & Chua, C. K. (2017). Automated detection of coronary artery disease using different durations of ECG segments with convolutional neural network. *Knowledge-Based Systems*, 132, 62-71. doi:[10.1016/j.knosys.2017.06.003](https://doi.org/10.1016/j.knosys.2017.06.003)
- Andersen, R. S., Peimankar, A., & Puthusserypady, S. (2019). A deep learning approach for real-time detection of atrial fibrillation. *Expert Systems with Applications*, 115, 465-473. doi:[10.1016/j.eswa.2018.08.011](https://doi.org/10.1016/j.eswa.2018.08.011)
- Balci, F., & Oralhan, Z. (2020). LSTM ile EEG Tabanlı Kimliklendirme Sistemi Tasarımı. *Avrupa Bilim ve Teknoloji Dergisi, Özel Sayı (HORA)*, 135-141. doi:[10.31590/ejosat.779526](https://doi.org/10.31590/ejosat.779526)
- Buscema, P. M., Grossi, E., Massini, G., Breda, M., & Della Torre, F. (2020). Computer aided diagnosis for atrial fibrillation based on new artificial adaptive systems. *Computer Methods and Programs in Biomedicine*, 191, 105401. doi:[10.1016/j.cmpb.2020.105401](https://doi.org/10.1016/j.cmpb.2020.105401)
- Chen, T., & Guestrin, C. (2016, August). *Xgboost: A scalable tree boosting system*. In: Proceedings of the 22nd ACM SIGKDD International Conference on Knowledge Discovery and Data Mining (pp. 785-794). doi:[10.1145/2939672.2939785](https://doi.org/10.1145/2939672.2939785)
- Chen, C., Hua, Z., Zhang, R., Liu, G., & Wen, W. (2020). Automated arrhythmia classification based on a combination network of CNN and LSTM. *Biomedical Signal Processing and Control*, 57, 101819. doi:[10.1016/j.bspc.2019.101819](https://doi.org/10.1016/j.bspc.2019.101819)
- Chen, X., Cheng, Z., Wang, S., Lu, G., Xv, G., Liu, Q., & Zhu, X. (2021). Atrial fibrillation detection based on multi-feature extraction and convolutional neural network for processing ECG signals. *Computer Methods and Programs in Biomedicine*, 202, 106009. Doi:[10.1016/j.cmpb.2021.106009](https://doi.org/10.1016/j.cmpb.2021.106009)
- Ciregan, D., Meier, U., & Schmidhuber, J. (2012, June). *Multi-column deep neural networks for image classification*. In: 2012 IEEE Conference on Computer Vision and Pattern Recognition (CVPR) (pp. 3642-3649). doi:[10.1109/CVPR.2012.6248110](https://doi.org/10.1109/CVPR.2012.6248110)
- Deng, L., & Yu, D. (2014). Deep Learning: Methods and Applications. *Foundations and Trends in Signal Processing*, 7(3-4), 197-387. doi:[10.1561/20000000039](https://doi.org/10.1561/20000000039)
- Faust, O., Shenfield, A., Kareem, M., San, T. R., Fujita, H., & Acharya, U. R. (2018). Automated detection of atrial fibrillation using long short-term memory network with RR interval signals. *Computers in Biology and Medicine*, 102, 327-335. doi:[10.1016/j.compbiomed.2018.07.001](https://doi.org/10.1016/j.compbiomed.2018.07.001)
- Fukushima, K., & Miyake, S. (1982). Neocognitron: A self-organizing neural network model for a mechanism of visual pattern recognition. In: S-i. Amari, & M. A. Arbib (Eds.), *Competition and Cooperation in Neural Nets* (pp. 267-285). Springer, Berlin, Heidelberg. doi:[10.1007/978-3-642-46466-9_18](https://doi.org/10.1007/978-3-642-46466-9_18)
- Guo, L., Sim, G., & Matuszewski, B. (2019). Inter-patient ECG classification with convolutional and recurrent neural networks. *Biocybernetics and Biomedical Engineering*, 39(3), 868-879. doi:[10.1016/j.bbe.2019.06.001](https://doi.org/10.1016/j.bbe.2019.06.001)
- Hagiwara, Y., Fujita, H., Oh, S. L., Tan, J. H., San Tan, R., Ciaccio, E. J., & Acharya, U. R. (2018). Computer-aided diagnosis of atrial fibrillation based on ECG signals: A review. *Information Sciences*, 467, 99-114. doi:[10.1016/j.ins.2018.07.063](https://doi.org/10.1016/j.ins.2018.07.063)
- Jin, Y., Qin, C., Huang, Y., Zhao, W., & Liu, C. (2020). Multi-domain modeling of atrial fibrillation detection with twin attentional convolutional long short-term memory neural networks. *Knowledge-Based Systems*, 193, 105460. doi:[10.1016/j.knosys.2019.105460](https://doi.org/10.1016/j.knosys.2019.105460)
- Kalidas, V., & Tamil, L. S. (2019). Detection of atrial fibrillation using discrete-state Markov models and Random Forests. *Computers in Biology and Medicine*, 113, 103386. doi:[10.1016/j.compbiomed.2019.103386](https://doi.org/10.1016/j.compbiomed.2019.103386)
- Kim, T.-Y., & Cho, S.-B. (2019). Predicting residential energy consumption using CNN-LSTM neural networks. *Energy*, 182, 72-81. doi:[10.1016/j.energy.2019.05.230](https://doi.org/10.1016/j.energy.2019.05.230)
- Kiranyaz, S., Ince, T., & Gabbouj, M. (2015). Real-time patient-specific ECG classification by 1-D convolutional neural networks. *IEEE Transactions on Biomedical Engineering*, 63(3), 664-675. doi:[10.1109/TBME.2015.2468589](https://doi.org/10.1109/TBME.2015.2468589)

- Król-Józaga, B. (2022). Atrial fibrillation detection using convolutional neural networks on 2-dimensional representation of ECG signal. *Biomedical Signal Processing and Control*, 74, 103470. doi:[10.1016/j.bspc.2021.103470](https://doi.org/10.1016/j.bspc.2021.103470)
- Kumar, M., Pachori, R. B., & Acharya, U. R. (2018). Automated diagnosis of atrial fibrillation ECG signals using entropy features extracted from flexible analytic wavelet transform. *Biocybernetics and Biomedical Engineering*, 38(3), 564-573. doi:[10.1016/j.bbe.2018.04.004](https://doi.org/10.1016/j.bbe.2018.04.004)
- Li, H., Pan, D., & Chen, C. P. (2014). Intelligent prognostics for battery health monitoring using the mean entropy and relevance vector machine. *IEEE Transactions on Systems, Man, and Cybernetics: Systems*, 44(7), 851-862. doi:[10.1109/TSMC.2013.2296276](https://doi.org/10.1109/TSMC.2013.2296276)
- Mitchell, R., & Frank, E. (2017). Accelerating the XGBoost algorithm using GPU computing. *PeerJ Computer Science*, 3, e127. doi:[10.7717/peerj-cs.127](https://doi.org/10.7717/peerj-cs.127)
- Moody, G. B., & Mark, R. G. (1983). A new method for detecting atrial fibrillation using R-R intervals. *Computers in Cardiology*, 227-230.
- Pascanu, R., Mikolov, T., & Bengio, Y. (2012). Understanding the exploding gradient problem. Computing Research Repository (CoRR). arxiv.org/abs/1211.5063v1
- Petmezas, G., Haris, K., Stefanopoulos, L., Kilintzis, V., Tzavelis, A., Rogers, J. A., Katsaggelos, A. K., & Maglaveras, N. (2021). Automated atrial fibrillation detection using a hybrid CNN-LSTM network on imbalanced ECG datasets. *Biomedical Signal Processing and Control*, 63, 102194. doi:[10.1016/j.bspc.2020.102194](https://doi.org/10.1016/j.bspc.2020.102194)
- Pourbabaee, B., Roshtkhari, M. J., & Khorasani, K. (2018). Deep convolutional neural networks and learning ECG features for screening paroxysmal atrial fibrillation patients. *IEEE Transactions on Systems, Man, and Cybernetics: Systems*, 48(12), 2095-2104. doi:[10.1109/TSMC.2017.2705582](https://doi.org/10.1109/TSMC.2017.2705582)
- Sadeghi, D., Shoeibi, A., Ghassemi, N., Moridian, P., Khadem, A., Alizadehsani, R., Teshnehlab, M., Gorriz, J. M., Khozeimeh, F., Zhang, Y.-D., Nahavandi, S., & Acharya, U. R. (2022). An overview of artificial intelligence techniques for diagnosis of Schizophrenia based on magnetic resonance imaging modalities: Methods, challenges, and future works. *Computers in Biology and Medicine*, 146, 105554. doi:[10.1016/j.compbiomed.2022.105554](https://doi.org/10.1016/j.compbiomed.2022.105554)
- Shoeibi, A., Khodatari, M., Jafari, M., Moridian, P., Rezaei, M., Alizadehsani, R., Khozeimeh, F., Gorriz, J. M., Heras, J., Panahiazar, M., Nahavandi, S., & Acharya, U. R. (2021). Applications of deep learning techniques for automated multiple sclerosis detection using magnetic resonance imaging: A review. *Computers in Biology and Medicine*, 136, 104697. doi:[10.1016/j.compbiomed.2021.104697](https://doi.org/10.1016/j.compbiomed.2021.104697)
- Song, S., Huang, H., & Ruan, T. (2019). Abstractive text summarization using LSTM-CNN based deep learning. *Multimedia Tools and Applications*, 78(1), 857-875. doi:[10.1007/s11042-018-5749-3](https://doi.org/10.1007/s11042-018-5749-3)
- Stollenga, M. F., Byeon, W., Liwicki, M., & Schmidhuber, J. (2015). Parallel multi-dimensional LSTM, with application to fast biomedical volumetric image segmentation. In: Proceedings of the Advances in Neural Information Processing Systems (pp. 2998-3006).
- Wang, J., Wang, P., & Wang, S. (2020). Automated detection of atrial fibrillation in ECG signals based on wavelet packet transform and correlation function of random process. *Biomedical Signal Processing and Control*, 55, 101662. doi:[10.1016/j.bspc.2019.101662](https://doi.org/10.1016/j.bspc.2019.101662)
- Wei, X., Li, J., Zhang, C., Liu, M., Xiong, P., Yuan, X., Li, Y., Lin, F., & Liu, X. (2019). Atrial fibrillation detection by the combination of recurrence complex network and convolution neural network. *Journal of Probability and Statistics*, 2019. doi:[10.1155/2019/8057820](https://doi.org/10.1155/2019/8057820)
- Xiong, Z., Stiles, M. K., & Zhao, J. (2017, September). Robust ECG signal classification for detection of atrial fibrillation using a novel neural network. In: 2017 Computing in Cardiology (CinC), vol.44, (pp. 1-4). doi:[10.22489/CinC.2017.066-138](https://doi.org/10.22489/CinC.2017.066-138)
- Yao, Q., Wang, R., Fan, X., Liu, J., & Li, Y. (2020). Multi-class arrhythmia detection from 12-lead varied-length ECG using attention-based time-incremental convolutional neural network. *Information Fusion*, 53, 174-182. doi:[10.1016/j.inffus.2019.06.024](https://doi.org/10.1016/j.inffus.2019.06.024)

Yin, Y., Zheng, X., Hu, B., Zhang, Y., & Cui, X. (2021). EEG emotion recognition using fusion model of graph convolutional neural networks and LSTM. *Applied Soft Computing*, *100*, 106954. doi:[10.1016/j.asoc.2020.106954](https://doi.org/10.1016/j.asoc.2020.106954)

Zarei, R., He, J., Huang, G., & Zhang, Y. (2016). Effective and efficient detection of premature ventricular contractions based on variation of principal directions. *Digital Signal Processing*, *50*, 93-102. doi:[10.1016/j.dsp.2015.12.002](https://doi.org/10.1016/j.dsp.2015.12.002)

Zhang, S., Wu, Y., Che, T., Lin, Z., Memisevic, R., Salakhutdinov, R. R., & Bengio, Y. (2016). Architectural complexity measures of recurrent neural networks. In: D. Lee, M. Sugiyama, U. Luxburg, I. Guyon, & R. Garnett (Eds.) *Advances in Neural Information Processing Systems 29 (NIPS 2016)*.



Gazi University

Journal of Science

PART A: ENGINEERING AND INNOVATION

<http://dergipark.org.tr/gujisa>

An Investigation of Benford's Law Divergence and Machine Learning Techniques for Intra-Class Separability of Fingerprint Images

Aamo IORLIAM^{1*} , Emmanuel ORGEM¹ , Yahaya I. SHEHU² ¹Department of Mathematics & Computer Science, BSU, Makurdi, Nigeria²Shehu Shagari College of Education, Sokoto, Nigeria

Keywords	Abstract
Benford's Law	Protecting a biometric fingerprint database against attackers is very vital in order to protect against false acceptance rate or false rejection rate. A key property in distinguishing biometric fingerprint images is by exploiting the characteristics of these different types of fingerprint images. The aim of this paper is to perform an intra-class classification of fingerprint images using Benford's law divergence values and machine learning techniques. The usage of these Benford's law divergence values as features fed into the machine learning techniques has proved to be very effective and efficient in the intra-class classification of biometric fingerprint images. The effectiveness of our proposed methodology was demonstrated on five datasets resulting in a total of 367 samples. All the machine learning techniques used in this experiment were trained using the k-fold cross validation and the dataset was split into ten times (10-folds). The models achieved high intra-class classification mean accuracies of 99.72% for the Convolutional Neural Networks (CNN), and 95.90% for the Naïve Bayes. Again, the Decision Tree and Logistic Regression, achieved accuracies of 95.62%, and 94.47%, respectively. These results showed that Benford's law features and machine learning techniques, especially the CNN and Naïve Bayes can be effectively applied for the intra-class classification of fingerprint images. The implication of these results is that the different types of fingerprint images can be effectively discriminated using Benford's law divergence values and machine learning technique for forensics and biometrics applications.
Divergence Values	
Machine Learning Techniques	
Intra-Class Separability	
Fingerprint Images	

Cite

Iorliam, A., Orgem, E., & Shehu, Y. I. (2022). An Investigation of Benford's Law Divergence and Machine Learning Techniques for Intra-Class Separability of Fingerprint Images. *GU J Sci, Part A, 9(3)*, 211-224.

Author ID (ORCID Number)	Article Process	
A. Iorliam, 0000-0001-8238-9686	Submission Date	22.02.2022
E. Orgem, 0000-0003-3211-876X	Revision Date	26.04.2022
Y. I. Shehu, 0000-0001-8924-9344	Accepted Date	08.09.2022
	Published Date	26.09.2022

1. INTRODUCTION

Biometric experts have been dependent on fingerprints over the years for verification and identification purposes. There exist different types of fingerprint images which include contact-less acquired fingerprints, optically acquired fingerprints, and synthetically generated fingerprints (Hildebrandt et al., 2013; Maltoni et al., 2009). Since these fingerprints are used for different purposes, they should not be intentionally or unintentionally used for another purpose as this may cause a serious security threat (Iorliam et al., 2016). Therefore, this paper performs an investigation of machine learning techniques for intra-class classification of fingerprint images to classify fingerprint images of different types that have the same modality.

It has been reported in the literature that since 1938, Benford's law has proved beyond reasonable doubt that it possesses the capability to detect/classify original/untampered data from fake/tampered data (Benford, 1938; Hill, 1998; Iorliam et al., 2016). This interesting law (Benford's law) is therefore adopted for the intra-class separability of fingerprint images. Firstly, the gray-scale fingerprint images are used to calculate the first digit distribution of the JPEG coefficients using Equation 2. Furthermore, Equation 3 is used to calculate Benford's law divergence values. These divergence values are fed as inputs into the machine learning techniques such as the Naïve Bayes, Decision Tree, Logistic Regression, and Convolutional Neural Networks.

*Corresponding Author, e-mail: aamoiorliam@gmail.com

The applicability of this research is that it can serve as a preliminary forensic tool in classifying different types of fingerprint images for forensics and biometric applications. The major contributions of this work are summarized as follows:

- i. We propose a novel use of Benford's law divergence values to improve the intra-class classification of fingerprint images.
- ii. We provide a detailed analysis of the novel intra-class classification of fingerprint images using an empirical study based on theoretical and empirical perspectives.
- iii. We used only six Benford's law features (reduced features) and performed intra-class classification with a high-performance evaluation.

The rest of the paper is organized as follows. Related works are described in Section 2. Section 3 describes our experimental setup, need for intra-class separability of fingerprint images, datasets used, divergence metric determination, data pre-processing for intra-class separability of fingerprint images, and evaluation metrics used in our paper. Results and discussions are presented in Section 4. Conclusion and future work are presented in Section 5.

2. RELATED WORKS

Benford's law has proved to be very effective in detecting forged/tampered images (Fu et al., 2007; Iorliam 2016; Iorliam et al., 2017). The Benford's law was first discovered in 1881 by Simon Newcomb, where he noticed that the first pages of the logarithm table containing the first digits were worn more than the last pages of the logarithm table, which meant that people were looking up for numbers starting with 1 more often than numbers starting with 2, and so on (Hill, 1998). Unfortunately, Newcomb could not prove why the theory and formula worked. Then in 1938, Frank Benford proposed the Benford's law, also referred to as the first digit law, which states that multi-digit numbers beginning with 1, 2, or 3 appear more frequently than multi-digit numbers beginning with 4, 5, 6, 7, 8 and 9 (Benford, 1938; Iorliam et al., 2016). Therefore, original/untampered data is expected to follow Benford's law, which is illustrated in Figure 1.

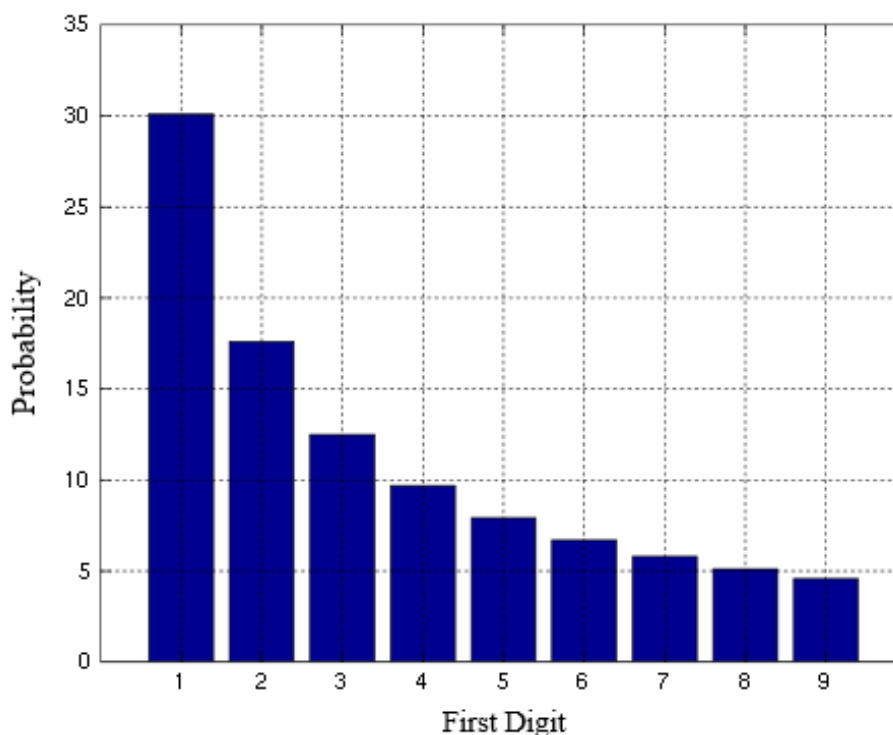


Figure 1: The first digit probability distribution of Benford's law (Benford, 1938; Iorliam et al., 2016).

Taking into consideration the Most Significant Digit, where 0 is not included, and a dataset under investigation satisfies Benford's law, the standard Benford's law is expressed in Equation 1.

$$p(x) = \log_{10}\left(1 + \frac{1}{x}\right), x = 1, 2, 3, \dots, 9 \quad (1)$$

where x is the first digit of the number and $p(x)$ refers to the probability distribution of x .

Since the inception of Benford's law, it is expected that naturally generated datasets should obey this law, whereas tampered or randomly generated datasets should deviate from this law. This inherent characteristic of the Benford's law can lead to important applications in forensics such as detecting anomalies or fraud in a given dataset (Iorliam & Shangbum, 2017; Satapathy et al., 2020) or classifying different types of biometric images (Iorliam et al., 2016; 2017).

Intra-class separability of biometric images means the classification of biometric images that appear to be identical (closely related) (Iorliam et al., 2017). For instance, fingerprint images such as contact-less acquired latent fingerprints, optically acquired fingerprints and synthetically generated fingerprints are closely related due to the fact that they cannot be easily classified based on their physical appearance, hence classifying them could be referred to as intra-class classification of fingerprint images (Iorliam et al., 2016). Even though intra-class classification of biometric images seems to be a novel area, Table 1 summarizes the related work in this area.

Table 1: Summary of Related Works

S/No	Author (s)	Implementation Strategy	Advantages
1	Hildebrandt and Dittmann (2015)	The model employed the use of Benford's law and WEKA's Bagging classifier in 10-fold stratified cross-validation.	Differentiated between real latent fingerprints and printed fingerprints using Benford's law in the spatial domain.
2	Iorliam et al. (2016)	Applied Benford's law and neural networks for the classification of biometric images.	A novel approach for the source identification of captured biometric images.
3	Iorliam and Shangbum (2017)	Used Benford's law with SVM in the biometric fingerprint tampering detection and separability of fingerprint images.	A novel approach to fight against insider attackers and hackers for securing biometric fingerprint images.
4	Hildebrandt (2020)	A thesis that contributed to digital forensics, latent fingerprint processing, and latent fingerprint forgery detection.	A novel contribution to digitized forensic and latent fingerprints.
5	Bonettini, et al. (2021)	Used Benford's law features with a simple Random Forest classifier.	Discriminated GAN-generated images from natural photographs.
6	Our Proposed Method	Used Benford's law features with Naive Bayes, Decision Tree, Logistic Regression, and CNN.	Effectively reduced features and achieved high intra-class separability of fingerprint images for forensics and biometrics applications.

To the best of the researcher's knowledge and review presented, this paper presents for the first time the novel use of Benford's law features with machine learning techniques to accurately classify the fingerprint images.

3. EXPERIMENTAL SETUP

The goal of this experiment is to utilize the acquired Benford's law divergence values from fingerprint images as proposed by Fu et al. (2007) and Iorliam et al. (2017) for the separability of fingerprint images.

In essence, the intra-class classification of biometric fingerprint images is performed on Benford's law divergence values of DB1, DB2, DB3, DB4, and the artificially acquired contact-less latent fingerprints images. The 10-fold cross-validation is applied on the extracted Benford's law divergence values. These fingerprint features are then fed into the Naive Bayes, Decision Tree, Logistic Regression, and Convolutional Neural Networks (CNN) algorithms as input data for separability purposes. The need for the separability of fingerprint images is discussed in Section 3.1.

3.1. Need for Intra-Class Separability of Fingerprint Images

The two key uses of biometrics are verification and identification. Verification is usually a 1-to-1 matching, whereas identification is a 1-to-many matching. For more than a century, fingerprints have been used for identification purposes (Jain et al., 1997; Iorliam et al., 2017). Fingerprints are used for different purposes as explained by Iorliam et al. (2017). Therefore, it is very important to avoid using a particular type of fingerprint for another purpose either intentionally or unintentionally. This can be achieved by studying the characteristic of each type of the different fingerprints and as such identifying the source of the captured fingerprint images. This could be possible if the source hardware that captured the fingerprint image is identified (Bartlow et al., 2009). One way to do this is by utilizing Benford's law divergence values with machine learning techniques to achieve the fingerprint images separability.

3.2. Data Sets Used

The FVC2000 (2000) fingerprint datasets which consists of four different fingerprint databases (DB1, DB2, DB3, and DB4) are used in this paper. Furthermore, artificially printed contact-less acquired latent fingerprint images are used for this research. Therefore, a total of five different datasets are used for testing our proposed model. The first four (4) sets of datasets each contain 80 grayscale fingerprint images (FVC2000, 2000). While the artificially printed contact-less acquired latent fingerprint images have 48 fingerprint biometric images (Hildebrandt et al., 2013). Other details about the datasets used are provided in Table 2.

Table 2: Summary Description of Datasets

Source	Dataset	Sensor Type	Sample No
FVC2000 (2000)	DB1	Low-cost Optical Sensor captured by "Secure Desktop Scanner".	80
	DB2	Low-cost Optical Capacitive Sensor captured by "TouchChip"	80
	DB3	Optical Sensor "DF-90"	80
	DB4	Synthetically generated images from Synthetic Generator	80
Hildebrandt et al., 2013	DB5	Artificially printed contact-less acquired latent fingerprint images	48

3.3. Divergence Metric Determination

Benford's law divergence values are obtained based on the biometric fingerprint dataset used in this paper described in Section 3.2. The divergence metric is used to show how close or far a particular dataset is using the standard or generalized Benford's law. In any case, smaller divergence yields a better fitting. In this paper, the first digit distributions of the JPEG coefficients are extracted from the gray-scale images as demonstrated by Iorliam et al. (2016).

Fu et al. (2007), extended the standard Benford's law to the Generalized Benford's law which closely follows the logarithmic law as expressed in Equation 2.

$$p(x) = N \log_{10} \left(1 + \frac{1}{s + x^q} \right) \quad (2)$$

where N is the normalization factor which makes $p(x)$ a probability distribution. The model parameters s and q describe the distributions for different fingerprint images and different compressions of the Quality Factor (QF). Through experiments, Fu et al. (2007), provided values for N , s , and q using the Matlab toolbox, which returns the Sum of Squares due to Error (SSE). The N , s , and q values are as shown in Table 3 for the Generalized Benford's law experiments.

Table 3: Model Parameters Used for the Generalized Benford's law (Fu et al., 2007)

Q-factor	Model Parameters			Goodness-of fit (SSE)
	N	q	s	
100	1.456	1.47	0.0372	$7.104e - 06$
90	1.255	1.563	-0.3784	$5.255e - 07$
80	1.324	1.653	-0.3739	$3.06838e - 06$
70	1.412	1.732	-0.337	$5.36171e - 06$
60	1.501	1.813	-0.3025	$6.11167e - 06$
50	1.579	1.882	-0.2725	$6.05446e - 06$

To test for conformity of a particular dataset (fingerprint images) to Benford's law, one of the most common criteria used is the chi-square goodness-of-fit statistics test (Acebo & Sbert, 2005; Li et al., 2012; Iorliam et al., 2016). The chi-square divergence is expressed in Equation 3.

$$x^2 = \sum_{x=1}^9 \frac{(P'x - Px)^2}{Px} \quad (3)$$

where $P'x$ is the actual first digit probability of the JPEG coefficients of the fingerprint biometric images and Px is the logarithmic law (Generalized Benford's law) as given in Eq. (2). In this study, the fingerprint datasets are singly compressed at a QF of 50 to 100 in a step of 10 (Iorliam et al., 2016). The divergence is calculated as an average on all the datasets earlier described in Table 2.

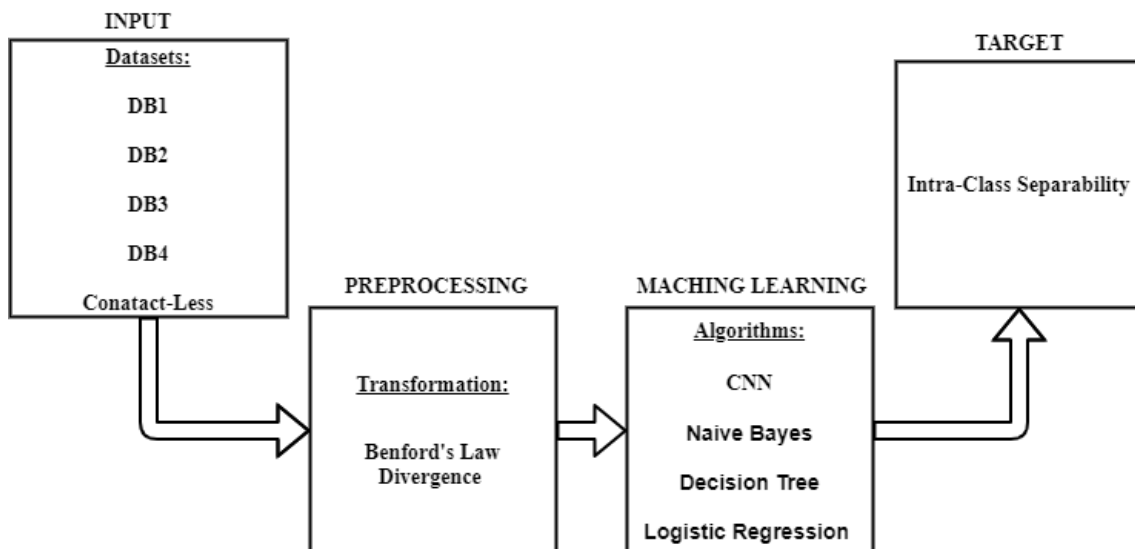
3.4. Data Pre-Processing for Intra-Class Separability of Fingerprint Images

In this paper, the fingerprint datasets are transformed into a format that can be easily interpreted by the machine learning techniques under consideration. The available biometric fingerprint images are transformed and this results in 368 instances with 6 features and a Class Label as shown in Table 4. The first 6 attributes are compression Quality Factors (QFs) ranging from 50 to 100 in a step of 10. The 7th attribute is the class label, which is represented as 0, 1, 2, 3, and 4 for DB1, DB2, DB3, DB4, and the artificially printed contact-less acquired latent fingerprint images (contact-less), respectively. The pre-processed values are achieved with the help of Benford's law divergence which is explained in Sections 3.3.

Table 4: The Pre-processed Dataset

QF-50	QF-60	QF-70	QF-80	QF-90	QF-100	Class Label
10.49719	10.80152	9.790624	8.71157	7.745091	7.761463	0
11.30665	10.93996	9.681446	8.675576	7.871395	8.270308	0
10.12913	10.14469	9.176165	8.658021	7.656819	7.184597	0
8.979308	9.382513	8.908421	8.30894	7.466352	6.91005	0
11.77114	11.00361	9.720688	8.637295	8.06052	8.575394	0
11.79356	11.31105	9.884672	8.865339	8.049554	8.608477	0
12.07603	11.50856	9.993754	8.806326	8.007224	8.698664	0
11.61334	11.30085	9.944549	8.701875	8.010162	8.350574	0
10.33387	10.20274	9.487949	8.407865	7.774554	7.828174	0
10.26303	9.98995	9.359262	8.556169	7.858129	8.139676	0
8.815993	9.117034	8.976531	8.549314	7.675995	7.306121	0
10.13061	9.755888	8.945211	8.413265	7.927866	8.046223	0

The divergence values (pre-processed dataset) therefore serve as inputs into the machine learning techniques (Naive Bayes, Decision Tree, Logistic Regression and CNN) algorithms considered in this paper. The Python programming language virtual platform (Google Colaboratory) is used to implement the proposed algorithms. The goal of our proposed method is to train these machine learning techniques to carry out the intra-class separability of fingerprint images. Therefore, to avoid any case of over-fitting of the pre-processed data used in this experiment, the 10-fold cross validation is applied on both the training and testing of the model. These algorithms are selected for usage because they are well suited for the labeled datasets considered in this paper. Figure 2 summarises the schematic diagram of the proposed model.

**Figure 2: Schematic Diagram of the Proposed Model**

3.5. Evaluation Metrics

To evaluate the proposed model, the following evaluation metrics are used:

- i. **Accuracy:** This is mathematically expressed by the formula:

$$\text{Accuracy} = (\text{TP} + \text{TN}) / (\text{TP} + \text{TN} + \text{FP} + \text{FN})$$

Where:

TP (True Positive): The outcome where the model correctly predicts the positive class.

TN (True Negative): The outcome where the model correctly predicts the negative class.

FP (False Positive): The outcome where the model incorrectly predicts the positive class.

FN (False Negative): The outcome where the model incorrectly predicts the negative class.

- ii. **Precision:** This is shown mathematically as:

$$\text{Precision} = (\text{TP}) / (\text{TP} + \text{FP})$$
- iii. **Recall:** This is shown mathematically as:

$$\text{Recall} = (\text{TP}) / (\text{TP} + \text{FN})$$
- iv. **F1-Score:** This is mathematically expressed as:

$$\text{F1-Score} = (2 \times \text{Precision} \times \text{Recall}) / (\text{Precision} + \text{Recall}).$$

4. RESULTS AND DISCUSSIONS

A. Naive Bayes Performance Results

The pre-processed fingerprint data is split ten times (10-folds) and fed into the Gaussian Naïve Bayes algorithm. As shown in Table 5, the Naïve Bayes algorithm achieved a mean accuracy of 95.90%, with a mean F1 score of 96.15%, the mean Precision value of 96.75%, and a 96.25% mean Recall value.

Table 5: Naive Bayes Results

Mean Accuracy:	95.90%
Mean F1 Score:	96.15%
Mean Precision:	96.75%
Mean Recall:	96.25%

Again, Figure 3 shows the confusion matrix result for the Naïve Bayes algorithm. The resulting confusion matrix shows that DB1, and contact-less classes were excellently classified at an accuracy of 100 percent.

However, for DB2, 11% of the fingerprint images were misclassified as DB3, and 89% of the fingerprint images were accurately classified as DB2. Considering DB3, 12% of the fingerprint images were misclassified as DB2, and 88% of the fingerprint images were accurately classified as DB3. For the DB4, 1% of the fingerprint images was misclassified as DB1 and 99% of the fingerprint images were accurately classified as DB4.

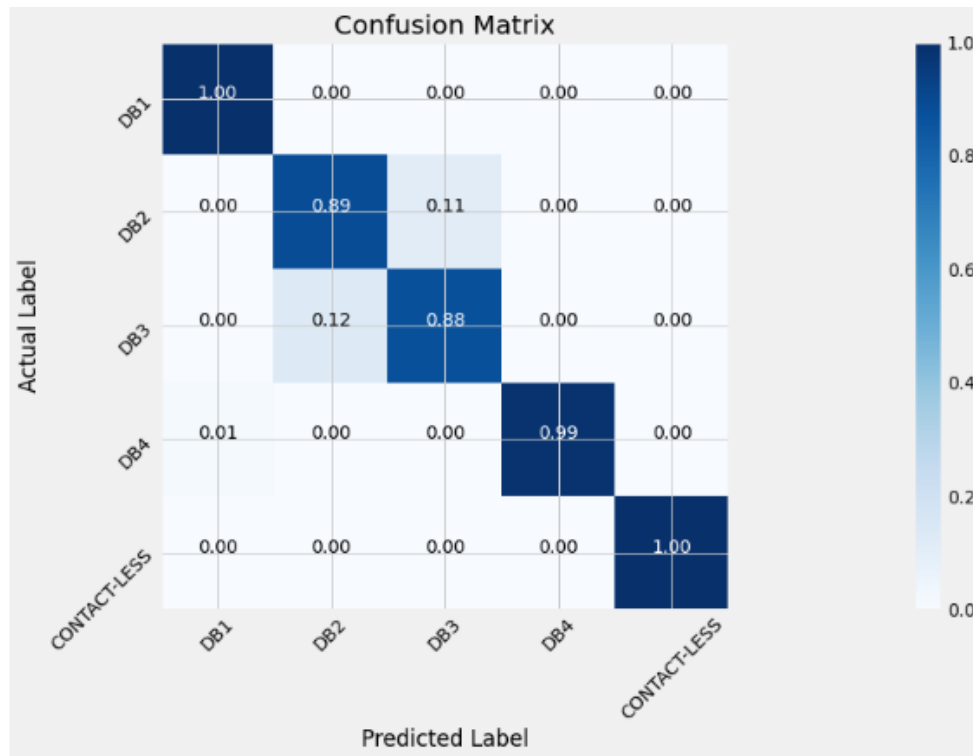


Figure 3: The Confusion Matrix for the Naïve Bayes Algorithm

B. Decision Tree Performance Results

The pre-processed fingerprint data is split ten times (10-folds) and fed into the Decision Tree algorithm. As shown in Table 6, the Decision Tree algorithm achieved a mean accuracy of 95.62 %, with a mean F1 score of 96.42%, the mean Precision value of 96.87%, and a 96.25% mean Recall value.

Table 6: Decision Tree Results

Mean Accuracy:	95.62 %
Mean F1 Score:	96.42%
Mean Precision:	96.87%
Mean Recall:	96.25%

The Decision Tree confusion matrix shows that DB1, DB4, and contact-less classes were excellently classified at 100% accuracy as shown in Figure 4. However, 10% of the fingerprint images in DB2 were misclassified as DB3, and 7% of the fingerprint images in DB3 were misclassified as DB2.

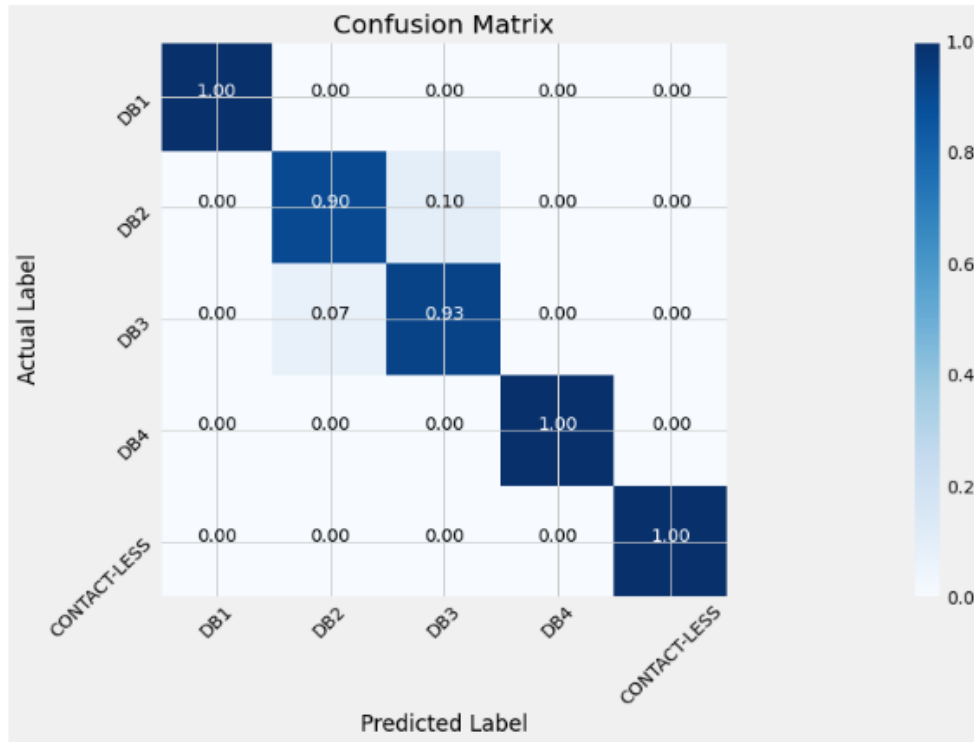


Figure 4: The Confusion Matrix for the Decision Tree Algorithm

C. Logistic Regression Performance Results

The Logistic Regression is also used to classify the fingerprint images into DB1, DB2, DB3, DB4, and the artificially acquired contact-less latent fingerprints images, taking into consideration the independent variables as QF’s ranging from 50 to 100 in a step of 10. The pre-processed fingerprint data is split ten times (10-folds) and fed into the Logistic Regression algorithm. In the Logistic Regression, the “max_iter=4000” to enable the algorithm converge properly.

The Logistic Regression algorithm achieved a mean accuracy of 94.47%, with a mean F1 score of 94.47%, the mean Precision value of 94.47%, and a 94.47% mean Recall value as shown in Table 7.

Table 7: Logistic Regression Results

Accuracy:	94.47%
F1 Score:	94.47%
Precision:	94.47%
Recall:	94.47%

The Logistic Regression confusion matrix shows that DB1, and contact-less classes were accurately classified with an accuracy of 100%. For the DB2, 11% of the fingerprint images were misclassified as DB3. Considering DB3, 12% of the fingerprint images were misclassified as DB2, and for the DB4, 1% of the fingerprint images were misclassified as DB1 as shown in Figure 5.

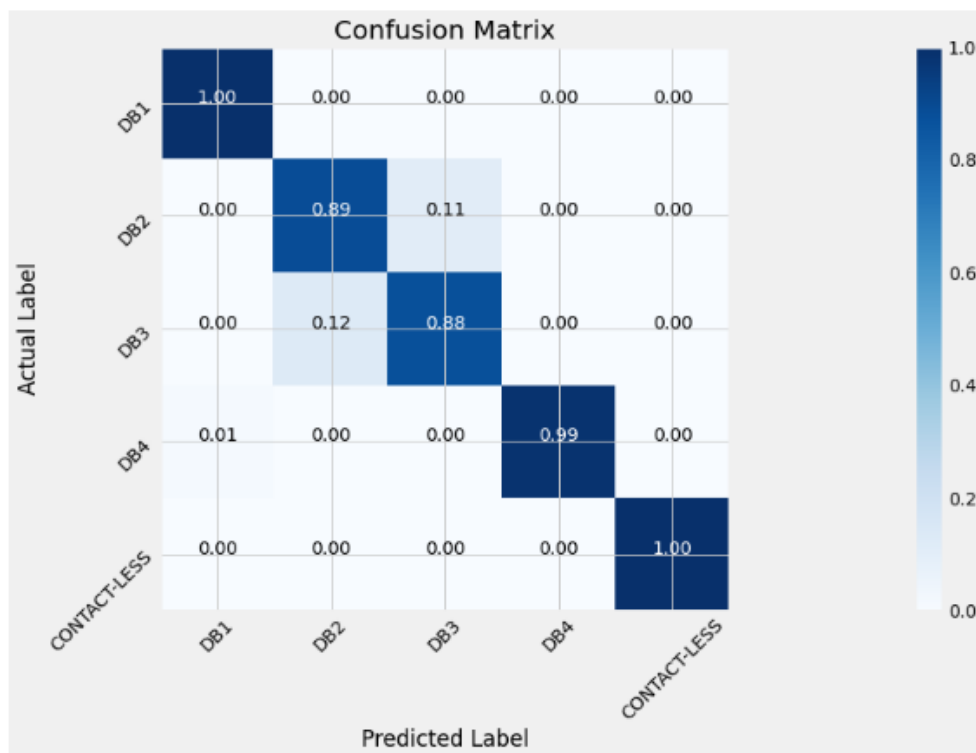


Figure 5: The Confusion Matrix for the Logistic Regression Algorithm

D. Convolutional Neural Network (CNN) Results

The pre-processed fingerprint data is split ten times (10-folds) and fed into the CNN. The sequential model “sequential ()” is used as the first layer. Furthermore, the first hidden layer had 6 input parameters, and 480 neurons. The rectified linear activation function (ReLU) is first chosen due to its ability to achieve higher performance. Another dense layer is added with 240 neurons. Again, the next dense layer is added with 120 neurons. The model is concluded with 5 dense layers, and a sigmoid activation function.

The binary_crossentropy is used as the loss function, the adam is used as the optimizer, and the accuracy is used as the metrics for the compilation of the CNN model. Two hundred (200) epochs are used in this experiment with a batch size of sixteen (16). Based on these parameters, Figure 6 shows the training loss versus epochs for the intra-class classification of fingerprint images for the CNN technique.

Based on the optimization capacity of the CNN, we always expect a lower loss to produce a better model, especially when considering the training vs. epochs.

We can see in Figure 6 that the loss tends more towards zero around 80 epochs and more. This shows that our proposed model performed well for the training and validation datasets, especially after 80 epochs.

Furthermore, the training accuracy vs. epochs considered in this experiment, for both the training and validation datasets, shows that epochs above 80 show more consistent and higher results that are closer to 1, as shown in Figure 7.

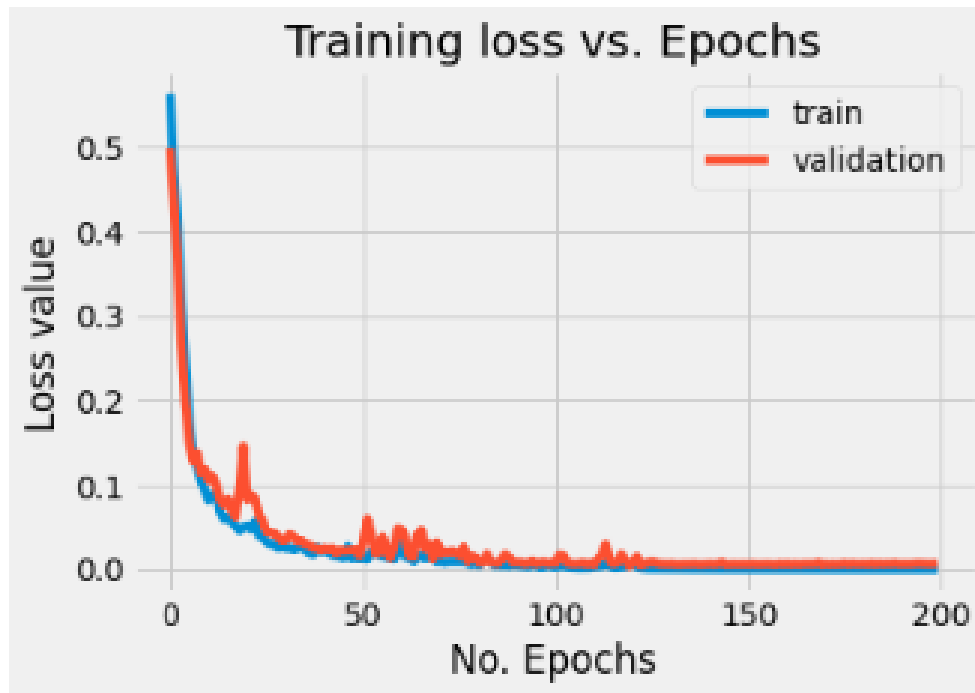


Figure 6: The CNN Training Loss Vs Epochs Graph

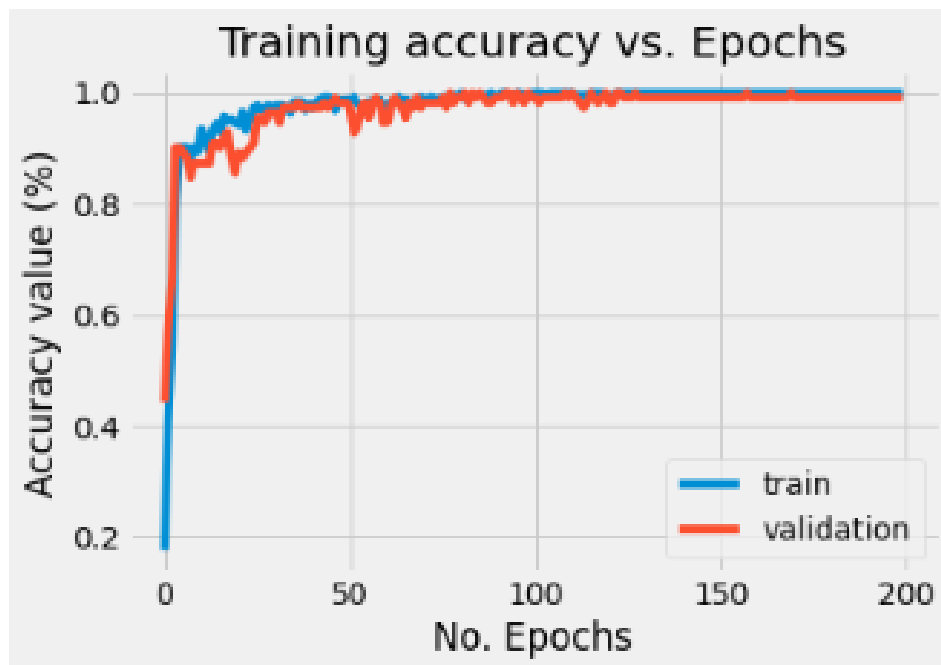


Figure 7: The CNN Training Accuracy vs Epochs Graph

Again, Figure 8 shows the confusion matrix for the intra-class classification using CNN. The confusion matrix shows that all the fingerprint images in DB1, DB4, and contact-less classes were correctly classified at 100% accuracy. While the DB2 fingerprint images were correctly classified at 90% accuracy, 10% of the DB2 fingerprint images were misclassified as DB3. Furthermore, the DB3 fingerprint images were correctly classified at 91% accuracy, and 9% of the DB3 fingerprint images were misclassified as DB1.

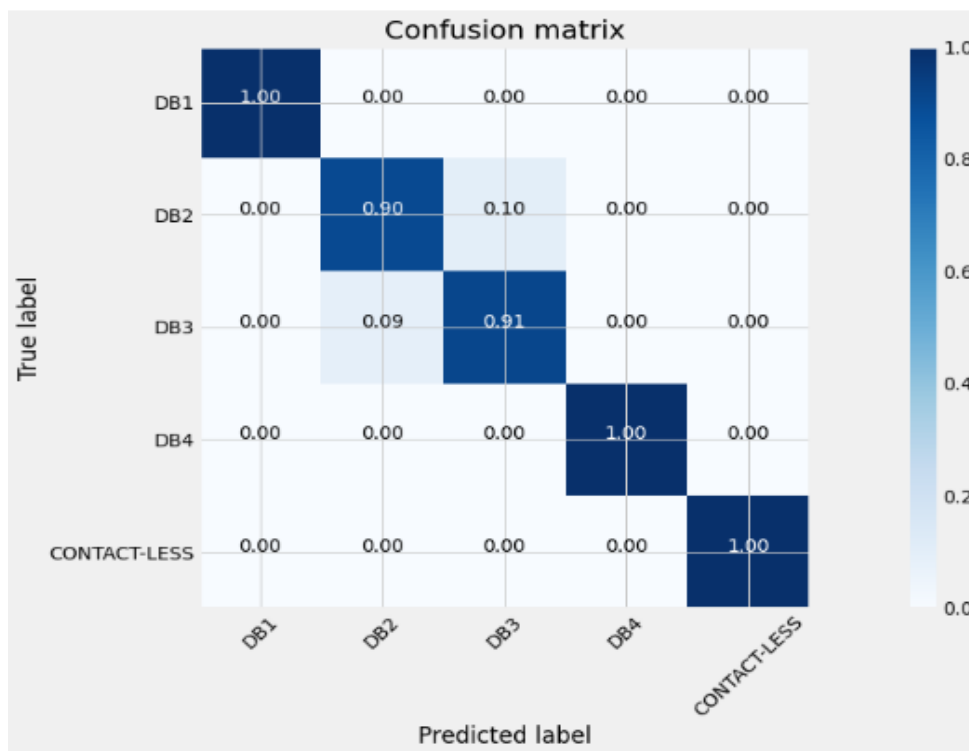


Figure 8: The Confusion Matrix for the CNN Algorithm

The novel proposed CNN method indeed performed the intra-class classification of fingerprint images accurately with an average classification accuracy of 99.72%.

For comparative purposes, our proposed method accuracy based on the Naïve Bayes (95.90%) outperformed that of Mishra and Maheshwary (2017) where they used the Naïve Bayes and SVM classifier for the classification of fingerprint images and achieved accuracies of 87.4% and 76.06%, respectively. Furthermore, we achieved similar results to that of Baştürk et al. (2018). Baştürk et al. (2018) recognised different types of fingerprint images using different machine learning techniques and observed that the deep neural network was more suited for the effective recognition of fingerprint images. Lastly, our proposed method when considering the CNN (99.72%) outperformed that of Qi et al. (2022). Qi et al. (2022) performed a gender-related classification based on fingerprint images using dense dilated convolution ResNet Autoencoder and achieved an average accuracy of 96.5%.

5. CONCLUSION AND FUTURE WORK

This paper proposed the novel use of Benford's law divergence values and machine learning techniques for the classification of fingerprint images by characteristics and/or sensor sources using Naive Bayes, Decision Tree, Logistic Regression, and CNN algorithms. It was shown that the Naive Bayes, Decision Tree, Logistic Regression and CNN algorithms successfully classified the fingerprint images with mean accuracies of 95.90%, 95.62%, 94.47%, and 99.72%, respectively.

This shows that our proposed method can effectively reduce features and achieve high intra-class separability results especially using the CNN and Naive Bayes algorithms. For future work, we plan to investigate other classification techniques such as Long Short-Term Memory (LSTM) for the intra-class classification and source identification of fingerprint images.

CONFLICT OF INTEREST

The authors declare no conflict of interest.

REFERENCES

- Acebo, E., & Sbert, M. (2005, May 18-20). *Benford's law for natural and synthetic images*. In: Proceedings of the First Eurographics Conference on Computational Aesthetics in Graphics, Visualization and Imaging (Computational Aesthetics'05) (pp. 169-176).
- Bartlow, N., Kalka, N., Cukic, B., & Ross, A. (2009, June 20-25). *Identifying sensors from fingerprint images*. In: 2009 IEEE Computer Society Conference on Computer Vision and Pattern Recognition Workshops (pp. 78-84). doi:[10.1109/CVPRW.2009.5204312](https://doi.org/10.1109/CVPRW.2009.5204312)
- Baştürk, A., Baştürk, N. S., & Qurbanov, O. (2018). A comparative performance analysis of various classifiers for fingerprint recognition. *Omer Halisdemir University Journal of Engineering Sciences*, 7(2), 504-513. doi:[10.28948/ngumuh.443160](https://doi.org/10.28948/ngumuh.443160)
- Benford, F. (1938). The law of anomalous numbers. *Proceedings of the American Philosophical Society*, 78(4), 551-572. [URL](#)
- Bonettini, N., Bestagini, P., Milani, S., & Tubaro, S. (2021, January 10-15). *On the use of Benford's law to detect GAN-generated images*. In: 25th International Conference on Pattern Recognition (ICPR) (pp. 5495-5502).
- Fu, D., Shi, Y. Q., & Su, W. (2007, January 28 - February 1). *A generalized Benford's law for JPEG coefficients and its applications in image forensics*. In: E. J. Delp III & P. W. Wong (Eds.), *Steganography, and Watermarking of Multimedia Contents IX* (SPIE 6505, Forensics III, pp. 65051L). doi:[10.1117/12.704723](https://doi.org/10.1117/12.704723)
- FVC2000. (2000), Fingerprint Verification Competition Databases. [URL](#)
- Hildebrandt, M. (2020). *On digitized forensics: novel acquisition and analysis techniques for latent fingerprints based on signal processing and pattern recognition*. PhD Thesis, Otto-von-Guericke-University of Magdeburg.
- Hildebrandt, M., & Dittmann, J. (2015, February 8-12). *Benford's Law based detection of latent fingerprint forgeries on the example of artificial sweat printed fingerprints captured by confocal laser scanning microscopes*. In: A. M. Alattar, N. D. Memon & C. D. Heitzenrater (Eds.), *Media Watermarking, Security, and Forensics 2015*, (SPIE 9409, Biometric, pp. 94090A). doi:[10.1117/12.2077531](https://doi.org/10.1117/12.2077531)
- Hildebrandt, M., Sturm, J., Dittmann, J., & Vielhauer, C. (2013, September 25-26). *Creation of a public corpus of contact-less acquired latent fingerprints without privacy implications*. In: B. Decker, J. Dittmann, C. Kraetzer & C. Vielhauer (Eds.), *Communications and Multimedia Security, 14th IFIP TC6/TC11 International Conference (CMS 2013)* (pp. 204-206). doi:[10.1007/978-3-642-40779-6_19](https://doi.org/10.1007/978-3-642-40779-6_19)
- Hill, T. P. (1998). The first digit phenomenon: A century-old observation about an unexpected pattern in many numerical tables applies to the stock market, census statistics and accounting data. *American Scientist*, 86(4), 358-363. [URL](#)
- Iorliam, A. (2016). *Application of power laws to biometrics, forensics and network traffic analysis*. PhD Thesis, University of Surrey (United Kingdom).
- Iorliam, A., & Shangbum, C. F. (2017). On the use of benford's law to detect jpeg biometric data tampering. *Journal of Information Security*, 8(3), 240-256. doi:[10.4236/jis.2017.83016](https://doi.org/10.4236/jis.2017.83016)
- Iorliam, A., Ho, A. T. S., Waller, A., & Zhao, X. (2016, September 17-19). *Using Benford's law divergence and neural networks for classification and source identification of biometric images*. In: Y. Q. Shi, H. J. Kim, F. Perez-Gonzalez & F. Liu (Eds.), *Digital Forensics and Watermarking, 15th International Workshop (IWDW 2016)* (pp. 88-105). doi:[10.1007/978-3-319-53465-7_7](https://doi.org/10.1007/978-3-319-53465-7_7)
- Iorliam, A., Ho, A. T. S., Poh, N., Zhao, X., & Xia, Z. (2017). Benford's law for classification of biometric images. In: C. Vielhauer (Eds.), *User-Centric Privacy and Security in Biometrics* (pp. 237-256). IET Digital Library. doi:[10.1049/PBSE004E_ch11](https://doi.org/10.1049/PBSE004E_ch11)
- Jain, A. K., Hong, L., Pankanti, S., & Bolle, R. (1997). An identity-authentication system using fingerprints. *Proceedings of the IEEE*, 85(9), 1365-1388. doi:[10.1109/5.628674](https://doi.org/10.1109/5.628674)

- Li, X. H., Zhao, Y. Q., Liao, M., Shih, F. Y., & Shi, Y. Q. (2012). Detection of the tampered region for JPEG images by using mode-based first digit features. *EURASIP Journal on Advances in Signal Processing*, 2012, 190. doi:[10.1186/1687-6180-2012-190](https://doi.org/10.1186/1687-6180-2012-190)
- Maltoni, D., Maio, D., Jain, A. K., & Prabhakar, S. (2009). *Handbook of fingerprint recognition*. Springer Science & Business Media.
- Mishra, A., & Maheshwary, P. (2017). A novel technique for fingerprint classification based on naive bayes classifier and support vector machine. *International Journal of Computer Applications*, 169(7), 58-62. doi:[10.5120/ijca2017914806](https://doi.org/10.5120/ijca2017914806)
- Satopathy, G., Bhattacharya, G., Puhan, N. B., & Ho, A. T. S. (2020, October 7-9). *Generalized Benford's Law for Fake Fingerprint Detection*. In: D. Dey, S. Dalai, S. Ray & B. Chatterjee (Eds.), 2020 IEEE Applied Signal Processing Conference (ASPCON) (pp. 242-246). doi:[10.1109/ASPCON49795.2020.9276660](https://doi.org/10.1109/ASPCON49795.2020.9276660)
- Qi, Y., Qiu, M., Lin, H., Chen, J., Li, Y., & Lei, H. (2022). Research on Gender-related Fingerprint Features, Extracting Fingerprint Features Using Autoencoder Networks for Gender Classification. [Preprint] doi:[10.21203/rs.3.rs-1399918/v1](https://doi.org/10.21203/rs.3.rs-1399918/v1)



Gazi University

Journal of Science

PART A: ENGINEERING AND INNOVATION

<http://dergipark.org.tr/gujisa>

The Effect of Nanostructured Titanium Surface on Protein Adsorption

Hasret Tolga ŞİRİN^{1*} , Ebru AKDOĞAN¹ ¹Ankara Hacı Bayram Veli Üniversitesi, Kimya Bölümü, Polatlı, 06900, Türkiye

Keywords	Abstract
Titanium Implant Nanotube Anodic Oxidation Protein Protein Adsorption	The amount and conformation of bovine serum albumin upon adsorption on titanium (Ti) surfaces containing nanotubes with different pore sizes were investigated. Nanotubes were created on the surfaces via anodization. Protein adsorption behavior on anodized surfaces were compared with the adsorption behavior on smooth and sanded Ti surfaces. The conformational changes in surface adsorbed proteins were evaluated using the second derivative and curve fitting methods applied to the Fourier transform infrared spectra of the surfaces. Results showed that the amount of protein adsorbed on the surfaces increased significantly with increasing surface roughness and a significant change in the conformation of the adsorbed protein occurred on every surface albeit in a different fashion. When anodized samples were considered, it was observed that the changes in the secondary structure seemed to be correlated with to the pore size of the nanotubes rather than the surface roughness.

Cite

Şirin, H.T., & Akdoğan E. (2022). The Effect of Nanostructured Titanium Surface on Protein Adsorption. *GU J Sci, Part A, 9(3)*, 225-232.

Author ID (ORCID Number)

H. T. Şirin, 0000-0002-5850-3052

E. Akdoğan, 0000-0002-1388-5595

Article Process

Submission Date 23.06.2022**Revision Date** 10.08.2022**Accepted Date** 16.09.2022**Published Date** 26.09.2022

1. INTRODUCTION

For many years, titanium (Ti) and its alloys are being used in hard tissue repair due to their good biological compatibility and mechanical properties. The roughness of the Ti implant surface is one of the most important factors affecting the bond between the bone and the implant (Sirin et al., 2016). The current trend in Ti biomaterials research is to develop surfaces with nanoscale topographic properties manipulate in vivo tissue response at the biomolecular and cellular level. The nano-topography of the surface determines the binding of important molecules in the blood, such as proteins, to the surface. Since the in vivo response to surface nanotopography at the cellular level is directed by the initial layer of surface adsorbed proteins, the design of biomaterial surfaces needs to consider optimizing protein adsorption and conformation (Lord et al., 2010).

The protein adsorption behavior, that can be defined as both the amount and the conformation of the surface bound proteins is a complex phenomenon affected by the physiochemical properties of the surface and the surrounding environment and the nature of the protein (Chen et al., 2022). Some of these effects, such as hydrophobic surfaces inducing more protein adsorption and protein denaturation, proteins adsorbing to surfaces at higher amounts when they are close to their isoelectric points, or protein adsorption being hampered when the surface and the protein bear the same charge due to electrostatic repulsions, have been extensively studied and widely elucidated (Barberi & Spriano, 2021). However, understanding the effect of surface nanotopography is an ongoing research interest. It is usually accepted that increased roughness affects protein-surface interactions by providing increased surface area and enhanced wettability (Barberi & Spriano, 2021). The surface nanotopography can dramatically change the protein adsorption behavior (Hu et al., 2022). For example, although the surface wettability is generally accepted as being correlated with protein adsorption and hydrophobic surfaces are shown to induce more protein adsorption and protein denaturation, for Ti surfaces,

*Corresponding Author, e-mail: tolga.sirin@hbv.edu.tr

it was reported that this correlation is valid for smooth Ti surfaces with rms roughness values lower than 1 nm. When the surface become rougher this correlation no longer holds ($Sq > 5\text{nm}$) (Barberi & Spriano, 2021). The protein conformation is also reported to significantly affected by nanomaterials. For example, a specific nanostructure such as nanowires can modulate protein conformation as to promote osteogenic differentiation better than other nanostructures (Li et al., 2020), the same nano-morphology can have a different effect on the adsorption behavior of different proteins (Yang et al., 2021). The conformation of proteins on TiO_2 nanotube arrays are reported to have a more critical role in subsequent cellular response and the conformation of a model protein fibronectin is reported to be determined by pore size of the arrays (Qi et al., 2021; Wu et al., 2022). Nano sized metal-organic frameworks have been reported to induce more vigorous conformational changes on the structure of human serum albumin than micro sized metal-organic frameworks (Gan et al., 2022).

In this study we aimed to investigate how nanostructures formed on Ti surface affects the amount and the conformation of surface adsorbed protein. For this purpose, surface nano structures were created in the form of nanotubes by anodic oxidation. The amount of protein (bovine serum albumin, BSA) adsorption on smooth, sanded and nanotube containing Ti surfaces as well as the changes in its conformation upon surface adsorption were compared. The significance of this study is that the results supports the paradigm that the protein adsorption behavior is dependent on nano-morphological features other than the surface roughness.

2. MATERIAL AND METHOD

2.1. Sample Preparation

Ti plates, cut into 1x2 cm dimensions, were cleaned sequentially in liquid detergent solution and 70% ethyl alcohol (Merck KGaA, Germany) by sonication (Elma GmbH, Germany). To remove the protective and inactive amorphous oxide layer on the surface Ti was etched in a 2% (v/v) HF (Merck KGaA, Germany); 3% (v/v) HNO_3 (Merck KGaA, Germany) solution under a fume hood for 5 minutes and washed with deionized water and left to dry in an oven at 70°C (Jeio Tech, Korea).

2.2. Anodic Oxidation and Sanding

Anodizing setup consisted of a DC power supply (Micro Medical Electronics, Turkey), Ti (anode) connected to the positive end of the source, platinum (cathode) connected to the negative end of the source, an electrolyte solution and a magnetic stirrer (Isotex, China) where the distance between the anode and cathode was kept constant at 4 cm. Ethylene glycol (Merck KGaA, Germany) containing 0.1M NH_4F (Merck KGaA, Germany) was used as electrolyte. Anodization processes were conducted at 20, 40, and 60 V for 20 minutes. After the process, the samples were rinsed with deionized water and dried at 70 °C. Sanded Ti plates (SB) were prepared using polishing papers. Samples were sanded with silicon carbide papers (3M), (P600, P1000, P2000, P2500, P3000), cut into pieces with 1x2 cm dimensions and cleaned sequentially in liquid detergent solution and 70% ethyl alcohol by sonication for 5 minutes. Finally, the samples were rinsed with deionized water and dried at 70°C.

2.3. Surface Characterization

Surface morphologies were evaluated using scanning electron microscope (TESCAN GAIA3 FIB-SEM)). The pore size and pore distribution of the TiO_2 nanotube arrays were analyzed using ImageJ program (1.53q) on the plan view of the surface. The morphology of the surfaces was investigated using atomic force microscopy (AFM, XE-100E, PSIA, South Korea) over an area of $1\mu\text{m} \times 1\mu\text{m}$ in tapping mode using. Mean roughness (Ra) value was calculated using the Gwyddion software (Gwyddion 2.60). The wettability of the surfaces was determined in terms of water contact angle (WCA) by an optical tensiometer (Attension Theta, Biolin Scientific, Sweden). The sessile drop method was used for this purpose.

2.4. Protein Adsorption

The amount of protein adsorption on the samples was determined using BSA (Serva Electrophoresis GmbH, Germany) as the model protein. For this purpose, samples were kept at 37°C for 24 hours in 1 mg/mL BSA solution in pH 7.4 phosphate buffered saline using a shaking water bath after which material surfaces were washed with the buffer solution for removing non-adsorbed proteins. Surface adsorbed proteins were extracted

using 1% sodium dodecyl sulfate (SDS, Merck KGaA, Germany) solution and its amount was determined using the bicinchoninic acid analysis (micro BCA, Thermo Scientific, USA), following the protocol included in the kit. Absorbance measurements were performed at a wavelength of 562 nm in a microplate reader (BMG LABTECH, Germany).

2.5. Protein Conformation

The spectra of protein adsorbed Ti surfaces were taken by averaging 512 scans for each sample using an attenuated total reflectance Fourier transform infrared spectrophotometer (FTIR-ATR, Bruker, USA) at a resolution of 4 cm^{-1} . A diamond crystal tip was used for the collection of the spectra. Following baseline correction, the amide-I band was further analyzed using the OriginPro software (Origin Lab, USA). The spectra were smoothed with 7-9 points Savitzky-Golay, the location of the component bands was determined from the second derivative of the spectra, and the component band positions and relative areas were determined using the curve fitting method. A Gaussian band shape was assumed and the band positions were not fixed during curve fitting (Akdoğan & Mutlu, 2012).

2.6. Statistical Analysis

For all measurements at least three samples were used ($n=3$) and the results are given as mean \pm standard deviation. Protein adsorption data were evaluated using one-way ANOVA and pairwise comparisons were made using Tukey's test at the 99.5% confidence level.

3. RESULTS AND DISCUSSION

3.1. Surface Characterization

SEM images of the anodized samples (Figure 1) confirmed nanotube formation on Ti surfaces. The pore diameter increased with increasing processing voltage and the Feret pore diameters of the nanotubes were calculated as $53 \pm 23\text{ nm}$, $62 \pm 33\text{ nm}$ and $125 \pm 17\text{ nm}$ for 20V, 40V and 60V samples, respectively.

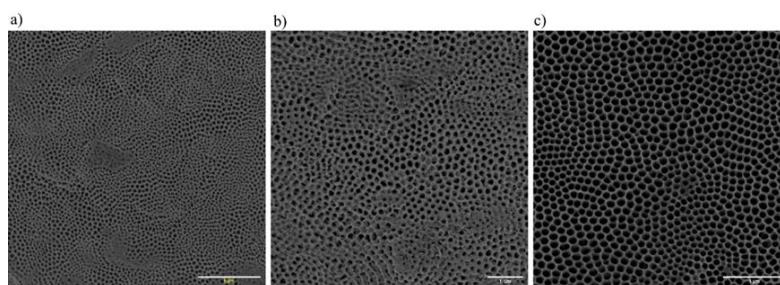


Figure 1. SEM images of anodized Ti surfaces at 50kX magnification a) 20V, b) 40V and c) 60V

The average roughness values (R_a) of the surfaces calculated from AFM images (Figure 2) were 7.04 nm, 13.91 nm, 16.21 nm, 18.30 nm and 18.89 nm for Ti, SB, 20V, 40V and 60V samples, respectively. Ti surface, is smoother than other surfaces, and both sanding and anodization processes increased the roughness of the surfaces. The surface roughness increased with the increasing applied voltage and this increase was more pronounced between the 20V and 40V sample surfaces than between the 40V and 60V sample surfaces.

The WCA values for Ti, SB, 20V, 40V and 60V were calculated as $78^\circ \pm 3^\circ$, $66^\circ \pm 1^\circ$, $37^\circ \pm 6^\circ$, $34^\circ \pm 2^\circ$ and $30^\circ \pm 2^\circ$, respectively. Although sanding increased the surface roughness, it only partially improved the surface wettability, while the effect of anodization process on WCA was more noticeable. Surface wettability determines the type interaction between the protein and the surface so that the hydrophobic interactions are dominant between proteins and hydrophobic surfaces, and electrostatic and van der Waals interactions are dominant between proteins and hydrophilic surfaces. In addition, surface hydrophilicity also affects the protein conformation such that protein denaturation becomes more significant as the hydrophobicity increased (Barberi & Spriano, 2021).

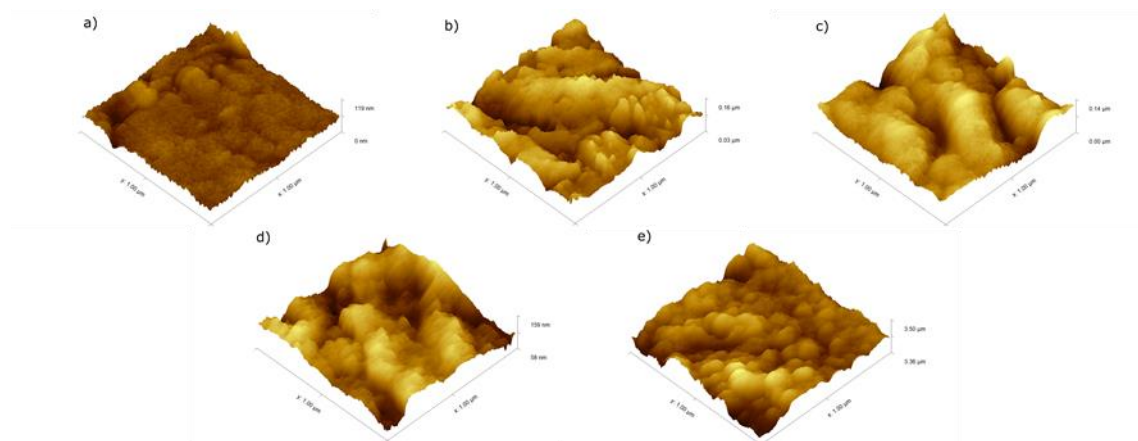


Figure 2. 3D AFM images of a) Ti, b) SB, c) 20V, d) 40V and e) 60V samples

3.2. Protein Adsorption

The amount of BSA adsorbed on Ti, SB, 20V, 40V and 60 V surfaces were; $295.59 \pm 34.6 \mu\text{g}/\text{cm}^2$, $368.03 \pm 29.34 \mu\text{g}/\text{cm}^2$, $387.76 \pm 15.13 \mu\text{g}/\text{cm}^2$, $401.33 \pm 22.68 \mu\text{g}/\text{cm}^2$ and $488.41 \pm 14.85 \mu\text{g}/\text{cm}^2$ respectively (Figure 3). However, the difference between the amount of BSA adsorbed on the SB, 20V and 40V sample surfaces at the 95% confidence level was not significant. With a hydrodynamic diameter of 7.2 nm, BSA can enter into nano-pores larger than 9 nm and can be adsorbed there, as the pores gets larger, more than one BSA molecule can be absorbed without significantly affecting each other's conformation. Hence, increased porosity in such surfaces is reported to be the main reason for an increased amount of protein adsorption (Singh et al., 2011, Liu et al., 2016). The pore sizes of all anodized samples are well over 9 nm and the increased amount of surface adsorbed protein compared to the Ti surface can be attributed to the increased porosity. In the literature, contradictory results have been reported as how sanding process affects protein adsorption concluding that random roughness provided by this process either increases or does not significantly affect the protein adsorption (Barberi & Spriano, 2021). In this study, the roughness obtained at Ra 13.9 nm level with sanding significantly increased BSA adsorption compared to the relatively smoother Ti surface. The fact that there is no dramatic difference between the WCA values of these two surfaces indicates that the increased surface area might be responsible for the increase in the amount of surface adsorbed protein.

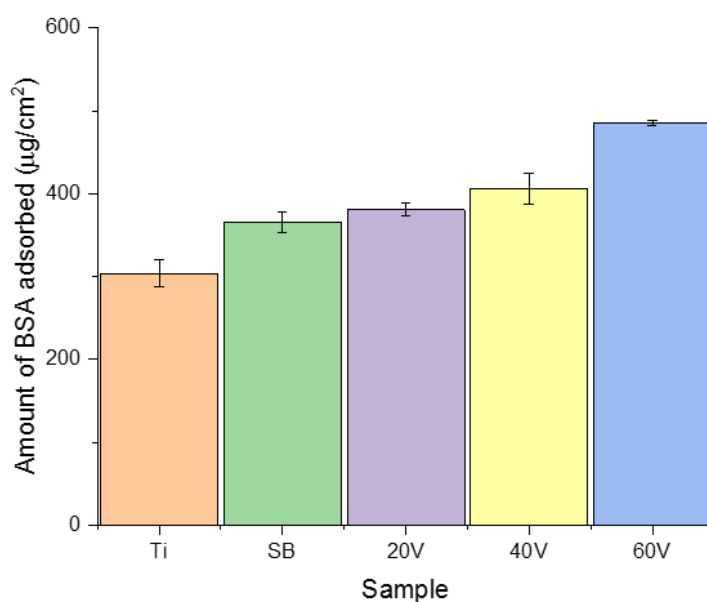


Figure 3. Comparison of the amount of BSA adsorbed on Ti, SB, 20V, 40V and 60V samples

3.3. Protein Conformation

Figure 4 represents the changes in the adsorbed BSA's secondary structure that were evaluated using amide-I band components. The side chain vibrations of tyrosine and arginine amino acids observed between 1611-1617 cm^{-1} were not included in the calculations. The bands corresponding to α -helix are positioned between 1649-1658 cm^{-1} , and the bands corresponding to random coils are positioned between 1641-1650 cm^{-1} (Byler & Susi, 1986; Akdoğan & Mutlu, 2012). It is not always straightforward to distinguish between these two components since their respective wavelengths are close and spectral artifacts arising from water vapor can affect the second derivative spectrum of the amide-I band and BSA is known to contain both components. Therefore, it can be accepted that the component bands between 1646-1650 cm^{-1} represent both α -helix and irregular structures (Giacomelli et al., 1999). Component bands observed between 1623-1630 cm^{-1} and 1669-1690 cm^{-1} were attributed to the β -sheet and β -turns, respectively (Byler & Susi, 1986; Giacomelli et al., 1999, Akdoğan & Mutlu, 2012). Amide-I band components for adsorbed BSA were calculated based on these band positions (Table 1). BSA gives maxima around 1655 cm^{-1} in solution, when adsorbed on the Ti surface, the maxima were observed at a wavelength close to this value, at 1657 cm^{-1} . The amide-I maxima was significantly shifted to lower wavelengths for BSA adsorbed on other sample surfaces suggesting a notable reduction in the α -helix structure. The data presented in Table 1 show that BSA undergoes significant conformational changes as a result of surface adsorption on all surfaces. The ratio of α -helix and random coil structure increased for BSA adsorbed on SB, 20V, 40V and 60V surfaces. The amide-I maxima shifted to 1647-1651 cm^{-1} , which indicates a decrease in the α -helix content of BSA but an increase in its random coil content. The β -layer content of BSA's secondary structure on the 60V surface increased dramatically. The α -helix and random coil contents tended to increase as the Ra value increased for 20V and 40V samples. However, despite an increase in Ra value for the 60V sample, the α -helix and random structure content deviates from this trend and decreases instead while the β -layer content increases significantly. It has been reported that a protein having a natural tendency to form helix structures can acquire secondary structure rich in β structures depending on the changes in ambient conditions, and the content of regular β structures can even reach up to 75% and form amyloid-like aggregates (Della Porta et al., 2016). When the anodized samples are compared it can be observed that both the Feret pore diameter and surface roughness increased somewhat proportionally for 20V and 40V samples, but the pore diameter on the 60V sample increased almost 2 times compared to that of the 40V sample. The α -helix and random coil content of BSA adsorbed on the surfaces increased with increasing surface roughness up to a certain pore size, but such a conclusion cannot be made for β -sheet and β -turn contents. It is also important to note that the average pore size obtained on all anodized samples was greater than the dimensions of BSA (15x4x4 nm) (La Verde et al., 2017).

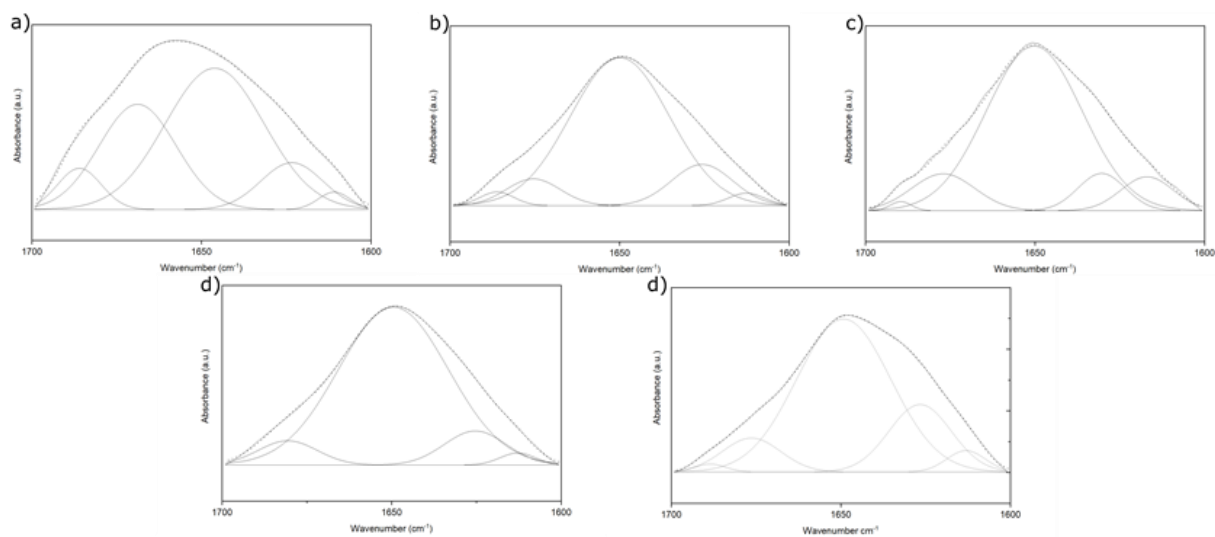


Figure 4. Amide-I component bands on; **a) Ti, b) SB, c) 20V, d) 40V and e) 60V** samples

The extent of changes in the secondary structure of BSA was not directly correlated with the WCA of the surfaces and BSA has undergone significant conformational changes even on the hydrophilic anodized surfaces. It is generally recognized that proteins undergo less denaturation upon adsorption on hydrophilic surfaces and the restriction of protein-surface interactions due to water-surface interactions on hydrophilic

TiO₂ surfaces were reported to cause less denaturation compared to hydrophobic surfaces (Zhao et al., 2020). However, this conclusion doesn't take the effect of surface morphology into consideration. No direct correlation between surface roughness the contents of secondary structure components were observed, but the way in which the secondary structure of BSA was changed was unique on each surface that has different Ra values. In addition, as the surface roughness increased the total α -helix and random helix content of the secondary structure components of BSA increased as well. The position of the amide-I band suggests that this change is the sum of the α -helix content decreasing and random coil content increasing. This finding is in agreement with the literature where a general reduction in α -helix content as a result of adsorption of BSA to hydrophilic surfaces is reported (Giacomelli et al., 1999). Surface roughness can affect how a protein behaves on a surface by influencing the surface hydrophilicity and by increasing the specific surface area with which the protein can interact. In particular, micro-sized roughness increases the surface area and consequently increases the amount of protein adsorption. However, there are conflicting data on the effect of nanometer roughness on protein adsorption. For example, Cai et al. (2006) reported that Ra values between 1.57-16.44 nm affect BSA adsorption to a lesser extent the adsorption of fibrinogen to a greater but a still a limited extent. Rockwell et al. (2012), on the other hand, reported that increased surface curvature increases protein adsorption, and Lu et al. (2012) reported that increasing surface roughness between 1-11 nm increases protein adsorption due to an increase in the surface free energy (Lu et al., 2012). Zhao et al. (2020) reported that upon BSA adsorption on TiO₂ nanofibers, a significant increase in β -turn and β -sheet content was observed while the random coil structure disappeared. The diameters of these structures varied between 184 ± 8 nm and 511 ± 17 nm. They interpreted that the dipole moment provided by the surface OH groups, which are strong enough to disrupt the H bonds in the protein structure, may have been responsible for the formation of a new secondary structure in the protein (Zhao et al., 2020). Yang et al. (2021) investigated the adsorption of globular proteins on smooth and nano-rippled TiOx/Ti and SiOx/Si. They reported that surfaces having less than 2 nm features at the vertical scale can significantly affect the amount protein adsorption and denaturation (Yang et al., 2021). Other researchers reported that for BSA, Ti nanotubes having inner diameters between 32 ± 4 - 80 ± 7 nm caused increased α -helix and β turn content in smaller pore sizes, while β -layer structure increased with high pore diameters (Jia et al., 2020). Our results are in accordance with Jia et al. (2020); the pore size rather than surface roughness influences the conformation BSA on anodized samples where regular β -sheet structure content increases with increasing pore size (Table 1).

Table-1. Secondary structure components of surface adsorbed BSA

	Ti		SB		20V		40V		60V	
Secondary structure	Wavenumber (cm ⁻¹)	%	Wavenumber (cm ⁻¹)	%	Wavenumber (cm ⁻¹)	%	Wavenumber (cm ⁻¹)	%	Wavenumber (cm ⁻¹)	%
α -helix and random coil	1646	52	1650	77	1650	72	1649	83	1649	69
β -sheet	1623	11	1626	13	1630	8	1625	10	1626	20
β -turns	1669, 1686	37	1675, 1689	10	1677, 1690	13	1681	7	1676, 1688	10
Side chains	1611	-	1613	-	1617	-	1613	-	1613	-

4. CONCLUSION

Our findings can be summarized as follows;

Although sanding increases the surface roughness, it partially improves the surface wettability, while the anodization process significantly increases the surface wettability

BSA undergoes significant conformational changes on all surfaces upon adsorption irrespective of surface hydrophilicity and roughness and the extent of the changes in conformation of BSA is not directly correlated with the surface hydrophilicity and the surface roughness

For anodized samples a correlation between the pore diameter and the secondary structure of surface adsorbed BSA adsorbed was observed.

Our results indicate that the protein adsorption behavior is dependent on nano-morphological features other than the surface roughness.

ACKNOWLEDGEMENT

This study has been funded by Ankara Hacı Bayram Veli University Scientific Research Projects Coordination Centre, Ankara, Turkey (Project No. 01/2020-24). SEM and AFM images and FTIR-ATR spectra were obtained at Hacettepe University, Advanced Technologies Research and Applications Center (HUNITEK), National Nanotechnology Research Center Institute of Materials Science and Nanotechnology (UNAM), and Eastern Anatolia High Technology Application and Research Center (DAYTAM) respectively.

CONFLICT OF INTEREST

The authors declare no conflict of interest.

REFERENCES

- Akdoğan, E., & Mutlu, M. (2012). Generation of amphoteric surfaces via glow-discharge technique with single precursor and the behavior of bovine serum albumin at the surface. *Colloids and Surfaces B: Biointerfaces*, 89, 289-294. doi:[10.1016/j.colsurfb.2011.09.005](https://doi.org/10.1016/j.colsurfb.2011.09.005)
- Barberi, J. & Spriano, S. (2021). Titanium and protein adsorption: an overview of mechanisms and effects of surface features. *Materials*, 14(7), 1590. doi:[10.3390/ma14071590](https://doi.org/10.3390/ma14071590)
- Byler, D. M. & Susi, H. (1986). Examination of the secondary structure of proteins by deconvolved FTIR spectra. *Biopolymer*, 25(3), 469-487. doi:[10.1002/bip.360250307](https://doi.org/10.1002/bip.360250307)
- Cai, K., Bossert, J., & Jandt, K. D. (2006). Does the nanometre scale topography of titanium influence protein adsorption and cell proliferation?. *Colloids and surfaces B: Biointerfaces*, 49(2), 136-144. doi:[10.1016/j.colsurfb.2006.02.016](https://doi.org/10.1016/j.colsurfb.2006.02.016)
- Chen, X., Chen, J., & Huang, N. (2022). The structure, formation, and effect of plasma protein layer on the blood contact materials: A review. *Biosurface and Biotribology*, 8(1), 1-14. doi:[10.1049/bsb2.12029](https://doi.org/10.1049/bsb2.12029)
- Della Porta, V., Bramanti, E., Campanella, B., Tiné, M. R., & Duce, C. (2016). Conformational analysis of bovine serum albumin adsorbed on halloysite nanotubes and kaolinite: A Fourier transform infrared spectroscopy study. *RSC Advances*, 6(76), 72386-72398. doi:[10.1039/C6RA12525E](https://doi.org/10.1039/C6RA12525E)
- Gan, N., Peng, X., Wu, D., Xiang, H., Sun, Q., Yi, B., Suo, Z., Zhang, S., Wang, X., & Li, H. (2022). Effects of Micro or Nano Size on the Biocompatibility of UiO67 from Protein Adsorption Behavior, Hemocompatibility and Histological Toxicity. *Journal of Hazardous Materials*, 435, 129042. doi:[10.1016/j.jhazmat.2022.129042](https://doi.org/10.1016/j.jhazmat.2022.129042)
- Giacomelli, C. E., Bremer, M. G., & Norde, W. (1999). ATR-FTIR study of IgG adsorbed on different silica surfaces. *Journal of Colloid and Interface Science*, 220(1), 13-23. doi:[10.1006/jcis.1999.6479](https://doi.org/10.1006/jcis.1999.6479)

- Hu, B., Liu, R., Liu, Q., Lin, Z., Shi, Y., Li, J., Wang, L., Li, L., Xiao, X., & Wu, Y. (2022). Engineering surface patterns on nanoparticles: New insights on nano-bio interactions. *Journal of Materials Chemistry B*, 10(14), 2357-2383. doi:[10.1039/D1TB02549J](https://doi.org/10.1039/D1TB02549J)
- Qi, H., Shi, M., Ni, Y., Mo, W., Zhang, P., Jiang, S., Zhang, Y., & Deng, X. (2021). Size-Confined Effects of Nanostructures on Fibronectin-Induced Macrophage Inflammation on Titanium Implants. *Advanced Healthcare Materials*, 10(20), 2100994. doi:[10.1002/adhm.202100994](https://doi.org/10.1002/adhm.202100994)
- Jia, E., Zhao, X., Lin, Y., & Su, Z. (2020). Protein adsorption on titanium substrates and its effects on platelet adhesion. *Applied Surface Science*, 529, 146986. doi:[10.1016/j.apsusc.2020.146986](https://doi.org/10.1016/j.apsusc.2020.146986)
- La Verde, V., Dominici, P., & Astegno, A. (2017). Determination of hydrodynamic radius of proteins by size exclusion chromatography. *Bio-protocol*, 7(8), e2230. doi:[10.21769/BioProtoc.2230](https://doi.org/10.21769/BioProtoc.2230)
- Li, K., Liu, S., Hu, T., Razanau, I., Wu, X., Ao, H., Huang, L., Xie, Y., & Zheng, X. (2020). Optimized nanointerface engineering of micro/nanostructured titanium implants to enhance cell–nanotopography interactions and osseointegration. *ACS Biomaterials Science & Engineering*, 6(2), 969-983. doi:[10.1021/acsbiomaterials.9b01717](https://doi.org/10.1021/acsbiomaterials.9b01717)
- Liu, C., Guo, Y., Hong, Q., Rao, C., Zhang, H., Dong, Y., Huang, L., Lu, X., & Bao, N. (2016). Bovine serum albumin adsorption in mesoporous titanium dioxide: pore size and pore chemistry effect. *Langmuir*, 32(16), 3995-4003. doi:[10.1021/acs.langmuir.5b04496](https://doi.org/10.1021/acs.langmuir.5b04496)
- Lord, M. S., Foss, M., & Besenbacher, F. (2010). Influence of nanoscale surface topography on protein adsorption and cellular response. *Nanotoday*, 5(1), 66-78. doi:[10.1016/j.nantod.2010.01.001](https://doi.org/10.1016/j.nantod.2010.01.001)
- Lu, J., Yao, C., Yang, L., & Webster, T. J. (2012). Decreased platelet adhesion and enhanced endothelial cell functions on nano and submicron-rough titanium stents. *Tissue Engineering Part A*, 18(13-14), 1389-1398. doi:[10.1089/ten.tea.2011.0268](https://doi.org/10.1089/ten.tea.2011.0268)
- Rockwell, G. P., Lohstreter, L. B., & Dahn, J. R. (2012). Fibrinogen and albumin adsorption on titanium nanoroughness gradients. *Colloids and Surfaces B: Biointerfaces*, 91, 90-96. doi:[10.1016/j.colsurfb.2011.10.045](https://doi.org/10.1016/j.colsurfb.2011.10.045)
- Singh, A. V., Vyas, V., Patil, R., Sharma, V., Scopelliti, P. E., Bongiorno, G., Podestà, A., Lenardi, C., Gade, W. N., & Milani, P. (2011). Quantitative characterization of the influence of the nanoscale morphology of nanostructured surfaces on bacterial adhesion and biofilm formation. *PloS one*, 6(9), e25029. doi:[10.1371/journal.pone.0025029](https://doi.org/10.1371/journal.pone.0025029)
- Sirin, H. T., Vargel, I., Kutsal, T., Korkusuz, P., & Piskin, E. (2016). Ti implants with nanostructured and HA-coated surfaces for improved osseointegration. *Artificial Cells, Nanomedicine, and Biotechnology*, 44(3), 1023-1030. doi:[10.3109/21691401.2015.1008512](https://doi.org/10.3109/21691401.2015.1008512)
- Wu, B., Tang, Y., Wang, K., Zhou, X., & Xiang, L. (2022). Nanostructured Titanium Implant Surface Facilitating Osseointegration from Protein Adsorption to Osteogenesis: The Example of TiO₂ NTAs. *International Journal of Nanomedicine*, 17, 1865-1879. doi:[10.2147/IJN.S362720](https://doi.org/10.2147/IJN.S362720)
- Yang, Y., Yu, M., Böke, F., Qin, Q., Hübner, R., Knust, S., Schwiderek, S., Grundmeier, G., Fischer, H., & Keller, A. (2021). Effect of nanoscale surface topography on the adsorption of globular proteins. *Applied Surface Science*, 535, 147671. doi:[10.1016/j.apsusc.2020.147671](https://doi.org/10.1016/j.apsusc.2020.147671)
- Zhao, F. H., Chen, Y. M., Hu, Y., Lu, X. G., Xiong, S. B., Wu, B. Y., Guo, Y. Q., Huang, P., & Yang, B. C. (2020). Conformation changes of albumin and lysozyme on electrospun TiO₂ nanofibers and its effects on MSC behaviors. *Colloids and Surfaces B: Biointerfaces*, 185, 110604. doi:[10.1016/j.colsurfb.2019.110604](https://doi.org/10.1016/j.colsurfb.2019.110604)



Gazi University

Journal of Science

PART A: ENGINEERING AND INNOVATION

<http://dergipark.org.tr/gujisa>

Optimal Cutting Conditions of Abrasive Waterjet Cutting for Ti-6Al-2Sn-2Mo Alpha-Beta Alloy Using EDAS and DFA Methods

Ugochukwu Sixtus NWANKITI^{1*} , Sunday Ayoola OKE¹ ¹Department of Mechanical Engineering, University of Lagos, Lagos, Nigeria

Keywords	Abstract
Abrasive Machining	Abrasive waterjet machining (AWJM), a known metal cutting process in manufacturing, is likely to be improved with the selection and use of the most influential parameters in machining decision-making. This work illustrates the development of two multicriteria indicators to optimize parameters for the abrasive waterjet machining process, providing optimization information for the surface morphology problem. The evaluation based on the distance from average solution (EDAS) method was used as the first indicator while the desirability function analysis (DFA) method reflects the second indicator. The results demonstrate a huge promise of both indicators, EDAS and DFA, to develop procedures for optimizing the parameters of Ti-6Al-2Sn-4Zr-2Mo alpha-beta alloy through the abrasive waterjet machining process. For the EDAS method, experimental trial 7 provided the best results with the water jet pressure of 220 bar, traverse speed of 40mm/min, and standoff distance of 1mm. The corresponding material removal rate is 151.667mm ³ /min while the roughness average is 2.76mm. The DFA method also provided the same results as those of the EDAS method. The present study is evidence of optimization of the parameters of Ti-6Al-2Sn-4Zr-2Mo alpha-beta alloy using the AWJM process. This warrants an intervention to enhance productivity and the economic gains of the company.
Waterjet	
Optimization	
Metal Alloys	
EDAS	
DFA	

Cite

Nwankiti, U. S., & Oke, S. A. (2022). Optimal Cutting Conditions of Abrasive Waterjet Cutting for Ti-6Al-2Sn-2Mo Alpha-Beta Alloy Using EDAS and DFA Methods. *GU J Sci, Part A, 9(3)*, 233-250.

Author ID (ORCID Number)	Article Process	
U. S. Nwankiti, 0000-0003-4186-9346	Submission Date	27.06.2022
S. A. Oke, 0000-0002-0914-8146	Revision Date	09.08.2022
	Accepted Date	11.08.2022
	Published Date	26.09.2022

1. INTRODUCTION

Waterjet machining (WJM) represents a modern, innovative process utilizing a non-conventional machining procedure, stimulated by a water stream propelled in high rapidity (Akkurt, 2004; Ergür, 2009; Hashish, 2014; Kartal, 2017; Karakurt et al., 2019). It is an alternative to the conventional metal subtraction methods of grinding and milling but with extraordinary impact in removing substantial materials from the surface of the material in rapid successions beyond the limits of the grinding and milling methods (Kartal, 2017; Karakurt et al., 2019). Besides, it displaces the conventional cutting method of hacksawing for some precision jobs where the surface finished by hacksawing is unacceptable by standards as the abrasive waterjet machine can cut the metals into two parts. The WJM is versatile and able to process plastics, rubber or walls where the convectional hacksawing or CNC cutting process has limitations. However, as abrasive material is used in machining, like metals and granite and embedded in the water, for the machining process, abrasive waterjet machining (AWJM) is a more appropriate term.

The AWJM process borrows from the principle of water erosion, which explains that as high-velocity water strikes the surface of a metal, material removal results (Karakurt et al., 2019; Wang et al., 2021). Depending on the softness or hardness of the material being cut, the choice of water is made (Sitek et al., 2021). While pure water has been involved in transforming the surfaces of soft materials, it is challenging to use it for cutting harder materials. This is done by mixing the water with abrasives (Singh et al., 2021). As abrasive

*Corresponding Author, e-mail: sa_oke@yahoo.com

particles are mixed with the water for the surface transformation of the Ti-6Al-25n-4Zr-2Mo alpha-beta alloy being considered here, the name abrasive waterjet machining emerges (Singh et al., 2021; Sitek et al., 2021). In practice, aluminium oxide, garnet, glass beads and sand are the largest commonly used abrasives. Furthermore, the Ti-6Al-25n-4Zr-2Mo alpha-beta stated above is referred to as near alpha titanium alloy. They are chosen in this article because of their suitability to build equipment and their components that are subjected to high temperatures and loads (Marya & Edwards, 2002; Bhamare et al., 2013). The wide applicability of the alloy includes jet engines, boilers, ovens and gas turbines. The Ti-6Al-25n-4Zr-2Mo (Ti-6-2-4-2) alloy is a preferred choice because of its remarkable strength-to-weight ratios, corrosion resistance, low Young's modulus and outstanding creep resistance.

However, research has proved that in different processes, the Ti-6Al-25n-4Zr-2Mo alloy can be optimised. For instance, in the laser shock peening process, the bending fatigue life of the Ti-6Al-25n-4Zr-2Mo alloy was enhanced by Bhamare et al. (2013). The authors concluded that the obtained optimal parametric set form thickness compression yielded an extensive enhancement of the bending fatigue life for the laser powder bed fusion process where the optimization of post-process heat treatments is the concern, Fleißner-Rieger et al. (2022) in utilising the Ti-6Al-25n-4Zr-2Mo (Ti-6-2-4-2) alloy concluded as follows. The authors declared that the optimization approach led to the alloy exhibiting optimized ductility and substantial growth of elongation at fracture. Moreover, Perumal et al. (2022) concluded that applying the wire electrical discharge machining to Ti-6242 (Ti-6Al-25n-4Zr-2Mo) alloy at testing at optimal situations yields enhanced material removal rate and acceptable surface finish. Likewise, Marya and Edwards (2002) concluded that in a laser bending optimization process using Ti-6Al-25n-4Zr-2Mo alloy, bending was achieved at an utmost value of roughly 0.65 of the melting temperature. Also, Perumal et al. (2021) declared that optimising the Ti-6Al-25n-4Zr-2Mo alloy in wire electrical discharge machining process using the analysis of variance showed the superior necessary parameters for surface roughness to be a pulse on time, pulse off time as well as a fused pulse on time and pulse off time, revealing contributions by the percentage of 22.71% and 36.88%, correspondingly.

In all the above studies, it is common to have applied the Ti-6Al-25n-4Zr-2Mo alloy in non-conventional processes and this is done to enhance the mechanical properties of the material such as tensile strength of 1110MPa, yield strength of 1050MPa, Poisson's ratio of 0.325, and an elastic modulus of 118GPa. The non-conventional systems process of difficult-to-machine materials is possible to be made by conventional machining. Furthermore, the inference from all these studies is that the Ti-6Al-25n-4Zr-2Mo alloy is an important material, which may be exploited by various processes. It is added that enormous processes and methods are still not being exploited. Thus the use of other optimization methods to enhance process parameters is a gap to be exploited. As much as the authors are aware, previous studies have failed to tackle the complex analysis and tedious information processing that may exist while attempting to optimize the abrasive waterjet machining parameters of Ti-6Al-25n-4Zr-2Mo alloy but also in selecting the most important AJWM process parameters from the multiple options feasible while still optimizing the parameters. Although solving the complexity and tedious information processing is the main issue of attaining high efficiency in the AWJM process a single characteristic assures that the process engineer diverts attention to the most important parameters in the process.

While justifying the necessity for more studies on the parametric predictions of the AWJM, Ergur (2009) argued that the paucity of knowledge that explains the hydraulic attributes of AWJM limits the understanding and expansion of the process control and optimization domain of the AWJM. Consequently, studies on optimization modelling and multicriteria analysis applied to abrasive waterjet machining have been fruitful in the previous years (Muthuramalingam et al., 2018; Perec and Musial, 2021). For example, Perec and Musial (2021) revealed the performance of the Hardox steel machined through the abrasive waterjet process on the application of multicriteria approach of entropy/VIKOR with the focus parameters as the cut kerf angle, abrasive flow rate over the cutting depth, pressure, cut surface roughness and feed rate. The method was declared feasible in this instance. Notwithstanding the complication of the approach while considering multiple parameters is an issue of concern. On the other hand, Muthuramalingam et al. (2021) applied the Taguchi-data envelopment analysis-oriented ranking using a multiresponse decision-making approach to improve responses that include material removal rate and surface roughness. It was concluded that standoff distance impacts energy in the greatest form for the abrasive waterjet machining process.

Besides, Percec et al. (2021) proposed the optimization of the hardox steel during the abrasive waterjet cutting procedure. The feasibility of the approach using the combined grey relational analysis and Taguchi method was confirmed. Miao et al. (2018) deployed multipass abrasive waterjet cutting to process the AISI 304 stainless steel. The optimization cutting turns to process the AISI 304 stainless steel were determined. Zohoor and Nourian (2012) deployed an algorithm to optimize the abrasive waterjet machining process using an experimental approach. It was concluded that the transverse speed and nozzle parameters impacting on the response, which is geometry kerf quality.

In Iqbal et al. (2011) the optimization of the abrasive jet process parameters was conducted on the AISI 4340 steel and aluminium 2219 using the analysis of variance as the tool of optimization to concurrently maximise various integrations of performance indices. Besides, Chen et al. (2019) eliminated shape errors at the external corners of the material. They declared that jet lag is the principal reason causing the bump error while the slow involve traversing speed causes overcut. While correcting those errors, the authors, ascertained that a bump removal angle and an approach to complete optimal length for the lead-in/lead-out lines were proposed for the respective errors of bump error and overcut. In another study, Wang et al. (2021) analysed the influence of processing parameters on the cutting front parameter for abrasive waterjet machining and reported as follows: the involved transverse speed was declared to have a substantial effect on the cutting front profile. However, the water pressure and abrasive flow rate were declared ineffective on the cutting front profile. The drawback of these articles is their inability to convert multiple responses into a single response, which promotes the concentration of efforts of the process engineer on specific parameters for enhanced process efficiency. Also, some of the methods are complicated and the process engineer may have difficulty applying them in practice.

Consequently, to avoid the restrictions of previous studies regarding complexity removal and the confusion of the process engineer in multiple-choice responses instead of dependence on the single response from enhanced efficiency, this study proposes two optimization approaches. The EDAS method is used as the foundation to enhance the efficiency of the abrasive waterjet machining process while processing the Ti-6Al-2Sn-4Zr-2Mo alloy while the DFA method converts the multiple responses into a single response to promote attention to the superior aspects of the AWJM process (Pradhan & Maity, 2018). As the authors are aware, this is the first time the two methods will be applied to solve the AWJM process optimization problem.

The EDAS method, originated by KeshavarzGhorabae et al. in the year 2015 works efficiently where conflicting features prevail (Maduekwe & Oke, 2022). As a multicriteria tool, the EDAS method permits the ranking of experimental trials from experiments to choose the best rank which generates optimal parameters and the corresponding responses (Okponyia & Oke, 2021; Maduekwe & Oke, 2022). The desirability function analysis connotes the concept of the outstanding quality of a parameter in which this outlier is taken as exhibiting an overwhelming quality that others cannot beat. Therefore, the focus on quality improvement should be on the single chosen parameter.

In this article, the EDAS method and not other multicriteria approaches were deployed because as distinct from other multicriteria methods, the EDAS method disallows the subjective interest of people as inputs to the computations using questionnaires are not usually associated with the traditional EDAS method (Okponyia & Oke, 2021; Maduekwe & Oke, 2022). Furthermore, the DFA method was adopted as an optimization method in this work and not another optimization method such as the Taguchi method because it avoids the problem of not being able to distinguish superior parameters from another. Unlike the Taguchi method, when the ranks of the experimental trials are made, and the best experimental trial is identified, the indices produced to represent each parameter at the optimal points usually distinguish one parameter from the other regarding superiority.

2. METHODS

In this article, two methods, namely the EDAS method and the DFA method were independently employed as adequate approaches to achieve parametric optimization in machining planning for abrasive waterjet machining. While acknowledging the responsibility to change the raw Ti-6Al-2Sn-4Zr-2Mo alloy into parts usage by the jet engines, for instance, a chief focus of the process engineer is to optimize the machining

process. To implement the EDAS method, two measures, namely the desirability of options, broken down to the negative and positive distances from the average solution are needed (Okponyia & Oke, 2021; Maduekwe & Oke, 2022). The author of the EDAS method prides in the method's evasion of the concept of the ideal and nadir solutions for the principal parameters of the AWJM process (Okponyia & Oke, 2021; Maduekwe & Oke, 2022). For more details on the EDAS method, information is obtainable from Ulutas (2017).

2.1. Basis to Select Abrasive Waterjet Cutting Parameters

This section discusses the basis that guided the choice of the principal parameters for the abrasive waterjet cutting process analysed in this work. The abrasive waterjet machining process has the following principal equipment being maintained: accumulation water transmission lines, waterjet catchers, accumulators, hydraulic nuts, fluid additive process, intensifier, on/off valve, filter, waterjet nozzles, water transmission lines and abrasive waterjet nozzle (Johnston, 1989). If any of these equipment components fail, pressure will not be built up and the goal of the machine will not be achieved. Therefore, the waterjet pressure may be a leading parameter in the assessment of the AWJM process. Thus, the maintenance engineer strives to keep the AWJM process in a good form, building and discharging the desired pressure during operation. As pressurized water is delivered through the diamond-based nozzle to a mixing compartment, the pressure acts, developing a vacuum and attracting abrasive particles (sometimes garnet sand) to a pool directed at the Ti-6Al-2Sn-4Zr-2Mo alpha-beta alloy for cutting to take place.

Furthermore, the maintenance engineer that delivers a functional system to the process engineer is aware that building up the waterjet pressure for service is not enough; it must be delivered at the point of need. This necessitates the equipment design to allow the pressure movement to be a seemingly unnoticed back and forth as well as cross-over movement. This is the rate at which the pressure delivery equipment acts between cuts. Consequently, in an abrasive waterjet machining process, the traverse speed is important from the perspective of deploying an effective cutting strategy in the process. Besides, between the nozzles tip and the Ti-6Al-2Sn-4Zr-2Mo alpha-beta alloy, a distance should be maintained for effective delivery of pressure. Thus, to commence and complete the AWJM process, the standoff distance is a requirement for inclusion in the analysis. It is noted that as a high standoff distance is maintained between the nozzle and the material being processed, a higher spread of the abrasive jet is guaranteed. Consequently, the cross-sectional area targeted expands. In sum, this section has advocated the inclusion of waterjet pressure, standoff distance and traverse speed as important components of the AWJM process and hence suggested inclusion in the present study. In this study, based on the basis established for the parameters of the AWJM process, the experimental data of Perumal et al. (2020) was applied to validate the methods of EDAS and DFA used on the problem of parametric optimization of the AWJM process using Ti-6Al-2Sn-4Zr-2Mo alpha-beta alloy.

2.2. System Information

In the application of both the EDAS and DFA methods, the starting point in the analysis is to know the influence of the AWJM process parameters (factors) on the responses (outputs such as material removal rate and surface roughness). As such the specification of the parameters in an experiment is essential. Furthermore, these parameters are attached to a restricted number of possible values and these are generally known as factor levels. More specifically defined, a factor (parameter) in the AWJM process experiment represents an organized independent variable that the process engineer has set at diverse levels. Also, the levels of a factor may be described as the number of variations a parameter is subjected to during the AWJM process experiment. The schematic representation of the abrasive waterjet is shown in Figure 1 while Table 1 shows the factors (parameters) and their levels. Figure 1 shows the static positioning of the abrasive waterjet machine and the workpiece. However, in reality, cutting is accomplished while the tip of the nozzle moves in a programmed manner over the surface of the work material to be cut (Wang et al., 2021). The jet of high-pressure fluid from the machine makes the holes and the desired shapes as the jet pass over the surface of the material without touching it. It is the jet that comes into contact with the material and does the cutting process. In all cases, the materials are immersed in a water pool that cools them. If the holes are cut, water passes from the lower part of the container where the material is immersed with its lower part touching the water for cooling purposes.

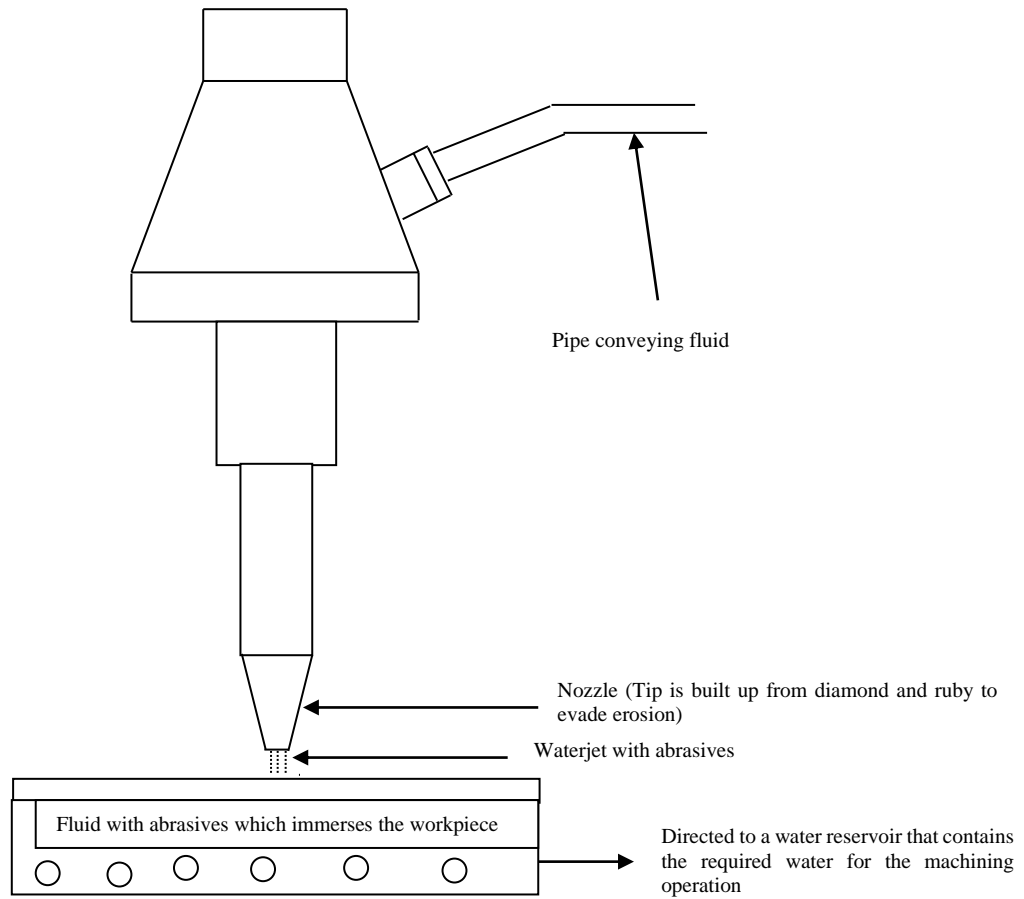


Figure 1. Schematic of the abrasive waterjet

The AWJM system consists of integrated parts that are well regulated including the hydraulic pump, hydraulic intensifier, drain and catcher system, accumulator, flow regulator valve, water reservoir, direction control valve, nozzle and mixing chamber or tube (Wang et al., 2021). The program control for the AWJM process is effective on the parts being manufactured. It is interesting to note that there are no tool changes (set up time) associated with the conventional CNC machine cutting system. As a result, substantial productivity of the system is guaranteed and the operator can produce more amounts of parts within the same time allocated to the conventional metal removal/cutting system. Furthermore, the program is flexible such that parts configuration changes could be made in a short period, thereby saving the enormous time lost to redrawing part configurations if the conventional CNC machine is to be used. Besides, the tailor-made program of the AWJM process allows the operator to cut shapes without previous knowledge of the CNC machine. Moreover, through the principle of particle erosion, the cutting of holes and part shapes are made in the AWJM process as opposed to the competing machining systems that work on frictional principles (i.e. friction drilling) and shearing. Thus, the abrasive waterjet machine produces superior outputs that avoid further finishing processes while eliminating additional machining activities such as reaming and boring and cost as well as ensuring that part integrity during service.

Table 1. Factors and their levels (Perumal et al., 2020)

Factor	Unit	Representation	Level 1	Level 2	Level 3
Water jet pressure	Bar	A	220	240	260
Traverse speed	mm/min	B	20	30	40
Standoff distance	Mm	C	1	2	3

Table 2 shows the orthogonal array, comprising columns that describe the test factors (parameters) and their associations. Usually, the format for defining an orthogonal array is to use the capital letter and follow it with a number that reveals the total number of an experiment to be conducted to arrive at the optimal parametric setting.

Table 2. Cumulative data showing experimental results at all levels of the L27 orthogonal array method(Perumal et al., 2020)

TrialNo	WJP (bar)	TS (mm/min)	SOD (mm)	MRR (mm³/min)	Ra (µm)
1	220	20	1	81.3333	3.0006
2	220	20	2	84.1666	2.8713
3	220	20	3	86.8333	2.6366
4	220	30	1	116.5000	2.8620
5	220	30	2	119.2500	3.0583
6	220	30	3	121.2500	2.8153
7	220	40	1	151.6670	2.7560
8	220	40	2	153.3330	3.7006
9	220	40	3	160.2130	3.2143
10	240	20	1	78.3330	2.7311
11	240	20	2	82.5140	2.7893
12	240	20	3	85.5010	2.8156
13	240	30	1	116.1100	2.8030
14	240	30	2	121.2500	3.0353
15	240	30	3	125.2500	2.9540
16	240	40	1	150.2400	3.0516
17	240	40	2	159.0120	2.9406
18	240	40	3	163.3330	3.2403
19	260	20	1	80.1230	2.4000
20	260	20	2	84.4500	2.6930
21	260	20	3	87.3333	3.0670
22	260	30	1	115.7500	2.4681
23	260	30	2	119.500	2.9566
24	260	30	3	125.1200	3.3196
25	260	40	1	150.6670	3.0363
26	260	40	2	157.2040	3.1643
27	260	40	3	165.3330	3.5261

2.3. EDAS Method

The methodology used in obtaining EDAS is shown below (Okponyia & Oke, 2021; Maduekwe & Oke, 2022):

Step 1: Determine the average solutions (Okponyia & Oke, 2021; Maduekwe & Oke, 2022):

$$AV_j = \frac{\sum_{i=1}^n X_{ij}}{n} \quad (1)$$

where;

AV_j is the average of the respective output values

X_{ij} is the output values

n is the number of output values obtained

The average solution implies the sum of all the sets of the respective outputs of the AWJM process outputs divided by the number of values that are added. However, practically, it seems that the process engineer is spreading the value of the whole set equally between every number and walking back to observe what ends the value for the numbers. The idea of average is extremely useful for the AWJM process as it makes sense when analysing data from a large pool of material processing using the AWJM scheme.

Step 2: Calculate the Positive Distance from Average (PDA) and the Negative Distance from Average (NDA)

The EDAS method takes the average solution as the cornerstone of the computation for the method. The stage places the average number in the middle of the computation. It observes that there is the possibility of having deviations both to the right or left of the middle number (i.e. average). Suppose a number system is imagined and placed at the middle number, then the values to the left of the middle number are taken as the negative distance from the middle while numbers to the right of the middle (average) number are assumed to be positive distances from the average. Thus, each parameter of the AJWM process is taken each time with the value obtained at every experimental trial. If the value for the first trial is to the left, then all the values to the left are noted and applied to the formula. Also, if the values are to the right, showing a positive distance from the middle (average), they are accounted for in the analysis.

For the PDA

When the output is to be maximized (Okponyia & Oke, 2021; Maduekwe & Oke, 2022):

$$PDA_{ij} = \frac{\max(0, (X_{ij} - AV_j))}{AV_j} \quad (2)$$

Equation (2) is used in the EDAS method to compute the positive distance from the average solutions. To apply Equation (2), the researcher counts only the positive numbers within the range of values considered. Then the sum of only the positive numbers is made. To maximize, the higher value of zero and the difference between the output value and the average of the respective output value is made. The obtained value is then divided by the average of the respective output values.

When the output is to be minimized (Okponyia & Oke, 2021; Maduekwe & Oke, 2022):

$$PDA_{ij} = \frac{\max(0, (AV_j - X_{ij}))}{AV_j} \quad (3)$$

Equation (3) is also used in the EDAS method to compute the positive distance from the average solutions but for the minimization case. To minimize, the higher value of zero and the difference between the average of the respective output values and the output value is obtained. The outcome is then divided by the average of the respective output values.

For the NDA

When the output is to be maximized (Okponyia & Oke, 2021; Maduekwe & Oke, 2022):

$$NDA_{ij} = \frac{\max(0, (AV_j - X_{ij}))}{AV_j} \quad (4)$$

Equation (4) shows the negative distance from the average solutions where the output is maximized. Here, the higher value between zero and the difference between the average of the respective output values and the output value is calculated. Then the emerging result is divided by the average of the respective output values.

When the output is to be minimized (Okponyia & Oke, 2021; Maduekwe & Oke, 2022):

$$NDA_{ij} = \frac{\max(0, (X_{ij} - AV_j))}{AV_j} \quad (5)$$

Equation (5) reveals the negative distance from the average solutions for a situation where the output is minimized. Here, the greater value between zero and the difference occurring between the output value of interest and the average of the various outputs is obtained.

Step 3: Obtain the Weighted sum of PDA and NDA

This is obtained by multiplying the PDA and NDA values by the weightage of the output.

Step 4: Obtain the SP_i (Sum of weighted PDA values) and SN_i (Sum of weighted NDA values) (Okponyia & Oke, 2021; Maduekwe & Oke, 2022):

$$SP_i = \sum_{j=1}^m PDA_{ij} \quad (6)$$

Equation (6) is the weighted sum of the positive distance from the average solutions. This is a method of analysis when conducting a sum of the AWJM process data to give some of the parameters more weights such that they exhibit greater influence on the results than other parameters. In this situation of weighing, the product of the response variable associated with specific parameters and the weight variable is found to obtain either the weighted sum of the negative distance from the average solution, Equation (6) or the weighted sum of the positive distance from the average solution Equation (7). Nonetheless, the number of observations considered for the response variable should be equal to that contemplated for the weights variable (Okponyia & Oke, 2021; Maduekwe & Oke, 2022).

$$SN_i = \sum_{j=1}^m w_j NDA_{ij} \quad (7)$$

Step 5: Normalize the values of SP and SN (Okponyia & Oke, 2021; Maduekwe & Oke, 2022):

$$NSP_i = \frac{SP_i}{\max_i(SP_i)} \quad (8)$$

Equation (8) shows the normalization formula for the sum of the weighted positive distance from the average solutions. It means that for the AWJM process data, the values evaluated are attuned from various magnitudes to a common magnitude such that a comparison of the strength of each experimental trial outcome from another could be judged. Besides, the added advantages of normalizing include the opportunity to eliminate redundant AWJM process data through observation. It also promotes the organization of the AWJM process database. Furthermore, the process engineer has the opportunity to logically group data. By considering Equation (8), the normalized values for the sum of the weighted positive distance from the average solution are obtained considering each $S.P_i$ and concurrently dividing it by the maximum value available for all the $S.P_i$. Equation (9) is obtained by first obtaining the ratio of the sum of weighted negative distances from the average solutions to the possible maximum values from all the $S.N_i$. This outcome is then subtracted from 1 (Okponyia & Oke, 2021; Maduekwe & Oke, 2022).

$$NSN_i = 1 - \frac{SN_i}{\max_i(SN_i)} \quad (9)$$

Step 6: Normalize the values of NSP and NSN (Okponyia & Oke, 2021; Maduekwe & Oke, 2022):

$$AS_i = \frac{1}{2}(NSP_i + NSN_i) \quad (10)$$

Further normalization of the values obtained from the previous step is pursued such that AS_i , defined as the averages of the values obtained from Equations (8) and (9) is obtained and termed Equation (10). The values of AS_i are ranked from largest to smallest values and the top ranking.

2.4. DFA method

The objective of the DFA is to find the optimal parametric setting that gives the best compromise considering two objectives:

1. Maximal Material Removal Rate (MRR)
2. Minimal Surface Roughness) (Ra)

Steps involved in implementing DFA (Pradhan & Maity, 2018):

1. Calculate the desirability index
2. Compute the composite desirability: Combining the individual desirability index of all responses to a single value
3. Determining the optimum level and its combination

to minimize Surface Roughness, The formula below is used to obtain the desirability index for the Surface Roughness

$$d_i = \begin{cases} 1, & y_j \leq y_{min} \\ \left(\frac{y_j - y_{max}}{y_{min} - y_{max}} \right)^r, & y_{min} \leq y_j \leq y_{max}, r \geq 0 \\ 0, & y_j \geq y_{min} \end{cases} \quad (11)$$

where

d_i is the desirability index

y_j is the current output value

y_{max} is the maximum output value

y_{min} is the minimum output value

r is the shape constant

Equation (11) is an index that allocates a score to three response categories (Pradhan & Maity, 2018). In the first category, a score of 1 is assigned when y_j is not greater than y_{min} . However, the second category is to assign a score of zero when y_j is not less than y_{min} . But the third category of score assignment is done when it is observed that the y_j is calculated which fall between y_{min} and y_{max} . Then a score is calculated based on the r th power of the ratio between the difference of y_{max} from y_j and the difference of y_{max} from y_{min} . In this case, all the values of r used should be positive. This description (Equation (11)) fits the surface roughness evaluation using the desirability function analysis since the mini values of surface roughness are beneficial to the process and therefore accommodated in the formula. The shape constant of 2 is adopted in this case. Furthermore, Equation (12) is used to obtain the desirability index for the material removal rate since it is to be maximized (Pradhan & Maity, 2018).

$$d_i = \begin{cases} 0, & y_j \leq y_{min} \\ \left(\frac{y_j - y_{max}}{y_{min} - y_{max}} \right)^r, & y_{min} \leq y_j \leq y_{max}, r \geq 0 \\ 1, & y_j \geq y_{max} \end{cases} \quad (12)$$

where

d_i is the desirability index

y_j is the current output value

y_{max} is the maximum output value

y_{min} is the minimum output value

r is the shape constant

However, when considering the material removal rate, the reverse is the case, Equation (12). Here, an index is formed which allocates scores to three different categories. For the first category, a score of zero is allocated when y_j is not greater than y_{min} . Nonetheless, for the second group, a score of 1 is made as to the y_j is not less than y_{min} . Moreover, for the third group, score assignment is conducted when it is observed that the y_j being computed falls between y_{max} and y_{min} . Then a score is computed depending on the r th power of the ratio between the difference of y_{min} from y_j and the difference of y_{min} from y_{max} . In this case, all these values of r used should be positive. This description stands for Equation (12).

$$d_c = \sqrt[w]{(d_1 \times d_2 \times \dots \times d_i)} \quad (13)$$

Where

d_c is the composite desirability

w is the number of responses

d_i is the individual desirability

Furthermore, Equation (13) is obtained as the composite desirability factor (Pradhan & Maity, 2018). This is achieved by first recognizing the number of responses available in the AWJM process optimization problem. Then, the individual desirability is computed. To obtain the composite desirability, d_c , each of the individual desirability is multiplied by one another and the w th root of the product obtained.

3. RESULTS AND DISCUSSION

This study into the optimization of process parameters of the AWJM process was conducted through an experiment involving three factors, namely, waterjet pressure, traverse speed and standoff distance. The level component of the factor-level framework has three levels, namely 1, 2 and 3. The AWJM process involved

the machining of the Ti-6Al-2Sn-4Zr-2Mo alpha-beta alloy, targeting the maximization of the material removal rate and the minimization of the surface roughness of the processed material. From the experiment, the results of the application of EDAS are shown after using Table 3 as an input, in Table 4. Afterwards, the final results are shown accordingly and then the results for the DFA method are displayed. For the EDAS method, by implementing Equations (1) to (10), the values of the AS_i , which were ranked are revealed. The DFA method shows a two-stage process where the desirability index is obtained with ranks of the experimental trials to reveal the superiority of an experimental trial over the other. Then, this provides a point where the optimal values for all the parameters, including the waterjet pressure, standoff distance and traverse speed are indicated together with the responses, which are the material removal rate and surface roughness.

3.1 Implementing EDAS

Step 1: Determine the average solutions

To obtain Table 3, Equation (1) is applied. Here, the computation of the AV_j is conducted by considering the values of each of the responses (material removal rate and surface roughness) and obtaining the averages.

Table 3. Obtaining average solutions for the material removal rate and the surface roughness

S. No	WJP (bar)	TS (mm/min)	SOD (mm)	MRR (mm ³ /min)	Ra (μm)	S. No	WJP (bar)	TS (mm/min)	SOD (mm)	MRR (mm ³ /min)	Ra (μm)
1	220	20	1	81.3333	3.0006	15	240	30	3	125.2500	2.9540
2	220	20	2	84.1666	2.8713	16	240	40	1	150.2400	3.0516
3	220	20	3	86.8333	2.6366	17	240	40	2	159.0120	2.9406
4	220	30	1	116.5000	2.8620	18	240	40	3	163.3330	3.2403
5	220	30	2	119.2500	3.0583	19	260	20	1	80.1230	2.4000
6	220	30	3	121.2500	2.8153	20	260	20	2	84.4500	2.6930
7	220	40	1	151.6670	2.7560	21	260	20	3	87.3333	3.0670
8	220	40	2	153.3330	3.7006	22	260	30	1	115.7500	2.4681
9	220	40	3	160.2130	3.2143	23	260	30	2	119.5000	2.9566
10	240	20	1	78.3330	2.7311	24	260	30	3	125.1200	3.3196
11	240	20	2	82.5140	2.7893	25	260	40	1	150.6670	3.0363
12	240	20	3	85.5010	2.8156	26	260	40	2	157.2040	3.1643
13	240	30	1	116.1100	2.8030	27	260	40	3	165.3330	3.5261
14	240	30	2	121.2500	3.0353	Average				120.0581	2.9595
Weightage										0.5	0.5

By starting with the material removal rate, the value of experimental trial 1 is 81.3333mm³/min. This is added to the next for experimental trial 2, which is 84.1666mm³/min to yield a cumulative value of 165.4999mm³/min. further cumulative additions and done on each other experimental trials 3, to 27 to obtain a total value of 3241.57mm³/min. when divided by the total number of observations, 27, the average value is 120.0581mm³/min. The same procedure is adopted for the computation of the roughness average, Ra, for surface roughness, which also has 27 experimental trials. In this case, the total value is 79.9068mm while the average is obtained as 79/9068mm. However, for further calculations, an equal weight of importance of the outputs is assumed it was not stated that the material removal rate is more important than surface roughness or the reverse. Hence, a 50:50 (i.e. 0.5 for material removal rate and 0.5 for roughness average) weight of outputs is given.

Step 2: Calculate the Positive Distance from Average (PDA) and the Negative Distance from Average (NDA)

Step 3: This is obtained by multiplying the PDA and NDA values by the weightage of the output.

Table 4. Positive Distance from Average (PDA) and Negative Distance from Average (NDA)

S.No.	Positive Distance from Average				Negative Distance from Average			
	MRR	MRR (weighted)	Ra	Ra (weighted)	MRR	MRR (weighted)	Ra	Ra (weighted)
1	0.0000	0.00000	0.0000	0.0000	0.3226	0.1613	0.0139	0.0069
2	0.0000	0.00000	0.0298	0.0149	0.2990	0.1495	0.0000	0.0000
3	0.0000	0.00000	0.1091	0.0546	0.2767	0.1384	0.0000	0.0000
4	0.0000	0.00000	0.0329	0.0165	0.0296	0.0148	0.0000	0.0000
5	0.0000	0.00000	0.0000	0.0000	0.0067	0.0034	0.0334	0.0167
6	0.0099	0.00496	0.0487	0.0244	0.0000	0.0000	0.0000	0.0000
7	0.2633	0.13164	0.0688	0.0344	0.0000	0.0000	0.0000	0.0000
8	0.2772	0.13858	0.0000	0.0000	0.0000	0.0000	0.2504	0.1252
9	0.3345	0.16723	0.0000	0.0000	0.0000	0.0000	0.0861	0.0430
10	0.0000	0.00000	0.0772	0.0386	0.3475	0.1738	0.0000	0.0000
11	0.0000	0.00000	0.0575	0.0288	0.3127	0.1564	0.0000	0.0000
12	0.0000	0.00000	0.0486	0.0243	0.2878	0.1439	0.0000	0.0000
13	0.0000	0.00000	0.0529	0.0264	0.0329	0.0164	0.0000	0.0000
14	0.0099	0.00496	0.0000	0.0000	0.0000	0.0000	0.0256	0.0128
15	0.0432	0.02162	0.0019	0.0009	0.0000	0.0000	0.0000	0.0000
16	0.2514	0.12570	0.0000	0.0000	0.0000	0.0000	0.0311	0.0156
17	0.3245	0.16223	0.0064	0.0032	0.0000	0.0000	0.0000	0.0000
18	0.3604	0.18022	0.0000	0.0000	0.0000	0.0000	0.0949	0.0474
19	0.0000	0.00000	0.1891	0.0945	0.3326	0.1663	0.0000	0.0000
20	0.0000	0.00000	0.0901	0.0450	0.2966	0.1483	0.0000	0.0000
21	0.0000	0.00000	0.0000	0.0000	0.2726	0.1363	0.0363	0.0182
22	0.0000	0.00000	0.1660	0.0830	0.0359	0.0179	0.0000	0.0000
23	0.0000	0.00000	0.0010	0.0005	0.0046	0.0023	0.0000	0.0000
24	0.0422	0.02108	0.0000	0.0000	0.0000	0.0000	0.1217	0.0608
25	0.2550	0.12748	0.0000	0.0000	0.0000	0.0000	0.0260	0.0130
26	0.3094	0.15470	0.0000	0.0000	0.0000	0.0000	0.0692	0.0346
27	0.3771	0.18855	0.0000	0.0000	0.0000	0.0000	0.1914	0.0957

The first segment of Table 4, which is the second to the fifth column, is computed from Equations (2) and (3) where the positive distance from the average solutions is considered with output to be maximized from Equation (2). This is relevant for the material removal rate because it is beneficial for the AWJM process to increase the rate of material removal in the system and attain utmost efficiency and power savings (energy cost reduction) since the elongated time of material removal gives the additional cost to the AWJM process. Consider experimental trial 1 in the first segment of Table 4, by applying Equation (2) for the material removal rate component of the table, the researchers seek to evaluate Equation (2) by first considering the numerator and then dividing the outcome by the denominator. The numerator instructs the researchers to obtain the maximum value between zero and the other component of the numerator. This other component, containing X_{ij} and AV_j represent 81.3333mm³/min (for X_{11}) and 120.0581mm³/min (for AV_j), respectively (Table 3). This yields 81.3333mm³/min-120.0581mm³/min (i.e. -38.72mm³/min). Then the maximum of zero and -38.7248 mm³/min is obtained as zero. By dividing this outcome, zero by the denominator, i.e. 120.0581mm³/min, a value of zero is finally obtained as displayed in the second column and experimental trial 1 in the first segment of Table 4. However, recall that a weight of 0.5 was achieved for the material removal rate. This, if multiplied by the outcome of the MRR (i.e. 0), as 0 x 0.5, a weighted MRR of 0 is obtained. As the same procedure is adopted for experimental trials 2 to 27, the results for columns two and three for Table 4 are obtained. Also, note that the same procedure is obtainable for the computation of the roughness average and the fourth and fifth columns of Table 4 are obtained. Hence, by calculating for all the experimental trials 1 to 27, all the columns for the MRR and Ra are completed with values of weighted MRR and weighted Ra accounted for.

The second segment of Table 4, which is the sixth to the ninth column is obtained from Equations (4) and (5) where the negative distance from the average solutions considered and the output is to be maximized (i.e. material removal rate) is for Equation (4). In Equation (5), the output is to be minimized (i.e. surface roughness measured by the roughness average, Ra in Table 4). By applying Equation (4) to the material removal rate component of the table, the researchers seek to appraise Equation (4) by first considering the numerator and then dividing the outcome by the denominator. The numerator reveals to the researchers that to obtain it, there should be a consideration of the maximum value between zero and the difference between the AV, and Xij. By starting with the experimental trial 1 in the second segment of Table 4, Table 3 is referred to first to extract the values of AVj and X11, for the MRR since the maximization of output is sought. The value of AVj - X11 is 120.0581mm³/min - 81.3333mm³/min and this gives 38.7248mm³/min. Then the maximum of 38.7248mm³/min and zero is given as 38.7248mm³/min. This value is divided by AVj (i.e. 120.0581mm³/min) to yield 0.3226mm³/min. When multiplied by the weight of 0.5, a weighted MRR value of 0.1613mm³/min is obtained. These values are shown for MRR and weighted MRR for experimental trial 1 in columns 6 and 7 of the second row of Table 4. By following a similar procedure, all the experimental trials 2 to 27 may be evaluated. Also, Equation (5) could be applied likewise for the NDAij where the surface roughness minimization is of interest and the second segment of Table 4 will be completed.

Step 4: Obtain the SPi (Sum of weighted PDA values) and SNi (Sum of weighted NDA values)

Here, Equations (6) and (7) are applied to produce Table 5.

Table 5. The Sum of weighted PDA and NDA values

S.No.	Sum of weighted PDA values			Sum of weighted NDA values		
	Weighted MRR	Weighted RA	SPi	Weighted MRR	Weighted RA	SPi
1	0.0000	0.0000	0.0000	0.1613	0.0069	0.1682
2	0.0000	0.0149	0.0149	0.1495	0.0000	0.1495
3	0.0000	0.0546	0.0546	0.1384	0.0000	0.1384
4	0.0000	0.0165	0.0165	0.0148	0.0000	0.0148
5	0.0000	0.0000	0.0000	0.0034	0.0167	0.0201
6	0.0050	0.0244	0.0293	0.0000	0.0000	0.0000
7	0.1316	0.0344	0.1660	0.0000	0.0000	0.0000
8	0.1386	0.0000	0.1386	0.0000	0.1252	0.1252
9	0.1672	0.0000	0.1672	0.0000	0.0430	0.0430
10	0.0000	0.0386	0.0386	0.1738	0.0000	0.1738
11	0.0000	0.0286	0.0288	0.1564	0.0000	0.1564
12	0.0000	0.0243	0.0243	0.1439	0.0000	0.1439
13	0.0000	0.0264	0.0264	0.0164	0.0000	0.0164
14	0.0050	0.0000	0.0050	0.0000	0.0128	0.0128
15	0.0216	0.0009	0.0226	0.0000	0.0000	0.0000
16	0.1257	0.0000	0.1257	0.0000	0.0156	0.0156
17	0.1622	0.0032	0.1654	0.0000	0.0000	0.0000
18	0.1802	0.0000	0.1802	0.0000	0.0474	0.0474
19	0.0000	0.0945	0.0945	0.1663	0.0000	0.1663
20	0.0000	0.0450	0.0450	0.1483	0.0000	0.1483
21	0.0000	0.0000	0.0000	0.1363	0.0182	0.1544
22	0.0000	0.0830	0.0830	0.0179	0.0000	0.0179
23	0.0000	0.0005	0.0005	0.0023	0.0000	0.0023
24	0.0211	0.0000	0.0211	0.0000	0.0608	0.0608
25	0.1275	0.0000	0.1275	0.0000	0.0130	0.0130
26	0.1547	0.0000	0.1547	0.0000	0.0346	0.0346
27	0.1886	0.0000	0.1886	0.0000	0.0957	0.0957

Note the Max SPi is 0.1886 while Max SNi is 0.1738.

Step 5: Normalize the values of SP and SN

Equations (8) and (9) are applied to the data to produce Table 6.

Table 6. Normalised values of SP and SN (positive), Normalised values of SP and SN (negative) and Ranking of ASi values

S.No.	Normalised Values of SP and SN (positive)		Normalised Values of SP and SN (negative)		Ranking of ASi values	
	SPi	NSPi	Sni	NSni	ASi	Rank
1	0.0000	0.0000	0.1682	0.0320	0.0160	27
2	0.0149	0.0790	0.1495	0.1398	0.1094	24
3	0.0546	0.2893	0.1384	0.2037	0.2465	20
4	0.0165	0.0874	0.0148	0.9147	0.5010	14
5	0.0000	0.0000	0.0201	0.8846	0.4423	17
6	0.0293	0.1555	0.0000	1.0000	0.5778	10
7	0.1660	0.8805	0.0000	1.0000	0.9403	1
8	0.1386	0.7350	0.1252	0.2795	0.5072	13
9	0.1672	0.8869	0.0430	0.7523	0.8196	4
10	0.0386	0.2047	0.1738	0.0000	0.1023	25
11	0.0288	0.1525	0.1564	0.1002	0.1264	23
12	0.0243	0.1289	0.1439	0.1718	0.1504	22
13	0.0264	0.1402	0.0164	0.9054	0.5228	12
14	0.0050	0.0263	0.0128	0.9263	0.4763	16
15	0.0226	0.1196	0.0000	1.0000	0.5598	11
16	0.1257	0.6666	0.0156	0.9105	0.7886	7
17	0.1654	0.8773	0.0000	1.0000	0.9387	2
18	0.1802	0.9558	0.0474	0.7270	0.8414	3
19	0.0945	0.5013	0.1663	0.0429	0.2721	19
20	0.0450	0.2388	0.1483	0.1466	0.1927	21
21	0.0000	0.0000	0.1544	0.1112	0.0556	26
22	0.0830	0.4403	0.0179	0.8968	0.6685	9
23	0.0005	0.0026	0.0023	0.9866	0.4946	15
24	0.0211	0.1118	0.0608	0.6499	0.3809	18
25	0.1275	0.6761	0.0130	0.9253	0.8007	6
26	0.1547	0.8205	0.0346	0.8009	0.8107	5
27	0.1886	1.0000	0.0958	0.4491	0.7246	8
			0.1738			

Step 6: Normalize the values of NSP and NSN

Equation (10) is applied to the data to obtain Table 6. The values of ASi are ranked from largest to smallest values and the top ranking. The optimal parametric setting is given to be located at number 7, and the input and output parameters at number 7 of the orthogonal array. It holds the optimal result where MRR is sought to be maximized and Ra is sought to be minimized. The optimal results are waterjet pressure of 220bar, traverse speed of 40mm/min, and stand-off distance of 1mm. However, the output is an MRR of 151.667mm³/min, and a roughness average, Ra, of 2.756mm.

To implement the desirability function, a two-stage process is followed. First, the desirability index and composite desirability is then formed. Table 7 shows the experimental values of the surface roughness response and the material removal rate and the corresponding desirability indices. To obtain Table 7, the following explanations prevail. Consider the second column and the first row which indicate the surface roughness value of 3.0006mm, extracted from the experimental data by Perumal et al. (2020). However, it is

known that surface roughness in the AWJM process is to be minimized. Then, Equation (11) is used to optimize the surface roughness. From the data are given in Perumal et al. (2020), the data for y_j , y_{min} and y_{max} are obtainable as y_j ($=y_1$ for experimental trial 1), y_{min} is 2.4000mm and y_{max} is 3.706mm. Notice that the analysis relates to experimental trial 1 and the corresponding surface roughness value is 3.0006mm, which is the entry in the last column of Table 2 for experimental trial 1. Also, the y_{max} value is read from the last column of experimental trial 8, which is the last column of Table 2. Also, the y_{min} is obtainable at experimental trial 19. Now, in applying Equation (11), the first option is to assign a value of 1 of $y_j \leq y_{min}$. But $y_j (=y_1) = 3.0006\text{mm}$ is not less but greater than y_{min} at a value of 2.4000mm. Therefore, the first option of $y_j \leq y_{min}$ is not respected. Then, the second option where the condition of assigning zero where $y_j \geq y_{max}$ is considered. Here, y_1 , which is 3.0006mm is not greater than y_{max} value of 3.706mm. Therefore, the second condition is violated. However, it is the third condition where the r th power of the ratio of the difference between y_j and y_{max} to the difference between y_{min} and y_{max} is considered. In this case, considering the numerator of the factor, $y_j - y_{max}$, the difference is 0.6006mm. Also considering the denominator, $y_{min} - y_{max}$ yields -0.3006mm since y_{min} is 2.400mm and y_{max} is 3.7006mm. The ratio of these two items yields -0.3. But this outcome of -0.3 is raised to be the power of 2, which makes the solution to be 0.09. This is used for further processing in the data analysis.

Table 7. Experimental values of surface roughness and the material removal rate values with their desirability index

S.No.	SR	SR-DI	MRR	MRR-DI	S.No.	SR	SR-DI	MRR	MRR-DI
1	3.0006	0.2897	81.3333	0.0012	15	2.9540	0.3296	125.2500	0.2908
2	2.8713	0.4066	84.1666	0.00450	16	3.0516	0.2490	150.2400	0.6831
3	2.6366	0.6693	86.8333	0.0095	17	2.9406	0.3415	159.0120	0.8600
4	2.8620	0.4157	116.5000	0.1925	18	3.2403	0.1253	163.3330	0.9546
5	3.0583	0.2439	119.2500	0.2212	19	2.4000	1.0000	80.1230	0.0004
6	2.8153	0.4633	121.2500	0.2433	20	2.6930	0.6002	84.4500	0.0049
7	2.7560	0.5275	151.6670	0.7105	21	3.0670	0.2373	87.3333	0.0107
8	3.7006	0.0000	153.3330	0.7432	22	2.4681	0.8980	115.7500	0.1850
9	3.2143	0.1398	160.2130	0.8858	23	2.9566	0.3272	119.5000	0.2239
10	2.7311	0.5557	78.3330	0.0000	24	3.3196	0.0858	125.1200	0.2892
11	2.7893	0.4909	82.5140	0.0023	25	3.0363	0.2609	150.6670	0.6913
12	2.8156	0.4630	85.5010	0.0068	26	3.1643	0.1700	157.2040	0.8219
13	2.8030	0.4763	116.1100	0.1885	27	3.5261	0.0180	165.3330	1.0000
14	3.0353	0.2617	121.2500	0.2433					

Step 2 - Compute the composite desirability

The aim of arriving at the composite desirability is to reduce the multi-repose objective function to a single response objective function. It is achieved by implementing a composite desirability equation to obtain the desirability by considering all the outputs and finding a compromise. Equation (13) is used to obtain the desirability (Figure 2).

The rank computations reveal the 1st, 2nd and 3rd positions to experimental trials 7 (MRR-DI, 0.7105; RA-DI, 0.5275; Comp_Des, 0.6122), 17 (MRR-DI, 0.8600; RA-DI, 0.3415; Comp_Des, 0.5419) and 25 (MRR-DI, 0.6913; RA-DI, 0.2609; Comp_Des, 0.4247), respectively.

In Perumal et al. (2020), the authors concluded by declaring the obtained optimal results as waterjet pressure of 260 bar, traverse speed of 40mm/min and standoff distance of 1mm. Compared to the results obtained by EDAS and DFA methods, particularly experimental trial 7 in Table 6 and validated by experimental trial 7 of Figure 2, where the instances are for the EDAS and DFA methods, respectively, our results are better as it requires less energy for its implementation in the AWJM process. The obtained results are waterjet pressure of 220bar, traverse speed of 40mm/min, and stand-off distance of 1mm. However, the output is an MRR of 151.667mm³/min, and a roughness average, Ra, of 2.756mm.

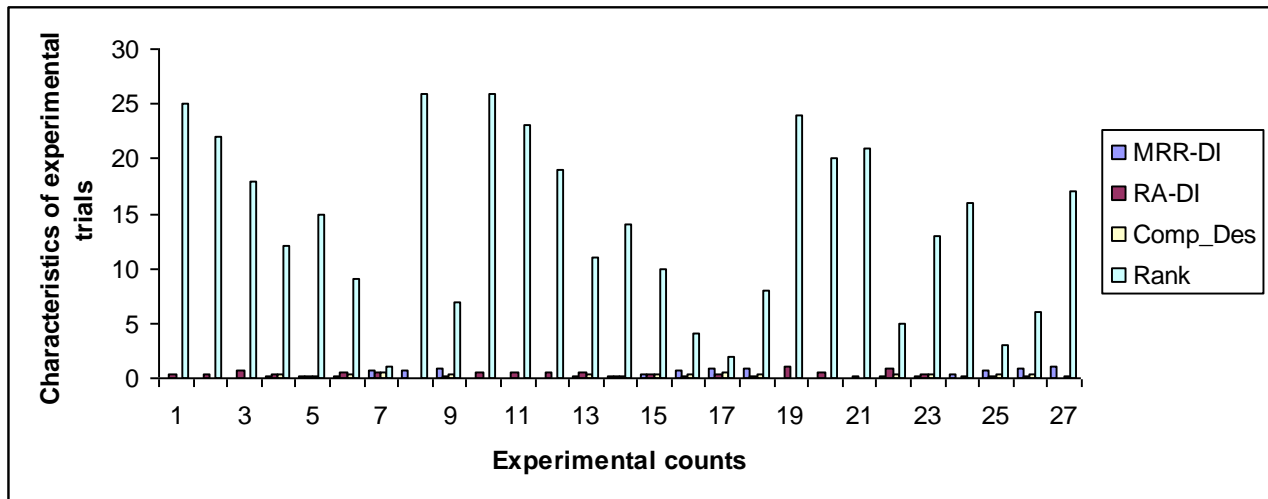


Figure 2. Desirability index of material removal rate and surface roughness with the composite desirability and the ranks according to the desirability of the parametric settings.

MRR-DI: desirability index of material removal rate;

RA-DI: desirability index of surface roughness (roughness average);

Comp_Des: composite desirability)

Furthermore, from the results of the case examining the abrasive waterjet machining using the Ti-6Al-2Sn-4Zr-2Mo alpha-beta alloy, it seems that both the EDAS method and the DFA method are suitable tools to articulate the optimization characteristics of the AWJM process. Undeniably, the EDAS method is capable to confine and handle parametric information and helping the decision-maker to decide on what threshold of input resources to use for the AWJM process. Consider the three parameters of waterjet pressure, traverse speed and standoff distance labelled as critical parameters in Perumal et al. (2020) whose data is used to validate the procedures of EDAS and DFA. The closest parameter to the operations in the abrasive waterjet orifice is perhaps the waterjet pressure. In this situation, the operator has two options to simulate the results of the waterjet pressure and the corresponding outcomes in material removal rate and surface roughness. The first option entails the operator mixing the granite particles with water within the mode boundaries while the mixed substance is passed through the orifice (Singh et al., 2021). A second option is to add the granite to water before passing it to the nozzle and afterwards, the AWJM is applied to cut the Ti-6Al-2Sn-4Zr-2Mo alpha-beta alloy. This is an action and other actions may include the operations of several other units of the abrasive waterjet machining process such as the accumulation water transmission lines, waterjet catchers, accumulators, hydraulic unit, fluid additive process, intensifier, on/off valve, filters, waterjet nozzles, water transmission lines and abrasive water jet nozzle (Johnston, 1989). Thus, all the above actions could be made flexible such that the sensitivity of the parameters could be estimated. This means that the EDAS method allows the process engineer to explain the influence of changes in parametric values of one or more parameters in individual or combined states on the outcomes (material removal rate and surface roughness). Furthermore, the process engineer is satisfied with the adaptability of the DFA method when developing possible outcomes with varying levels of inputs. The clarity and simplicity of the EDAS and DFA methods are important advantages that support the transmission of information between the operator and the process engineer in the AWJM process, leading to more accurate and reliable results for decision-making. Besides, both the EDAS and DFA methods may be deployed for synergy with other methods such as Taguchi and data envelopment analysis which is crucial when developing action plans from performance outcomes.

4. CONCLUSIONS

The study sheds light on the optimal parametric determination of the Ti-6Al-2Sn-4Zr-2Mo alloy processed through abrasive waterjet machining and provides recommendations when two robust methods of EDAS and DFA were applied. The applications of the two methods led to the following conclusions. The applications of both the EDAS and DFA methods as multicriteria abrasive waterjet cutting decision-making tools to solve

the new problem of process parametric optimization using the Ti-6Al-2Sn-4Zr-2Mo alpha-beta material is feasible. In the process of the Ti-6Al-2Sn-4Zr-2Mo alloy for high temperature and loading applications, there is a need to focus on a waterjet of 220bar, traverse speed of 40mm/min and standoff distance of 1mm. the accompanying metal removal rate is 151.667mm³/min and the roughness average of 2.76mm. These results apply to both methods as the DFA method validated the results of the EDAS method. More prospective studies could develop methods that integrate the EDAS and DFA methods where one method overcomes the drawbacks of the other. Apart, additional studies may consider the sensitivity analysis of the parameters based on each method.

CONFLICT OF INTEREST

The authors declare no conflict of interest.

REFERENCES

- Akkurt, A. (2004). Waterjet cutting systems and assesment of their industrial applications. *Journal of Polytechnic*, 7(2), 129-139
- Bhamare, S., Ramakrishnan, G., Mannava, S. R., Langer, K., Vasudevan, V. K., & Qian, D. (2013). Simulation-based optimization of laser shock peening process for improved bending fatigue life of Ti-6Al-2Sn-4Zr-2Mo alloy. *Surface and Coatings Technology*, 232, 464-474. doi:[10.1016/j.surfcoat.2013.06.003](https://doi.org/10.1016/j.surfcoat.2013.06.003)
- Chen, M., Zhang, S., Zeng, J., Chen, B., Xue, J., & Ji, L. (2019). Correcting shape error on external corners caused by the cut-in/cut-out process in abrasive water jet cutting. *The International Journal of Advanced Manufacturing Technology*, 103, 849-859. doi:[10.1007/s00170-019-03564-x](https://doi.org/10.1007/s00170-019-03564-x)
- Ergür, H. S. (2009). Theoretical analysis of abrasive waterjet and modelling with artificial neural network. *Journal of Engineering and Architecture Faculty of Eskişehir Osmangazi University*, 22(2), 179-197
- Fleißner-Rieger, C., Pfeifer, T., Turk, C., & Clemens, H. (2022) Optimization of the post-process heat treatment strategy for a near- α titanium base alloy produced by laser powder bed fusion. *Materials*, 15(3), 1032. doi:[10.3390/ma15031032](https://doi.org/10.3390/ma15031032)
- Hashish, M. (2014). Waterjet Machining Process. In: A. Nee (Eds.), *Handbook of Manufacturing Engineering and Technology* (pp. 1-30). Springer. doi:[10.1007/978-1-4471-4976-7_75-1](https://doi.org/10.1007/978-1-4471-4976-7_75-1)
- Iqbal, A., Dar, N. U., & Hussain, G. O. (2011). Optimization of abrasive water jet cutting of ductile materials. *Journal of Wuhan University of Technology - Materials Science Edition*, 26, 88-92. doi:[10.1007/s11595-011-0174-8](https://doi.org/10.1007/s11595-011-0174-8)
- Johnston, C. E. (1989). Waterjet/Abrasive Waterjet Machining. In: *ASM Handbook, 16, Machining* (pp. 520-527). ASM International. doi:[10.31399/asm.hb.v16.a0002158](https://doi.org/10.31399/asm.hb.v16.a0002158)
- Karakurt, İ., Aydın, G., Yıldırım, F., & Kaya, S. (2019, April 16-19). *Current technological developments in cutting applications by abrasive waterjet*. In: 26th International Mining Congress and Exhibition of Turkey (pp. 1334-1339).
- Kartal, F. (2017). A review of the current state of abrasive water-jet turning machining method. *International Journal of Advanced Manufacturing Technology*, 88, 495-505. doi:[10.1007/s00170-016-8777-z](https://doi.org/10.1007/s00170-016-8777-z)
- Maduekwe, V. C., & Oke, S. A. (2022). The application of the EDAS method in the parametric selection scheme for maintenance plan in the Nigerian food industry. *Journal Rekayasa Sistem Industri*, 11(1), 1-22. doi:[10.26593/jrsi.v11i1.4349.1-22](https://doi.org/10.26593/jrsi.v11i1.4349.1-22)
- Marya, M., & Edwards, G. R. (2002). An analytical model for the optimization of the laser bending of titanium Ti-6Al-2Sn-4Zr-2Mo. *Journal of Materials Processing Technology*, 124(3), 337-344. doi:[10.1016/S0924-0136\(02\)00223-6](https://doi.org/10.1016/S0924-0136(02)00223-6)
- Miao, X., Qiang, Z., Wu, M., Song, L., & Ye, F. (2018). The optimal cutting times of multipass abrasive water jet cutting. *The International Journal of Advanced Manufacturing Technology*, 97, 1779-1786. doi:[10.1007/s00170-018-2011-0](https://doi.org/10.1007/s00170-018-2011-0)

- Muthuramalingam, T., Vasanth, S., Vinothkumar, P., Geethapriyan, T., & Rabik, M. M. (2018). Multi criteria decision making of abrasive flow oriented process parameters in abrasive water jet machining using taguchi–DEAR Methodology. *Silicon*, 10, 2015-2021. doi:[10.1007/s12633-017-9715-x](https://doi.org/10.1007/s12633-017-9715-x)
- Okponyia, K.O., & Oke, S.A. (2021). Novel EDAS-Taguchi and EDAS-Taguchi-Pareto methods for wire EDM process parametric selection of Ni55.8Ti (nitinol) shape memory alloy. *International Journal of Industrial Engineering and Engineering Management*, 3(2), 105-122. doi:[10.24002/ijieem.v3i2.4998](https://doi.org/10.24002/ijieem.v3i2.4998)
- Perec, A., & Musial, W. (2021). Multiple Criteria Optimization of Abrasive Water Jet Cutting Using Entropy-VIKOR Approach. In: S. Hloch, D. Klichová, F. Pude, G. M. Krolczyk & S. Chattopadhyaya (Eds.), *Advances in Manufacturing Engineering and Materials II* (pp. 50-62). Springer. doi:[10.1007/978-3-030-71956-2_5](https://doi.org/10.1007/978-3-030-71956-2_5)
- Perec, A., Musial, W., Prazmo, J., Sobczak, R., Radomska-Zalas, A., Fajdek-Bieda, A., Nagnajewicz, S., & Pude, F. (2021). Multi-criteria Optimization of the Abrasive Waterjet Cutting Process for the High-Strength and Wear-Resistant Steel Hardox®500. In: D. Klichová, L. Sitek, S. Hloch & J. Valentinčič (Eds.), *Advances in Water Jetting* (pp. 145-154). Springer. doi:[10.1007/978-3-030-53491-2_16](https://doi.org/10.1007/978-3-030-53491-2_16)
- Perumal, A., Azhagurajan, A., Kumar, S.S., Kailasanathan, C., Rajan, R.P., Rajan, A.J., Venkatesan, G., & Rajkumar, P.R. (2020). Experimental investigation on surface morphology and parametric optimization of Ti-6Al-2Sn-4Zr-2Mo alpha beta alloy through AWJM. *Tierarztliche Praxis*, 40, 1681-1702.
- Perumal, A., Azhagurajan, A., Kumar, S. S., Prithivirajan, R., Baskaran, S., Rajkumar, P. R., Kailasanathan C., & Venkatesan, G. (2021). Influence of optimization techniques on wire electrical discharge machining of Ti-6Al-2Sn-4Zr-2Mo alloy using modeling approach. *Journal of Inorganic and Organometallic Polymers and Materials*, 31, 3272-3289. doi:[10.1007/s10904-021-01953-y](https://doi.org/10.1007/s10904-021-01953-y)
- Perumal, A., Kailasanathan, C., Stalin, B., Kumar, S. S., Rajkumar, P. R., Gangadharan, T., Venkatesan, G., Nagaprasad, N., Dhinakaran, V., & Krishnaraj, R. (2022). Multiresponse optimization of wire electrical discharge machining parameters for Ti-6Al-2Sn-4Zr-2Mo (α - β) alloy using taguchi-grey relational approach. *Advances in Materials Science and Engineering*, 2022, 6905239. doi:[10.1155/2022/6905239](https://doi.org/10.1155/2022/6905239)
- Pradhan, S., & Maity, K. (2018). Optimization of machining parameter characteristics during turning of Ti-6Al-4V using desirability function analysis. *Materials Today: Proceedings*, 5(11-3), 25740-25749. doi:[10.1016/j.matpr.2018.11.094](https://doi.org/10.1016/j.matpr.2018.11.094)
- Singh, H., Bhoi, N.K., & Jain, P.K. (2021). Developments in abrasive water jet machining process-from 1980-2020. In: K. Gupta & A. Pramanik (Eds.), *Advanced Machining and Finishing, Handbooks in Advanced Manufacturing* (pp. 217-252). doi:[10.1016/B978-0-12-817452-4.00011-7](https://doi.org/10.1016/B978-0-12-817452-4.00011-7)
- Sitek, L., Hlaváček, P., Foldyna, J., Jarchau, M., & Foldyna, V. (2021). Pulsating abrasive water jet cutting using a standard abrasive injection cutting head – preliminary tests. In: D. Klichová, L. Sitek, S. Hloch & J. Valentinčič (Eds.), *Advances in Water Jetting* (pp. 186-196). Springer. doi:[10.1007/978-3-030-53491-2_20](https://doi.org/10.1007/978-3-030-53491-2_20)
- Ulutas, A. (2017) Sewing machine selection for a textile workshop by using EDAS method. *Journal of Business Research Turk*, 9(2), 169-183.
- Wang, S., Yang, F., Hu, D., Tang, C., & Lin, P. (2021). Modelling and analysis of abrasive water jet cutting front profile. *The International Journal of Advanced Manufacturing Technology*, 114, 2829-2837. doi:[10.1007/s00170-021-07014-5](https://doi.org/10.1007/s00170-021-07014-5)
- Zohoor, M., & Nourian, S.H. (2012). Development of an algorithm for optimum control process to compensate the nozzle wear effect in cutting the hard and tough material using abrasive water jet cutting process. *The International Journal of Advanced Manufacturing Technology*, 61, 1019-1028. doi:[10.1007/s00170-011-3761-0](https://doi.org/10.1007/s00170-011-3761-0)



Gazi University

Journal of Science

PART A: ENGINEERING AND INNOVATION

<http://dergipark.org.tr/gujisa>***In silico* Analyzes of miRNAs Associated with Root and Tuber in *S. commersonii***Aysel Ozgul KORAL¹ , Mine TURKTAS^{2*} ¹Cankiri Karatekin University, Faculty of Science, Biology Department, Cankiri, Turkey²Gazi University, Faculty of Science, Biology Department, Ankara, Turkey

Keywords	Abstract
Bioinformatics miRNA Root Solanum Commersonii Tuber	Potato is an industrial plant that is produced and consumed globally due to its cheapness, high yield in the unit area, high nutritional values. It is used in many different fields. It has been stated that wild species with various characteristics can be used in studies to increase productivity because they have greater rate of genetic variation than their domesticated relatives. One of the wild species of potato found in nature is <i>S. commersonii</i> Dunal. It is more resistant to many stresses than cultivated potato <i>S. tuberosum</i> L. Also, its tuber has better quality due to the fact that it contains a higher proportion of dry matter. With the aim of determining the effects of miRNAs in tuber production and root characteristics relation we aimed to detect miRNAs in two transcriptome libraries of <i>S. commersonii</i> . In this study miRNAs were evaluated for the first time in the wild potato transcriptome data using <i>in silico</i> analysis. A number of miRNAs were identified, and their potential roles in tuber were discussed.

CiteKoral, A. O., Turktas, M. (2022). *In silico* Analysis of miRNAs Associated with Root and Tuber in *S. commersonii*. *GU J Sci, Part A*, 9(3), 251-258

Author ID (ORCID Number)	Article Process	
A. O. Koral, 0000-0002-1206-5130	Submission Date	07.07.2022
M. Turktas, 0000-0001-8089-3774	Revision Date	15.08.2022
	Accepted Date	15.08.2022
	Published Date	26.09.2022

1. INTRODUCTION

Potato is a plant belonging to the Solanaceae family that is consumed heavily as a vegetable in the fourth place in the world. It is an industrial plant that is produced and consumed globally due to its cheapness, high yield in the unit area, high nutritional values and being used in many different fields. Although there are 2000 genera of potato plant in nature, about 180 of these can produce tubers. Yet, only eight of these tuber-producing genera have been cultured for use in the food field (Dilsiz & Yorgancılar, 2018).

It has been stated that wild species with various characteristics can be used in studies to increase productivity, because they have greater rate of genetic variation than their genetically bred relatives (Hajjar & Hodgkin, 2007). Therefore it has been proposed that wild potato species contain important characters such as disease resistance and therefore the wild species are used in breeding studies.

S. commersonii is a tuber-bearing wild potato. It has a higher quality tuber structure and starch content, yet it is more resistant to many stresses when compared to the commonly grown cultivated species (*S. tuberosum* L.) (Hanneman & Bamberg, 1986). Due to these important features, its genome was recently sequenced (Aversano et al., 2015). The genome size is about 80 Mb, and the study revealed that there are several genes effective in stress response in the genome of *S. commersonii* which are not present in *S. tuberosum* L. Moreover, duplications have been found in some gene regions in the wild potato genome suggesting that they provide advantages in adaptation to stress.

During the root formation system of the potato plant in the soil, white extensions occur between the roots which are called stolons. With the swelling of the ends of the stolons, tubers are formed. The tubers of the

*Corresponding Author, e-mail mturktas@gazi.edu.tr

plants are rich in starch. Consequently, tubers of the potato plant are the main carbohydrate source in many diets. Formation of stolons, the underground stems, in potato is known as tuberization. Tuberization is a complex process and affected by several factors. Various mechanisms are involved in tuberization in potato plant. In tuber formation, signals are received and processed in the leaves of the plant and these mobile signal molecules are transported towards the stolon tip (Chapman, 1958). As the signal molecules reach to stolon end, the cell growth at the stolon end begins to longitudinal growth. This causes bulging of the stolon. Following that, the starch synthesis in the leaves and the transport of these starches to the stolon form tuber development signals with the accumulation of starches at the tip of the stolon.

The tuberization in potato is a dynamic process and occurs with the interaction of many environmental and internal factors. Although, the physiology of tuberization is well-known, the molecular mechanisms of tuber formation in potatoes has not been completely elucidated. Thus, understanding of the tuberization process is vital for improvement of tuber quality and yield.

One of the molecules in the formation of tuber in the potato plant involved in this process is microRNAs (miRNAs) (Natarajan et al., 2017). They are non-coding small RNA molecules which repressing their target genes in many biological processes. Due to these important roles, studies have been conducted on the detection of miRNAs in many organisms, such as computer-based *in silico* methods in which the motif content and secondary structures of miRNAs are analyzed.

Until now, there are studies performed on miRNA analysis in potato. It has been reported that potato-specific miR193, miR152 and conserved miR172-1, and miR172-5 were significantly expressed in the tuberization development process in potato (Lakhotia et al., 2014). Besides, it has been shown that miR164-1, miR399-1, miR157-1, miR171-1 have key roles in tuberization (Kondare et al., 2018). Besides, potato-specific miR53, miR172, and miR399, which are miRNAs transportable in vascular tissues, are found to be effective in tuberization (Marín-González & Suárez-López, 2012). Some of those miRNAs target genes involved in signaling pathways, gibberellic acid, auxin, jasmonic acid, signaling, while the targets of many miRNAs are still unknown.

It is also known that production of tuber is associated with root characteristics such as mass, length (Ahmadi et al., 2017). Therefore we aimed to evaluate this relation in term of miRNAs in root and tuber. We performed *in silico* analysis of miRNAs in transcriptome libraries of *S. commersonii* root and tuber. This is the first study on detailed miRNA analysis in underground organs of the wild potato using *in silico* analysis. Comparative analysis of wild potato will increase our knowledge of the usage of wild species in crop breeding and improvement.

2. MATERIAL AND METHOD

In this study transcriptome libraries of *S. commersonii* root and tuber with the accession numbers of SRR1687231 and SRR1687232, respectively, were analysed. The raw data was obtained from NCBI databank using SRA-Toolkit (v. 2.11.1). The miRNA sequences were obtained from miRBase (22.1). Since there is any *S. commersonii* miRNA is available in the databank, miRNA sequences of *S. tuberosum* (SolTub3.0) which is the most closely related species was used.

Blast+ (v. 2.12) was used for homology analysis between the *S. tuberosum* miRNAs and *S. commersonii* transcriptome sequences. E-value was set as 0.01. The resulting sequences were analysed, and the read counts of the identified miRNAs were extracted by in home perl script. The blast analysis was also performed on the cDNA data of *S. tuberosum* in order to exclude false positive miRNAs from the results by analyzing the mRNA target regions of the matching reads. The protein coded sequences were extracted from the data. The miRNAs showing 2-fold difference between the libraries were assigned as differentially expressed miRNAs.

3. RESULTS AND DISCUSSION

RESULTS As a result of the bioinformatics analysis, total of 47 miRNAs were identified. Among them, 32 miRNAs showed different expression levels between the transcriptome libraries. The miRNAs of Stu-miR477b-3p, Stu-miR482a/b-3p, Stu-miR5303e/f/g/h/i/j, Stu-miR6023, Stu-miR6026-3p, Stu-miR6027, Stu-

miR7122-5p, Stu-miR7982a/b, Stu-miR7983-3p, Stu-miR7997c, Stu-miR8011b-3p, Stu-miR8011b-5p, Stu-miR8026, Stu-miR8030-3p were up-regulated in root transcriptome library. While Stu-miR7987 was found to be expressed more in the tuber than the root. Although some miRNAs with very low read counts showed difference in expression between the libraries, they were not classified as differential miRNAs due to their low read count. The 15 miRNAs showed similar expression levels between the libraries. The read counts are given in Table 1.

Table 1. Read counts of miRNAs in *S. commersonii* root and tuber transcriptome libraries

miRNA name	SRR1687231_1 (Root)	SRR1687232_1 (Tuber)
stu-miR156d-3p	1	0
stu-miR156f-3p	2	0
stu-miR477a-3p	2	0
stu-miR477b-3p	5	0
stu-miR482a-3p	12	1
stu-miR482b-3p	5	0
st-miR482d-3p	2	0
stu-miR482e-3p	2	0
stu-miR5303a	25	20
stu-miR5303b	25	20
stu-miR5303c	25	20
stu-miR5303d	25	20
stu-miR5303e	26	3
stu-miR5303f	38	9
stu-miR5303g	154	40
stu-miR5303h	93	36
stu-miR5303i	154	40
stu-miR5303j	90	16
stu-miR6023	43	14
stu-miR6026-3p	6	0
stu-miR6027	10	0
stu-miR7122-5p	16	1

Table 1. (continued)

miRNA name	SRR1687231_1 (Root)	SRR1687232_1 (Tuber)
stu-miR7981-3p	1	3
stu-miR7982a	9	0
stu-miR7982b	9	0
stu-miR7983-3p	7	1
stu-miR7987	0	5
stu-miR7996a	1	0
stu-miR7996b	1	0
stu-miR7996c	1	0
stu-miR7997c	9	0
stu-miR8001a	2	0
stu-miR8001b-5p	1	0
stu-miR8006-5p	1	3
stu-miR8007a-3p	3	0
stu-miR8007a-5p	0	1
stu-miR8007b-3p	1	0
stu-miR8011b-3p	4	1
stu-miR8011b-5p	4	1
stu-miR8014-5p	1	0
stu-miR8020	4	4
stu-miR8025-3p	2	0
stu-miR8026	5	0
stu-miR8029	1	0
stu-miR8030-3p	2	0
stu-miR8031	1	0
stu-miR8032b-3p	36	18

4. DISCUSSION

Tuberization is an important process in potato and several mechanisms play parts in the formation of tuber in the potato plant. Among these mechanisms, miRNAs play vital roles, but there is still insufficient information about the effects of miRNA on tuberization in potato. Moreover, in wild potato which has high quality tuber structure there is any information. For that reason, we aimed to evaluate the miRNA influences in root and tuber of wild potato.

The relation between tuber production and root characteristics is known (Ahmadi et al., 2017). The comparative analyses indicated that many miRNAs are differentially expressed in tuber and root which shows organ specific regulation of the miRNAs in wild potato. Besides, the differentially expressed miRNAs are mainly related with tuberization. The results proved that the presence of miRNAs in tuberization process in wild potato.

Kondhare et al. (2018) found that *Stu-miR8006-5p* expression was increased in stolon tissues. The miRNA affects on phosphatase 2c which plays role in abscisic acid (ABA) signaling (Fujii et al., 2009). Moreover, it was proposed that ABA is vital in potato tuberization (Marschner et al., 1984). Since the expression pattern of *miR8006-5p* in our analysis was found to be similar to the previous study, the results showed that *miR8006* act on tuberization via ABA signaling.

The other differentially expressed miRNAs detected in *S. commersonii* were *miR482a* and *miR482b*. It has been reported that the expression of *Stu-miR482a-3p* in stolon tissue is increased in *S. tuberosum* and it takes part in the initial phase of tuberization (Chi et al., 2015). In another study, it was reported that this miRNA targets both *StARF8* (auxin response factors 8), which is involved in the auxin synthesis pathway and plays an activator role in tuberization, and *StSUT1* (sucrose transporter 1) gene, which is involved in sucrose transport and plays an activator role in tuberization (Kondhare et al., 2020). Thus, it appears that auxin signaling is essential in the initial tuberization step. A situation consistent with this finding was also found in our results. Observing that *Stu-miR482a-3p* is significantly suppressed in tuberous tissue, it can be understood that it is required only in the early stage of tuberization. On the other hand, although the effect of *Stu-miR482b-3p* has not been not known exactly, its relationship with tuberization was detected for the first time in this study.

Kondhare et al. (2018) indicated that *Stu-miR5303f* and *Stu-miR5303g* were involved in stolon-tuber transition in *S. tuberosum*. Moreover *Stu-miR5303g* regulates Ca^{2+} release and expression of inositol monophosphatase 3 gene. It is also involved in ABA signaling (Jia et al., 2019). Thus, it appears that Ca^{2+} release and ABA signaling is essential in the initial tuberization step. It has been reported that *Stu-miR5303f/g* stimulates TAS-like loci of unknown function in tuberization (Kondhare et al., 2018). Confirming the fact that *Stu-miR5303* is needed in early tuberization stage, in our study *Stu-miR5303 e, f, g, h, i, j* forms were found to be suppressed in tuber. *Stu-miR5303e, h, j, i* have not been not known exactly, their relationship with tuberization was detected for the first time in this study.

There is another tuberization related miRNA known as *miR477*. It has been stated that *miR477a/ b-5p* is involved in the expression regulation of *DELLA* which is a GRAS transcription factor (Kim et al., 2005) and required for radial formation and development in the root and early stolon in tuberization in *S. tuberosum* (Kondhare et al., 2018). In our study, the expression of *miR477a/ b* was increased in root. However, it should be noted that the miRNA counts are very low in the libraries. Therefore, the read count are insufficient to make a firm decision.

In our study it was found that *Stu-miR6023* was suppressed in tuber. *Stu-miR6023* controls *StuPME21575* which is a pectinesterase (Yan et al., 2020). It is known that tuber pectin methyl esterase activity (PME) is a potential factor influencing the textural properties (Ross et al., 2011). It is concluded that down regulation of *miR6023* in tuber stimulated the expression of pectinesterase in starch and changed the pectin content in wild potato tuber. It is speculated that the differences in pectin structure between wild and domesticated potato might be related with miRNAs.

miR7983 is a *Solanaceae* species specific miRNA and cleaves hydroxyproline-rich glycoprotein (HRGP) which is a major group of wall glycoproteins (Kondhare et al., 2018). HRGPs are involved in numerous

processes such as cell wall integrity pathway (Johnson et al., 2017). Our analysis indicated that differential expression of miR7983 might be related with cell wall architecture heterogeneity between root and tuber in wild potato.

It was found that St-miR6026-3p targets GA 2-oxidase gene (StGA2ox1) which is a key gibberellic acid metabolic gene and involved in stolon-to-tuber transition potato (Kondhare et al., 2018). Confirming the fact that suppression of miR6026 results in tuber development, St-miR6026-3p was down-regulated in tuber in our study.

One of the major categories of small RNAs is phased secondary small interfering RNAs (phasiRNAs) (Liu et al., 2020). It was shown that miR7122 triggers phasiRNA production (Xia et al., 2013). In our study expression of miR7122 was repressed in tuber. Although functions of the phasiRNA are still poorly defined, this is the first study showing their contribution in root and tuber interaction.

In silico analysis revealed that miR6027 was up-regulated in root transcriptome library. In literature it was shown that miR6027 represses Sw-5b gene which is resistance gene (de Oliveira et al., 2018). The miRNA also plays a role in phasiRNA biogenesis (Seo et al., 2018). Therefore this is the first study indicating the role of miR6027 in tuberization. On the other hand since both miR7122 and miR6027 which are involved in phasiRNA biogenesis were up-regulated in root, it can be inferred that phasiRNAs have important functions in potato root.

miR7982 is another stress related miRNA which was identified in *Cajanus cajan* (Shanmugavadeivel et al., 2016). In our study, it was observed that St-miR7982a and b were suppressed in tuber and were detected for the first time in relation to tuberization.

miR7997c targets bZIP transcription factors targeting several genes involved in defense responses, growth and development (Cheng et al., 2016). Our study revealed its role in root and tuber involvement for the first time.

Until now, any information has been found in the literature on which pathways stu-miR8011b-3p, 5p, stu-miR8032b-3p, stu-miR8026, stu-8011b-3p and stu-8011b-5p are involved. However, these miRNAs were significantly suppressed in tuber tissue in our study, and their relationship with tuber and root relevance was detected for the first time. Therefore, it is necessary to investigate the genes affected by these miRNAs with further studies.

5. CONCLUSION

In this study, significant differences were determined in terms of miRNA expression level of tuber and root. As a result of *in silico* analysis of tuber and root transcriptome libraries of *S. commersonii* that the most miRNAs were found to be effective in cell wall architecture, textural properties, tuberization. Moreover, involvement of some miRNAs in root and tuber relation was detected for the first time, and this study serves important data in understanding the roles of miRNAs in wild potato. However, with the purpose of understanding the efficiency of these miRNAs further functional analyzes should be performed. The miRNAs should be clarified in more detail, so that the obtained data could be transferred to *S. tuberosum* for breeding studies in terms of increasing tuber quality.

CONFLICT OF INTEREST

The authors declare no conflict of interest.

REFERENCES

- Ahmadi, S. H., Agharezaee, M., Kamgar-Haghighi, A. A., & Sepaskhah, A. R. (2017). Compatibility of root growth and tuber production of potato cultivars with dynamic and static water-saving irrigation managements. *Soil Use and Management*, 33(1), 106-119. doi:[10.1111/sum.12317](https://doi.org/10.1111/sum.12317)
- Aversano, R., Contaldi, F., Ercolano, M. R., Grosso, V., Iorizzo, M., Tatino, F., Xumerle, L., Molin, A. D., Avanzato, C., Ferrarini, A., Delledonne, M., Sanseverino, W., Cigliano, R. A., Capella-Gutierrez, S.,

- Gabaladón, T., Frusciante, L., Bradeen, J. M., & Carputo, D. (2015). The *Solanum commersonii* genome sequence provides insights into adaptation to stress conditions and genome evolution of wild potato relatives. *The Plant Cell*, 27(4), 954-968. doi:[10.1105/tpc.114.135954](https://doi.org/10.1105/tpc.114.135954)
- Chapman, H. W. (1958). Tuberization in the Potato Plant. *Physiologia Plantarum*, 11, 215-224. doi:[10.1111/j.1399-3054.1958.tb08460.x](https://doi.org/10.1111/j.1399-3054.1958.tb08460.x)
- Cheng, H.-Y., Wang, Y., Tao, X., Fan, Y.-F., Dai, Y., Yang, H., & Ma, X.-R. (2016). Genomic Profiling of Exogenous Abscisic Acid-Responsive MicroRNAs in Tomato (*Solanum lycopersicum*). *BMC Genomics*, 17(1), 423. doi:[10.1186/s12864-016-2591-8](https://doi.org/10.1186/s12864-016-2591-8)
- Chi, M., Liu, C., Su, Y., Tong, Y., & Liu, H. (2015). Bioinformatic Prediction of Upstream MicroRNAs of PPO and Novel MicroRNAs in Potato. *Canadian Journal of Plant Science*, 95(5), 871-877. doi:[10.4141/cjps-2014-308](https://doi.org/10.4141/cjps-2014-308)
- de Oliveira, A. S., Boiteux, L. S., Kormelink, R., & Resende, R. O. (2018). The Sw-5 Gene Cluster: Tomato Breeding and Research Toward Orthotospovirus Disease Control. *Frontiers in Plant Science*, 9, 1055. doi:[10.3389/fpls.2018.01055](https://doi.org/10.3389/fpls.2018.01055)
- Dilsiz, S., & Yorgancılar, M. (2018). Patates (*Solanum Tuberosum* L.) Bitkisinde Sakkaroz ve Oksin-Sitokinin Uygulamalarının Mikro Yumurru Oluşumuna Etkileri. *Selçuk Tarım ve Gıda Bilimleri Dergisi*, 32(3), 274-281. doi:[10.15316/SJAFS.2018.94](https://doi.org/10.15316/SJAFS.2018.94)
- Fujii, H., Chinnusamy, V., Rodrigues, A., Rubio, S., Antoni, R., Park, S.-Y., Cutler, S. R., Sheen, J., Rodriguez, P. L., & Zhu, J.-K. (2009). *In vitro* Reconstitution of an Abscisic acid Signalling Pathway. *Nature*, 462, 660-664. doi:[10.1038/nature08599](https://doi.org/10.1038/nature08599)
- Hajjar, R., & Hodgkin, T. (2007). The Use of Wild Relatives in Crop Improvement: A Survey Of Developments over The Last 20 Years. *Euphytica*, 156(1-2), 1-13. doi:[10.1007/s10681-007-9363-0](https://doi.org/10.1007/s10681-007-9363-0)
- Hanneman, R. E. Jr., & Bamberg, J. B. (1986). Inventory of Tuber-Bearing Solanum Species. *Bulletin 533 of Research Division of the College of Agriculture and Life Sciences*, University of Wisconsin, Madison USA.
- Johnson, K. L., Cassin, A. M., Lonsdale, A., Wong, G. K.-S., Soltis, D. E., Miles, N. W., Melkonian, M., Melkonian, B., Deyholos, M. K., Leebens-Mack, J., Rothfels, C. J., Stevenson, D. W., Graham, S. W., Wang, X., Wu, S., Pires, J. C., Edger, P. P., Carpenter, E. J., Bacic, A., ... Schultz, C. J. (2017). Insights into the Evolution of Hydroxyproline-Rich Glycoproteins from 1000 Plant Transcriptomes. *Plant Physiology*, 174(2), 904-921. doi:[10.1104/pp.17.00295](https://doi.org/10.1104/pp.17.00295)
- Jia, Q., Kong, D., Li, Q., Sun, S., Song, J., Zhu, Y., Liang, K., Ke, Q., Lin, W., Huang, J. (2019). The Function of Inositol Phosphatases in Plant Tolerance to Abiotic Stress. *International Journal of Molecular Sciences*, 20(16), 3999. doi:[10.3390/ijms20163999](https://doi.org/10.3390/ijms20163999)
- Kondhare, K. R., Malankar, N. N., Devani, R. S., & Banerjee, A. K. (2018). Genome-Wide Transcriptome Analysis Reveals Small RNA Profiles Involved in Early Stages of Stolon-to-Tuber Transitions in Potato under Photoperiodic Conditions. *BMC Plant Biology*, 18(1), 284. doi:[10.1186/s12870-018-1501-4](https://doi.org/10.1186/s12870-018-1501-4)
- Kondhare, K. R., Natarajan, B., & Banerjee, A. K. (2020). Molecular Signals that Govern Tuber Development in Potato. *The International Journal of Developmental Biology*, 64(1-2-3), 133-140. doi:[10.1387/ijdb.190132ab](https://doi.org/10.1387/ijdb.190132ab)
- Kim, J., Jung, J.-H., Reyes, J. L., Kim, Y.-S., Kim, S.-Y., Chung, K.-S., Kim, J. A., Lee, M., Lee, Y., Narry Kim, V., Chua, N.-H., & Park, C.-M. (2005). microRNA-directed cleavage of *ATHB15* mRNA regulates vascular development in Arabidopsis inflorescence stems. *The Plant Journal*, 42(1), 84-94. doi:[10.1111/j.1365-313X.2005.02354.x](https://doi.org/10.1111/j.1365-313X.2005.02354.x)
- Lakhotia, N., Joshi, G., Bhardwaj, A. R., Katiyar-Agarwal, S., Agarwal, M., Jagannath, A., Goel, S., & Kumar, A. (2014). Identification and Characterization of miRNAome in Root, Stem, Leaf and Tuber Developmental Stages of Potato (*Solanum tuberosum* L.) by High-Throughput Sequencing. *BMC Plant Biology*, 14(1), 6. doi:[10.1186/1471-2229-14-6](https://doi.org/10.1186/1471-2229-14-6)

- Liu, Y., Teng, C., Xia, R., & Meyers, B. C. (2020). PhasiRNAs in Plants: Their Biogenesis, Genic Sources, and Roles in Stress Responses, Development, and Reproduction. *The Plant Cell*, 32(10), 3059-3080. doi:[10.1105/tpc.20.00335](https://doi.org/10.1105/tpc.20.00335)
- Marín-González, E., & Suárez-López, P. (2012). "And yet it moves": Cell-to-Cell and Long-Distance Signaling by Plant MicroRNAs. *Plant Science*, 196, 18-30. doi:[10.1016/j.plantsci.2012.07.009](https://doi.org/10.1016/j.plantsci.2012.07.009)
- Marschner, H., Sattelmacher, B. & Bangerth, F. (1984). Growth Rate of Potato Tubers and Endogeneous Contents of Indolylacetic Acid. *Physiologia Plantarum*, 60(1), 16-20. doi:[10.1111/j.1399-3054.1984.tb04242.x](https://doi.org/10.1111/j.1399-3054.1984.tb04242.x)
- Natarajan, B., Bhogale, S. & Banerjee, A. K. (2017). The Essential Role of MicroRNAs in Potato Tuber Development: a mini review. *Indian Journal of Plant Physiology*, 22(4), 401-410. doi:[10.1007/s40502-017-0324-x](https://doi.org/10.1007/s40502-017-0324-x)
- Ross, H. A., Wright, K. M., McDougall, G. J., Roberts, A. G., Chapman, S. N., Morris, W. L., Hancock, R. D., Stewart, D., Tucker, G. A., James, E. K., & Taylor, M. A. (2011). Potato Tuber Pectin Structure is Influenced by Pectin Methyl Esterase Activity and Impacts on Cooked Potato Texture. *Journal of Experimental Botany*, 62(1), 371-381. doi:[10.1093/jxb/erq280](https://doi.org/10.1093/jxb/erq280)
- Seo, E., Kim, T., Park, J. H., Yeom, S.-I., Kim, S., Seo, M.-K., Shin, C., & Choi, D. (2018). Genome-Wide Comparative Analysis in Solanaceous Species Reveals Evolution of Micrnas Targeting Defense Genes in *Capsicum spp.* *DNA Research : An International Journal for Rapid Publication of Reports on Genes and Genomes*, 25(6), 561-575. doi:[10.1093/dnares/dsy025](https://doi.org/10.1093/dnares/dsy025)
- Shanmugavadivel, P. S., Soren, K. R., Konda, A. K., Chaturvedi, S. K., & Singh, N. P. (2016). Identification of Potential Stress Responsive Micrnas and Their Targets in *Cajanus spp.* *Agri Gene*, 1, 33-37. doi:[10.1016/j.aggene.2016.06.001](https://doi.org/10.1016/j.aggene.2016.06.001)
- Xia, R., Meyers, B. C., Liu, Z., Beers, E. P., Ye, S., & Liu, Z. (2013). MicroRNA Superfamilies Descended from miR390 and Their Roles in Secondary Small Interfering RNA Biogenesis in Eudicots. *The Plant Cell*, 25(5), 1555-1572. doi:[10.1105/tpc.113.110957](https://doi.org/10.1105/tpc.113.110957)
- Yan, C., Wang, Q., Zhang, N., Wang, J., Ren, X., Xue, B., Pu, X., Xu, Z., & Liao, H. (2020). High-Throughput MicroRNA and mRNA Sequencing Reveals that MicroRNAs May Be Involved in Pectinesterase-Mediated Cold Resistance in Potato. *Phyton-International Journal of Experimental Botany*, 89(3), 561-586. doi:[10.32604/phyton.2020.010322](https://doi.org/10.32604/phyton.2020.010322)



Gazi University

Journal of Science

PART A: ENGINEERING AND INNOVATION

<http://dergipark.org.tr/gujisa>

A New Numerical Approach Using Chebyshev Third Kind Polynomial for Solving Integrodifferential Equations of Higher Order

Abdullahi Muhammed AYINDE¹ , Adewale Adeyemi JAMES^{2*} , Ajimoti Adam ISHAQ³ , Taiye OYEDEPO⁴ ¹Department of Mathematics, Modibbo Adama University, Yola, Nigeria²Department of Mathematics & Statistics, American University of Nigeria, Yola, Nigeria³Department of Physical Sciences, Al-Hikmah University, Ilorin, Nigeria⁴Federal College of Dental Technology and Therapy, Enugu, Nigeria

Keywords	Abstract
Degree of Approximant	There are several classifications of linear Integral Equations. Some of them include; Volterra Integral Equations, Fredholm Linear Integral Equations, Fredholm-Volterra Integrodifferential. In the past, solutions of higher-order Fredholm-Volterra Integrodifferential Equations [FVIE] have been presented. However, this work uses a computational techniques premised on the third kind Chebyshev polynomials method. The performance of the results for distinctive degrees of approximation (M) of the trial solution is cautiously studied and comparisons have been additionally made between the approximate/estimated and exact/definite solution at different intervals of the problems under consideration. Modelled Problems have been provided to illustrate the performance and relevance of the techniques. However, it turned out that as M increases, the outcomes received after every iteration get closer to the exact solution in all of the problems considered. The results of the experiments are therefore visible from the tables of errors and the graphical representation presented in this work.
Exact Solution	
Third Kind Chebyshev Polynomial	
Trial Solution	
Volterra-Fredholm Integrodifferential Equations	

Cite

Ayinde, A. M, James, A. A., Ishaq A. A., & Oyedepo, T. (2022). A New Numerical Approach Using Chebyshev Third Kind Polynomial for Solving Integrodifferential Equations of Higher Order. *GU J Sci, Part A*, 9(3), 259-266.

Author ID (ORCID Number)	Article Process
A. M Ayinde, 0000-0002-2563-0952	Submission Date 25.03.2022
A. A James, 0000-0003-2257-5596	Revision Date 07.07.2022
A. A. Ishaq, 0000-0002-8931-5708	Accepted Date 29.08.2022
T. Oyedepo, 0000-0001-9063-8806	Published Date 27.09.2022

1. INTRODUCTION

Integrodifferential equations have been observed in several ways and on several occasions. These include; Biology models, Chemical Kinetics, Mechanics, glass-forming procedures, and so many other difficult areas like Dynamics, Economics, Electromagnetism, Astro-Physics, Modelling, and Nano-Hydrodynamics.

Worthy of note is the fact that many authors have also given numerous and analytical methods for solving Integrodifferential equations. Some examples include;

Eslahchi et al. (2012) combined the Adomian's decompositions technique with a Wavelet-Galerking approach to solving Integrodifferential Equations. To establish an approximate solution of higher-order linear Fredholm Integrodifferential equations, a realistic matrix technique can be used (Kurt & Sezer, 2008) which possess a constant coefficient beneath the initial boundary condition in phrases of Taylor polynomials, numerical solution of mixed linear Integrodifferential difference equations is considered using the Chebyshev collocation method.

This method is mainly dependent on Chebyshev expansion approach. The specified conditions and the mixed linear Integrodifferential difference equation are transformed into matrix equations, which equate to a system

*Corresponding Author, e-mail: adewale.james@aun.edu.ng

of linear algebraic equations, in this approach (Gulsu et al., 2010). A numerical solution of the system of linear Volterra Integrodifferential equations is proposed in (Rashidinia & Tahmasebi, 2012) where the Taylor series method was developed and modified to solve the system of linear Volterra Integrodifferential equations. Sezer and Gulsu (2005) explores the polynomial solution from the most generic linear Fredholm Integrodifferential difference equation using the Taylor matrix technique. Wazwaz (2011) also considered non-linear Volterra Integrodifferential equations, but with a comparative approach to solving Integrodifferential equations, using the differential numerical approach; Lapace transform-Adomian decomposition methods were specifically combined. (Rashed, 2004; Wazwaz, 2010) used the application Lagrange interpolation to compute the numerical solutions of integral-differential equations. Yusufoglu (2007) solved Integrodifferential equations by hiring an efficient algorithm. Akgonullu et al. (2011) presented higher-order linear Fredholm Integrodifferential equations with variable coefficients in terms of Hermite polynomials. Taiwo and Fesojoye (2015) solved Fractional-order Integrodifferential equations by presenting perturbation Least-square Chebyshev method. A new numerical scheme for solving the Volterra-Integrodifferential equation system using Genocchi polynomials is presented in (Loh & Phang, 2018). Sakran (2019) constructs an algorithm for solving singularly perturbed Volterra integral type and integrodifferential equations based on a finite expansion in Chebyshev polynomials of the third kind. Rabiei et al. (2019) investigated the numerical solution of Volterra integrodifferential equations using the General linear method; in the work, the order conditions of the proposed method are derived using B-series and rooted trees techniques. Lotfi and Alipanah (2020) describes the Legendre spectral element method for solving integrodifferential equations. Samaher (2021) proposes a reliable iterative method for resolving many types of Volterra-Fredholm integrodifferential equations, and the iterative method is used to obtain series solutions to the problems under consideration. Adebisi et al. (2021) employed the Galerkin method to solve Volterra integrodifferential equations using Chebyshev polynomials as the basis function.

The work of (Shah & Singh, 2015) prompted us to study the linear Integrodifferential equations. In the work, the basis function used for the class of initial value problems was the Homotopy Analysis Method this triggered a study of the work, and it was again applied to Integrodifferential equations (Linear Case). We taken into consideration a standard Higher-order linear Volterra, and Fredholm Integrodifferential equation of the form;

$$B_{01}\varphi^m(z) + B\varphi^{m-1}(z) + \dots + B_{m-1}\varphi'(z) + B_m\varphi(z) + \lambda \int_{h(z)}^{i(z)} K(z,s)\varphi(s)dt = f(z) \quad (1)$$

subject to the conditions

$$\varphi(p) = P \text{ \& } \varphi(q) = Q \quad (2)$$

where B^i 's are real constants; i, h are finite constants; $K(z,s)$ and $f(z)$ are specified given real-valued functions; φ are unknown constants to be determined. We then solved these problems by assuming an approximate solution given by Equation (4) below.

2. BASIC DEFINITION

This section contains basic definition that are essential to the research work in this paper.

2.1. Integrodifferential Equations (Wazwaz, 2010)

Integrodifferential equations (IDEs) are equations in which the unknown function $\varphi(z)$ is written with the integral sign and also has an ordinary derivative $\varphi^{(k)}$. The following is a typical Integrodifferential equation:

$$\varphi^{(k)}(z) = f(z) + \lambda \int_{h(z)}^{i(z)} K(z,s)\varphi(s)ds \quad (3)$$

$i(z)$ and $h(z)$ are integration limits that can be constants, variables, or blended. λ is a free parameter, $f(z)$ is a specified function, and $K(z,s)$ stands for kernel.

If the limit $\varphi(z)$ is substituted by a variable of integration z , we have the Volterra Integro-differential equation, and if the limit of integration is constants, we have the Fredholm Integro-differential equation.

2.2. Collocation Method

A method of evaluating an approximate solution in a suitable collection of functions, sometimes referred to as a trial solution or basis function.

2.3. Exact Solution

If a solution may be expressed in a closed form, it's known as an exact solution. Examples are polynomials, exponential functions, trigonometric functions, or an aggregate of or extra of these standard functions.

2.4. Approximate Solution

An approximate solution denoted by $\varphi_M(z)$ is given in the form

$$\varphi_M(z) = \sum_{i=0}^M b_j \zeta_m(z) \quad (4)$$

where $b_j (j \geq 0)$ are to be determined.

2.5. Chebyshev Polynomials of Third Kind (Loh & Phang, 2018)

The Chebyshev polynomial of the third kind in $[-1, 1]$ of degree m is represented by $V_m(z)$, where:

$$V_m(z) = \cos \frac{\left(m + \frac{1}{2}\right) \vartheta}{\cos\left(\frac{\vartheta}{2}\right)}, \quad \text{where } z = \cos \vartheta \quad (5)$$

This elegance of Chebyshev polynomials satisfied the subsequent recurrence relation given by

$$V_0(z) = 1, \quad V_1(z) = 2z - 1, \quad V_m(z) = 2zV_{m-1}(z) - V_{m-2}(z), \quad m = 2, 3, \dots \quad (6)$$

The Chebyshev polynomial of the third kind in $[\alpha, \beta]$ of degree, m is represented by $V_m^*(z)$, where:

$$V_m^*(z) = \cos \frac{\left(m + \frac{1}{2}\right) \vartheta}{\cos\left(\frac{\vartheta}{2}\right)}, \quad \cos \vartheta = \frac{2z - (\alpha + \beta)}{\beta - \alpha}, \quad \vartheta \in [0, \pi] \quad (7)$$

3. THE RESEARCH METHODOLOGY

Equation (1) was solved using the third kind of Chebyshev polynomials and the standard collocation method.

3.1. The Standard Collocation Method Employs a Third-Order Chebyshev Polynomial Basis

The standard collocation method can be used to solve the well-known problem provided in equation (1), subject to the conditions given in equation (2). This is accomplished by assuming a form trial solution.

$$\varphi_m(z) = \sum_{i=0}^M b_j V_j^*(z) \quad (8)$$

where b_j , $j = 0, 1, M$ are undefined constants and $V_j^*(z) (j \geq 0)$ are 1/3-order Chebyshev polynomials described in equations (5-7). In most instances, a larger M , produces a better approximate solution, and b_j is the

specialized coordinate referred to as the degree of freedom. Thus, differentiating equation (8) with respect to m th-times as functions of z , to obtain the following equations

$$\left. \begin{aligned} \varphi'_m(z) &= \sum_{i=0}^M b_j V_j^{*'}(z) \\ \varphi''_m(z) &= \sum_{j=0}^M b_j V_j^{*''}(z) \\ &\vdots \\ \varphi^{(m)}(z) &= \sum_{j=0}^M b_j V_j^{*(m)}(z) \end{aligned} \right\} \quad (9)$$

As a result of putting Equations (8-9) into Equation (1), we get

$$\begin{aligned} B_{01} \sum_{j=0}^M b_j V_j^{*(m)}(z) + B_{11} \sum_{j=0}^M b_j V_j^{*(m-1)}(z) + B_{21} \sum_{j=0}^M b_j V_j^{*(m-2)}(z) \\ + B_{m1} \sum_{j=0}^M b_j V_j^*(z) + \lambda \int_{h(z)}^{i(z)} K(z, t) \left(\sum_{j=0}^M b_j V_j^*(t) \right) dt = f(z) \end{aligned} \quad (10)$$

The integral part of Equation (10) is evaluated to produce

$$\begin{aligned} B_{01} \sum_{i=0}^M b_j V_j^{*(m)}(z) + B_{11} \sum_{j=0}^M b_j V_j^{*(m-1)}(z) + B_{21} \sum_{j=0}^M b_j V_j^{*(m-2)}(z) + \\ + B_{m1} \sum_{j=0}^M b_j V_j^*(z) + \lambda G(z) = f(z) \end{aligned} \quad (11)$$

$$\text{and } G(z) = \int_{h(z)}^{i(z)} K(z, t) \left(\sum_{i=0}^M b_j V_j^*(t) \right) dt$$

We collocate the resulting equation after simplification at the point $z = z_k$

$$\begin{aligned} B_{01} \sum_{i=0}^M b_j V_j^{*(m)}(z_k) + B_{11} \sum_{j=0}^M b_j V_j^{*(m-1)}(z_k) + B_{21} \sum_{j=0}^M b_j V_j^{*(m-2)}(z_k) + \\ \cdots + B_{m1} \sum_{j=0}^M b_j V_j^*(z_k) + \lambda G(z_k) = f(z_k) \end{aligned} \quad (12)$$

where

$$z_k = \alpha + \frac{(\beta - \alpha)k}{M}; \quad k = 1, 2, \dots, M - 1 \quad (13)$$

Equation (12) is then transformed into a matrix as

$$B \underline{z} = \underline{d} z_k \quad (14)$$

where

$$B = \begin{pmatrix} b_{11} & b_{12} & b_{13} & \cdots & b_{1,m} \\ b_{21} & b_{22} & b_{23} & \cdots & b_{2,m} \\ b_{31} & b_{32} & b_{33} & \cdots & b_{3,m} \\ \vdots & \vdots & \vdots & \ddots & \vdots \\ b_{m,1} & b_{m,2} & b_{m,3} & \cdots & b_{m,m} \end{pmatrix} \quad (15)$$

$$\underline{z} = (z_1, z_2, z_3, \dots, z_m)^T \quad (16)$$

$$\underline{d} = (f(d_1), f(d_2), f(d_3) \dots, f(d_m))^T \quad (17)$$

Consequently, Equation (12) yields a (M-1) algebraic linear system of equations in (M+1) unknown constants, and the specified conditions in Equation (12) yield m additional equations (2). We now have an algebraic linear system of equations with (M+1) variables. These equations are then solved using Maple 18 software to provide (M+1) unknown constants b_j ($j \geq 0$), which are then used to approximate the solution given by Equation (8).

4. PROBLEMS AND RESULTS

With third-kind Chebyshev as the basis functions, the standard collocation approximation approach on higher-order integrodifferential equations was demonstrated. At different intervals of the problems under consideration, the results obtained by the exact solution were compared with the approximate solution.

4.1. Problem 1 (Akgonullu et al., 2011)

Here, we looked at the Fredholm Integrodifferential equation of second order.

$$\varphi''(z) = e^z - \frac{4}{3}z + \int_0^1 zt\varphi(t)dt. \quad (18)$$

with initial conditions

$$\varphi(0) = 1, \quad \varphi'(0) = 2 \quad (19)$$

The exact solution is as follows

$$\varphi(z) = z + e^z \quad (20)$$

4.2. Problem 2 (Wazwaz, 2011)

Here, we considered the second-order linear Volterra Integrodifferential equation

$$\varphi''(z) = 2 - 2z \sin z - \int_0^z (z-t)\varphi(t)dt. \quad (21)$$

with initial conditions

$$\varphi(0) = 0, \quad \varphi'(0) = 0 \quad (22)$$

The exact solution is given as

$$\varphi(z) = z \sin z \quad (23)$$

4.3. Problem 3 (Wazwaz, 2011)

Here, we considered the second-order linear Volterra Integrodifferential equation

$$\varphi^{(v)}(z) = -1 + z - \int_0^z (z-t)\varphi(t)dt. \quad (24)$$

with initial conditions

$$\varphi(0) = -1, \quad \varphi'(0) = 1, \quad \varphi''(0) = 1, \quad \varphi'''(0) = 1 \tag{25}$$

The exact solution is

$$\varphi(z) = \sin x - \cos x \tag{26}$$

Note: We defined absolute error as follows:

$$\text{Absolute Error} = |\varphi(z) - \varphi_M(z)| \tag{27}$$

where, $\varphi(z)$ stands for the exact solution and $\varphi_M(z)$ stands for the approximate solution obtained for the various M values.

4.4. Tables of Errors and Approximate for the Problems

Table 1. Table of Error and Approximate for Problem 1

Z	φ (Exact)	φ (Approximate) For Case M = 5	φ (Approximate) For Case M = 10	Absolute (Error) For M = 5	Absolute (Error) For M = 10
0.0	1.00000000000000	1.0000000020000	1.000004792000	2.00 e-09	4.79e-06
0.2	1.4214027581602	1.4213780016409	1.421407783585	2.48 e-05	5.03e-06
0.4	1.8918246976413	1.8917670852221	1.891831437531	5.76 e-05	6.74e-06
0.6	2.4221188003905	2.4220279027664	2.422126707764	9.09 e-05	7.91e-06
0.8	3.0255409284925	3.0254159909159	3.025548507593	1.25 e-04	7.58e-06
1.0	3.7182818284590	3.7181120074800	3.718293781960	1.61 e-04	1.11e-05

Table 2. Table of Error and Approximate for Problem 2

Z	φ (Exact)	φ (Approximate) For Case M = 5	φ (Approximate) For Case M = 10	Absolute (Error) For M = 5	Absolute (Error) For M = 10
0.0	0.00000000000000	-5.000000000e-11	-1.13494000e-07	5.00e-11	1.13e-10
0.2	0.039733866159	0.0396474110875	0.039734121852	8.65e-05	2.56e-07
0.4	0.155767336923	0.1555676200122	0.155767558521	1.91e-04	2.22e-07
0.6	0.338785484037	0.2394579599488	0.338785316341	9.93e-04	1.68e-07
0.8	0.573884872711	0.5734637964333	0.573884334512	4.21e-04	5.38e-07
1.0	0.841470984808	0.7045186581451	0.841470029934	5.53e-04	9.55e-07

Table 3. Table of Error and Approximate for Problem 3

Z	φ (Exact)	φ (Approximate) For Case M = 6	φ (Approximate) For Case M = 10	Absolute (Error) For M = 6	Absolute (Error) For M = 10
0.0	-1.00000000000000	-0.999999999900	1.000000006000	1.00e-10	6.00e-09
0.2	-0.781397247046	-0.781397490149	-0.781397249066	2.43e-07	2.10e-09
0.4	-0.531642651694	-0.531645288439	-0.531642645501	2.64e-05	6.20e-09
0.6	-0.260693141515	-0.260702948221	-0.260693148269	9.81e-05	6.80e-09
0.8	0.020649381552	0.020625391964	0.020649386322	2.31e-05	4.77e-09
1.0	0.841470984808	0.7045186581451	0.841470029934	5.53e-04	9.55e-07

5. CONCLUSION

In terms of error and approximate solutions, Table 1-3 provide the numerical solutions for the Fredholm-Volterra Integrodifferential equations computed using the third kind of Chebyshev polynomial basis function. In all of the problems solved, the approximate solution is much closer to the precise solution when evaluated at an equally spaced interior point.

However, as shown in the tables of errors, the obtained results provide a good approximation to the precise solution for varying degrees of M, in other words, as M increases, the obtained results provide a good approximation to the exact solution with a few iterations. As a result, we conclude that the method was realistic and effective under the given circumstances.

CONFLICT OF INTEREST

The authors declare no conflict of interest.

AVAILABILITY OF DATA AND MATERIAL

Not applicable

REFERENCES

- Adebisi, A. F., Ojurongbe, T. A., Okunlola, K. A., & Peter, O. J. (2021). Application of Chebyshev polynomial basis function on the solution of Volterra integro-differential equations using Galerkin method. *Mathematics and Computational Sciences*, 2(4), 41-51. doi:[10.30511/mcs.2021.540133.1047](https://doi.org/10.30511/mcs.2021.540133.1047)
- Akgonullu, N., Şahin, N., & Sezer, M. (2011). A Hermite Collocation Method For The Approximation Solutions of Higher-Order Linear Fredholm Integrodifferential equations. *Numerical Methods for Partial Differential Equations*, 27(6), 1707-1721. doi:[10.1002/num.20604](https://doi.org/10.1002/num.20604)
- Eslahchi, M. R., Mehdi, D., & Sanaz, A. (2012). The third and fourth kinds of Chebyshev polynomials and best uniform approximation. *Mathematical and Computer Modelling*, 55(5-6), 1746-1762. doi:10.1016/j.mcm.2011.11.023
- Gulsu, M., Ozturk, Y., & Sezer, M. (2010). A New Collocation Method for Solution of Mixed Linear Integrodifferential equations. *Applied Mathematics and Computation*, 216(7), 2183-2198. doi:10.1016/j.amc.2010.03.054
- Kurt, N., & Sezer, M. (2008). Polynomial solution of high-order linear Fredholm integro-differential equations with constant coefficients. *Journal of the Franklin Institute*, 345(8), 839-850. doi:10.1016/j.jfranklin.2008.04.016
- Loh, R. J., & Phang, C. (2018). A new numerical scheme for solving system of Volterra integro-differential equation. *Alexandria Engineering Journal*, 57(2), 1117-1124. doi:[10.1016/j.aej.2017.01.021](https://doi.org/10.1016/j.aej.2017.01.021)
- Lotfi, M., & Alipanah, A. (2020). Legendre spectral element method for solving Volterra-integro differential equations. *Results in Applied Mathematics*, 7, 100116. doi:[10.1016/j.rinam.2020.100116](https://doi.org/10.1016/j.rinam.2020.100116)
- Rabiei, F., Abd Hamid, F., Abd Majid, Z., & Ismail, F. (2019). Numerical solutions of Volterra integro-differential equations using General Linear Method. *Numerical Algebra, Control and Optimization*, 9(4), 433-444. doi:[10.3934/naco.2019042](https://doi.org/10.3934/naco.2019042)
- Rashed, M. T. (2004). Lagrange interpolation to compute the numerical solutions differential, Integral, and Integrodifferential equations. *Applied Mathematics and Computation*, 151(3), 869-878, doi:[10.1016/S0096-3003\(03\)00543-5](https://doi.org/10.1016/S0096-3003(03)00543-5)
- Rashidinia, J., & Tahmasebi, A. (2012). Taylor Series Method for the System of Linear Volterra Integrodifferential Equations. *Journal of Mathematics and Computer Science*, 4(3), 331-343. doi:[10.22436/jmcs.04.03.06](https://doi.org/10.22436/jmcs.04.03.06)

- Sakran, M. R. A. (2019). Numerical solutions of integral and integro-differential equations using Chebyshev polynomial of the third kind. *Applied Mathematics and Computation*, 35, 66-82. doi:[10.1016/j.amc.2019.01.030](https://doi.org/10.1016/j.amc.2019.01.030)
- Samaher, M. Y. (2021). Reliable Iterative Method for solving Volterra - Fredholm Integro Differential Equations. *Al-Qadisiyah Journal of Pure Science*, 26(2), 1-11. doi:[10.29350/qjps.2021.26.2.1262](https://doi.org/10.29350/qjps.2021.26.2.1262)
- Sezer, M., & Gulsu, M. (2005). Polynomial solution of the most general linear Fredholm integrodifferential-difference equations by means of Taylor matrix method. *Complex Variables Theory and Application An International Journal*, 50(5), 367-382. doi:[10.1080/02781070500128354](https://doi.org/10.1080/02781070500128354)
- Shah, K., & Singh, T. (2015). Solution of second kind Volterra integral and integro-differential equation by Homotopy analysis method. *International Journal of Mathematical Archive*, 6(4), 49-59.
- Taiwo, O. A., & Fesojoye, M. O. (2015). Perturbation Least-Squares Chebyshev method for solving fractional order integro-differential equations. *Theoretical Mathematics and Applications*, 5(4), 37-47.
- Wazwaz, A. M. (2010). The combined Laplace transform-Adomian decomposition method for handling nonlinear Volterra integro-differential equations. *Applied Mathematics and Computation*, 216(4), 1304-1309. doi:[10.1016/j.amc.2010.02.023](https://doi.org/10.1016/j.amc.2010.02.023)
- Wazwaz, A. M. (2011). *Linear and Nonlinear Integral Equations Methods and Applications*. Higher Education Press, Beijing and Springer-Verlag Berlin Heidelberg.
- Yusufoglu (Agadjanov), E. (2007). An efficient algorithm for solving Integrodifferential equations system. *Applied Mathematics and Computation*, 192(1), 51-55. doi:[10.1016/j.amc.2007.02.134](https://doi.org/10.1016/j.amc.2007.02.134)



Gazi University

Journal of Science

PART A: ENGINEERING AND INNOVATION

<http://dergipark.org.tr/gujsa>

The Production of Organic Photodetectors and Determination of Electrical Properties for Optical Sensor Applications

Serdar KARADENİZ^{1*} , Behzad BARIŞ² , Hande KARADENİZ¹ , Murat YILDIRIM³ ¹Giresun University, Faculty of Engineering, Giresun-TURKEY²Giresun University, Faculty of Arts and Sciences, Giresun-TURKEY³Selçuk University, Faculty of Science, Konya-TURKEY

Keywords	Abstract
Schottky Diode	In this work, metal-semiconductor photodiodes with organic interlayers were produced, and their electrical properties were investigated under different light intensities. CongoRed was used as interlayer and grown as a thin film using spin coating technique on p-type silicon substrates cleaned by different chemical methods. The changes in electrical parameters of completed Al/CongoRed/p-Si/Al diodes were investigated under dark and different light intensity. From results obtained, it has been seen that the fabricated devices show photodiode properties, and as a result, they can be employed in opto-electronic applications.
Photodiode	
Organic Thin Film	
Photocurrent	

Cite

Karadeniz, S., Barış, B., Karadeniz, H., & Yıldırım, M. (2022). The Production of Organic Photodetectors and Determination of Electrical Properties for Optical Sensor Applications. *GU J Sci, Part A, 9(3)*, 267-275.

Author ID (ORCID Number)	Article Process	
S. Karadeniz, 0000-0002-1792-8134	Submission Date	05.07.2022
B. Barış, 0000-0003-3041-6413	Revision Date	25.07.2022
H. Karadeniz, 0000-0002-1028-767X	Accepted Date	01.09.2022
M. Yıldırım, 0000-0002-4541-3752	Published Date	27.09.2022

1. INTRODUCTION

Today, with increasing energy demand, the studies on efficient and low cost opto-electronic devices that convert the light into the electrical energy have become important. These devices fabricate using a variety of inorganic, organic, composite and hybrid materials. In recent years, inorganic and organic materials have been often used to develop the electronic characteristics of devices Aoki (2017), and especially organic photodiodes have attracted a lot of attention by researchers due to its electrical and optical characteristics.

Organic photodiodes made of semiconductor/semiconductor or metal/semiconductor structures are devices that convert light into electrical current. Sometimes these structures are also called photo-detectors or photo-sensors. Photodiodes can be used in optical communication and many opto-electronic applications. These structures operate under reverse bias in spite of a normal diode.

Metal/semiconductor structures, also known as Schottky barriers, are formed by coating a thin metal film on a semiconductor. Since high-temperature methods are not used during the production of these structures, no degeneration is observed in carriers (minority) within this structure. However, due to the high thermionic emission dark current, the usage of these structures as solar cells is not effective when compared to the pn junction solar cells. This dark current created by the thermionic emission can be reduced by placing a layer at the metal/semiconductor interface. The structure formed as a result of this process is called "metal/insulator/semiconductor Schottky barrier or briefly MIS type structure. These structures have some advantages than over pn junctions. In such structures, minority carrier lifetimes are preserved. Because low temperature methods are used in their production and thus doping effects are eliminated.

*Corresponding Author, e-mail: serdar.karadeniz@giresun.edu.tr

Studies on devices that combine both organic and inorganic materials are of great interest because of their expansive application areas such as sensors, optics and opto-electronics. In particular, due to their porous structures and very large surface areas, the porous silicones have become ideal candidates for hosting certain organic molecules such as sensitive dyes, surfactants and polymers (Chouket et al., 2010).

The addition of organic dyes to a metal/semiconductor interface has enabled the production of many useful devices such as optical wave-guides, light intensifiers, laser materials and sensors. In the past years, organic azo dye has become an attractive material, and has found applications because of its optical properties such as nonlinear optical effects and polarized photo-induced anisotropy (Pham et al., 1995). These materials also have potential application areas as gas sensors, and the absorption bands can be changed as needed.

CongoRed is an organic compound ($C_{32}H_{22}N_6Na_2O_6S_2$) and azo dye that has excellent adhesion to surfaces and broad applicability in light-induced photoisomerization, and has potential uses for reversible optical data storage. Therefore, it is adopted as stable organic semiconductors as an interlayer material for different electronic and opto-electronic applications and used between metal and inorganic semiconductor. Different diode structures and decorated nanoparticles studies related to CongoRed, which is widely studied, can be found in the literature (Kaçuş et.al., 2020; Kocuyigit et. al., 2021; 2022).

In this study, the photodiode properties of Schottky structures with organic interlayers have been determined under the dark and different illumination intensities. For this purpose, Al/CongoRed/p-Si/Al photodiodes have been fabricated, and the current-voltage measurements have been executed to analyze the photoconductive behavior of structures at room temperature.

2. MATERIAL AND METHOD

2.1. Substrate Cleaning

In production of organic photodiodes, boron-doped (p-type) silicon semiconductor crystals with a surface (100) orientation grown by Czochralski method were used as a substrate. The diameter, resistivity and thickness of semiconductors were 50.8 mm, 0.8 Ω .cm and 500 μ m, respectively. The substrates were subjected to a series of chemical cleaning processes. First, in order to remove the dust and other residues from the surface, an ultrasonic cleaner was used to wash the substrates with trichloroethylene, acetone and isopropyl alcohol, respectively, for 5 min. Then, it was cleaned in a sequence of sulfuric acid + hydrogen peroxide (1:1), and ammonia + hydrogen peroxide (1:1) for 10 minutes. For the etching process, in a sequence of deionized water + hydrofluoric acid (15:1), and nitric acid + hydrofluoric acid + acetic acid (2:1:1) for 2 minutes. After every process the substrates were washed with de-ionized water (18.3 M Ω). Finally, substrates were dried using nitrogen gas.

2.2. Formation of Ohmic Contacts

After the chemical cleaning process, the substrates were placed into the evaporation system to achieve ohmic contact, and 1500 Å thick (99.999%) pure aluminum metal was evaporated on the back surfaces of substrates under a pressure of approximately 1.8×10^{-6} Torr. A thickness monitor with a crystal sensor was used to obtain the desired thickness. 10-15 Å/sec was chosen to control the coating speed during the evaporation process. Aluminum coated substrates were heat treated in vacuum environment for ohmic contact formation. For this, the substrates were placed on a special heater made of a 0.1 mm thick tantalum (Ta) plate and heated to create ohmic contact. With this method, the barrier width was reduced by forming an extreme doped layer with same doping type (p^+) as the semiconductor at the Al/p-Si back contact. In this case, the contact resistance gets smaller and made the barrier transparent to the charge carriers.

2.3. Growing of CongoRed Thin Films

CongoRed has been purchased from Sigma-Aldrich. The ohmic contact formed substrates were placed in a spin coating device to form thin films on their front surfaces. CongoRed solution (0.3% by weight in ethanol) was dropped onto the substrate surfaces with the help of a 25 μ l micropipette. The spin coating device was rotated at 2500 rpm for 30 seconds. Then, the CongoRed coated silicon substrates were removed from the coating device and maintained in a nitrogen environment for 45 minutes to remove the solvent.

2.4. Formation of Rectifying Contacts

The crystals coated with CongoRed on their surfaces were placed again into the evaporation system to form rectifying contacts. Aluminum metal rectifying contacts with a diameter of 1.0 mm and 1000 Å thick were formed onto the organic thin film coated surfaces at a pressure of 2×10^{-6} Torr. The schematic diagram of an Al/CongoRed/p-Si/Al structure is shown in Figure 1.

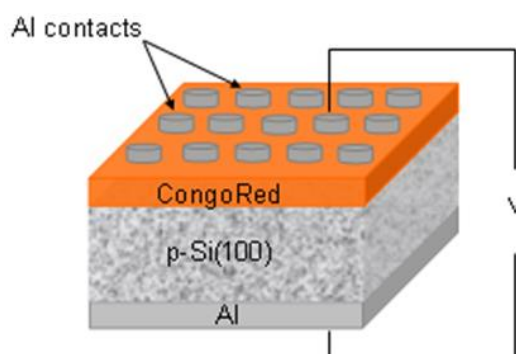


Figure 1. The schematic diagram of Al/CongoRed/p-Si/Al structure

2.5. Electrical Measurements

Current-voltage (I-V) measurement of Al/CongoRed/p-Si/Al structures was carried out within the range of -5 to +5 volts, under the dark and different light intensity (20 - 100 mW/cm²) and at room temperature. For this, Sciencetech brand filter 1.5AM solar simulator was used. The basic device properties such as ideality factor (n), saturation current (I₀), barrier height (Φ_B), and series resistance, R_s of the structures were determined from the measurements at various illumination intensity.

3. RESULTS

Figure 2 depicts the I-V characteristics of Al/CongoRed/p-Si/Al structures obtained under the dark and various light intensity. As seen in Figure 2, the linearity in the LnI-V curves is generally formed in a small bias region. This case strengthens the possibility that the thermionic emission (TE) or minority carrier injection is effective in the current mechanism of the structures. Since the density of states is in equilibrium with the semiconductor and show continuity in the high voltage region, a deviation from linearity has been observed. However, the fabricated organic-based Schottky structures have exhibited a good rectification behavior. Moreover, it is seen from Figure 2, the applied illumination intensities have a systematic effect on the current-voltage curves of device.

It is possible to analyze the diode parameters of the structures by the relationship known as thermionic emission theory. By this theory, $V > 3kT$ is accepted and the following expressions are used for the current-voltage curves.

$$I = I_0 \left[\exp\left(\frac{qV}{nkT}\right) - 1 \right] \quad (1)$$

$$I_0 = AA^*T^2 \exp\left(-\frac{q\Phi_B}{kT}\right) \quad (2)$$

Where A, k, T and q are contact area, Boltzmann constant, absolute temperature in Kelvin and electronic load, respectively. A* is effective Richardson coefficient with the value of $32 \text{ Acm}^{-2}\text{K}^{-2}$ for p-type silicon. I₀ has found by extrapolating the linear curves to zero bias voltage.

The Φ_B values of Al/CongoRed/p-Si/Al structures is obtained from the point where the linear curve intersects the current axis using the Equation (3). The oxide tunneling probability of the holes is accepted as unity and n has estimated from the slope of the LnI-V curve with the help of Equation (4):

$$\Phi_B = \frac{kT}{q} \ln \left(\frac{AA^*T^2}{I_0} \right) \quad (3)$$

$$n = \frac{q}{kT} \frac{dV}{d \ln(I)} \quad (4)$$

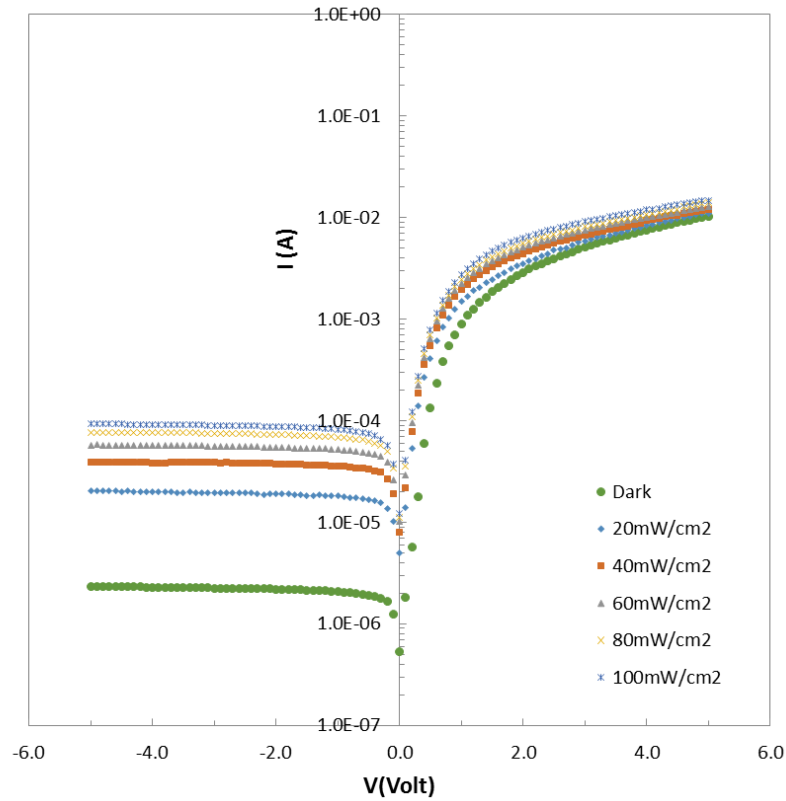


Figure 2. Current-voltage curves of Al/CongoRed/p-Si/Al structures at dark and different light intensities

The n and Φ_B values of Al/CongoRed/p-Si/Al structures have calculated for dark and different lighting intensities and are given in Table 1. The obtained n values are in the range of 3.33 to 5.42 and far from the ideal diode characteristics. The high ideality factor has attributed to the interface states or the barrier inhomogeneity (Kyoung et al., 2016). The Φ_B value of Al/CongoRed/p-Si/Al structures has decreased with increasing illumination intensity and obtained in the range of 0.631 - 0.528 eV. The decrease in Φ_B with increase in lighting intensity is attributed to the incremented load carriers as a result of the illumination. Moreover, the increasing in light intensity has increased the current in the reverse bias region from 2.31×10^{-6} to 9.25×10^{-5} A at 100 mW/cm². These results are in agreement with literature, and they showed that Al/CongoRed/p-Si/Al structures work as a photosensitive device. Table 1 shows the saturation current values of Al/CongoRed/p-Si/Al structures obtained depending on illumination intensity at room temperature.

Table 1. The diode parameters of Al/CongoRed/p-Si/Al structures depending on the illumination intensity

	n	I_0 (A)	Φ_B (eV)
Dark	3.33	5.66×10^{-7}	0.631
20 mW/cm ²	4.80	1.12×10^{-5}	0.554
40 mW/cm ²	5.12	1.80×10^{-5}	0.542
60 mW/cm ²	5.26	2.28×10^{-5}	0.536
80 mW/cm ²	5.41	2.72×10^{-5}	0.531
100 mW/cm ²	5.42	3.02×10^{-5}	0.528

An important parameter to consider when determining the electrical characteristics of metal/semiconductor structures is the series resistance (R_s). Series resistance can occur for many reasons, such as inhomogeneous impurity distribution in the semiconductor, the depletion layer on the semiconductor surface edge under the rectifier contact, the bulk resistance or a dirty film layer formed between the bulk and the ohmic contact. The R_s value of a structure can be calculated by different methods (Norde, 1979; McLean, 1986; Manificier et al., 1988). In the calculation of R_s of fabricated devices, the modified Norde function ($F(V, \gamma)$) has been used for ideality factor greater than unity (Bohlin, 1986).

$$F(V, \gamma) = \frac{V}{\gamma} - \frac{kT}{q} \ln\left(\frac{I(V)}{AA^*T^2}\right) \tag{5}$$

Where γ is an optional coefficient ($1 < n < \gamma$) greater than n . $I(V)$ expression is the current estimated from current-voltage curves. The Φ_B value of the device is given through the relation

$$\Phi_B = F(V_o, \gamma) - \left(\frac{1}{\gamma} - \frac{1}{n}\right)V_o - \frac{kT}{q} \frac{(\gamma - n)}{n} \tag{6}$$

where, $F(V_o, \gamma)$ and V_o are the modified Norde function and the corresponding voltage value, respectively, at the minimum of the $F(V)$ curves. Accordingly, R_s can be estimated with the help of the following relationship.

$$R_s = \frac{kT}{q} \left(\frac{\gamma - n}{I_o}\right) \tag{7}$$

Figure 3 depicts the $F(V)$ - V curves obtained at dark and different illumination intensities by using forward bias I-V measurements. As seen in figure, all Norde functions give a minimum of about 0.4V. The obtained R_s and $\Phi_B(I-V)$ values of Al/CongoRed/p-Si/Al structures depending on the illumination intensity are given in Table 2. The barrier height values estimated by using Norde technique are compatible with the values obtained from I-V characteristics. As seen in Table 2, the series resistance decreased with increasing light intensity.

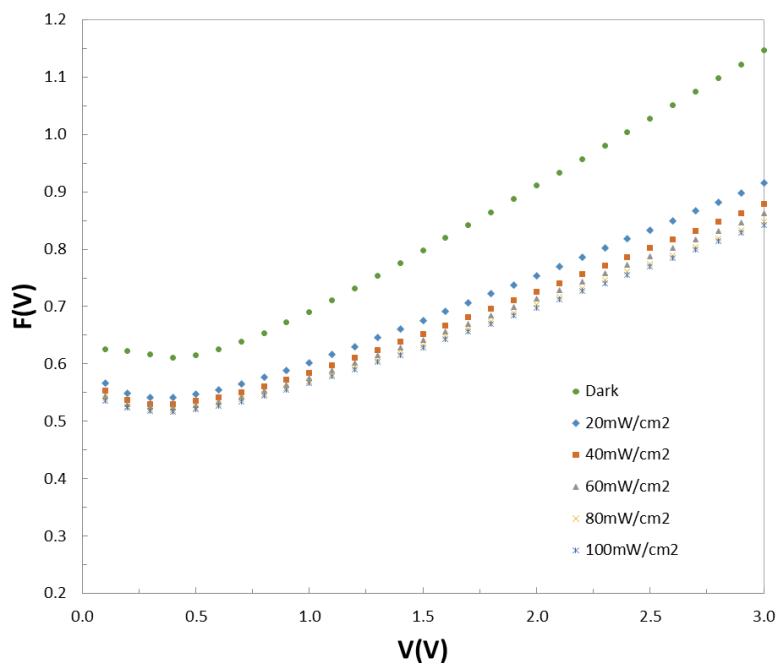


Figure 3. $F(V)$ - V curves of Al/CongoRed/p-Si/Al structures depending on illumination intensity
Table 2. R_s and Φ_B values of Al/CongoRed/p-Si/Al structures depending on illumination intensity at room temperature

	Dark	20mW/cm ²	40mW/cm ²	60mW/cm ²	80mW/cm ²	100mW/cm ²
Φ_B (eV)	0.626	0.547	0.538	0.532	0.527	0.524
R_s (Ω)	290.5	175.5	73.6	64.6	59.7	55.0

Photoresponse (R) and photosensitivity (S) parameters of structures; have determined using following expressions;

$$R = \frac{J_{ph} - J_d}{P_{in}} \quad (8)$$

$$S = \frac{I_{ph}}{I_d} \quad (9)$$

where, J_{ph} , J_d , I_d and I_{ph} are the photo-current density, dark current density, dark current and photocurrent, respectively. P_{in} is the intensity of incident light coming onto the surface. The R and S values of Al/CongoRed/p-Si/Al structures have found to be 0.11 A/W and 39, respectively, for 2.94×10^{-4} A/cm² dark current at 100 mW/cm² illumination intensity, and these values are in agreement with the literature. In addition, the obtained photoresponse value of fabricated device is 1.32 times greater than that of the Al/Ru(II)complex/p-Si photodiode Imer et al. (2019) and 12.2 times higher than that of the Al/Quaterphenyl/p-Si photodiode Attia et al. (2016) and 40.7 times higher than that of the Al/Cu(II)complex/p-Si photodiode (Dayan et al., 2020). It has been seen from the results that the produced device has a good photodiode properties.

The photoconductivity behavior of diodes has been analyzed with the following relationship.

$$I_{ph} = BP^m \quad (10)$$

Where B is a coefficient and P is lighting intensity. The m term is the lighting constant and estimated from the slope of graph $\ln(I_{ph}) - \ln(P)$. This parameter defines the type of photoconductivity mechanism of structures. If the value of the m is between 0.5 and 1, it indicates that photoconductivity is pertaining to the trap levels, and values greater than 1 indicate that photoconductivity is because of the empty trap levels (Yıldırım, 2019). Figure 4 depicts the $\ln(I_{ph}) - \ln(P)$ graph of Al/CongoRed/p-Si/Al structures and exhibits a linear photoconductive mechanism manner of Al/CongoRed/p-Si/Al structure. The illumination coefficient has found to be 0.95 for this structure. This value is in the range of $0 < m < 1$ and indicates that the distribution of localized states is continuous existed at the interface (Cavas et al., 2013).

To better understand the mechanism of photoconductivity, the reaction time measurements should be performed in addition to the evaluation of photocurrent changes. Figure 5 gives the transient photo-current curves of Al/CongoRed/p-Si/Al structures depending on different lighting intensities. The transient photo-current measurements help to demonstrate the photoresponse characteristics for various power densities during the on and off position of the device. When illumination begins, the free charge carriers increase and contribute to the flow of current, and consequently the photo-current values rapidly attain saturation. When the illumination ends, the charge carriers decrease and the photo-current drops quickly to its initial level. This represents a reversible switching behavior of device. It is seen from Figure 5, the device responds quickly under different illumination intensities and reaches its maximum photocurrent value in less than a second. This shows that the produced Al/CongoRed/p-Si/Al structures exhibit photoconductive behaviors. Certain photocurrent values observed in each curve under single illumination has attributed to the

distribution of charge carriers. They can be captured by traps created by crystal defects or re-excited towards the conduction band by other energy levels (Dahlan et al., 2015).

When the light has turned on, the current of device increased rapidly from 1.27×10^{-6} to 8.95×10^{-5} A and remained almost constant until the light has turned off (Figure 5, at 100 mW/cm^2). Meanwhile, the amount of charge in the trap centers of the device increased depending on the illumination intensity.

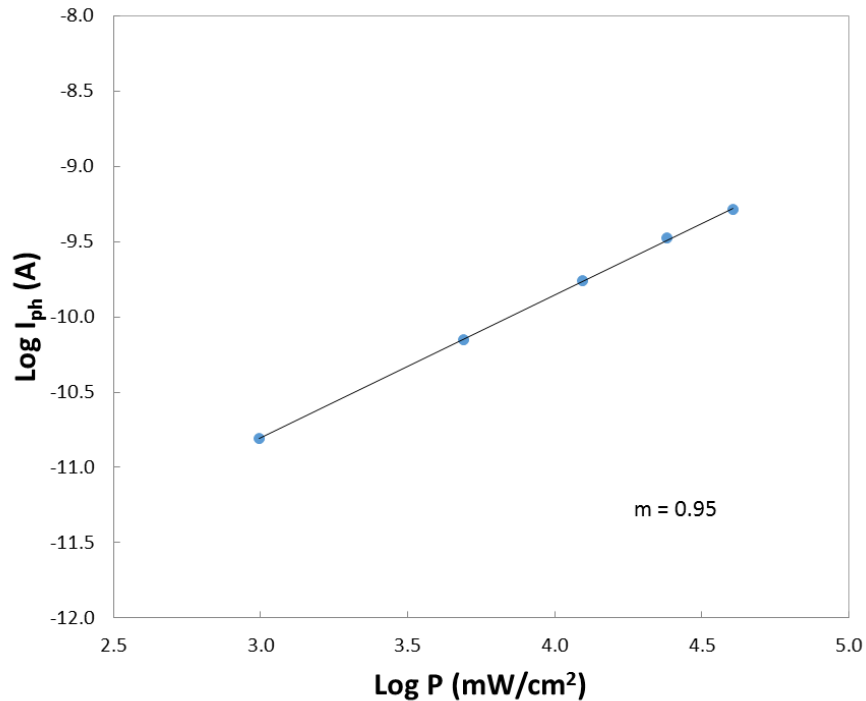


Figure 4. The variation of photocurrent of Al/CongoRed/p-Si/Al structures depending on illumination intensity

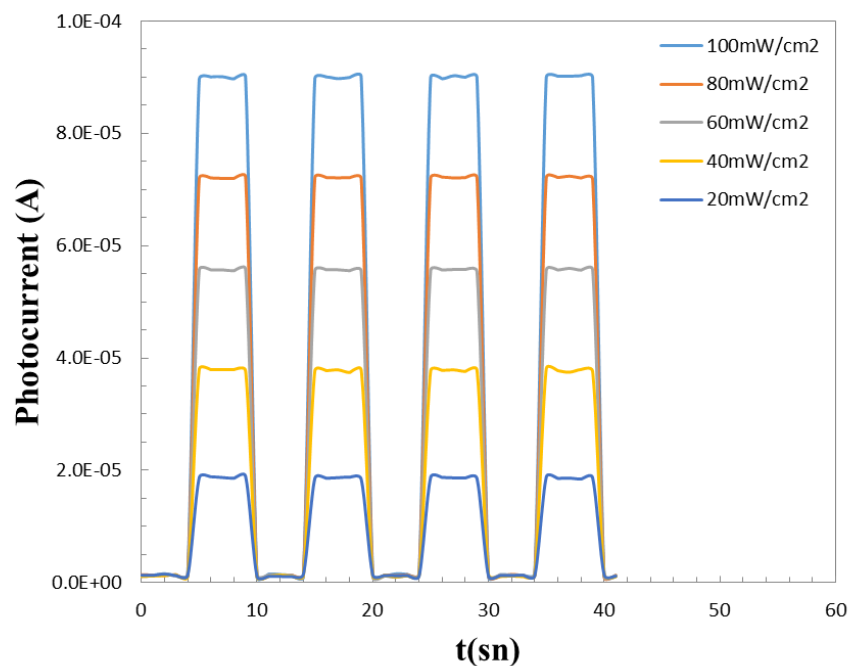


Figure 5. Transient photocurrent curves of Al/CongoRed/p-Si/Al structures

4. CONCLUSIONS

This study is aimed at the usability of Al/CongoRed/p-Si/Al structures with organic interlayer as a photodiode device. Therefore, an organic compound CongoRed has grown as an interlayer in a metal/semiconductor Schottky structure using spin coating technique. The sensitivity to the light of fabricated structures has been investigated at dark and under different light intensities.

When forward bias I-V curves of Al/CongoRed/p-Si/Al structures are examined, it is seen that different illumination intensities have a systematic effect on the I-V curves of the structure and this effect causes an increase in device current depending on the light intensity. The n value of the structures is greater than unity and the linear region in the semilogarithmic current-voltage curves is small. This strengthens the possibility that TE or minority carrier injection is effective in the current mechanism of the structures. Since the density of states is in equilibrium with the semiconductor and show continuity in the high voltage region, a deviation from linearity has been observed. However, the fabricated organic-based Schottky structures have shown a well rectification behavior.

Since n value is greater than unity, the modified Norde function is used to calculate R_s values of devices. From experimental results, it is seen that the R_s decreased with increasing of illumination intensity.

The photosensitivity and photoresponse parameters of the structures have been determined and found to be in agreement with previously published similar studies. From the obtained illumination coefficient using photoconductivity curves, it is concluded that the photo-conductivity mechanism is realized by empty trap levels. In this study, the experimental results show that the produced organic-based Al/CongoRed/p-Si/Al structures exhibit photodiode properties and could be used in opto-electronic applications.

ACKNOWLEDGMENT

This work (Project Number: FEN-BAP-A-150219-13) is supported by BAP Office of Giresun University.

CONFLICT OF INTEREST

There is no conflict of interest between the authors.

REFERENCES

- Aoki, Y. (2017). Photovoltaic performance of Organic Photovoltaics for indoor energy harvester. *Organic Electronics*, 48, 194-197. doi:[10.1016/j.orgel.2017.05.023](https://doi.org/10.1016/j.orgel.2017.05.023)
- Attia, A. A., Saadeldin, M. M., Soliman, H. S., Gadallah, A.-S., & Sawaby, K. (2016). Structural and optical properties of p-quaterphenyl thin films and application in organic/inorganic photodiodes. *Optical Materials*, 62, 711-716. doi:[10.1016/j.optmat.2016.10.046](https://doi.org/10.1016/j.optmat.2016.10.046)
- Bohlin, K. E. (1986). Generalized Norde plot including determination of the ideality factor. *Journal of Applied Physics*, 60(3), 1223-1224. doi:[10.1063/1.337372](https://doi.org/10.1063/1.337372)
- Cavas, M., Farag, A. A. M., Alahmed, Z. A., & Yakuphanoglu, F. (2013). Photosensors based on Ni-doped ZnO/p-Si junction prepared by sol-gel method, *Journal of Electroceramics*, 31(3-4), 298-308. doi:[10.1007/s10832-013-9839-3](https://doi.org/10.1007/s10832-013-9839-3)
- Chouket, A., Elhouichet, H., Koyama, H., Gelloz, B., Oueslati, M., & Koshida, N. (2010). Multiple energy transfer in porous silicon/Rh6G/RhB nanocomposite evidenced by photoluminescence and its polarization memory. *Thin Solid Films*, 518(6/1), S212-S216. doi:[10.1016/j.tsf.2009.10.091](https://doi.org/10.1016/j.tsf.2009.10.091)
- Dahlan, A. S., Tataroglu, A., Al-Ghamdi A. A., Al-Ghamdi, A. A., Bin-Omran, S., Al-Turki, Y., El-Tantawy, F., & Yakuphanoglu, F. (2015). Photodiode and photocapacitor properties of Au/CdTc/p-Si/Al device. *Journal of Alloys and Compounds*, 646, 1151-1156. doi:[10.1016/j.jallcom.2015.06.068](https://doi.org/10.1016/j.jallcom.2015.06.068)
- Dayan, O., Imer, A. G., Al-Sehemi, A. G., Özdemir, N., Dere, A., Şerbetçi, Z., Al-Ghamdi, A. A., & Yakuphanoglu, F. (2020). Photoresponsivity and photodetectivity properties of copper complex-based photodiode. *Journal of Molecular Structure*, 1200, 127062. doi:[10.1016/j.molstruc.2019.127062](https://doi.org/10.1016/j.molstruc.2019.127062)

- Imer, A. G., Dere, A., Al-Sehemi, A. G., Dayan, O., Serbetci, Z., Al-Ghamdi, A. A., & Yakuphanoglu, F. (2019). Photosensing properties of ruthenium (II) complex-based photodiode. *Applied Physics A*, 125(3), 204. doi:[10.1007/s00339-019-2504-1](https://doi.org/10.1007/s00339-019-2504-1)
- Kaçuş, H., Çırak, Ç., & Aydoğan, Ş. (2020). Effect of illumination intensity on the characteristics of Co/Congo Red/p-Si/Al hybrid photodiode. *Applied Physics A*, 126(2), 139. doi:[10.1007/s00339-019-3242-0](https://doi.org/10.1007/s00339-019-3242-0)
- Kocyigit, A., Yılmaz, M., Aydoğan, S., İncekara, Ü., & Kacus, H. (2021). Comparison of n and p type Si-based Schottky photodiode with interlayered Congo red dye. *Materials Science in Semiconductor Processing*, 135, 106045. doi:[10.1016/j.mssp.2021.106045](https://doi.org/10.1016/j.mssp.2021.106045)
- Kocyigit, A., Yılmaz, M., İncekara, Ü., Şahin, Y., & Aydoğan, Ş. (2022). The light detection performance of the congo red dye in a Schottky type photodiode. *Chemical Physics Letters*, 800, 139673. doi:[10.1016/j.cplett.2022.139673](https://doi.org/10.1016/j.cplett.2022.139673)
- Kyoung, S., Jung, E.-S., & Sung, M. Y. (2016). Post-annealing processes to improve inhomogeneity of Schottky barrier height in Ti/Al 4H-SiC Schottky barrier diode. *Microelectronic Engineering*, 154, 69-73. doi:[10.1016/j.mee.2016.01.013](https://doi.org/10.1016/j.mee.2016.01.013)
- Manificier, J.-C., Brortryb, N., Ardebili, R. & Charles, J.-P. (1988). Schottky diode: Comments concerning the diode parameters determination from the forward I-V plot. *Journal of Applied Physics*, 64(5), 2502-2504. doi:[10.1063/1.341632](https://doi.org/10.1063/1.341632)
- McLean, A. B. (1986). Limitations to the Norde I-V plot. *Semiconductor Science and Technology*, 1(3), 177-179. doi:[10.1088/0268-1242/1/3/003](https://doi.org/10.1088/0268-1242/1/3/003)
- Norde, H. (1979). A modified forward I-V plot for Schottky diodes with high series resistance. *Journal of Applied Physics*, 50(7), 5052-5053. doi:[10.1063/1.325607](https://doi.org/10.1063/1.325607)
- Pham, V. P., Manivannan, G., & Lessard, R. A. (1995). New azo-dye-doped polymer systems as dynamic holographic recording media. *Applied Physics A*, 60(3), 239-242. doi:[10.1007/BF01538397](https://doi.org/10.1007/BF01538397)
- Yıldırım, M. (2019). Characterization of the framework of Cu doped TiO₂ layers: An insight into optical, electrical and photodiode parameters. *Journal of Alloys and Compounds*, 773, 890-904. doi:[10.1016/j.jallcom.2018.09.276](https://doi.org/10.1016/j.jallcom.2018.09.276)



Gazi University

Journal of Science

PART A: ENGINEERING AND INNOVATION

<http://dergipark.org.tr/gujsa>

Effects of Electric Vehicles and Charging Stations on Microgrid Power Quality

Suleyman ADAK^{1*} , Hasan CANGI² , Ridvan KAYA¹ , Ahmet Serdar YILMAZ³ ¹Mardin Artuklu University, MYO, Dept. Electric and Energy, Mardin-Turkey²Hascan Engineering Limited Company, Mardin-Turkey³Kahramanmaraş Sutcu Imam University, Faculty of Architecture Engineering, Dept. of Electrical and Electronics Eng. Kahramanmaraş-Turkey

Keywords	Abstract
Electric Vehicle	In this study, integration of renewable energy sources and Electric Vehicles (EVs) into a micro-grid was modeled and analyzed. The microgrid is divided into four important parts; a diesel generator, acting as the base power generator; a photovoltaic (PV) farm combined with a wind farm, to produce electrical energy; a vehicle to grid (V2G) system installed next to the last part of the microgrid which is the load of the microgrid. The size of the microgrid represents approximately a community of a thousand households during a low consumption day in spring or fall. There are 100 electric vehicles in the base model which means that there is a 1:10 ratio between the cars and the households. This is a possible scenario in a foreseeable future. The continuous increase in their rate in energy production makes micro-grids important. Microgrids can be designed to meet the energy needs of hospitals, universities or charging stations of electric cars, as well as to meet the energy needs of a district, village or industrial site. Charging stations are needed to charge the electric vehicle battery. In this study, the effects of electric vehicles on the microgrid network are analyzed. Electric vehicles have non-linear circuit elements in their structures. Therefore, they are a source of harmonic current in the microgrid. They negatively affect the power quality of the microgrid. The battery in electric vehicles is charged with direct current. The alternating current from the microgrid needs to be converted to direct current.
Harmonic Source	
Charging Station	
Power Quality	
Vehicle to Grid (V2G)	

Cite

Adak, S., Cangi, H., Kaya, R., & Yilmaz, A. S. (2022). Effects of Electric Vehicles and Charging Stations on Microgrid Quality. *GU J Sci, Part A*, 9(3), 276-286.

Author ID (ORCID Number)	Article Process	
S. Adak, 0000-0003-1436-2830	Submission Date	02.08.2022
H. Cangi, 0000-0001-6954-7299	Revision Date	15.08.2022
R. Kaya, 0000-0003-4164-7276	Accepted Date	29.08.2022
A. S. Yılmaz, 0000-0002-5735-3857	Published Date	27.09.2022

1. INTRODUCTION

It is thought that electric cars will have a significant impact on the automotive industry in the future. This type of car not only saves fuel, but also reduces city pollution and carbon emissions. The degree of reduction in carbon dioxide emissions depends on electricity generation, and a 30% reduction is expected in the future. Electric cars use one or more electric motors (Erhan et al., 2013; Özçelik et al., 2019). The energy needs of these vehicles are supplied from the energy stored in their batteries. Electric motors provide strong and stable acceleration with instant torque (Liu et al., 2015; Lee et al., 2017). Electric cars have some advantages over internal combustion engine vehicles; they reduce local air pollution, reduce dependency on oil importing countries. It will be very important to provide bidirectional charging in the future. Electric vehicles can feed the grid and serve the system when needed. Electric vehicles can act as “mobile stations” in a way that can store unused electricity and transmit it back to the grid (Izgi et al., 2012; Yong et al., 2018). With the EV market growing fast, the emerging wireless EV charging technology has attracted more and more attention in recent years. The basic components of the electric car are given in Figure 1.

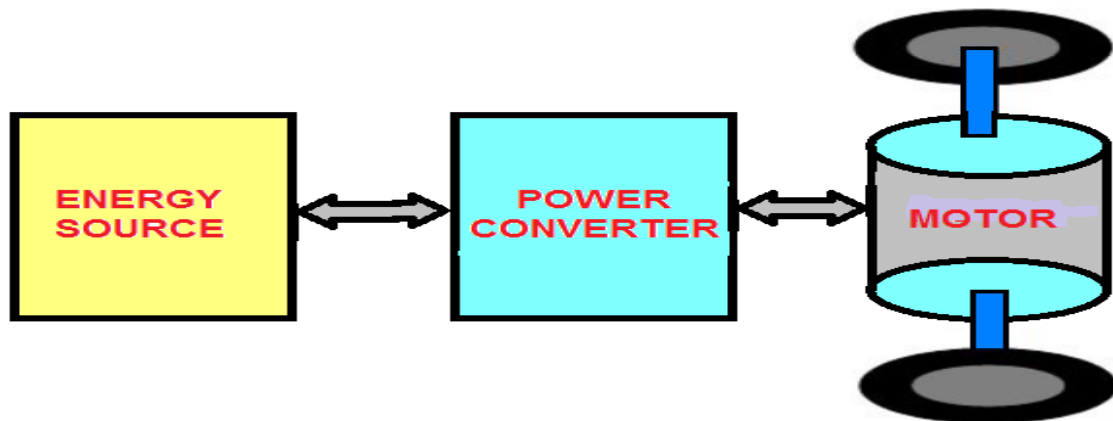


Figure 1. Basic Structure of Electric Vehicle

The second method is to overcome PV variation to use a local storage in the PV powered EV charging station. Electric motors give instant torque, providing powerful and balanced acceleration (Ashique et al., 2017). Priorities that may be important for the automotive industry, charging technology developers, urban planners and researchers:

- Acceleration of the electric vehicle market with the development of charging infrastructure
- Development and implementation of smart charging mechanisms for load management
- Taking region-specific measures to avoid overloads and voltage drops in the network
- Evaluation, development and implementation of new business models for charging electric vehicles
- Continuing planned investments in distribution networks in parallel with the increase in electricity demand
- Renewable energy integration in the charging of electric vehicles
- Evaluation and planning should be done in order to benefit from the advantages provided by electric vehicles.

The electric vehicle have an electric motor, batteries and an AC-DC converter to control the engine. The batteries of the electric vehicle can be charged wherever electricity is available, such as at home and in the workplace (Fathabadi, 2015). In principle, stored electricity is used for transportation. However, the stored electricity can be transferred back to the microgrid. There are different charging stations, such as AC charging station, DC charging station and inductive charging station. DC charging stations are the fastest growing type (Chandra Mouli et al., 2016). The EV market is still far from completing its development in our country, and many of the studies focus on battery technology, the use of the electric motor and technical details about the internal equipment.

2. HARMONIC COMPONENTS PRODUCED BY ELECTRIC VEHICLES

Modern electric vehicles inject harmonic components into the microgrid during charging. The harmonic components of the current wave forms are higher than the harmonic components of the voltage wave form. THD level can affect the microgrid power system. In addition microgrid power quality will be affected by the THD value. The analysis THD level is important in the charging station. Non-linear loads that increasing use of with in electric vehicles caused disorders in the sinusoidal form of current and voltage signals. Non-linear waveform contain harmonic components (Kong et al., 2019). AC/DC and DC/AC converters charging systems are used in at electric car. They are the most important of harmonic sources. Electric car and electrical components are given as follows. Electric vehicles consist of an electric motor powered by a battery pack. The main advantage of electric vehicles is that they emit zero emissions and are environmentally friendly. They also do not consume any fossil fuels, so they use a sustainable form of energy to power the vehicle. The main components of electric vehicles are as given in Figure 2.

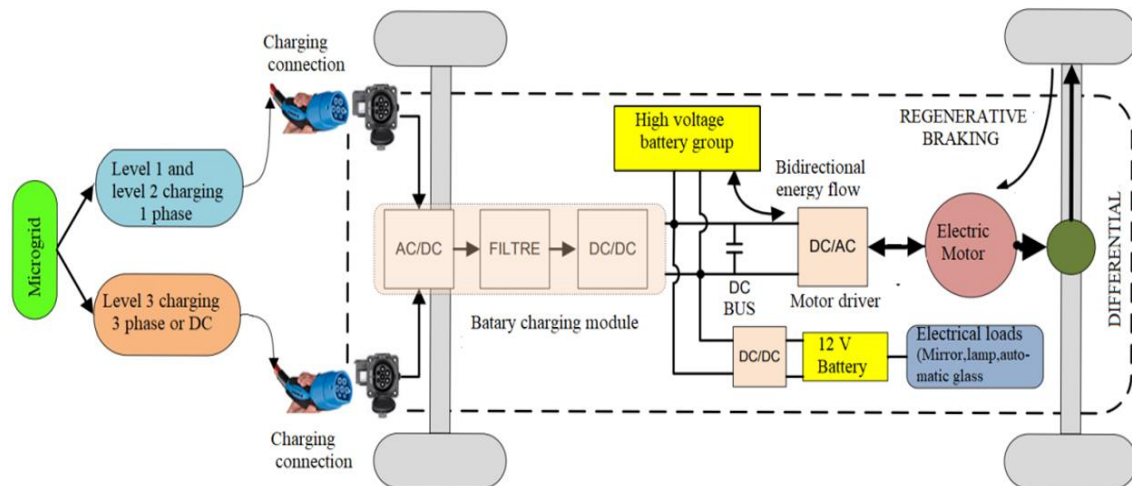


Figure 2. Structure of Electric Vehicle

Aforementioned harmonics create integer multiples of the main harmonics (50 Hz), i.e. 150Hz, 250Hz, 350Hz and 750Hz are the 3rd 5th, 7th, ..., and 15th harmonics (Rüstemli et al., 2015). Total harmonic distortion (THD) is generally caused by a non-linear waveform in smart microgrid. Harmonics in the power system occurs the following hazards at smart microgrid: Overheating in power transmission lines.

- Overheating in power distribution lines.
- Harmonics occur resonance in the smart microgrid
- Life span of life transformers and electronics devices.
- Distraction of the reactive capacitors.
- Protective switches in microgrid enables to open timeless.
- Noises causes in communication facilities.

Nowadays, renewable energies have substantially importance in smart microgrid. Such these systems do not harm to the environment. In contrast, they are environment friendly (Erhan et al., 2013; Yapıcı et al., 2016). THD is a common measurement of the level of harmonic distortion present in smart microgrids. THD_V can be defined as follows:

$$THD_V = \frac{\sqrt{V_2^2 + V_3^2 + V_4^2 + \dots + V_n^2}}{V_1} \quad (1)$$

If the harmonics are equal to the "0", THD_V will be equal to the "0". Where, V_n , is the RMS voltage of nth harmonic and $n=1$ is the voltage of fundamental frequency. THD_I can be defined as follows:

$$THD_I = \frac{\sqrt{I_2^2 + I_3^2 + I_4^2 + \dots + I_n^2}}{I_1} \quad (2)$$

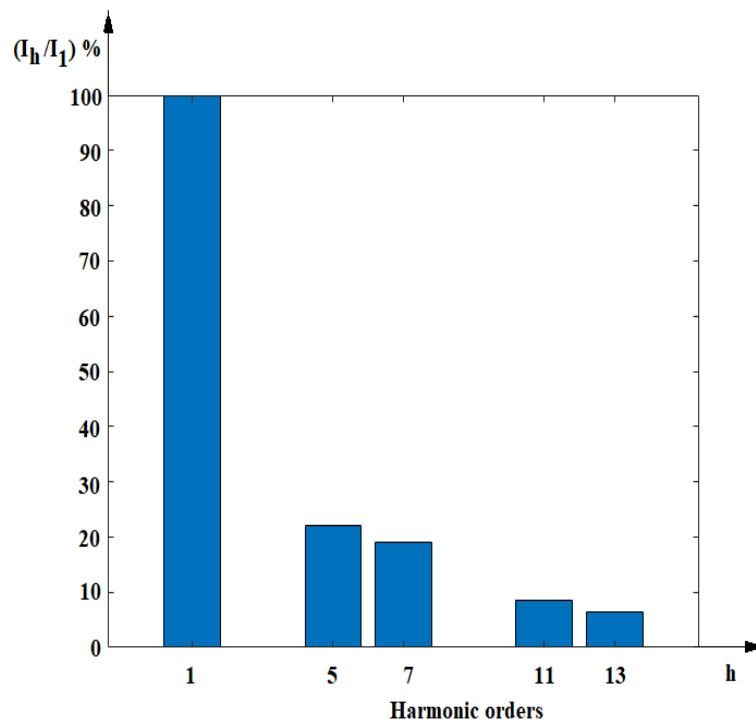
Where, I_n is the effective current of nth harmonic, and $n = 1$ is the fundamental of current. When the harmonics components are equal to zero, THD_I will be "0". THD_I value is bigger than THD_V value in microgrids that charging station is located. A controversial situation for PV inverter is the harmonics level. The IEEE 929 standard permits a limit of 5% for the current total harmonic distortion.

The mathematical solutions and Matlab applications have been observed that 5th & 7th harmonics occur in the microgrids, any or both of these sources of non-sinusoidal non-linear elements in general. The existence of harmonics for both current and voltage of the microgrids mean that the distortion of sinusoidal waves. Electric vehicles are a source of harmonics in the microgrid. The harmonic components injected into the microgrid while charging the 16 kW battery used in the electric vehicle are given in Table 1.

Table 1. The Harmonics Current Drawn from the Microgrid during the Charging of EVs

The Harmonic Components	Amplitude
1	100
5	22
7	19
11	8.5
13	6.5
THD _I	31.90 (%)

Harmonic distortion in the control with PWM is considerably reduced. Thyristor-based rectification creates 28.16 (%) total harmonic distortion, while PWM-based rectification creates 0.18 (%) distortion. Researching and understanding the harmonic distortion caused by EVs is of great importance to ensure the continuous and reliable operation of the microgrid. The changing of harmonic components is given in Figure 3.

**Figure 3.** The Harmonic Components of the Current during the Charging of EVs

In the case of low level EVs with normal charge, harmonic levels and voltage drops are low and losses are minimal. Accordingly, when the charge is low, normal charge state and EV penetration level is 20 (%), THD (%) is 3.12 (%) between 08.00-17.00. THD (%) was calculated as 44.92 between 17:00 and 23:00 of the time when the EV penetration level was 80 (%) in overload and fast charge condition. As a result, an increase in transformer loading values will increase heating and decrease transformer life. The widespread use of EVs will create a huge load problem for the low voltage distribution network. Today, electric vehicles need low range and continuous charging. Positioning of charging stations is very important.

3. ANALYSIS OF THE MICROGRID WHERE ELECTRIC VEHICLES ARE CHARGED

Electric vehicles are made up of two parts. Electric vehicles provide the energy needs of their batteries, and the movement of the vehicle is provided by the electric motor. Batteries in electric vehicles need to be charged from an external energy source. In this case, vehicles need to be charged. Electric vehicles have

different types of charging. There are different types of charging stations according to charging speed and voltage. The development of electric vehicles continues in parallel with the developments in battery technology (Khooban et al., 2017; Diaz et al., 2018). Obstacles to electric vehicle development are increasing the range and shortening the charging time. Today, intensive studies are carried out to solve these problems.

The quick method to charge an electric vehicle is to charge the vehicle in DC. In order to shorten the charging times of electric vehicles, the power of the charging stations is increased. For this reason, the number of charging stations with a power over 350 kW is increasing day by day. There are multiple charging sockets at the charging stations to charge more vehicles at the same time. Charging dozens of vehicles at the same time can cause serious problems on the microgrid. One of the problems is the increase in load demand on the grid. Only eight of these vehicles could be one at a time. Charging at the station will create an instantaneous energy need of 1 MW. The integration of renewable energy sources and Electric Vehicles into a microgrid is modeled in Figure 4.

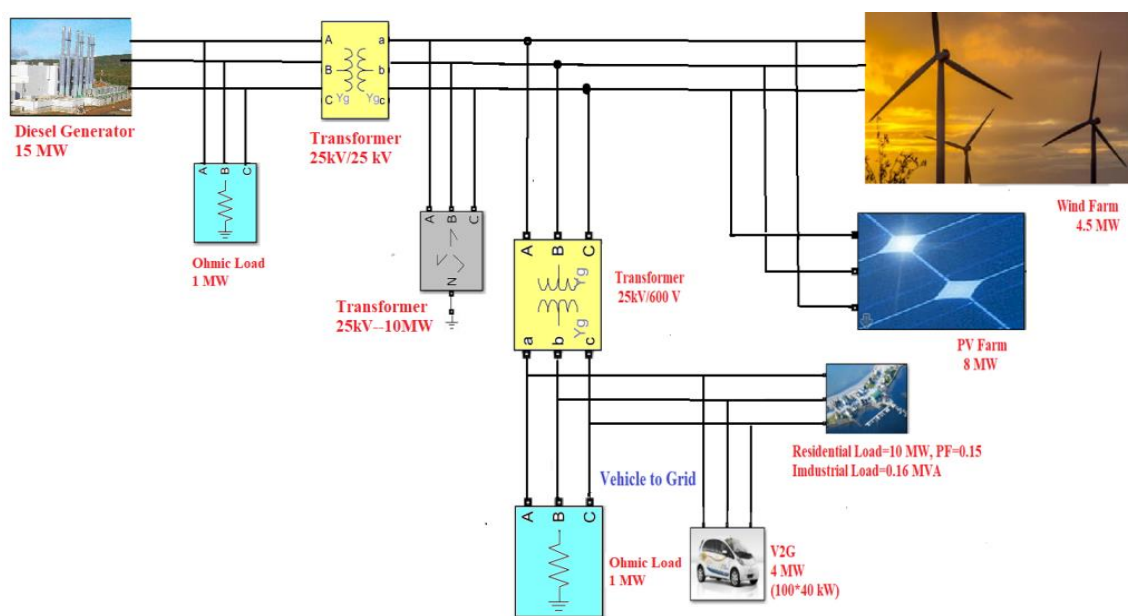


Figure 4. Microgrid and Electrical Vehicles

The analyzed microgrid consists of four parts. Diesel generators are acting as the primary power generator; PV plant with a wind turbines to produce green energy; the V2G system as a load on the network. It consists of a community of one thousand households with low consumption as microgrid load and 100 electric vehicles. There is a 1:10 ratio between electric vehicles and households. Increasing renewable energy production helps save the environment. Nevertheless, the energy production of renewable energy sources are strictly depending on environmental factors.

Microgrid systems to work perfectly and secure depend on the fundamental of quantities such as current and voltage which are sinusoidal waveform and 50 Hz frequency. But, such these fundamental quantities lose their sinusoidal characteristics because of many reasons, and unwanted harmonic component occur in the microgrid system. When the studies in the literature are scanned, many studies focus on the effect of charging of electric vehicles on the microgrid and the determination of the locations of charging stations within certain criteria.

The rapid increase of EVs increases the power demand and this causes an extra load on the microgrid. As a result, fluctuations in the microgrid increase. The diesel generator in the micro-grid ensures that the power consumed and the power produced are balanced. We can find the deviation in the grid frequency from the rotor speed of the synchronous machine. In Figure 5, the amount of energy produced by the diesel generator throughout the day is given.

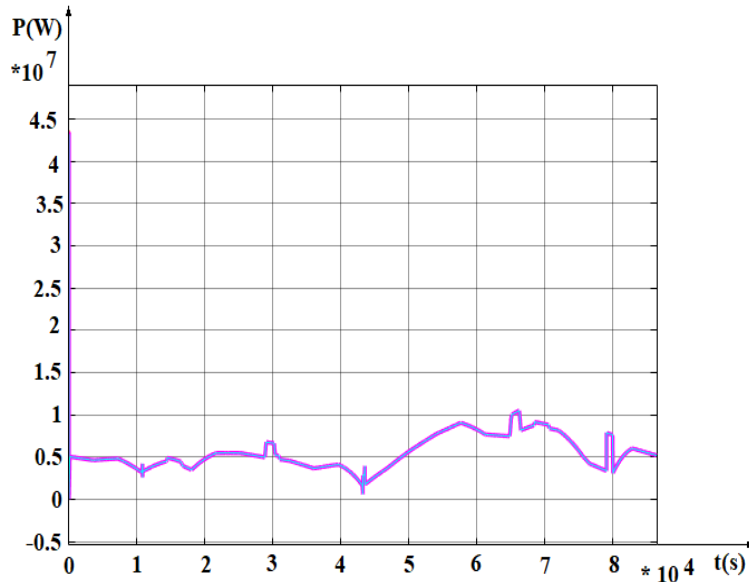


Figure 5. Active Power Generated by the Diesel Generator throughout the Day

High cost of diesel generator and polluting the environment are its disadvantages. However, in cases where the energy demand is not met with renewable energy sources, the energy to be produced by the diesel generator is needed.

The DC coupling capacitor, which provides electric vehicle charging, also provides reactive power compensation. Compensation control is provided by two-way electric vehicle fast charging stations. There are two renewable energy sources in the microgrid. Firstly, the PV plant produces energy proportional to the amount of irradiation in the environment. In Figure 6, the amount of energy produced in solar panels during the day is given.

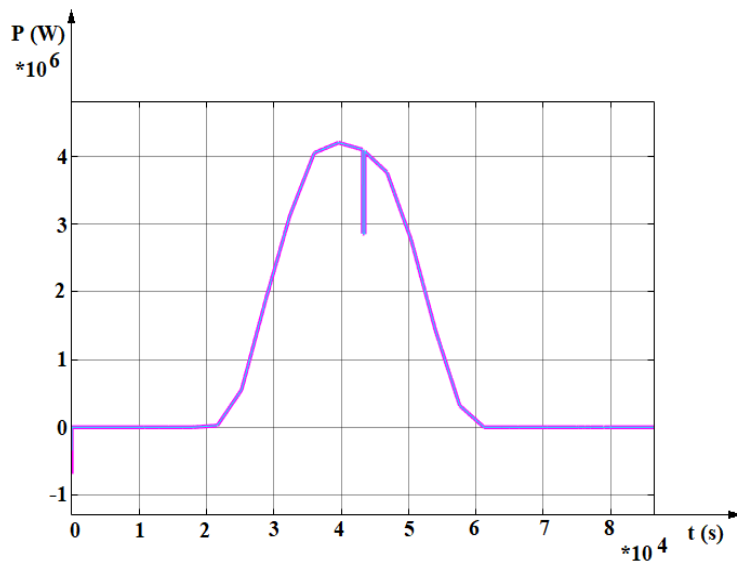


Figure 6. Active Power Generated by the Solar Power Plant throughout the Day

In the solar farm used in the micro-grid, direct current is produced by absorbing the solar irradiation. The amount of energy produced depends on the type of material used in the panel and the amount of solar irradiance that the panels absorb.

The wind farm generates electrical power linearly proportional to the wind. It generates the rated power when the wind speed reaches its rated value. When the wind speed exceeds its maximum value, the wind is

disabled from the microgrid until it reaches its nominal value. In Figure 7, the amount of energy produced by the wind farm throughout the day in the microgrid is given.

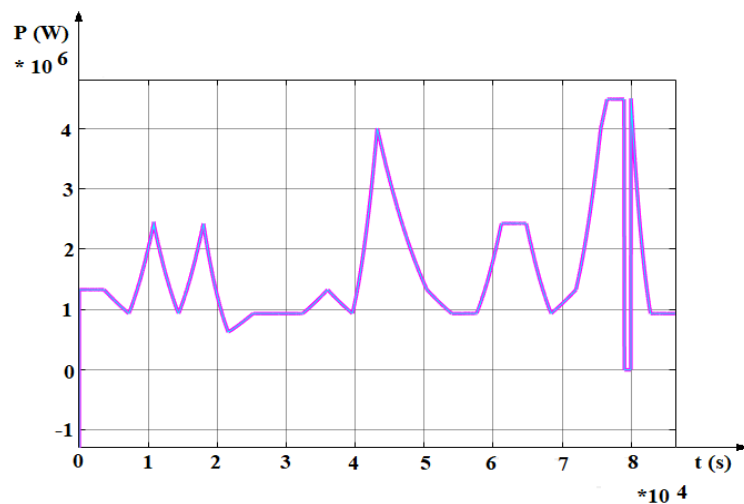


Figure 7. Active Power Generated by the Wind Power Plant throughout the Day

The use of wind power plants in the micro-grid is constantly increasing due to the fact that they are a renewable energy source, their simple structure and high efficiency. However, wind farms are different from other conventional power plants. Due to its structure, some problems occur during their connection to the microgrid.

The biggest advantage of EVs is the V2G application. This application is only applied to electric vehicles. Basically, it provides direct power flow from the vehicle to the distribution microgrid. The participation of electric vehicles in V2G technology requires higher charge and discharge rates of the battery and this causes the batteries to deteriorate faster. Charging stations are classified as level 1, level 2 and level 3. Level 1 slow charge, level 2 normal charge, level 3 indicates 3-phase or DC fast charging. In Figure 8, the current value charged from the EV to the microgrid during the day is given.

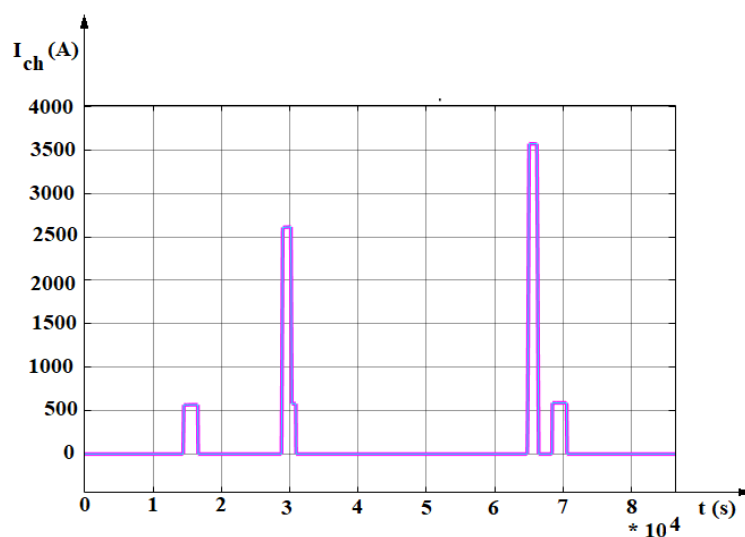


Figure 8. Current Injected Into the Microgrid from Electric Vehicles throughout the Day

V2G is basically the transmission of electricity from the batteries of electric vehicles to the microgrid. In the electrical system, the batteries of electric vehicles act as storage. With vehicle-to-grid technology, a vehicle battery is charged and discharged according to different signals such as energy production or consumption.

EV charging causes an increase in the load per transformer when energy consumption in the microgrid is intense. This creates major problems in balancing the energy supply. If many electric vehicles are charged from the same phase, a phase imbalance occurs in the microgrid. Unplanned charging of electric vehicles causes serious problems in the microgrid. Simultaneous charging of a large number of EVs can cause a voltage drop at the connectors of the chargers. During charging, electric vehicles consume high active power from the network, caused power losses in the microgrid. Positioning the charging stations in suitable places and choosing the right power capacity can minimize the power loss in the microgrid. Emission-free public transport, such as electric buses, improves local air quality and reduces noise pollution. Figure 9 shows the charging of an electric bus.



Figure 9. Charging the Electric Bus

Electric buses need EV charging stations equipped with smart systems to meet the charging needs. Batteries in electric vehicles are charged with Direct Current (DC) due to their nature. Since charging limitations for DC power support much higher speeds than AC power, electric vehicles can be charged with DC power at very high speeds, in very short times.

V2G have 2 functions. It controls the charge of the batteries and uses the existing power to regulate the grid when transients occur. V2G ensures that existing distributed energy storage devices are instantly available. Various applications of battery types enter the market.

The energy stored in the electric vehicle is transmitted back to the micro grid with bidirectional charging. In this way, electric vehicles will turn into a demand-side source and electric vehicle users will be able to earn additional income.

Electric vehicles and residential load drawn active power from the microgrid during the day The charging time required for charging an electric vehicle with a 64 kWh battery at different speeds from 0% to 80% is given in Table 2.

Table 2. Charging Speed and Times in Electric Vehicles (Speirs, 2020)

Charge Type	Charge Speed	Range Reached in One Hour Charge	Duration
Charge device (8 A)	1.8 kW	10 km	35 hour
1-phase AC Charger	7.4 kW	40 km	9 hour
3-phase AC Charger	22 kW	120 km	3 hour
DC Charge	25 kW	150 km	1.5 hour (up to 80%)
Fast DC Charge	50 kW	300 km	1 hour (up to 80%)
Ultra Fast DC Charge	175 kW	1000 km	15 minute (up to 80%)

The charging speed and duration of electric vehicles are related to how fast the batteries are filled. The factor that determines the charging speed of the batteries is primarily the chemicals used in the battery. It is possible to increase the charging speed and shorten the charging time by using chemicals that are more resistant to high current. The load consists of a residential load and an asynchronous machine to represent the effect of industrial inductive load on the microgrid. The variation of active power consumed by residences throughout the day is given in Figure 10.

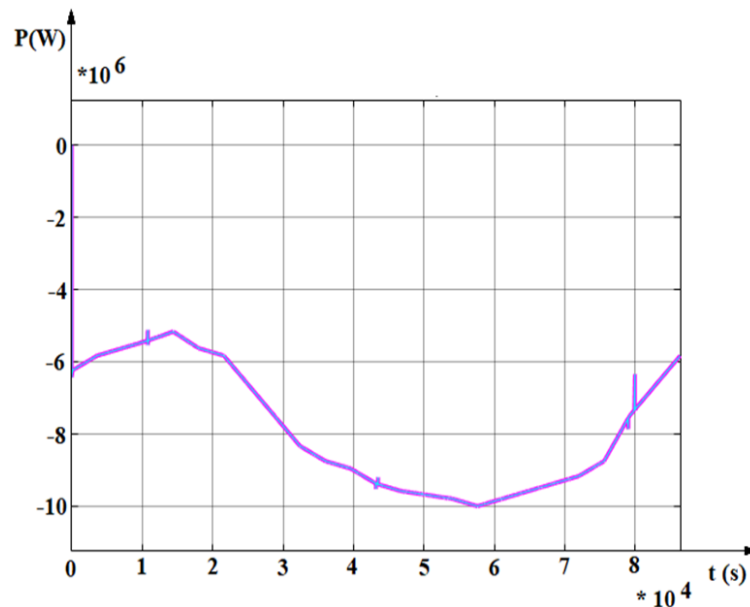


Figure 10. Residential Load Drawn Active Power from the Microgrid during the Day

The residential load is represented by the active power drawn at a specified power factor. The torque of the induction machine is directly proportional to the square of the rotor speed. Despite their potential benefits, there are some reasons why electric cars are not widely adopted. Electric cars are importantly more costly than a conventional internal combustion engine vehicle and hybrid electric vehicles owing to the additional cost of lithium-ion batteries. However, battery prices are decreasing with mass production and are expected to decrease further. Most internal combustion engine vehicles are considered to have unlimited range and fill their tanks at gas stations in a very short time. In contrast, EVs have less range on a single charge, and charging can take a long time. The transport sector is obliged for 24% of CO₂ emissions, which is about three-quarters of CO₂ emissions. For this reason, countries strongly encourage the use of electric vehicles.

4. CONCLUSION

Since the main problem in electric vehicles is the battery capacity and accordingly the range, regenerative braking is of great importance in these vehicles. The electric vehicle consumes 72 kW of power when climbing a steep slope, and the electric machine works as a generator when descending the same slope. It has been observed that it transfers a power of 24kW to the battery. It has been proven by scientific studies that electric vehicles are an alternative to internal combustion engines in terms of both efficiency and environmental pollution. Reactive power elimination is applied to secure voltage regulation of the microgrid. Reactive power support improves power factor and reduces power losses in power lines. In addition, it leads to increased productivity. Electric vehicles connected to the microgrid can provide reactive power compensation.

The charging time depends on the power source and the vehicle's charging capacity. The charging time is found by dividing the battery capacity of the electric vehicle by the charging power. The capacity value of an electric vehicle is 60 kWh. It is charged at a charging station with a charge value of 7 kW. It has been observed that the battery of this vehicle is charged up to 80 (%) in 8 hours.

Electric vehicles are modeled as harmonic current sources in microgrids due to the power electronics-based converters that exist in their structures. As electric vehicles increase day by day, necessary measures should be taken by making necessary studies on their power quality, especially on harmonic components. In proportion to the increase in electric vehicles, the number of charging stations is increasing day by day. Apart from settlements such as parking lots, shopping centers and mass housing, people can also set up electric vehicle charging stations individually in their homes. All these developments mean additional load for the electricity grid. For microgrids with high penetration of renewable energy sources and electric vehicles, the stochastic charging/discharging of the electric vehicles would result in a large impact on the secure and stable operation of the microgrids. Therefore, the coordinated control between electric vehicles and renewable energy sources becomes an important challenge for keeping the microgrid stable.

CONFLICT OF INTEREST

The authors declare no conflict of interest.

REFERENCES

- Ashique, R. H., Salam, Z., Bin Abdul Aziz, M. J., & Bhatti, A. R. (2017). Integrated photovoltaic-grid dc fast charging system for electric vehicle: A review of the architecture and control. *Renewable and Sustainable Energy Reviews*, 69, 1243-1257. doi:[10.1016/j.rser.2016.11.245](https://doi.org/10.1016/j.rser.2016.11.245)
- Erhan, K., Ayaz, M., & Özdemir, E. (2013). *Elektrikli Araç Şarj İstasyonlarının Güç Kalitesi Üzerine Etkileri - Impact of Charging Stations for Electric Vehicles on Power Quality*. In: Akıllı Şebekeler ve Türkiye Elektrik Şebekesinin Geleceği Sempozyumu, (pp.1-5).
- Diaz, C., Ruiz, F., & Patino, D. (2018). *Smart Charge of an Electric Vehicles Station: A Model Predictive Control Approach*. In: IEEE Conference on Control Technology and Applications (CCTA 2018), (pp. 54-59), doi:[10.1109/CCTA.2018.8511498](https://doi.org/10.1109/CCTA.2018.8511498)
- Fathabadi, H. (2015). Utilization of electric vehicles and renewable energy sources used as distributed generators for improving characteristics of electric power distribution systems. *Energy*, 90(1), 1100-1110. doi:[10.1016/j.energy.2015.06.063](https://doi.org/10.1016/j.energy.2015.06.063)
- Khooban, M. H., Niknam, T., Blaabjerg, F., & Dragičević, T. (2017). A new load frequency control strategy for micro-grids with considering electrical vehicles. *Electric Power Systems Research*, 143, 585-598. doi:[10.1016/j.epsr.2016.10.057](https://doi.org/10.1016/j.epsr.2016.10.057)
- Izgi, E., Öztopal, A., Yerli, B., Kaymak, M. K., & Şahin, A. D. (2012). Short–mid-term solar power prediction by using artificial neural networks. *Solar Energy*, 86(2), 725-733. doi:[10.1016/j.solener.2011.11.013](https://doi.org/10.1016/j.solener.2011.11.013)
- Kong, W., Luo, Y., Feng, G., Li, K., & Peng, H. (2019). Optimal location planning method of fast charging station for electric vehicles considering operators, drivers, vehicles, traffic flow and power grid. *Energy*, 186, 115826. doi:[10.1016/j.energy.2019.07.156](https://doi.org/10.1016/j.energy.2019.07.156)
- Lee, B.-K., Kim, J.-P., Kim, S.-G., & Lee, J.-Y. (2017). An isolated/bidirectional PWM resonant converter for V2G (H) EV On-Board charger, *IEEE Transactions on Vehicular Technology*, 66(9), 7741-7750, doi:[10.1109/TVT.2017.2678532](https://doi.org/10.1109/TVT.2017.2678532)
- Liu, L., Kong, F., Liu, X., Peng, Y., & Wang, Q. (2015). A review on electric vehicles interacting with renewable energy in smart grid. *Renewable and Sustainable Energy Reviews*, 51, 648-661. doi:[10.1016/j.rser.2015.06.036](https://doi.org/10.1016/j.rser.2015.06.036)
- Chandra Mouli, G. R., Bauer, P., & Zeman, M. (2016). System design for a solar powered electric vehicle charging station for workplaces, *Applied Energy*, 168, 434-443. doi:[10.1016/j.apenergy.2016.01.110](https://doi.org/10.1016/j.apenergy.2016.01.110)
- Özçelik, M. A., Utma, A. & Yılmaz, A. S. (2019). Micro PV/Wind hybrid based smart energy management system . *The International Journal of Materials and Engineering Technology*, 2(2), 54-59.



Rüstemli, S., Okuducu, E., Almalı, M.N., & Efe, S. B. (2015). Reducing the Effects of Harmonics on the Electrical Power Systems with Passive Filters. *Bitlis Eren University Journal of Science and Technology*, 5(1), 1-10. doi:[10.17678/beujst.57339](https://doi.org/10.17678/beujst.57339)

Yapıcı, R., Güneş, D., & Yörükeren, N. (2016). *Elektrikli Şarj İstasyonlarının Dağıtım Şebekesine Olası Etkileri*. 21-27. [PDF](#)

Yong, J. Y., Ramachandaramurthy, V. K., Tan, K. M., & Selvaraj, J. (2018). Experimental Validation of a Three-Phase Off-Board Electric Vehicle Charger With New Power Grid Voltage Control. *IEEE Transactions on Smart Grid*, 9(4), 2703-2713. doi:[10.1109/TSG.2016.2617400](https://doi.org/10.1109/TSG.2016.2617400)



The Effect of the Parameters on Al 7075 Coated with MAO Method by Adding Nano Ti-Powder

Mehmet Erbil ÖZCAN^{1*} , Latif ÖZLER¹ ¹Firat University, Faculty of Engineering, 23200 Elazığ, Turkey

Keywords	Abstract
Micro Arc Oxidation Wear Coating AA7075 Titanium	Coating processes are carried out in many areas of industry to improve the surface properties of materials such as wear and corrosion resistance or appearance. One of these coating processes is ceramic-based surface coatings. In order to obtain harder, denser and more uniform coatings, the substrate material is coated with a ceramic-based material at the desired thickness. In this study, 7075 series aluminum was coated with nano Ti powder and non-additive micro arc oxidation (MAO) method in a solution consisting of KOH, NaAlO ₂ and Na ₃ PO ₄ , and the effects of process parameters on coating thickness and wear behavior were experimentally investigated and the results were analyzed. According to the results obtained, it was observed that as the coating voltage, frequency and coating time increased, the wear rate decreased and a harder structure against wear is obtained. In addition, it was determined that the samples with nano titanium powder were less worn than the non-additive samples. According to SEM, EDX and XRD analyses, Al ₂ O ₃ phase was observed in the coatings made without adding titanium particles; It has been observed that in addition to the Al ₂ O ₃ main phase, TiO ₂ and SiO phases are also formed in titanium doped coatings.

Cite
Özcan, M. E., & Ozler, L. (2022). The Effect of the Parameters on Al 7075 Coated with MAO Method by Adding Nano Ti-Powder. *GU J Sci, Part A, 9(3)*, 287-298.

Author ID (ORCID Number)	Article Process
M. E. Ozcan, 0000-0003-1641-8279	Submission Date 25.07.2022
L. Ozler, 0000-0002-0595-153X	Revision Date 24.08.2022
	Accepted Date 14.09.2022
	Published Date 28.09.2022

1. INTRODUCTION

The primary goal of most materials science researchers is to improve the properties of metals and metal alloys, such as corrosion, wear and fatigue resistance, to minimize losses from wear and corrosion. Losses from corrosion and wear in the world constitute 3-5% of national income on average. Today, a significant part of the processes performed to eliminate these losses and improve the main properties of materials such as wear resistance consists of surface coating processes.

Coating with micro arc oxidation (MAO, also called as PEO, plasma electrolytic oxidation) method is based on the principle of coating the surface with a thick, hard, wear and corrosion resistant layer thanks to the plasma discharges caused by the electrochemical reactions of the substrate immersed in an electrolyte solution (Huang et al., 2004). The substrate material is connected to the power supply as the anode and the tank as the cathode. The substrate material is immersed in the electrolytic bath in the tank, which also acts as a cathode, and voltage is applied. Due to this voltage, electrodes surround the plasma and the oxide formed passes to the substrate and forms a film layer. It is possible to change the composition of the film layer in coatings with MAO by adding different chemicals to the electrolyte fluid (Li et al., 2013). MAO, an environmentally friendly coating method, has very different mechanical and physical structures. The most important advantage of coating with MAO method is lower investment cost compared to other coating methods (Zhu et al., 2007). Due to this advantage, the MAO method is frequently used in the automotive, aerospace, machinery, manufacturing and

*Corresponding Author, e-mail: meozcan@firat.edu.tr

textile industries (Nie et al., 1999; Arslan et al., 2009; Shen et al., 2013; H.-Y. Wang et al., 2014; J.-H. Wang et al., 2014; Shao et al., 2014).

Arslan et al. (2009) coated AA2014 material with Al_2O_3 using the MAO method and investigated the high temperature wear behavior. In the study, micro hardness measurements were also made; The structure of the coating was examined by SEM, EDX and XRD analysis. While sometimes mounds were seen in the microstructure of the coating, pits have also occurred at the same time. When the surface roughness values were examined, the surface roughness of the substrate material was $R_a = 0.1$ micron, while the surface roughness after coating was obtained as $R_a = 0.87$ micron.

Nie et al. (1999) coated the Al6082 substrate with Al-Si-O using the micro arc oxidation method and examined the hardness and wear behavior of the coatings. It has been reported that the wear resistance of the obtained coating is very good and its hardness has a value of 2400 HV. It has also been stated that with the increase in coating thickness, the wear resistance increases. Zhu et al. (2007) investigated the wear behavior of samples by coating Al-Si substrate in an alkali-silicate solution with a PH value of 10 by micro arc oxidation method. Wear tests of the samples were carried out under 50 N normal load and it was determined that delamination wear mechanism occurred as a result of wear. It was stated that the wear resistance increased when compared to the coated substrate material. Shokouhfar and Allahkaram (2017) coated the titanium-based substrate with micro arc oxidation method in their study. In the study, nano-sized SiC, Al_2O_3 and TiO_2 powders were added to the coating solution and the corrosion and wear behavior of the samples were investigated. It has been reported that the nanoparticles added to the solution reduce the wear rate, friction coefficient, corrosion current density and surface roughness.

Ma et al. (2022a), made coatings in silicate electrolyte on different Mg-Li alloy substrate materials by plasma electrolytic oxidation method. Structural analysis, coating thickness, corrosion and wear resistance of these coatings were investigated. According to the results obtained, the addition of Al and Y phases to the substrate caused the formation of finer grains and caused the formation of AlLi and Al₂Y phases. In addition, Mg-Li alloys caused a more resistant structure against corrosion. It was observed that the coating with Mg-14Li-3Al-1Y backing material was the most corrosion resistant combination with 7.485×10 icorr.

Ma et al. (2022b), made coatings by adding boron carbide and carbon particles on the Mg-Li substrate by the plasma electrolytic oxidation method. The effect of the added B₄C and C particles on the microstructure was investigated. It was observed that the B₄C coating added to the results of the experiments closed the micropores in the structure. The added carbon particles form protrusions on the coating surface, which indicates that the added powders have been successfully integrated into the coating. It was seen that both reinforcing powders increased the coating thickness and helped to obtain a more non-porous structure by reducing the pores in the structure. This contributed positively to wear and corrosion resistance. As a result, B₄C and C supplements added to the electrolyte liquid of the coating made with the PEO method improved the coating properties in a positive way.

There are many studies on the coating of the cutting tool in machining technology, where cutting tool wear is frequently encountered (Salimiasl & Rafighi, 2017; Rafighi, 2021; Şahinoğlu & Rafighi, 2021; Das et al., 2022). When these studies are examined, it is seen that a material with both more economical and desired properties is obtained by adapting the coating processes to the existing material.

In the literature search, it has been seen that there are many studies that have been coated with the MAO method. The difference of this study from the others made a use of solution that has not been used before consisting of KOH, NaAlO_2 and Na_3PO_4 by adding Ti powders into the solution during coating, and the effect of these solution elements on the coating performance was examined. In the current study, the effect of Ti powder on the structure and mechanical properties of the coating was examined, and a final product with the desired properties was obtained. It has been an original study, different from other studies, with the effect of the solution used and the supplementation.

2. MATERIAL AND METHOD

In this study, AA7075 aluminum was coated with micro arc oxidation method and the effect of test parameters on coating thickness and wear was investigated using MAO coating device powered by AC current (Table 1). The sample names given depending on the parameters are also given in Table 1. In the coating process, an electrolytic solution was used, unlike other studies, a mixture of 4 g/l Na₃PO₄ (Sodium Phosphate), 1 g/l KOH (Potassium Hydroxide) and 3 g/l NaAlO₂ (Sodium Aluminate). In Ti added coatings, nano-titanium powder (0.8 g/l) was added to the same coating solution and mixed homogeneously (Table 2). The mixing of titanium powder into the solution was done with a mechanical mixer. The AA7075 substrate material was immersed in the solution to become the anode through the hole drilled on the sample holder in the MAO coating device. The AA7075 substrate material is connected to the sample holder in the MAO coating device as an anode through a hole. The coating chamber was connected to the positive pole as the cathode, and the sample was made ready for the oxide coating process. The system, whose anode and cathode were adjusted as mentioned, was made ready for coating and the coating process was carried out using parameters such as voltage, amperage and time. As seen in Figure 1a, after the sample was connected as an anode, the coating process started by giving the appropriate current and voltage to the parameters and the 25.4x25.4 mm sample was coated. Olympus Tokyo brand optical microscope was used for coating thickness measurements of coated substrate materials and SEM images of the coatings were examined and EDX and XRD analyzes were made.

Table 1. Process parameters and sample names

Sample Name	Coating Time (min)	Frequency (Hz)	Voltage (Volt)
K1,K2,K3	10	100	450,500,550
K4,K5,K6		350	450,500,550
K7,K8,K9	20	100	450,500,550
K10,K11,K12		350	450,500,550
K13,K14,K15	30	100	450,500,550
K16,K17,K18		350	450,500,550
K19,K20,K21	10	100	450,500,550
K22,K23,K24		350	450,500,550
K25,K26,K27	20	100	450,500,550
K28,K29,K30		350	450,500,550

Wear tests were carried out on a diamond abrasive disc in accordance with ASTM G99 standard, using a 50 rpm rotation speed and 2 kgf (~2 daN) force on a Block-on-disc test device. The test sample was contacted with the pneumatic system on the abrasive shaft and the contact force was adjusted with the help of the valve in the system and controlled by the load cell (Figure 1b). At the end of 500, 1000 and 1500 meters of wear distances, the samples were weighed with a precision of 10⁻⁵ g and the amount of wear was obtained. The experimental study plan is given in Figure 2.

Table 2. Chemicals used in the experiments

Chemical	Amount (g/l)
KOH (Potassium Hydroxide)	1
NaAlO ₂ (Sodium Aluminate)	3
Na ₃ PO ₄ (Sodium Phosphate),	4
Ti (only Ti added coatings)	0.8

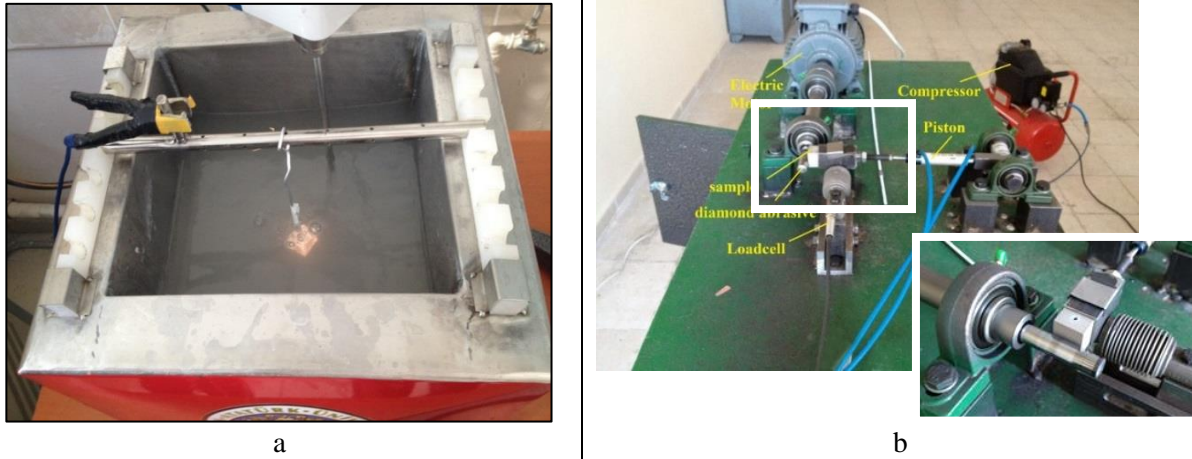


Figure 1. a) MAO coating process, b) Wear tester

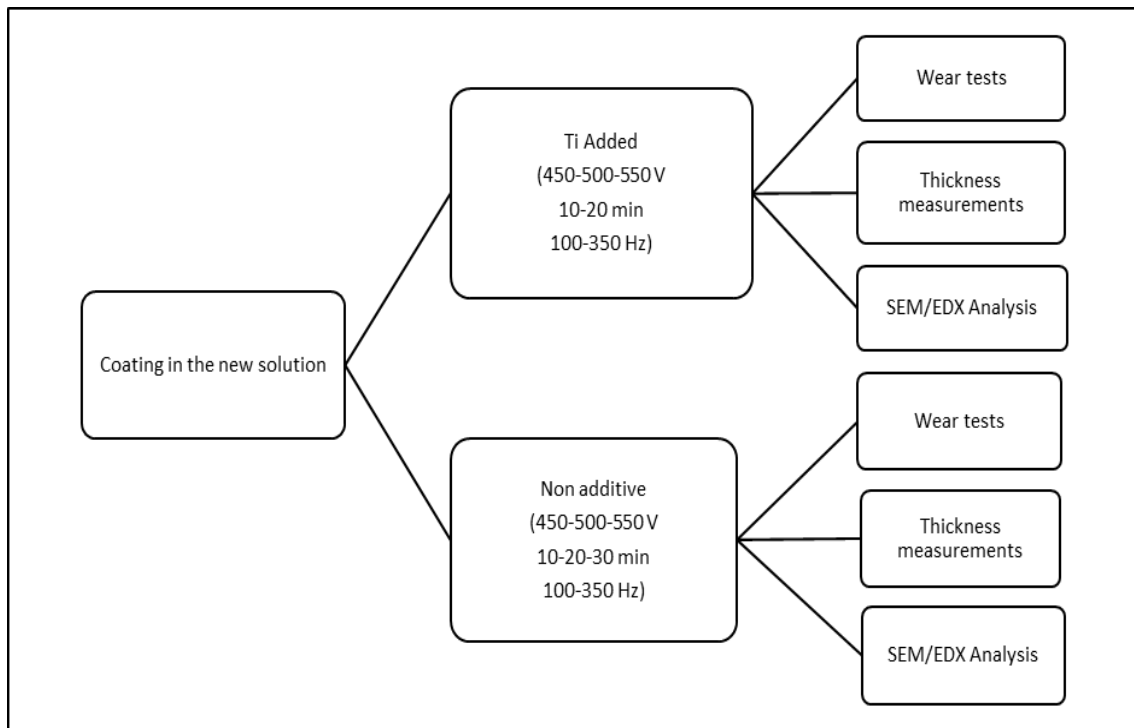


Figure 2. Scheme of experimental Plan

3. RESULTS AND DISCUSSION

After the coating processes, microstructure examinations and wear tests of the samples were made and the results were as follows.

The thickness values of the coatings carried out in Ti added and non-added solutions were given in Figure 3. The thickness values of the coatings made without Ti addition at 100 Hz frequency and 450, 500 and 550 Voltage were respectively measured as 3.2, 7 and 8 μm , while the coatings made at 350 Hz and 450, 500 and 550 V were measured respectively as 3.9, 9 and 10 microns. (Figure 3a). When the thickness of the Ti-added coatings was examined, the thickness value of the coating made at 100 Hz and 450 V was 3.6 micron, while 8 microns at 550 V were obtained. Likewise, the thickness value of the coating made at 350 Hz was 5.1 microns at 450 V, while 12 microns were obtained at 550 V (Figure 3b). In coatings without Ti addition, the increase in voltage increased the coating thickness. While there was no significant change in the coating thickness at 450 and 500 V values in Ti added coatings, the coating thickness increased at 550 V, and the highest coating

thickness value was obtained (Figure 3b). In all coatings, the highest coating thicknesses were obtained at 350 Hz and 550 V.

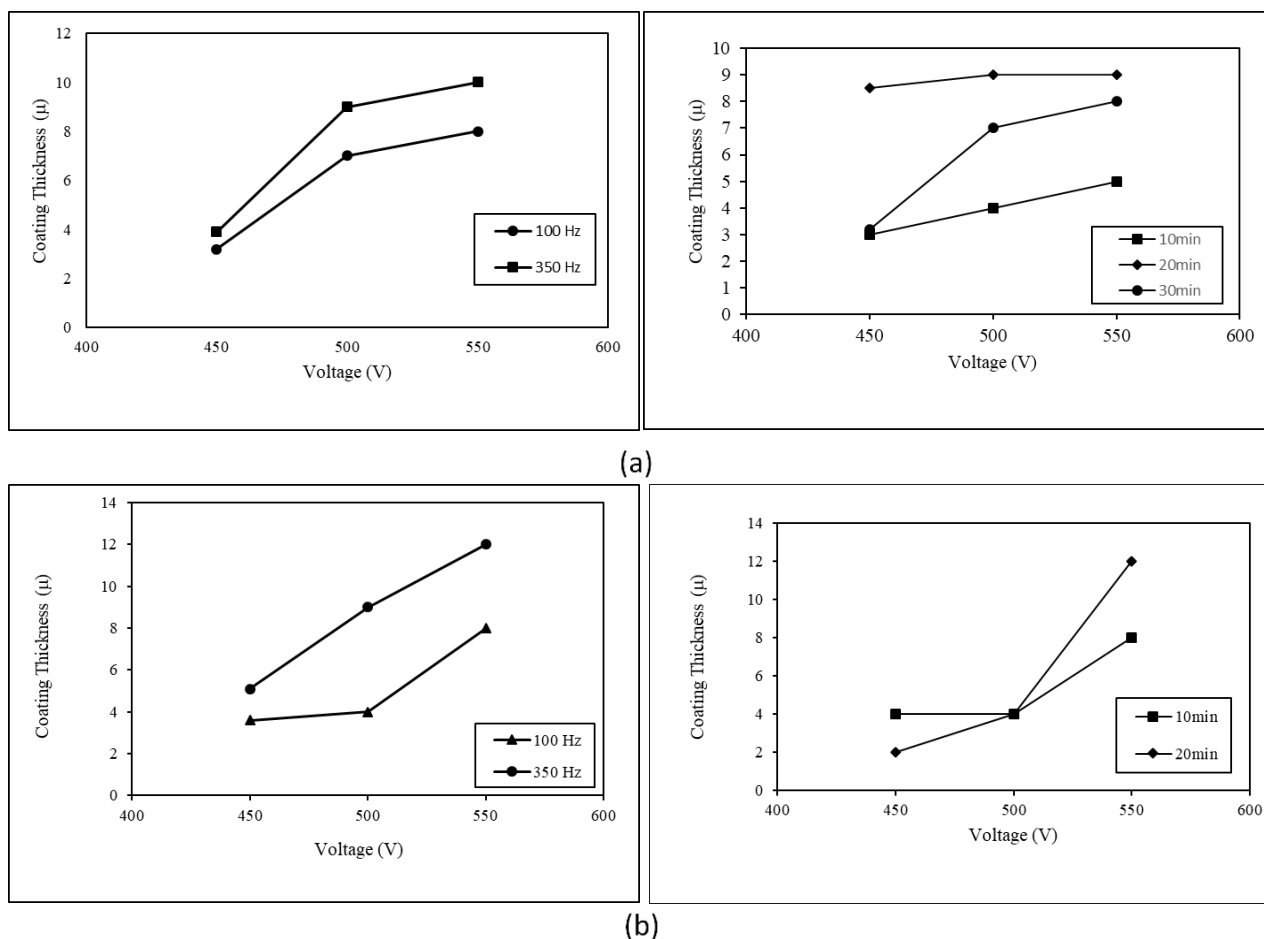


Figure 3. Effect of coating parameters on coating thickness **a)** without Ti addition, **b)** with Ti addition

According to Equation 1, arc power increases in direct proportion to the square of the voltage. Since the increase in voltage increases the arc power, it increases the coating thickness (Zhu et al., 2007). Since the voltage changes as a function of time, the arc occurs at the peaks of the functional curve. At the same time, the increase in voltage and frequency increases the peaks on the graph, increasing the amount of arc per unit time.

$$P = \frac{V^2}{R} \quad (1)$$

P; power (watt), V; the voltage (Volt) and R symbolize the resistance (ohm). When the effect of coating time on coating thickness was examined, it was determined that coating thickness first increased and then decreased with the in-crease of coating time (Figure 3b). When the thickness of the 450V coated samples was examined, it was measured as 3 microns on coating for 10 minutes, 8 microns for 20 minutes and 3.2 microns for 30 minutes. When the thickness of the coatings made at 550 V was examined, it was measured as 5 microns in the coating for 10 minutes and 9 microns in the coating for 20 minutes, while the coating thickness of the sample coated for 30 minutes was measured as 8 microns. Increasing the coating time increases the coating thickness by increasing the amount of arc formed on the substrate per unit time (Dudareva & Gallyamova, 2019). On the other hand, the excessive arc that occurs in long coating times disrupts the coating structure. In high frequency coatings, the coating process could not be done because the coating device draws excessive current and causes it to work noisy.

The increase in the coating time increases the thickness of the oxide layer on the surface of the substrate by accumulating a larger amount of coating material on the substrate surface and a more resistant structure is obtained (Figure 4) (Nie et al., 1999; Shokouhfar & Allahkaram, 2017).

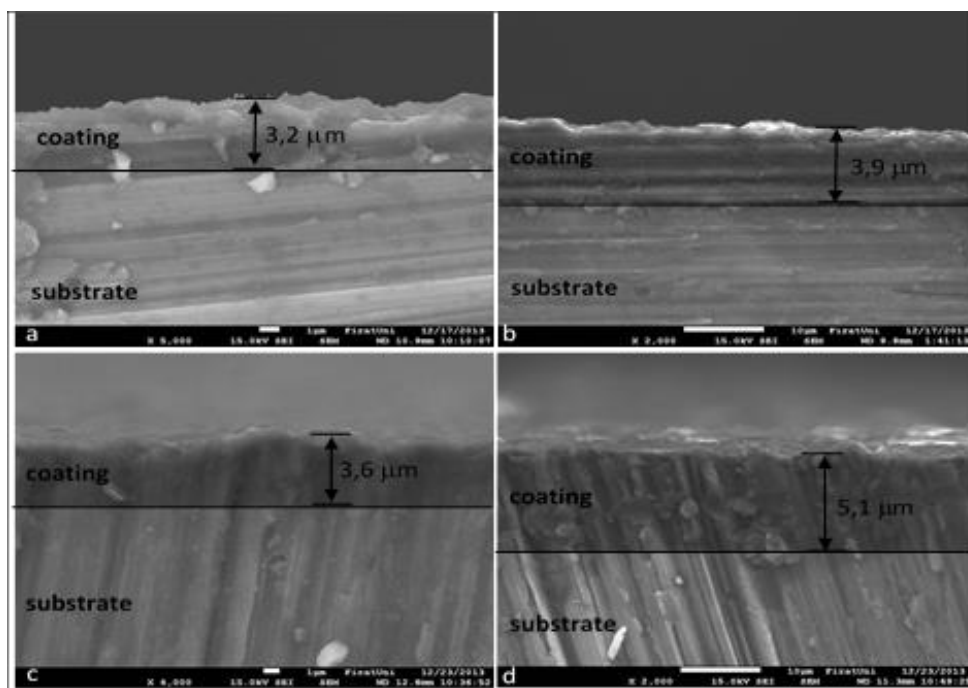


Figure 4. SEM images of *a)* 10min, 100 Hz, 450 V, Ti-free, *b)* 10 min, 350 Hz, 450 V, Ti-free, *c)* 10 min, 100 Hz, 450 V, Ti-added, *d)* 10 min, 350 Hz, 450 V, Ti-added

The wear amount of the coatings without the addition of nano titanium powder was given in Figure 5a. According to Figure 5a, increasing the coating time decreased the amount of wear. When the effect of coating time on the wear amount for 500 m wear distance was examined, the wear amount of the samples coated for 10 minutes was 120×10^{-5} g; The amount of wear was 102×10^{-5} g in the samples coated for 20 minutes, and 57×10^{-5} g was obtained in the samples coated for 30 minutes by continuing to decrease. When the wear amounts of Ti added and non Ti added coatings were compared (Figure 5c) the Ti added sample worn 102×10^{-5} g while the Ti added sample worn 68×10^{-5} g, at 1000 m the Ti added sample was 206×10^{-5} g while the Ti added sample was worn for 500 m. It was 147×10^{-5} g worn. On the 1500 m wear distance, it was observed that the samples with Ti addition of 317×10^{-5} g and 195×10^{-5} g were less worn. In addition, in wear above a certain wear distance for thin coatings, the coating material was worn by the abrasive disc in a short time and the disc contacts the softer substrate material (Lin et al., 2003). When the wear tests of the coating samples made with the addition of Nano Ti powders were examined, it was seen that the additional powder significantly reduced the wear rate of the coating. This is due to the formation of wear-resistant titanium dioxide and silicon dioxide phases with the aluminum oxide phase formed on the substrate during coating (Figure 6, Figure 7b). Free form nano Ti particles increase the wear resistance of the coating (Li et al., 2013; Tosun et al., 2019; Odabasi & Odabasi, 2020).

In Figure 5b, the wear amounts of the samples coated at frequencies of 100 and 350 Hz are given. According to Figure 5b, the wear amount of the samples coated at 450 V voltage and 100 Hz frequency was 226×10^{-5} g, while the wear amount of the sample coated at 450 V voltage and 350 Hz frequency was measured as 161×10^{-5} g. While the wear amount of the sample coated at 500 V voltage and 100 Hz frequency was 187×10^{-5} g, the wear amount of the sample coated at 500 V voltage and 350 Hz was 156×10^{-5} . Likewise, the wear amount of the sample coated at 550V voltage and 100 Hz frequency was 180×10^{-5} g, while the wear amount of the coating made at 350 Hz frequency was 149×10^{-5} g. The increase in frequency has decreased the amount of wear by increasing the coating thickness. Increasing frequency value increases the amount of arc per unit of time. By increasing the number of peaks in the voltage-time change graph at the same time, the coating thickness increases and the amount of wear decreases. When the SEM images of the non-additive

coatings were examined, the coating thickness of the sample coated at 100 Hz frequency was 3.2 microns, while the coating thickness of the sample coated at 350 Hz frequency was 3.9 microns (Figure 4a, 4b). According to the SEM images of Ti added coatings, the coating thickness was 3.6 microns at a frequency of 100 Hz, while 5.1 microns at a frequency of 350 Hz (Figure 4c, 4d).

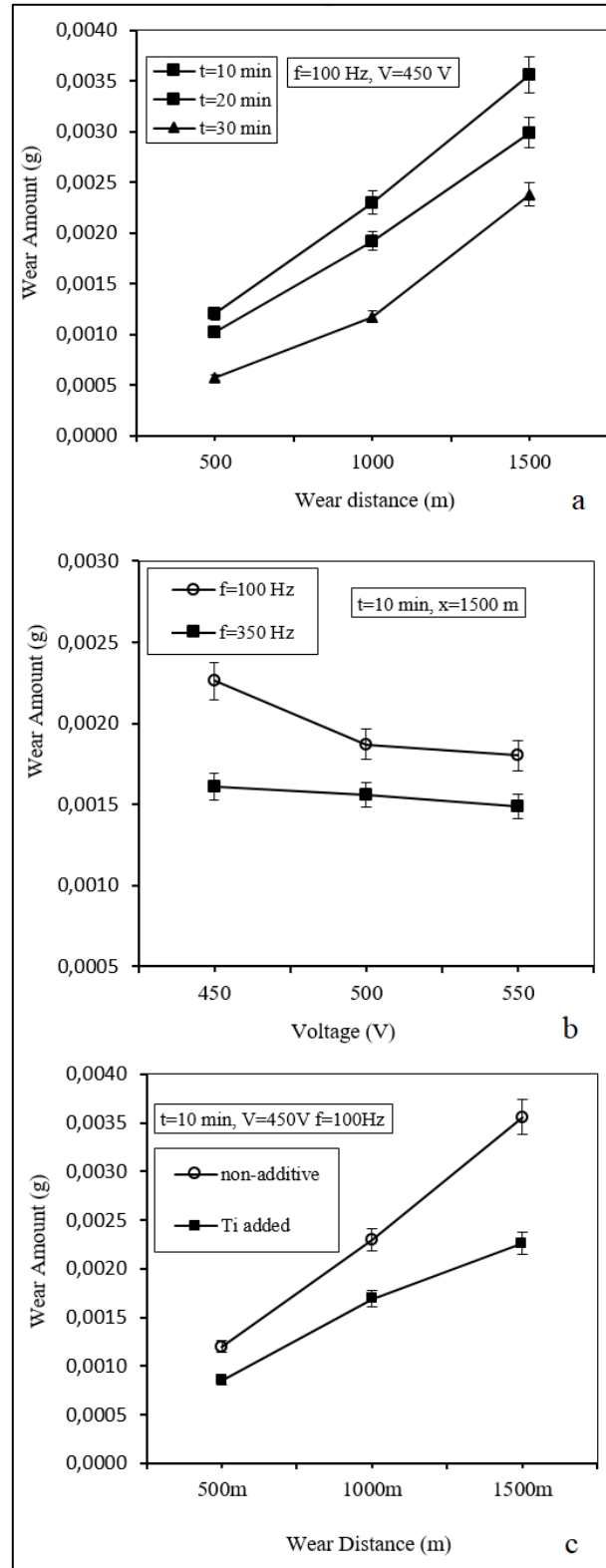


Figure 5. The effects of parameters on wear amount, **a)** Wear distance – wear amount at different times, **b)** Voltage – Wear amount, **c)** Wear distance – Wear amount of non-additive and Ti added solution

When the effect of the voltage on the wear rate was examined in Figure 5b, it was seen that the wear rate decreased as the voltage increased. In the wear tests performed at a frequency of 100 Hz, the wear rate for 450 V voltage was 226×10^{-5} g, for 500 V it was 187×10^{-5} g and for 550 V the wear rate was reduced to 180×10^{-5} g. In the experiments conducted at 350 Hz, the amount of wear at 450 V was 161×10^{-5} g, while at 500 V it was 156×10^{-5} g, decreasing at 550 V. Increasing arc power creates a more non-uniform coating structure on coating area (Zhu et al., 2007). At the same time, the structure formed as non-uniform and porous increases the surface roughness and friction coefficient (Lin et al., 2003). With the increasing thickness of the coating, a more irregular structure is formed and the wear resistance increases. In addition, high voltage values disrupt the structure of the coating and create an irregular coating thickness structure.

In Figure 5c, the wear rates of the coatings made in the solution with and without the addition of Ti powder are compared. Considering the wear amount for 1000 m wear distance of the samples, the wear amount of the samples coated with Ti-free solution was 230×10^{-5} g and the wear amount of the Ti added samples was 169×10^{-5} g. Similarly, for the samples coated with a Ti-free solution for 1500 m wear distance, 356×10^{-5} g was obtained, and 226×10^{-5} g was obtained for samples coated with a Ti-added solution. While the thickness of Ti added coatings made in 10 minutes was 3.6 microns, the thickness of Ti added coatings made under the same conditions was 3.2 micron (Figure 4a, 4c). Free Ti particles added to the solution adhere to the substrate with the arc formed during coating, increasing the coating thickness. Furthermore, in Figure 4 the porosity distribution within the coating structure was observed as homogeneous.

As a result of the regional EDX analysis of the Ti doped coatings, it was observed that the main component of the coating was Al_2O_3 , along with the formation of SiO and TiO_2 compounds (Figure 6). At the same time, it was observed that Ti particles were in free form in the coating structure. Li et al. (2013) stated that when Ti is added at an appropriate concentration, free nano Ti particles are formed in the structure of the coating. When the EDX analysis was examined on the basis of elements, it was observed that there was 10.99% aluminum and 0.11% titanium according to the weight of oxygen at 88.69%. The presence of a high amount of oxygen during EDX analysis indicated that the micro arc oxidation coating was monolithic and composed predominantly of Al_2O_3 (Muhaffel et al., 2021). In addition to Al_2O_3 , TiO_2 and SiO compounds were also observed according to the analysis result as a result of high oxygen component.

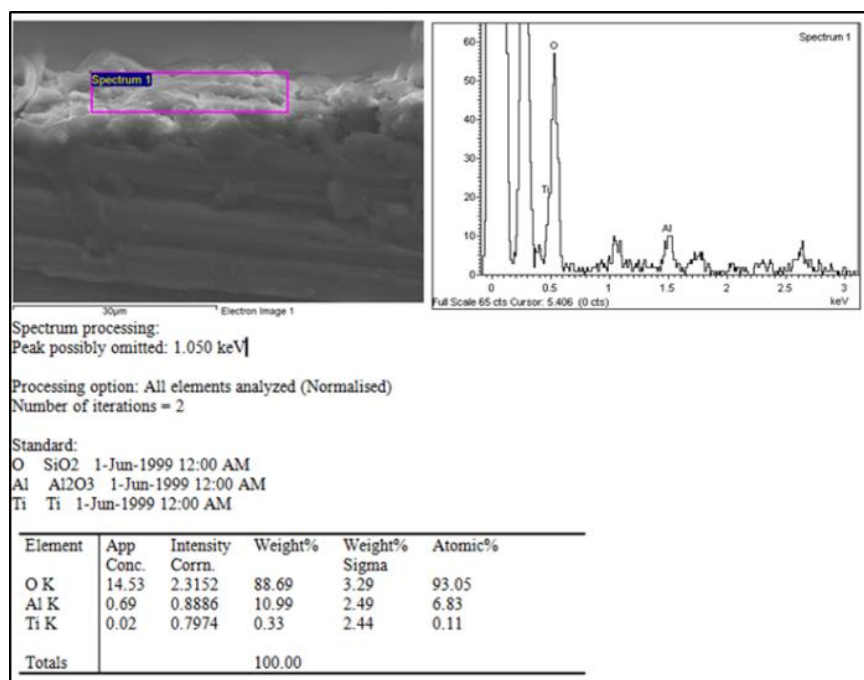


Figure 6. EDX analysis result (Powder: Ti-doped, Frequency:350 Hz, Voltage:550 V, Time: 20 min)

According to the XRD analysis of the sample coated with a normal solution (Ti-free), it was determined that the aluminum oxide phase, which is the main component of both substrate and coating, was seen in the microstructure (Figure 7a). The aluminum oxide phase was located at $2\theta = 38,360^\circ$ and $2\theta = 78,159^\circ$, while

the Fe phase was observed at $2\theta = 44,580^\circ$ and $2\theta = 64,960^\circ$. It was observed that TiO_2 and SiO phases were also formed along with the main phase of aluminum oxide in samples coated with the solution containing Ti (Figure 7b).

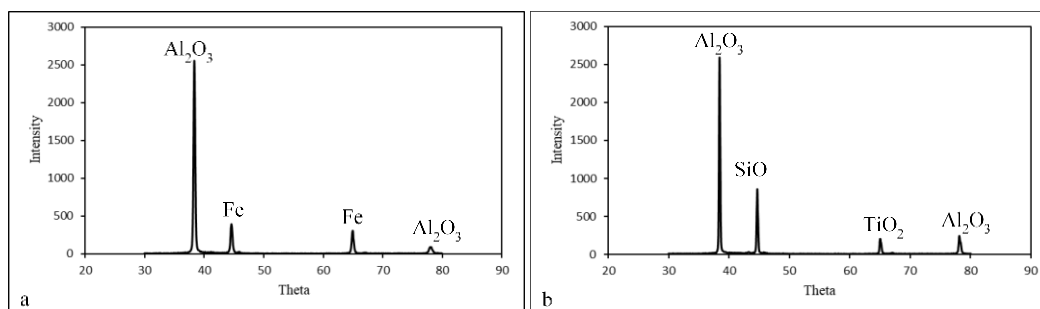


Figure 7. XRD analysis results of **a)** Ti free, 500 V, 10 min, 100 Hz, **b)** Ti added, 500 V, 10 min, 100 Hz

While aluminum oxide phases were seen at $2\theta = 38.440^\circ$ and $2\theta = 78.1$, the silicon oxide phase was observed at $2\theta = 44.680$ and the titanium dioxide phase at $2\theta = 65.001$. Nano Ti particles added to the coating solution combined with oxygen to form the TiO_2 phase with high wear resistance.

In Figure 8, SEM images of the samples with/without Ti added, taken after wear tests, were given. While the adhesive and abrasive wear mechanism were seen together in the worn zone of the Ti added sample, which was coated at 450 V voltage value (Figure 8a), the abrasive wear mechanism was predominantly observed in the Ti added sample (Figure 8b). In line with the experiments and literature information, it has been shown that the main wear mechanism of the TiO_2 coating is abrasive wear (Mu et al., 2013). When the SEM image of the sample without Ti added coated at 550V voltage was examined, it was seen that the dominant wear mechanism was the adhesive wear mechanism (Figure 8c). Abrasive wear was predominantly prominent in Ti- added coating (Figure 8d). It has been determined that the predominant wear type in the wear mechanisms of Ti-added samples is abrasive wear (Ding et al., 2018; Özler et al., 2020).

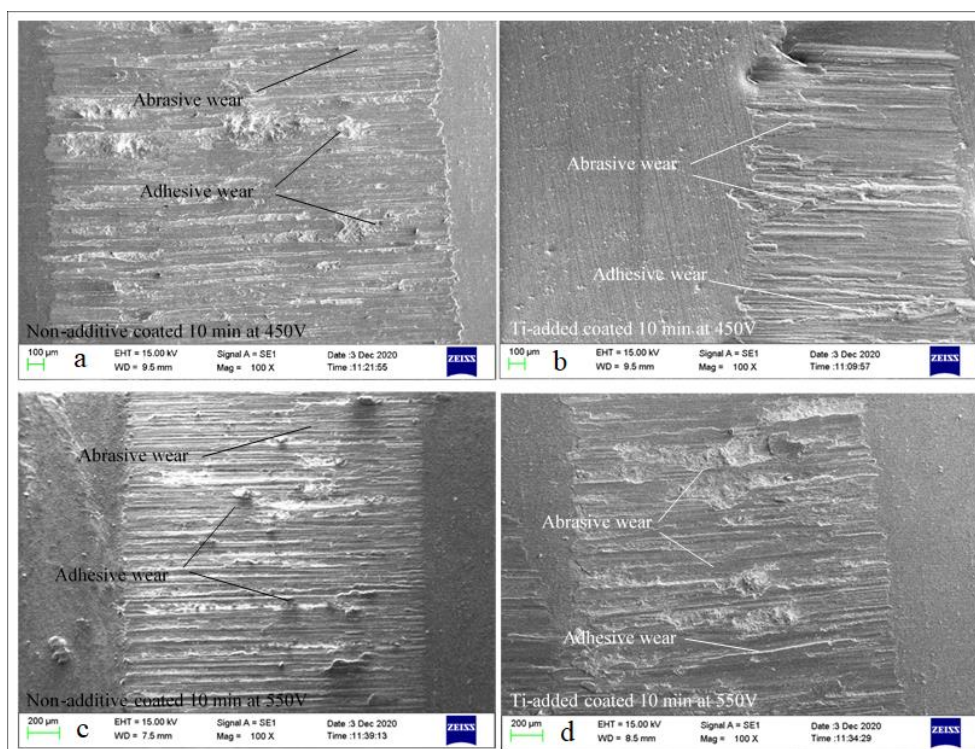


Figure 8. SEM images of samples after wear tests, **a)** Non additive coated 10 min at 450 V, **b)** Ti-added coated 10 min at 450 V, **c)** Non-additive coated 10 min at 550 V, **d)** Ti-added coated 10 min at 550 V

4. CONCLUSION

In this study, 7075 series aluminum material was coated by micro arc oxidation method with and without Ti addition, and the following results were obtained by examining the effect of coating parameters on thickness and wear:

- As the applied voltage increased during coating, the amount of wear of the coating decreased. Increasing the amount of voltage increases the thickness of the coating. For this reason, the rate of wear has decreased.
- As the frequency increased during coating, the thickness of coating part increased and the amount of wear of the coating decreased. Increasing the frequency increases the number of electrons passing per unit volume and causes more coating material to be deposited on the substrate surface. When the coatings made at 100 Hz and 350 Hz frequency values were compared, it was seen that thicker coatings were obtained with the increase in the frequency value. This accumulation has created a structure more resistant to wear in the coated substrate material.
- As the coating time increased, the coating thickness increased and the amount of wear decreased accordingly. The longer the time, the longer the substrate material will be exposed to the arc and the more coating material will be deposited on the surface and the higher the wear resistance.
- According to the EDX analysis of Ti added sample, SiO compound was found together with the main phase of Al₂O₃. However, it was also seen that Ti particles were in free form in the coating.
- According to the regional XRD analysis taken from the Ti added coating surface, it was observed that TiO₂ and SiO compounds were formed in addition to the main phase of Al₂O₃.
- The addition of Ti added to the coating solution reduced the amount of wear of the coated samples. This is due to the Al₂O₃ phase deposited on the substrate during the coating and the TiO₂ and SiO phases formed next to the main phase. While the Ti phase is free in the microstructure of the coating, the nano-sized Ti particles have increased the resistance to wear during the coating.

ACKNOWLEDGEMENT

The authors acknowledge the Firat University Scientific Research Projects Unit (FUBAP-MF-13.04) for financial support for this study.

CONFLICT OF INTEREST

The authors declare no conflict of interest.

REFERENCES

- Arslan, E., Totik, Y., Demirci, E. E., Vangolu, Y., Alsaran, A., & Efeoglu, I. (2009). High temperature wear behavior of aluminum oxide layers produced by AC micro arc oxidation. *Surface and Coatings Technology*, 204(6-7), 829–833. doi:[10.1016/j.surfcoat.2009.09.057](https://doi.org/10.1016/j.surfcoat.2009.09.057)
- Das, A., Kamal, M., Das, S. R., Patel, S. K., Panda, A., Rafighi, M., & Biswal, B. B. (2022). Comparative assessment between AlTiN and AlTiSiN coated carbide tools towards machinability improvement of AISI D6 steel in dry hard turning. *Proceedings of the Institution of Mechanical Engineers, Part C: Journal of Mechanical Engineering Science*, 236(6), 3174-3197. doi:[10.1177/09544062211037373](https://doi.org/10.1177/09544062211037373)
- Ding, L., Hu, S., Quan, X., & Shen, J. (2018). Effect of Ti on the microstructure evolution and wear behavior of VN alloy/Co-based composite coatings by laser cladding. *Journal of Materials Processing Technology*, 252(October 2017), 711-719. doi:[10.1016/j.jmatprotec.2017.10.042](https://doi.org/10.1016/j.jmatprotec.2017.10.042)
- Dudareva, N., & Gallyamova, R. (2019). The Cnfluence of Chemical Composition of Aluminum Alloys on the Quality of Oxide Layers Formed by Microarc Oxidation. *Materials Today: Proceedings*, 11, 89–94. doi:[10.1016/j.matpr.2018.12.112](https://doi.org/10.1016/j.matpr.2018.12.112)
- Huang, P., Zhang, Y., Xu, K., & Han, Y. (2004). Surface modification of titanium implant by microarc oxidation and hydrothermal treatment. *Journal of Biomedical Materials Research - Part B Applied Biomaterials*, 70(2), 187–190. doi:[10.1002/jbm.b.30009](https://doi.org/10.1002/jbm.b.30009)

- Li, H.-X., Song, R.-G., & Ji, Z.-G. (2013). Effects of nano-additive TiO₂ on performance of micro-arc oxidation coatings formed on 6063 aluminum alloy. *Transactions of Nonferrous Metals Society of China (English Edition)*, 23(2), 406–411. doi:[10.1016/S1003-6326\(13\)62477-2](https://doi.org/10.1016/S1003-6326(13)62477-2)
- Lin, D. C., Wang, G. X., Srivatsan, T. S., Al-Hajri, M., & Petraroli, M. (2003). Influence of titanium dioxide nanopowder addition on microstructural development and hardness of tin-lead solder. *Materials Letters*, 57(21), 3193–3198. doi:[10.1016/S0167-577X\(03\)00023-5](https://doi.org/10.1016/S0167-577X(03)00023-5)
- Ma, X., Jin, S., Wu, R., Ji, Q., Hou, L., Krit, B., & Betsofen, S. (2022a). Influence alloying elements of Al and Y in Mg–Li alloy on the corrosion behavior and wear resistance of microarc oxidation coatings. *Surface and Coatings Technology*, 432(December 2021). doi:[10.1016/j.surfcoat.2021.128042](https://doi.org/10.1016/j.surfcoat.2021.128042)
- Ma, X., Jin, S., Wu, R., Zhang, S., Hou, L., Krit, B., Betsofen, S., & Liu, B. (2022b). Influence of combined B₄C/C particles on the properties of microarc oxidation coatings on Mg-Li alloy. *Surface and Coatings Technology*, 438(March), 128399. doi:[10.1016/j.surfcoat.2022.128399](https://doi.org/10.1016/j.surfcoat.2022.128399)
- Mu, M., Liang, J., Zhou, X., & Xiao, Q. (2013). One-step preparation of TiO₂/MoS₂ composite coating on Ti6Al4V alloy by plasma electrolytic oxidation and its tribological properties. *Surface and Coatings Technology*, 214, 124–130. doi:[10.1016/j.surfcoat.2012.10.079](https://doi.org/10.1016/j.surfcoat.2012.10.079)
- Muhaffel, F., Baydogan, M., & Cimenoglu, H. (2021). A study to enhance the mechanical durability of the MAO coating fabricated on the 7075 Al alloy for wear-related high temperature applications. *Surface and Coatings Technology*, 409(December 2020), 126843. doi:[10.1016/j.surfcoat.2021.126843](https://doi.org/10.1016/j.surfcoat.2021.126843)
- Nie, X., Leyland, A., Song, H. W., Yerokhin, A. L., Dowey, S. J., & Matthews, A. (1999). Thickness effects on the mechanical properties of micro-arc discharge oxide coatings on aluminium alloys. *Surface and Coatings Technology*, 116–119, 1055–1060. doi:[10.1016/S0257-8972\(99\)00089-4](https://doi.org/10.1016/S0257-8972(99)00089-4)
- Odabasi, H. K., & Odabasi, A. (2020). Wear and corrosion behavior of Mg-based alloy reinforced with TiC and ZrC particles. *Materialpruefung/Materials Testing*, 62(12), 1161–1171. doi:[10.3139/120.111601](https://doi.org/10.3139/120.111601)
- Özler, L., Tosun, G., & Özcan, M. E. (2020). Influence of B₄C powder reinforcement on coating structure, microhardness and wear in friction surfacing. *Materials and Manufacturing Processes*, 35(10), 1135–1145. doi:[10.1080/10426914.2020.1772480](https://doi.org/10.1080/10426914.2020.1772480)
- Rafighi, M. (2021). Comparison of Ceramic and Coated Carbide Inserts Performance in Finish Turning of Hardened AISI 420 Stainless Steel. *Journal of Polytechnic*, 24(3), 1295–1302. doi:[10.2339/politeknik.892146](https://doi.org/10.2339/politeknik.892146)
- Salimiasl, A., & Rafighi, M. (2017). Titreşim ve Kesme Kuvveti Esaslı Takım Aşınmasının Bulanık Mantıkla İzlenmesi ve Tahmini Monitoring and Estimating of Vibration and Cutting Force Based Tool Wear via Fuzzy Logic. *Journal of Polytechnic*, 20(1), 111–120.
- Shao, Z. C., Zhang, Q. F., Wang, M., & Yang, L. (2014). Preparation of black coating on AM50 alloys by microarc oxidation (MAO). *Materials and Manufacturing Processes*, 29(9) 1095–1100. doi:[10.1080/10426914.2014.921695](https://doi.org/10.1080/10426914.2014.921695)
- Shen, D., Li, G., Guo, C., Zou, J., Cai, J., He, D., Ma, H., & Liu, F. (2013). Microstructure and corrosion behavior of micro-arc oxidation coating on 6061 aluminum alloy pre-treated by high-temperature oxidation. *Applied Surface Science*, 287, 451–456. doi:[10.1016/j.apsusc.2013.09.178](https://doi.org/10.1016/j.apsusc.2013.09.178)
- Shokouhfar, M., & Allahkaram, S. R. (2017). Effect of incorporation of nanoparticles with different composition on wear and corrosion behavior of ceramic coatings developed on pure titanium by micro arc oxidation. *Surface and Coatings Technology*, 309, 767–778. doi:[10.1016/j.surfcoat.2016.10.089](https://doi.org/10.1016/j.surfcoat.2016.10.089)
- Şahinoğlu, A., & Rafighi, M. (2021). Investigation of tool wear, surface roughness, sound intensity, and power consumption during hard turning of AISI 4140 steel using multilayer-coated carbide inserts. *Journal of Engineering Research (Kuwait)*, 9(4B), 377–395. doi:[10.36909/jer.8783](https://doi.org/10.36909/jer.8783)
- Tosun, G., Ozler, L., & Ozcan, M. E. (2019). Gradient composite coatings on AA5754 using friction stir process. *Surface Engineering*, 36(5), 1–9. doi:[10.1080/02670844.2019.1665279](https://doi.org/10.1080/02670844.2019.1665279)

- Wang, H.-Y., Zhu, R.-F., Lu, Y.-P., Xiao, G.-Y., He, K., Yuan, Y. F., Ma, X.-N., & Li, Y. (2014). Effect of sandblasting intensity on microstructures and properties of pure titanium micro-arc oxidation coatings in an optimized composite technique. *Applied Surface Science*, 292, 204–212. doi:[10.1016/j.apsusc.2013.11.115](https://doi.org/10.1016/j.apsusc.2013.11.115)
- Wang, J.-H., Du, M.-H., Han, F.-Z., & Yang, J. (2014). Effects of the ratio of anodic and cathodic currents on the characteristics of micro-arc oxidation ceramic coatings on Al alloys. *Applied Surface Science*, 292, 658–664. doi:[10.1016/j.apsusc.2013.12.028](https://doi.org/10.1016/j.apsusc.2013.12.028)
- Zhu, M. H., Cai, Z. B., Lin, X. Z., Ren, P. D., Tan, J., & Zhou, Z. R. (2007). Fretting wear behaviour of ceramic coating prepared by micro-arc oxidation on Al-Si alloy. *Wear*, 263(1-6), 472–480. doi:[10.1016/j.wear.2007.01.050](https://doi.org/10.1016/j.wear.2007.01.050)



Gazi University

Journal of Science

PART A: ENGINEERING AND INNOVATION

<http://dergipark.org.tr/gujisa>

Molecular Docking, HOMO-LUMO, Quantum Chemical Computation and Bioactivity Analysis of vic-Dioxim Derivatives Bearing Hydrazone Group Ligand and Their Ni^{II} and Cu^{II} Complexes

Şerife Gökçe ÇALIŞKAN^{1*} , Onur GENÇ¹ , Fatma EROL² , Nursabah SARIKAVAKLI³ ¹Aydın Adnan Menderes University, Faculty of Sciences and Arts, Department of Physics, 09010, Aydın, TURKIYE²Gazi University, Technical Sciences Vocational School, Ostim, 06374, Ankara, TURKIYE³Aydın Adnan Menderes University, Faculty of Sciences and Arts, Department of Chemistry, 09010, Aydın, TURKIYE

Keywords	Abstract
vic-dioxim	Molecular docking process was performed to investigate the interactions between the synthesized compounds and human epidermal growth factor protein kinase domain EGFR (PDB ID:1M17) and cyclin-dependent kinase-2 CDK2 (PDB ID:3IG7) proteins. HOMO LUMO orbital energy analysis, quantum chemical calculations were made and the bioactivity parameters of the compounds were evaluated. Ni ^{II} and Cu ^{II} complexes of the L ¹ H ₂ L ² H ₂ and L ³ H ₂ ligands showed higher binding affinity to EGFR and CDK2. Especially, [Cu(L ¹ H) ₂] and [Cu(L ² H) ₂] complexes can be suggested as hit compounds against CDK2 and EGFR, respectively. These were supported by the inhibition constant values which were the lowest when compared to others. L ¹ H ₂ L ² H ₂ and L ³ H ₂ ligands had the lowest binding energy values when compared to metal complexes. Also, [Cu(L ² H) ₂] complex had a high binding energy value against EGFR. [Ni(L ² H) ₂] and [Cu(L ² H) ₂] complexes with EGFR had the highest LE and FQ values and these were found to be in the recommended range. Furthermore, [Cu(L ³ H) ₂] had an acceptable FQ value however its LE value was out of range. Besides, [Cu(L ² H) ₂] had a potent and sufficient electrophile ability (acceptor) among other compounds. In conclusion, these compounds may be suitable compounds for further analysis in anti-cancer drug development with low toxic and targeted properties.
Hydrazones	
Molecular Docking	
HOMO-LUMO	
Bioactivity	

Cite

Çalışkan, S. G., Genç, O., Erol, F., & Sarıkavaklı, N. (2022). Molecular Docking, HOMO-LUMO, Quantum Chemical Computation and Bioactivity Analysis of vic-Dioxim Derivatives Bearing Hydrazone Group Ligand and Their Ni^{II} and Cu^{II} Complexes. *GU J Sci, Part A, 9(3)*, 299-313.

Author ID (ORCID Number)	Article Process
Ş. G. Çalışkan, 0000-0001-5421-3472	Submission Date 10.08.2022
O. Genç, 0000-0002-9061-7519	Revision Date 22.09.2022
F. Erol, 0000-0002-4103-0148	Accepted Date 26.09.2022
N. Sarıkavaklı, 0000-0002-9359-7672	Published Date 29.09.2022

1. INTRODUCTION

In recent years, transition metal complexes carrying vic-dioxime ligands have been the subject of intense studies due to their applications in many scientific fields such as coordination chemistry, biomedicine and electrochemistry. The interaction of a central metal with surrounding ligands (atoms, ions or molecules) has been a major area of interest in coordination chemistry (Rija et al., 2011). From the beginning 1905s vic-dioximes have been used widely as chelating agents in coordination chemistry (Tschugaeff, 1907; Canpolat & Kaya, 2005). vic-dioximes and hydrazones are interesting objects because of their wide application in medicine, industry and analytical chemistry. vic-dioxim derivatives act as amphoteric ligands due to the presence of weakly acidic -OH groups and basic -C=N groups. Therefore, they can form highly stable complexes with most of the transition metals in the periodic table (Serin, 2001, Smith et al., 2003, Kurtoglu & Baydemir, 2007).

Compounds bearing hydrazone and/or oxime linkage attracted the attention of many scholars because of their ability to form stable metal complexes with various transition metals, in addition to the presence of N-OH

*Corresponding Author, e-mail: gcaliskan@adu.edu.tr

moiety, which could enhance their chelation ability and make it more flexible in the reduction, oxidation, and conjugation with organic and inorganic compounds.

These compounds also play an important role in fields such as stereochemistry, structure isomerism, spectroscopy, a model for biological system, cation exchange and ligand exchange chromatography, analytical reagents, as well as catalysts in various chemical processes (Soga et al., 2001; Park et al., 2005).

New anti-cancer drug development studies are gaining more importance day by day and the studies in this field are increasing rapidly. There are proteins responsible for cancer cell development, proliferation and differentiation, which are important targets that must be inhibited by newly synthesized compounds. For example, epidermal growth factor receptor (EGFR), vascular endothelial growth factor receptor (VEGFR), cyclin-dependent kinase-2 (CDK2) are responsible for the growth, nutrition and proliferation of tumour cells (Haider et al., 2021). Various studies have been conducted experimentally and theoretically to investigate the effects of newly synthesized compounds against these target proteins (Altamimi et al., 2021; Horchani et al., 2021; Fouad & Adly, 2021). For instance, Horchani et al. (2021) investigated the inhibitory effects of synthetic pyrazolo-primidinones tethered with hydrazide-hydrazones on EGFR by means of molecular docking and cell viability and Fouad and Adly (2021) reported the molecular docking results of Cu^{2+} and Zn^{2+} nanocomplexes against CDK2 cancer target protein. However, in these studies, quantum chemical calculations of the compounds were not performed and their bioactivity was not analyzed. Literature search reveals that there are no reports based on molecular docking, HOMO-LUMO, quantum chemical computation and bioactivity analysis on hydrazone group-bearing vic-dioxim derivatives and their metal complexes against cancer target proteins EGFR and CDK2. Because of this scarcity observed in the literature, we wanted to reveal the effects of vic-dioxim derivatives carrying the hydrazone group and their metal complexes against cancer target proteins EGFR and CDK2 by molecular docking, HOMO-LUMO, quantum chemical computation and bioactivity analysis.

In the present work, three unsymmetric vic-dioxim derivatives bearing the hydrazone group and their metal complexes with Ni^{II} and Cu^{II} metal ions which were synthesized by us for the first time in our previous study (Sarikavakli & Cakici, 2012) were investigated by means of HOMO-LUMO, quantum chemical computation, bioactivity analysis and molecular docking against the target cancer proteins EGFR and CDK2.

2. MATERIAL AND METHOD

In this study, our starting material, anti-glyoxime hydrazine, (GH_2), which was synthesized and brought to the literature by us for the first time in our previous study, was synthesized with anti-chlorglyoxime and hydrazine hydrate (Sarikavakli & Irez, 2005).

According to the literature; anti-glyoxime hydrazine, (GH_2), was prepared by reported procedures vic-dioxime ligands containing the hydrazone group, anti-p-hydroxybenzaldehydeglyoxime hydrazone (L^1H_2); (1Z,2E)-N'-[(E)-(2,3-dihydroxyphenyl)methylidene]-2-(hydroxyimino)ethanehydroximohydrazide; (L^2H_2); (1Z,2E)-2-(hydroxyimino)-N'-[(E)-(2-hydroxy-3-methoxyphenyl)methylidene]ethanehydroximohydrazide, (L^3H_2) have been prepared from (1Z,2E)-2-(hydroxyimino)ethanehydroximohydrazide, p-hidroksibenaldehit, o-pyrocatechualdehyde or o-vanillin. Mononuclear $[\text{M}(\text{L}^1\text{H})_2]$, $[\text{M}(\text{L}^2\text{H})_2]$ and $[\text{M}(\text{L}^3\text{H})_2]$, where $\text{M}=\text{Ni}^{\text{II}}$ and Cu^{II} complexes of the bidentate ligands were synthesized according to the literature (Sarikavakli & Cakici, 2012) (Figure 1-4).

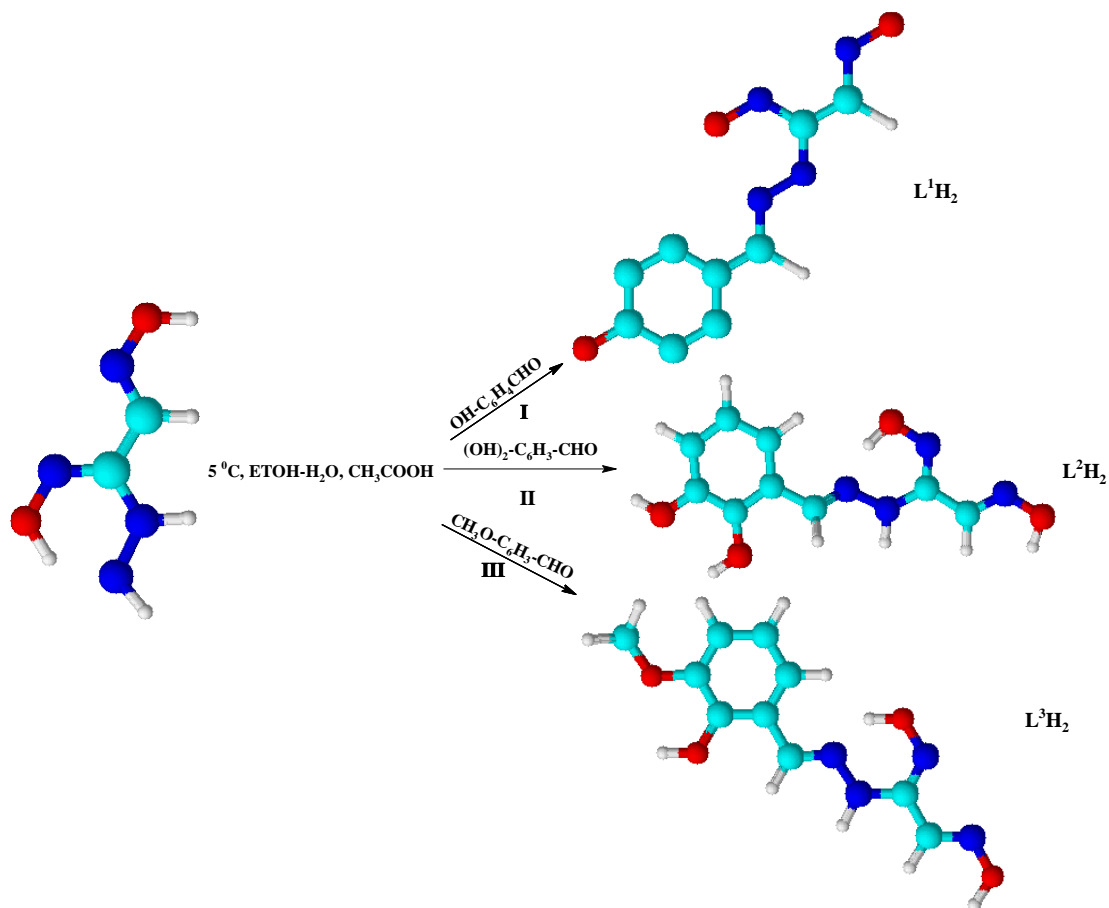


Figure 1. Chemical structures of ligands

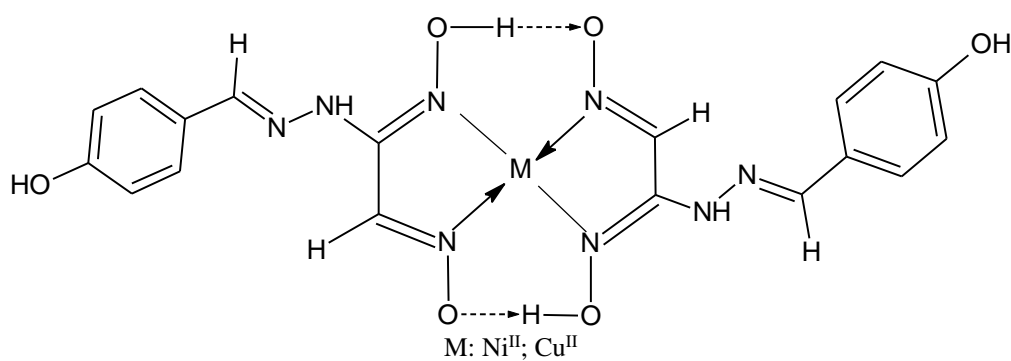


Figure 2. Complexes of expected structures of the ligand [L^1H_2]

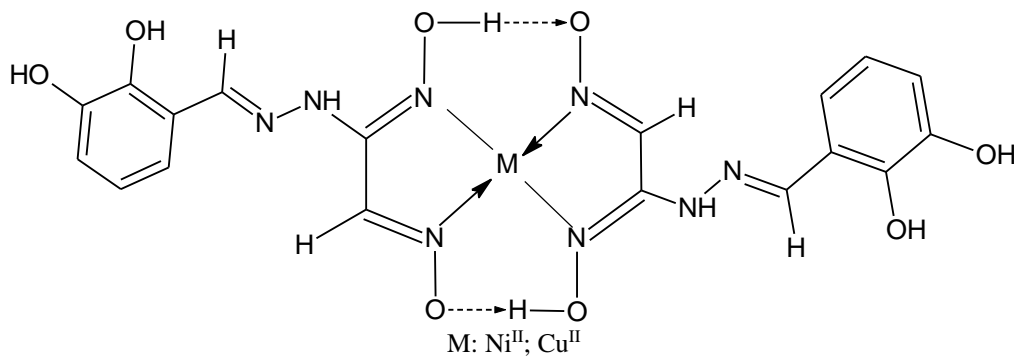


Figure 3. Complexes of expected structures of the ligand [L^2H_2]

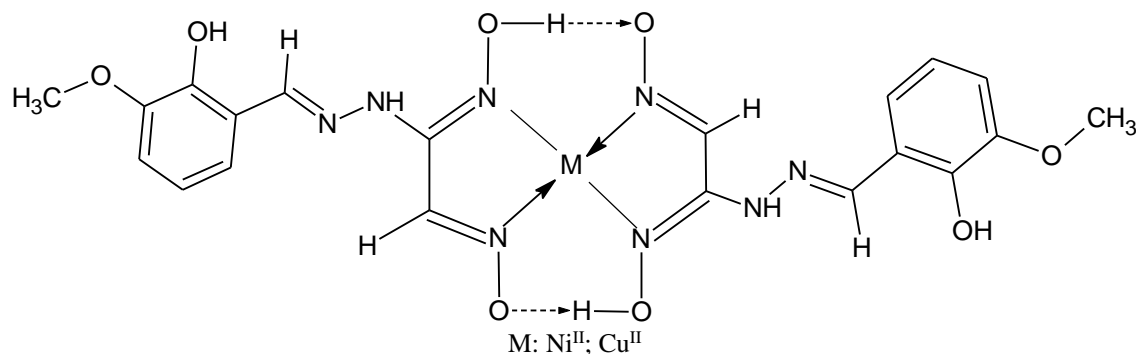


Figure 4. Complexes of expected structures of the ligand [L^3H_2]

2.1. Molecular Docking Studies

2.1.1. Protein preparation

Epidermal growth factor protein kinase domain EGFR (PDB ID:1M17) and cyclin-dependent kinase-2 CDK2 (PDB ID:3IG7)'s 3-D structures were obtained from Protein Databank (<https://www.rcsb.org/>). The preparation process includes the deletion of water molecules, polar hydrogen atom addition and Kollmann charge addition and is performed by using Autodock tools 1.5.7 software (ADT, The Scripps Research Institute, La Jolla, CA, USA). The prepared protein was saved in PDBQT format finally.

2.1.2. Ligand preparation

2-D ligand and metal complex structures were sketched by ChemSketch software. The optimization process was performed by Avogadro v1.2.0 software and the final forms of the compounds were converted into 3-D and saved in pdb format. The setting of torsion tree and the rotatable and non-rotatable bounds present in the ligand was performed by using Autodock tools 1.5.7 software (ADT, The Scripps Research Institute, La Jolla, CA, USA). They were saved in PDBQT format.

2.1.3. Molecular docking

Autodock Vina (Trott & Olson, 2009) was used for molecular docking of the synthesized compounds against target proteins EGFR and CDK2. Grid values were adjusted by Autogrid utility of AutoDock software so as to cover the target protein. Its size was set to $100 \text{ \AA} \times 100 \text{ \AA} \times 100 \text{ \AA}$ by 0.375 \AA separation. The interactions that occurred between the compounds and target proteins were visualized by PyMol (DeLano, 2013) and DS visualizer software (Accelrys, 2014).

Inhibition constant (K_i) values of the compounds were reached by means of equation (1) where Gibbs free energy (ΔG) was obtained from the docking process, R is the gas constant ($R = 1.99 \text{ cal/mol K}$) and T is the absolute temperature (298.15 K). Low K_i value indicates the potency of being a hit compound.

$$K_i = 10^{(\Delta G \div RT)} \quad (1)$$

2.4. Ligand Bioactivity

For the discovery of a potent compound, a candidate for a novel drug, the affinity parameter is insufficient, there must be evaluated the bioactivity properties of the compound also. The most preferred ligand bioactivity parameters are called ligand efficiency (LE) and fit quality (FQ) and are calculated by equations (2)-(4).

$$LE = -\frac{\Delta G}{HA} \quad (2)$$

$$LE_{scale} = 0.873e^{-0.026 \times HA} - 0.064 \quad (3)$$

$$FQ = LE \div LE_{scale} \quad (4)$$

2.5. Quantum Chemical Descriptors

The molecules' geometry optimization was performed by using the Density Functional Theory (DFT) method with B3LYP functional and a basis set of 6-31G. Afterward, the ORCA input files were created by Avogadro v1.2.0 software. Highest occupied molecular orbital (HOMO) and lowest unoccupied molecular orbital (LUMO) were extracted from ORCA output file directly and IboView (Knizia, 2022) was used to visualize the structure of the molecules in detail. The difference between HOMO and LUMO values was calculated according to equation (5).

$$\Delta E_{gap} = |E_{HOMO} - E_{LUMO}| \quad (5)$$

According to Koopmans' theorem (Koopmans, 1934) the initial ionization energy (I) and electron affinity (A) are approximately equal to the minus values of HOMO and LUMO, respectively. Moreover, electronegativity (χ), chemical potential (π), global hardness (η), global softness (σ), and global electrophilicity (ω) were calculated according to equations (6-10) (Koopmans, 1934).

$$\chi = \frac{1}{2}(I + A) \quad (6)$$

$$\eta = \frac{1}{2}(I - A) \quad (7)$$

$$\pi = -\frac{1}{2}(I + A) \quad (8)$$

$$\sigma = \frac{1}{\eta} = \frac{2}{(I - A)} \quad (9)$$

$$\omega = \frac{\chi^2}{2\eta} \quad (10)$$

3. RESULTS AND DISCUSSION

3.1. Chemistry

In this study, vic-dioxime ligands containing the hydrazone group were obtained according to the method specified in the literature (Sarikavakli & Irez, 2005; Sarikavakli & Cakici, 2012). Synthesis of the target compounds was achieved using 1:1 molar ratios (Figure 1). The target compounds anti-glyoxime hydrazine, (GH₂), and benzaldehyde derivatives in absolute ethanol at 25⁰C gave three substituted (1Z,2E)-2-(hydroxyimino)ethanohydroximohydrazide (L¹H₂); (L²H₂) and (L³H₂).

The ligands (L¹H₂); (L²H₂) and (L³H₂) were complexed with divalent (Ni^{II} and Cu^{II}) metal salts to yield mononuclear complexes corresponding to the general formula ML₂ (Sarikavakli & Irez, 2005).

3.2. Molecular Docking

L^1H_2 , L^2H_2 , L^3H_2 ligands and their Ni^{II} and Cu^{II} metal complexes were docked with target proteins EGFR and CDK2 to evaluate the interactions. Table 1 includes the binding energy and inhibition constant values. Interactions types that occurred between the compounds and target protein molecules were also depicted in Table 2 in detail.

Our results include four types of H bond interactions as conventional hydrogen bond, carbon-hydrogen bond, salt bridge and pi-donor hydrogen bond, four types of hydrophobic interactions as alkyl, pi-alkyl, pi-sigma, pi-pi stacked and three types of electrostatic interactions as attractive charge, pi-anion and pi-cation interactions in Table 2.

Table 1. Binding energy (affinity) and inhibition constants of the compounds with target proteins of EGFR (PDB ID: 1M17) and CDK2 (PDB ID: 3IG7)

Compound	Target Protein	Binding Affinity	Inhibition Constant
		(kcal/mol)	μM
L^1H_2	1M17	-6.4	0.014
	CDK2	-5.2	0.010
[Ni(L^1H) ₂]	1M17	-7.5	0.008
	CDK2	-7.2	0.013
[Cu(L^1H) ₂]	1M17	-7.0	0.019
	CDK2	-7.7	0.006
L^2H_2	1M17	-6.4	0.014
	CDK2	-5.5	0.063
[Ni(L^2H) ₂]	1M17	-8.3	0.008
	CDK2	-7.2	0.013
[Cu(L^2H) ₂]	1M17	-8.9	0.003
	CDK2	-7.6	0.007
L^3H_2	1M17	-6.3	0.016
	CDK2	-5.7	0.045
[Ni(L^3H) ₂]	1M17	-7.7	0.006
	CDK2	-7.1	0.016
[Cu(L^3H) ₂]	1M17	-8.2	0.009
	CDK2	-6.5	0.012

For the binding to EGFR target protein, the first three highest binding energies were determined in [Cu(L^2H)₂] (-8.9kcal/mol), [Ni(L^2H)₂] (-8.3kcal/mol) and [Cu(L^3H)₂] (-8.2kcal/mol) complexes. Other compounds had lower binding energy values given in Table 1. Furthermore, the smallest inhibition constant which is related to the high potent of binding belongs to [Cu(L^2H)₂] complex.

However, the binding energy values of the compounds with CDK2 target protein were lower than the EGFR's when compared. The highest binding energy value belongs to [Cu(L^1H)₂] complex with -7.7kcal/mol. This result was supported by the inhibition constant value of [Cu(L^1H)₂] which was the lowest one when compared to the others of CDK2.

Table 2. Interaction types occurred between the compounds and target protein molecules

Compound	Target proteins					
	EGFR			CDK2		
	H-Bond	Hydrophobic	Electrostatic	H-Bond	Hydrophobic	Electrostatic
L ¹ H ₂	Lys721(3.289 Å) Lys721(2.831 Å) Asp831(2.473 Å)	Phe699(4.112 Å)	Glu738(5.335 Å) Asp831(4.433 Å) Asp831(4.161 Å) Asp831(3.952 Å) Asp831(4.112 Å) Phe699(4.871 Å)	Thr218(2.820 Å) Thr198(2.769 Å)	Leu202(5.293 Å)	-
[Ni(L ¹ H) ₂]	Asp831(3.543 Å)	Lys855(5.039 Å)	Asp813(4.759 Å) Asp831(2.943 Å) Asp831(4.583 Å) Asp831(3.734 Å) Lys721(4.525 Å) Glu738(3.949 Å)	Thr198(3.085 Å) Thr218(3.010 Å) Val251(2.028 Å)	Pro253(5.477 Å) Arg217(4.005 Å)	-
[Cu(L ¹ H) ₂]	Glu734(2.175 Å)	-	Asp831(5.520 Å) Asp831(4.982 Å) Asp831(4.288 Å) Asp813(4.939 Å) Glu734(4.313 Å)	Thr218(2.665 Å) Arg200(3.544 Å)	Pro254(5.124 Å) Arg217(5.176 Å)	-
L ² H ₂	Glu738(1.959 Å) Arg817(2.789 Å)	-	Asp831(4.205 Å) Asp831(4.077 Å) Asp831(3.766 Å) Phe699(4.023 Å)	Thr182(2.950 Å) Arg274(1.938 Å)	-	-
[Ni(L ² H) ₂]	Arg817(3.131 Å) Glu738(2.550 Å) Glu738(2.438 Å)	-	Asp813(5.576 Å) Asp831(4.863 Å) Asp831(4.215 Å)	Ala244(2.645 Å) Arg217(2.192 Å) Leu202(2.312 Å) Arg217(3.495 Å) Trp243(3.481 Å) Val251(3.766 Å) Gln246(4.197 Å)	Arg200(4.620 Å)	Arg200(4.889 Å)
[Cu(L ² H) ₂]	Asp831(3.013 Å) Asp831(3.337 Å) Asp831(3.380 Å) Asn818(3.013 Å)	Ala731(5.318 Å)	Asp831(3.791 Å) Asp831(4.881 Å) Asp831(5.069 Å) Asp831(4.392 Å) Asp831(3.026 Å) Asp831(2.792 Å) Glu738(5.251 Å) Glu734(3.649 Å)	Lys142(2.931 Å) Val29(2.181 Å) Ile63(1.923 Å)	Val29(3.885 Å) Lys65(3.830 Å)	
L ³ H ₂	Lys721(3.283 Å) Lys721(2.809 Å) Phe699(2.966 Å) Asp831(2.576 Å)	Phe699(4.177 Å) Val702(5.496 Å)	Glu738(5.368 Å) Asp831(4.225 Å) Asp831(3.967 Å) Asp831(4.090 Å) Phe699(4.821 Å)	Glu51(2.462 Å) Arg122(2.871 Å) Leu54(2.193 Å) Val123(3.440 Å)	Leu58(4.884 Å) His121(4.585 Å) Leu54(4.637 Å) Val123(5.307 Å)	Glu51(4.906 Å)
[Ni(L ³ H) ₂]	Asp831(3.583 Å) Ile854(4.009 Å)	Cys773(4.183 Å) Arg817(4.644 Å) Lys855(4.074 Å) Trp856(5.136 Å) Val702(5.414 Å) Pro853(4.925 Å) Ile854(5.356 Å) Ala896(5.267 Å)	Asp831(4.683 Å) Asp831(4.742 Å) Asp813(5.494 Å) Asp831(3.824 Å) Phe699(3.949 Å)	Thr182(3.034 Å) Ala277(2.980 Å) Ala116(2.430 Å) Phe117(3.557 Å) Ser120(3.589 Å)	Phe117(5.440 Å)	-
[Cu(L ³ H) ₂]	Lys721(2.949 Å) Phe699(2.314 Å)	Phe699(5.332 Å) Arg724(4.246 Å) Ala698(5.130 Å) Arg724(5.337 Å)	Glu734(5.556 Å) Asp831(4.206 Å) Asp831(3.778 Å)	Ser261(3.374 Å) Ser261(3.341 Å) Gln265(3.165 Å) Gln265(3.206 Å) Gln265(3.374 Å) Glu257(2.487 Å) His283(2.846 Å)	Ile275(4.746 Å) Pro284(5.012 Å)	Glu257(4.793 Å)

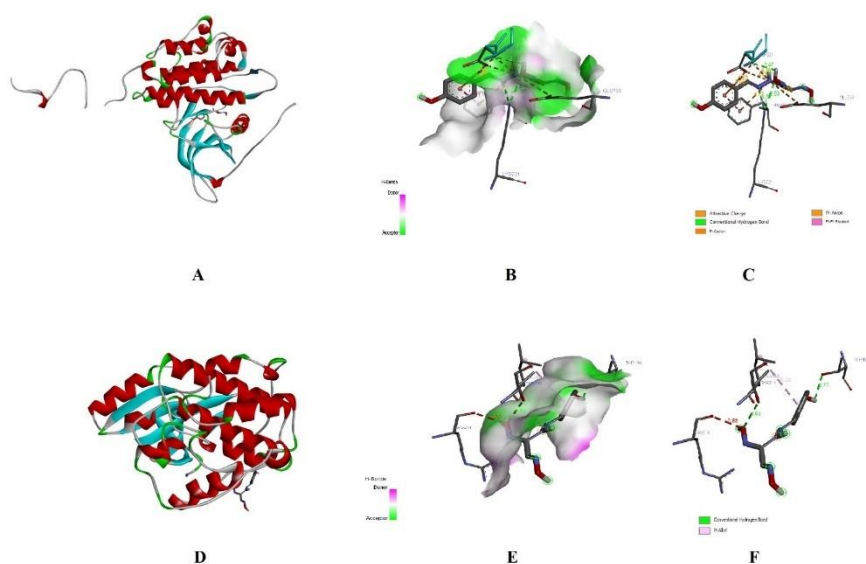


Figure 5. A, D) 3D diagram, B, E) 2D diagram, C, F) Hydrogen bonding interactions of L^1H_2 with EGFR and CDK2, respectively

Figure 5 showed that L^1H_2 interacts with EGFR target protein through three conventional hydrogen bonds (Lys721, Asp831), one pi-pi stacked interaction (Phe699), three attractive charge interactions (Glu738, Asp831), one pi-cation (Phe699) and two pi-anion interactions (Asp831). Also, with CDK2 target protein, there were two conventional hydrogen bonds (Thr218, Thr198) and one pi-alkyl interaction (Leu202) occurred.

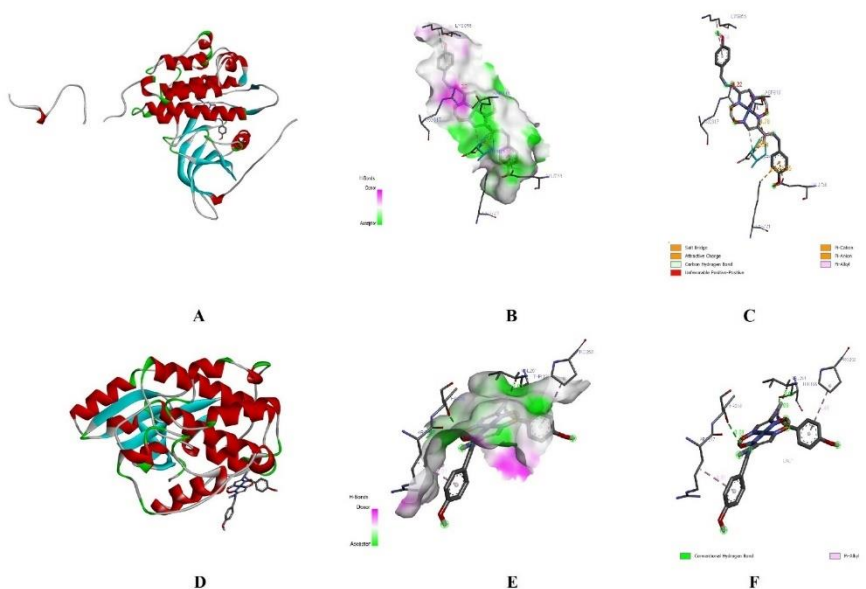


Figure 6. A, D) 3D diagram, B, E) 2D diagram, C, F) Hydrogen bonding interactions of $[Ni(L^1H)_2]$ with EGFR and CDK2, respectively

In Figure 6, $[Ni(L^1H)_2]$ formed a conventional hydrogen bond with EGFR by Asp831 residue and had one pi-alkyl (Lys855), one salt bridge (Asp831), three attractive charge (Asp813, Asp831), one pi-cation (Lys721) and one pi-anion (Glu738) interactions with this target protein EGFR. Furthermore, $[Ni(L^1H)_2]$ had three conventional hydrogen bonds with Thr198, Thr218 and Val251 residues and had pi-alkyl interactions with Pro253 and Arg217 amino acids.

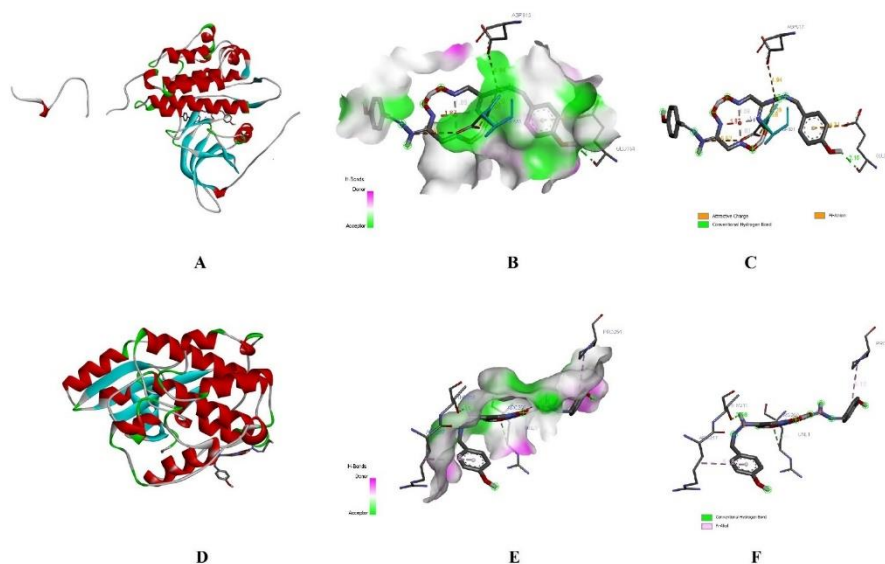


Figure 7. A, D) 3D diagram, B, E) 2D diagram, C, F) Hydrogen bonding interactions of $[Cu(L^1H)_2]$ with EGFR and CDK2, respectively

Figure 7 showed the interactions between $[Cu(L^1H)_2]$ and target proteins EGFR and CDK2. $[Cu(L^1H)_2]$ bound to Glu734 amino acid through a conventional hydrogen bond and had a pi-anion interaction. Furthermore, it formed three attractive charge interactions with Asp831 and one with Asp813 amino acids. Moreover, there was observed a conventional hydrogen bond with Thr218, carbon-hydrogen bond with Arg200, pi-alkyl interactions with Pro254 and Arg217 amino acids of CDK2 protein.

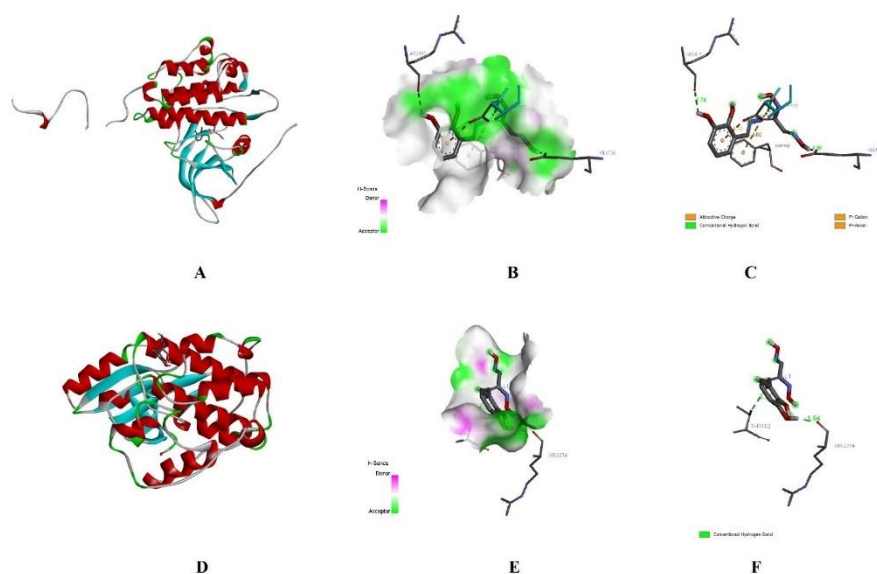


Figure 8. A, D) 3D diagram, B, E) 2D diagram C, F) Hydrogen bonding interactions of L^2H_2 with EGFR and CDK2, respectively

There were two conventional hydrogen bonds occurred between L^2H_2 and Glu738 and Arg817 amino acids of EGFR target protein. Also, there were formed 2 attractive charge interactions and one pi-anion interaction with Asp831 and one pi-cation interaction with Phe699 amino acids (Figure 8A-C). Furthermore, L^2H_2 formed only two conventional hydrogen bonds with Thr182 and Arg274 amino acids of CDK2 target protein (Figure 8D-F).

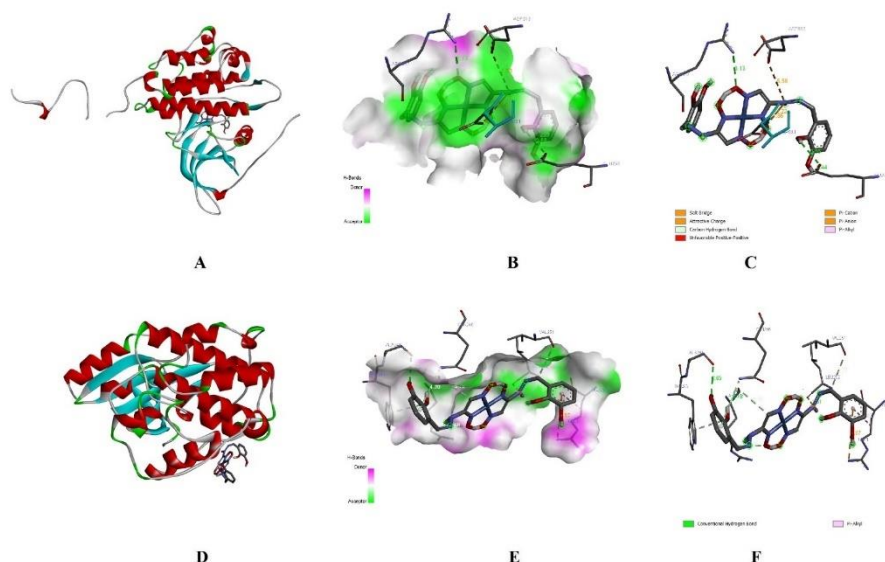


Figure 9. A, D) 3D diagram, B, E) 2D diagram
C, F) Hydrogen bonding interactions of $[\text{Ni}(\text{L}^2\text{H})_2]$ with EGFR and CDK2, respectively

In Figure 9 the interactions between the $[\text{Ni}(\text{L}^2\text{H})_2]$ complex and EGFR, CDK2 target proteins were shown. $[\text{Ni}(\text{L}^2\text{H})_2]$ interacted with Arg817 and Glu738 amino acids of EGFR by conventional hydrogen bonds and with Asp831 and Asp813 amino acids by attractive charge interactions. Furthermore, $[\text{Ni}(\text{L}^2\text{H})_2]$ formed three conventional hydrogen bonds with Ala244, Arg217 and Leu202 amino acids, four carbon-hydrogen bonds with Arg217, Trp243, Arg217 and Val251 amino acids, one pi-donor hydrogen bond with Gln246, one pi-cation and one pi-alkyl with Arg200 amino acid of CDK2.

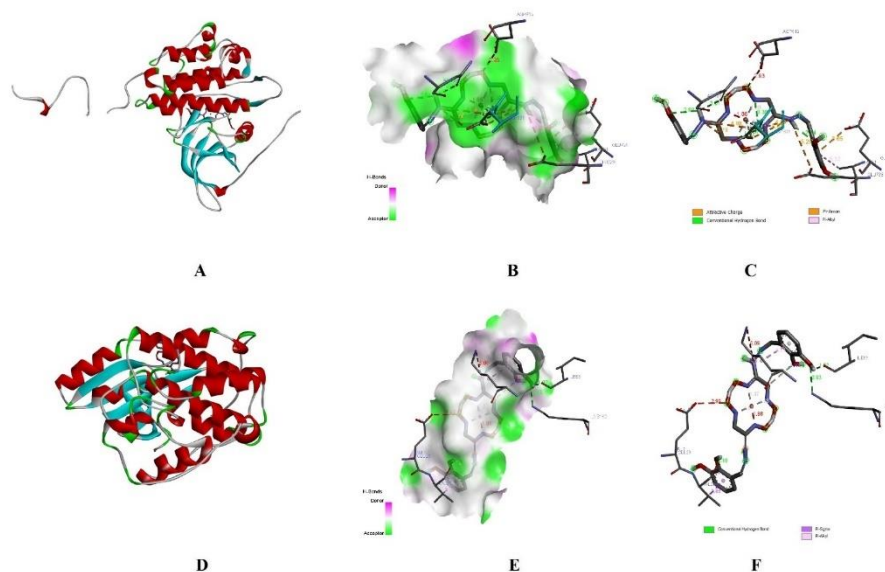


Figure 10. A, D) 3D diagram, B, E) 2D diagram,
C, F) Hydrogen bonding interactions of $[\text{Cu}(\text{L}^2\text{H})_2]$ with EGFR and CDK2, respectively

The interactions between $[\text{Cu}(\text{L}^2\text{H})_2]$ and EGFR were presented in Figure 10A-C. $[\text{Cu}(\text{L}^2\text{H})_2]$ was observed to form conventional hydrogen bonds three with Asp831 and one with Asn818 amino acids. Also, there were four attractive charge interactions with Asp831, one attractive charge interaction with Glu738, two metal acceptor interactions with Asp831, one pi-anion interaction with Glu734 and one pi-alkyl interaction with

Ala731 occurred. Moreover, $[\text{Cu}(\text{L}^2\text{H})_2]$ formed three conventional hydrogen bonds with Lys142, Val29 and Ile63 amino acids of CDK2, one pi-sigma interaction with Val29 and one pi-alkyl interaction with Lys65 amino acids (Figure 10D-F).

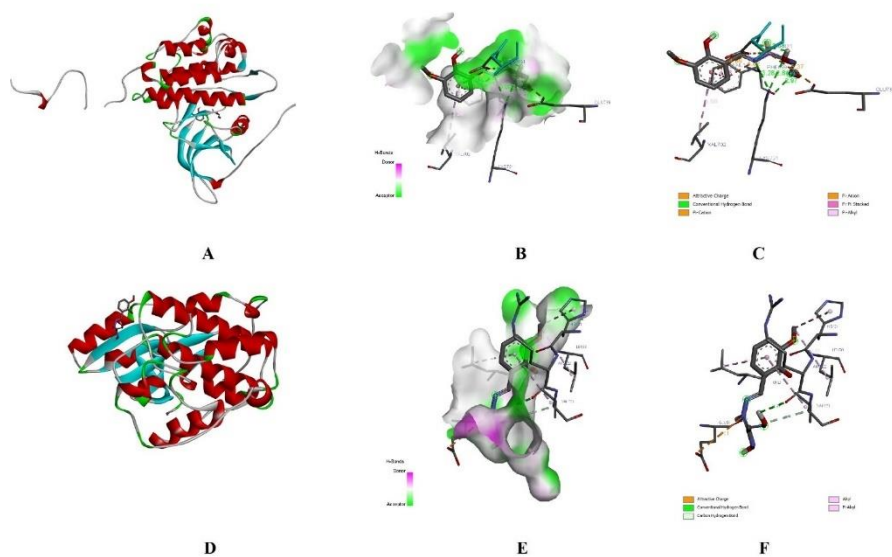


Figure 11. A, D) 3D diagram, B, E) 2D diagram, C, F) Hydrogen bonding interactions of L^3H_2 with EGFR and CDK2, respectively

L^3H_2 formed one conventional hydrogen bond with Lys721 and Phe699 and two with Asp831. In addition, L^3H_2 interacted with Phe699 via pi-cation and pi-pi stacked interactions. It had pi-anion interaction with Asp831 and pi-alkyl interaction with Val702 amino acids (Figure 11A-C). Furthermore, there occurred conventional hydrogen bonds between L^3H_2 and Glu51, Arg122, Leu54 amino acids of CDK2 protein and one carbon-hydrogen bond with Val123, one alkyl interaction with Leu58, one attractive charge interaction with Glu51 and one pi-alkyl interaction with His121, Leu54 and Val123 amino acids (Figure 11D-F).

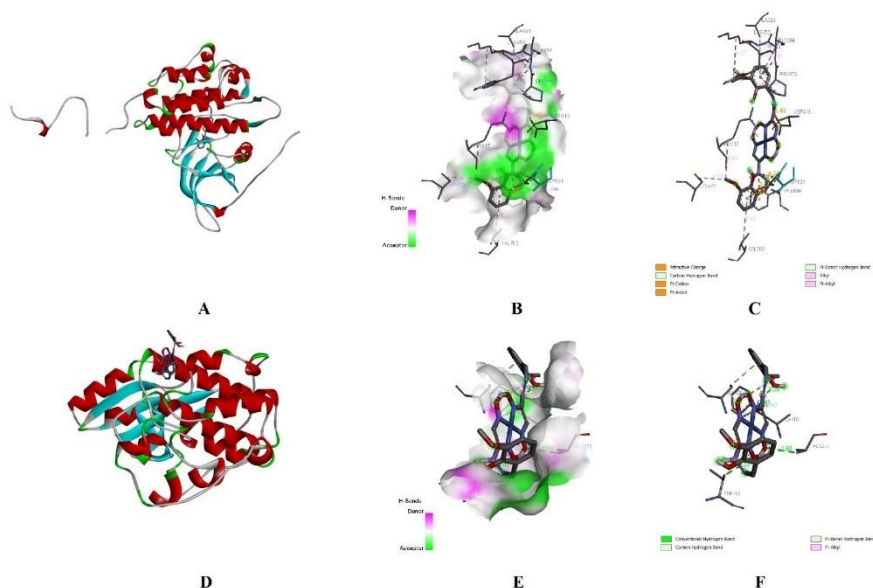


Figure 12. A, D) 3D diagram, B, E) 2D diagram, C, F) Hydrogen bonding interactions of $[\text{Ni}(\text{L}^3\text{H})_2]$ with EGFR and CDK2, respectively

$[\text{Ni}(\text{L}^3\text{H})_2]$ had one carbon-hydrogen bond with Asp831 and pi-donor hydrogen bond with Ile854 amino acids of EGFR. Also, it had alkyl interactions with Cys773, Arg817, Lys855 amino acids, pi-alkyl interactions with Trp856, Val702, Pro853, Ile854, Ala896 amino acids, attractive charge interactions with Asp831 and Asp813 amino acids of EGFR (Figure 12A-C). Furthermore, it formed conventional hydrogen bonds with Thr182, Ala277 and Ala116, carbon-hydrogen bond with Phe117, pi-donor hydrogen bond with Ser120 and pi-alkyl interaction with Phe117 amino acids of CDK2 target protein (Figure 12D-F).

In Figure 13 there were presented the interactions between $[\text{Cu}(\text{L}^3\text{H})_2]$ and target proteins EGFR and CDK2. Conventional hydrogen bonds were formed with Lys721 and Phe699 amino acids of EGFR. Also, there were one attractive charge interaction with Glu734, two pi-anion interactions with Asp831, one pi-pi stacked interaction with Phe699, one alkyl interaction with Arg724 and pi-alkyl interactions with Ala698 and Arg724 amino acids occurred. Moreover, there were formed conventional hydrogen bonds with Ser261, Gln265, Glu257 and His 283 amino acids, carbon-hydrogen bonds with Ser261 and Gln265 amino acids, alkyl interaction with Ile275, pi-alkyl interaction with Pro284 and attractive charge interaction with Glu257.

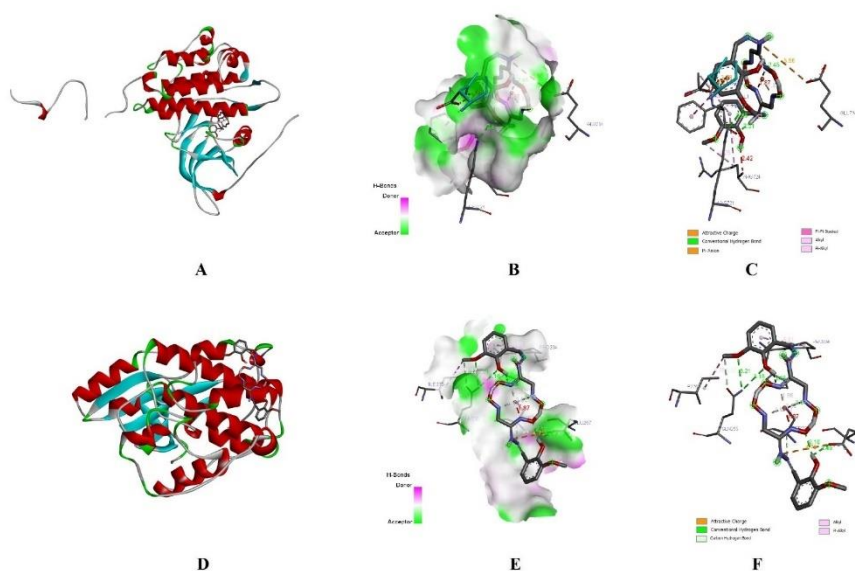


Figure 13. A, D) 3D diagram, B, E) 2D diagram, C, F) Hydrogen bonding interactions of $[\text{Cu}(\text{L}^3\text{H})_2]$ with EGFR and CDK2, respectively

3.3. Ligand Bioactivity

The bioactivity parameters LE and FQ results were given in Table 3 in detail. For approving the compound as a hit one, it must provide the conditions $LE \geq 0.3$, $FQ \geq 0.8$ (Sulaiman et al., 2019). $[\text{Ni}(\text{L}^2\text{H})_2]$ and $[\text{Cu}(\text{L}^2\text{H})_2]$ complexes with EGFR had the highest LE and FQ values and these were found to be in the recommended range. Furthermore, $[\text{Cu}(\text{L}^3\text{H})_2]$ had an acceptable FQ value however its LE value was out of range. The results confirm the binding energy results where $[\text{Ni}(\text{L}^2\text{H})_2]$, $[\text{Cu}(\text{L}^2\text{H})_2]$ and $[\text{Cu}(\text{L}^3\text{H})_2]$ had the highest binding scores against EGFR target protein.

Table 3. Bioactivity results of L^1H_2 , L^2H_2 , L^3H_2 ligands and their Ni^{II} and Cu^{II} metal complexes

Protein	Compound	Ligand Efficiency	LE scale	Fit Quality
EGFR	L^1H_2	0.400	0.512	0.781
	$[Ni(L^1H)_2]$	0.227	0.306	0.743
	$[Cu(L^1H)_2]$	0.212	0.306	0.693
	L^2H_2	0.376	0.497	0.757
	$[Ni(L^2H)_2]$	0.337	0.288	1.170
	$[Cu(L^2H)_2]$	0.354	0.288	1.229
	L^3H_2	0.350	0.483	0.725
	$[Ni(L^3H)_2]$	0.208	0.270	0.771
	$[Cu(L^3H)_2]$	0.222	0.270	0.821
CDK2	L^1H_2	0.325	0.512	0.635
	$[Ni(L^1H)_2]$	0.218	0.306	0.713
	$[Cu(L^1H)_2]$	0.233	0.306	0.763
	L^2H_2	0.324	0.497	0.651
	$[Ni(L^2H)_2]$	0.206	0.288	0.714
	$[Cu(L^2H)_2]$	0.217	0.288	0.754
	L^3H_2	0.317	0.483	0.656
	$[Ni(L^3H)_2]$	0.192	0.270	0.711
	$[Cu(L^3H)_2]$	0.176	0.270	0.651

3.4. Quantum Chemical Descriptors

ΔE_{gap} value specifies the conditions of the reactions. The kinetic stability of a molecule was determined by a high ΔE_{gap} value (Ferdous & Kawsar, 2020). In this case, the molecule is desperate to get more energy for jumping from the ground state to the excited one. The highest ΔE_{gap} value was found to belong to L^2H_2 and the lowest was the value of $[Cu(L^2H)_2]$ complex (Table 4). Furthermore, the lowest global hardness (η) and the highest global softness (σ) are related to the lowest ΔE_{gap} value (Allal et al., 2018). In our study, $[Cu(L^2H)_2]$ had the lowest η and the highest σ value when compared to other compounds. Besides, a high ω value corresponds to having a good electrophile property for a molecule (Rupa et al., 2022) where $[Cu(L^2H)_2]$ had the highest ω value in our study. Thus $[Cu(L^2H)_2]$ had a potent and sufficient electrophile ability (acceptor) among other compounds.

Table 4. Quantum chemical calculation results

Compounds	E_{HOMO} (eV)	E_{LUMO} (eV)	ΔE_{gap} (eV)	χ	π	η	σ	ω
L^1H_2	-0.209	0.399	0.608	-0.095	0.095	0.304	3.290	0.015
$[Ni(L^1H)_2]$	-0.273	-0.211	0.062	0.242	-0.242	0.031	32.363	0.945
$[Cu(L^1H)_2]$	-0.210	-0.201	0.009	0.205	-0.205	0.004	243.902	5.145
L^2H_2	-0.292	0.328	0.620	-0.177	0.018	0.310	3.231	0.001
$[Ni(L^2H)_2]$	-0.274	-0.212	0.062	0.243	-0.243	0.031	32.258	0.949
$[Cu(L^2H)_2]$	-0.208	-0.200	0.008	0.204	-0.204	0.004	250.000	5.202
L^3H_2	-0.222	0.380	0.602	-0.079	0.079	0.301	3.323	0.010
$[Ni(L^3H)_2]$	-0.272	-0.209	0.064	0.240	-0.240	0.032	31.104	0.898
$[Cu(L^3H)_2]$	-0.209	-0.198	0.010	0.204	-0.204	0.005	194.175	4.023

4. CONCLUSION

Molecular docking, bioactivity and quantum chemical properties of vic-Dioxim derivatives bearing hydrazone group and their Ni^{II} and Cu^{II} complexes were analysed. Ni^{II} and Cu^{II} complexes of the L¹H₂, L²H₂ and L³H₂ ligands showed higher binding affinity to EGFR and CDK2. Especially, [Cu(L¹H)₂] and [Cu(L²H)₂] complexes can be suggested as hit compounds against CDK2 and EGFR, respectively. These were supported by the inhibition constant values which were the lowest when compared to others. L¹H₂, L²H₂ and L³H₂ ligands had the lowest binding energy values when compared to metal complexes. Also, [Cu(L²H)₂] complex had a high binding energy value against EGFR. [Ni(L²H)₂] and [Cu(L²H)₂] complexes with EGFR had the highest LE and FQ values. Furthermore, [Cu(L²H)₂] had a potent and sufficient electrophile ability (acceptor) among other compounds. Therefore, these compounds may be suitable compounds for further analysis in anti-cancer drug development with low toxic and targeted properties.

ACKNOWLEDGEMENT

The authors received no financial support for this study.

CONFLICT OF INTEREST

The authors declare no conflict of interest.

REFERENCES

- Accelrys. (2014). Discovery Studio Visualizer Software. San Diego, CA: Accelrys.
- Allal, H., Belhocine, Y., & Zouaoui, E. (2018). Computational study of some thiophene derivatives as aluminum corrosion inhibitors. *Journal of Molecular Liquids*, 265, 668-678. doi:[10.1016/j.molliq.2018.05.099](https://doi.org/10.1016/j.molliq.2018.05.099)
- Altamimi, A. S., El-Azab, A. S., Abdelhamid, S. G., Alamri, M. A., Bayoumi, A. H., Alqahtani, S. M., Alabbas, A. B., Altharawi, A. I., Alossaimi, M. A., & Mohamed, M. A. (2021). Synthesis, Anticancer Screening of Some Novel Trimethoxy Quinazolines and VEGFR2, EGFR Tyrosine Kinase Inhibitors Assay; Molecular Docking Studies. *Molecules*, 26, 2992. doi:[10.3390/molecules26102992](https://doi.org/10.3390/molecules26102992)
- Canpolat, E., & Kaya, M. (2005). Synthesis and formation of a new vic-dioxime complexes. *Journal of Coordination Chemistry*, 58(14), 1217-1224. doi:[10.1080/00958970500130501](https://doi.org/10.1080/00958970500130501)
- DeLano, W. L. (2013). The PyMOL Molecular Graphics System. San Carlos, CA: DeLano Scientific LLC. [URL](http://www.pymol.org/)
- Ferdous, J., & Kawsar, S. M. A. (2020). Thermochemical, Molecular Docking and ADMET Studies of Some Methyl α -D-Glucopyranoside Derivatives. *The Chittagong University Journal of Science*, 42(1), 58-83. doi:[10.3329/cuj.s.v42i1.54238](https://doi.org/10.3329/cuj.s.v42i1.54238)
- Fouad, R., & Adly, O. M. I. (2021). Novel Cu²⁺ and Zn²⁺ nanocomplexes drug based on hydrazone ligand bearings chromone and triazine moieties: Structural, spectral, DFT, molecular docking and cytotoxic studies. *Journal of Molecular Structure*, 1225, 129158. doi:[10.1016/j.molstruc.2020.129158](https://doi.org/10.1016/j.molstruc.2020.129158)
- Haider, K., Rehman, S., Pathak, A., Najmi, A. K., & Yar, M. S. (2021). Advances in 2-substituted benzothiazole scaffold-based chemotherapeutic agents. *Archiv der Pharmazie*, 354(12), e2100246. doi:[10.1002/ardp.202100246](https://doi.org/10.1002/ardp.202100246)
- Horchani, M., Della Sala, G., Caso, A., D'Aria, F., Esposito, G., Laurenzana, I., Giancola, C., Costantino, V., Jannet, H. B., & Romdhane, A. (2021). Molecular Docking and Biophysical Studies for Antiproliferative Assessment of Synthetic Pyrazolo-Pyrimidinones Tethered with Hydrazone-Hydrazones. *International Journal of Molecular Sciences*, 22, 2742. doi:[10.3390/ijms22052742](https://doi.org/10.3390/ijms22052742)
- Knizia, G. (2022) IboView, Version 20150427, <http://www.iboview.org>, Accessed: 18/072022
- Koopmans, T. (1934). Über die Zuordnung von Wellenfunktionen und Eigenwerten zu den einzelnen Elektronen eines Atoms. *Physica*, 1(1-6), 104–113. doi:[10.1016/S0031-8914\(34\)90011-2](https://doi.org/10.1016/S0031-8914(34)90011-2)

- Kurtoglu, M., & Baydemir, S.A. (2007). Studies on Mononuclear Transition Metal Chelates Derived from a Novel (E, E)-Dioxime: Synthesis, Characterization and Biological Activity. *Journal of Coordination Chemistry*, 60(6), 655-665. doi:[10.1080/00958970600896076](https://doi.org/10.1080/00958970600896076)
- Park, H.-J., Lee, K., Park, S.-J., Ahn, B., Lee, J.-C., Cho, H., & Lee, K.-I. (2005). Identification of Antitumor Activity of Pyrazole Oxime Ethers. *Bioorganic and Medicinal Chemistry Letters*, 15(13), 3307-3312. doi:[10.1016/j.bmcl.2005.03.082](https://doi.org/10.1016/j.bmcl.2005.03.082)
- Rija, A., Bulhac, I., Coropceanu, E., Gorincioi, E., Calmîc, E., Barba, A., & Bologa, O. (2011). Synthesis and Spectroscopic Study of some Coordinative Compounds of Co(III), Ni(II) and Cu(II) with Dianiline- and Disulfanilamideglyoxime. *Chemistry Journal of Moldova*, 6(2), 73-78. doi:[10.19261/cjm.2011.06\(2\).16](https://doi.org/10.19261/cjm.2011.06(2).16)
- Rupa, S. A., Moni, M. R., Patwary, M. A. M., Mahmud, M. M., Haque, M. A., Uddin, J., & Abedin, S. M. T. (2022). Synthesis of Novel Tritopic Hydrazone Ligands: Spectroscopy, Biological Activity, DFT, and Molecular Docking Studies. *Molecules*, 27(5), 1656. doi:[10.3390/molecules27051656](https://doi.org/10.3390/molecules27051656)
- Sarikavakli, N., & Irez, G. (2005). Synthesis and Complex Formation of Some Novel vicDioxime Derivatives of Hydrazones. *Turkish Journal of Chemistry*, 29(1), 107-116.
- Sarikavakli, N., & Cakici, H. T. (2012). Synthesis and Characterization of Novel (Z, E)-vic-dioximes and their Transition Metal Complexes. *Asian Journal of Chemistry*, 24(3), 2643.
- Serin, S. (2001). New vic-dioxide transition metal complexes. *Transition Metal Chemistry*, 26(3), 300-306. doi:[10.1023/A:1007163418687](https://doi.org/10.1023/A:1007163418687)
- Smith, A. G., Tasker, P. A., & White, D. J. (2003). The Structures of Phenolic Oximes and their Complexes. *Coordination Chemistry Reviews*, 241(1-2), 61-85. doi:[10.1016/S0010-8545\(02\)00310-7](https://doi.org/10.1016/S0010-8545(02)00310-7)
- Soga, S., Sharma, S., Shiotsu, Y., Shimizu, M., Tahara, H., Yamaguchi, K., Ikuina, Y., Murakata, C., Tamaoki, T., Kurebayashi, J., Schulte, T., Neckers L., & Akinaga, S. (2001). Stereospecific Antitumor Activity of Radicoloxime Derivatives. *Cancer Chemotherapy Pharmacology*, 48(6), 435-445. doi:[10.1007/s002800100373](https://doi.org/10.1007/s002800100373)
- Sulaiman, K. O., Kolapo, T. U., Onawole, A. T., Islam, A., Adegoke, R. O., & Badmus, S. O. (2019). Molecular dynamics and combined docking studies for the identification of Zaire ebola virus inhibitors. *Journal of Biomolecular Structure and Dynamics*, 37(12), 3029-3040. doi:[10.1080/07391102.2018.1506362](https://doi.org/10.1080/07391102.2018.1506362)
- Trott, O., & Olson, A. J. (2009). AutoDock Vina: Improving the speed and accuracy of docking with a new scoring function, efficient optimization, and multithreading. *The Journal of Computational Chemistry*, 31, 455-461. doi:[10.1002/jcc.21334](https://doi.org/10.1002/jcc.21334)
- Tschugaeff, L. (1907). Über eine neue synthese der α -diketone. *European Journal of Inorganic Chemistry*. 40(1), 186-187. doi:[10.1002/cber.19070400127](https://doi.org/10.1002/cber.19070400127)





Gazi University

Journal of Science

PART A: ENGINEERING AND INNOVATION

<http://dergipark.org.tr/gujsa>

Evaluation of Electromagnetic Field Levels and Student Exposure at Aydın Adnan Menderes University Central Campus

Şerife Gökçe ÇALIŞKAN¹ , Mahmut Alp KILIÇ² , Didem BAKAY İLHAN³ , Mehran AKSEL⁴ , Onur GENÇ⁵ , Mehmet Dinçer BİLGİN^{6*} 

¹Aydın Adnan Menderes University, Faculty of Sciences and Arts, Department of Physics, Aydın, TURKIYE

²Aydın Adnan Menderes University, Faculty of Medicine, Department of Biophysics, Aydın, TURKIYE

³Aydın Adnan Menderes University, Faculty of Medicine, Department of Biophysics, Aydın, TURKIYE

⁴Aydın Adnan Menderes University, Faculty of Medicine, Department of Biophysics, Aydın, TURKIYE

⁵Aydın Adnan Menderes University, Faculty of Sciences and Arts, Department of Physics, Aydın, TURKIYE

⁶Aydın Adnan Menderes University, Faculty of Medicine, Department of Biophysics, Aydın, TURKIYE

Keywords	Abstract
Extremely Low-Frequency Electromagnetic Field Awareness ADU Central Campus Exposure	With the effect of developing technology, humanity is constantly exposed to more electromagnetic fields. Regional studies are gaining importance for determining the possible problems. In this study, extremely low-frequency electromagnetic field (ELF-EMF) measurements were carried out in Aydın Adnan Menderes University Central Campus in areas where university students are frequently found, at 25 randomly selected points, in the region where high voltage lines pass and around transformers, and to evaluate the awareness of university students about the ELF-EMF they are exposed to. For this purpose, the necessary magnetic field and electric field strength measurements were made and a questionnaire was applied to determine the awareness level of the students. Results were evaluated by comparing them with the ICNIRP limit values. Accordingly, it has been concluded that Aydın Adnan Menderes University Central Campus can be accepted as a relatively safe area since electromagnetic field exposure values are within the ICNIRP safe limit values. In addition, as a result of the questionnaire, it was determined that the young people were conscious to a certain extent about ELF-EMF, but they did not pay attention to protect themselves against the possible effects of ELF-EMF. It is important to make the necessary initiatives in order to raise awareness of young people on this issue.

Cite

Caliskan, S. G., Kilic, M. A., Bakay Ilhan, D., Aksel, M., Genc, O., & Bilgin, M. D. (2022). Evaluation of Electromagnetic Field Levels and Student Exposure at Aydın Adnan Menderes University Central Campus. *GU J Sci, Part A, 9(3)*, 314-322.

Author ID (ORCID Number)	Article Process
Ş. G. Çalışkan, 0000-0001-5421-3472	Submission Date 04.08.2022
M. A. Kılıç, 0000-0003-2645-1988	Revision Date 15.08.2022
D. Bakay İlhan, 0000-0001-8306-1308	Accepted Date 15.08.2022
M. Aksel., 0000-0002-3942-2257	Published Date 29.09.2022
O. Genç, 0000-0002-9061-7519	
M. D. Bilgin, 0000-0003-0754-0854	

1. INTRODUCTION

Radiation is electromagnetic wave (EMW) propagation and is associated with a center, radial direction with respect to the source. EMW is nothing but visible or invisible light according to its frequency and hence energy. In this respect, the speed of EMW in vacuum is 300000km per second (SI unit system). While anything with a temperature above zero degrees Kelvin (absolute zero) emits radiation and EMW, this can be for example infrared emission, radio wave emission, or nuclear radiation, depending on the energy of the emitted EMW. On the other hand, EMW is a wave with an electric and magnetic component. Electric field and magnetic field are transverse waves in terms of propagation direction and oscillation direction, oscillating in directions perpendicular to the EMW's propagation direction and to each other. When EMWs come together, electromagnetic field (EMF) is formed. Ionizing and non-ionizing radiation are the types of radiation. This distinction is made according to whether they have quanta carrying energy to ionize atoms or molecules (Umaç,

*Corresponding Author, e-mail: mdbilgin@adu.edu.tr

2019). While non-ionizing radiation does not create charged ions in the material it passes through, ionizing radiation with higher frequency and shorter wavelength can pose a serious threat to health.

The presence of EMF in our environment is inevitable, and with the rapid development of technology and the increase in the place of devices that make life easier, we are exposed to EMF at a high rate. Non-ionizing radiation includes two types due to the frequency components they contain: extremely low-frequency EMF (ELF-EMF) and radio frequency magnetic fields (RF-MF) (Alkayyali et al., 2021). Energy transmission lines (high voltage lines and transformers) and household electrical appliances (refrigerator, vacuum cleaner, hair dryer, iron, electric blanket, computer, etc.) are sources of ELF-EMF (Evcı et al., 2007). RF-MF is produced by base stations, cellular phones and radio-television transmitters. The effects of both types of EMF on human health have been reported (Gupta et al., 2022). Changes in nervous system activity, neurotransmitter release disorders, and functional changes in balance and learning are common examples of these effects (Kivrak et al., 2017).

The limit values for the possible effects of EMF on human health have been determined (Table 1) and accepted by the Commission on Non-Ionizing Radiation Protection (ICNIRP), which is also accepted by the World Health Organization (ICNIRP, 2002). Accordingly, the electric field strength limit value for high voltage lines and transformers is 5000V/m and the magnetic field strength limit value is 80A/m, which corresponds to approximately 1G. Electric field and magnetic field values decrease with distance from the ELF-EMF source (Raj et al., 2020). Therefore, it is accepted that being close to ELF-EMF sources will increase the health risk, and distance is considered an important variable in addition to the exposure level.

Table 1. The frequency-dependent limit values of ICNIRP

Frequency (f) Range	Electric Field Strength (V/m)	Magnetic Field Strength (µT)
Up to 1 Hz	-	4×10^4
1-8 Hz	10.000	$4 \times 10^4/f^2$
8-25 Hz	10.000	$5.000/f$
0.025-0.8 kHz	$250/f$	$5/f$
0.8-3kHz	$250/f$	6.25
3-150 kHz	87	6.25
0.15-1 MHz	87	$0.92/f$
1-10 MHz	$87/f^{1/2}$	$0.92/f$
10-400 MHz	28	0.092
400-2000 MHz	$1.375f^{1/2}$	$0.0046 \times f^{1/2}$
2-300 GHz	61	0.20

ELF-EMF was classified in the 2B category, which means "possibly carcinogenic" for humans, in accordance with the "precautionary principle" by the International Cancer Research Center (IARC) in 2002 (IARC, 2002). Although some epidemiological studies describe a relationship between various types of cancer and the use of ELF-EMF sources, there are also studies reporting opposite results (Franke et al., 2005; Kuribayashi et al., 2005; Barati et al., 2020). The main reason for these differences is the differences in electromagnetic field exposure times and control methods in these studies. For these reasons, the possible effects of electromagnetic field exposure on humans are one of the current problems that are still intensively researched and discussed today. In addition, symptoms such as psychological disorders (such as headaches, depression, etc.), immune system disorders, and effects due to decreased melatonin levels (such as sleep disorders) are also encountered due to exposure to ELF-EMF (Bolte et al., 2015). Considering such possible adverse effects, it is inevitable to locate EMF emitting devices and sources as far away from living areas as possible and to raise awareness about the electrical devices used.

The aim of the study was to perform ELF-EMF measurements in Aydın Adnan Menderes University Central Campus in areas where university students are frequent, at 25 randomly selected points, in the region where high voltage lines pass and around transformers, and to evaluate the awareness of university students about ELF-EMF they are exposed to.

2. MATERIAL AND METHOD

2.1. ELF-EMF Measurements

There are approximately 25000 students, 1500 personnel and more than 100 faculties, institutes, libraries, research hospitals, dormitories, rectorate, kindergartens, social facilities, mosques and shopping centers in Aydın Adnan Menderes University Central campus. In this study, electromagnetic field strength measurements were carried out at 25 randomly selected points in Aydın Adnan Menderes Central Campus and in areas where students are frequently found (classrooms, canteen, etc.) for 7 days in the morning and evening.

Magnetic field strength values were measured with Sypris gaussmeter (USA) and electric field strength values were measured with Narda EMR-300 (Germany) non-ionizing radiation meter. In addition, measurements were made in the areas under the energy transmission lines passing through the northern border of the campus and at a distance of 5 m from both sides, and around the transformers in the campus.

The measurements were made with Narda EMR-300 device and electric field probe in the 100 kHz-3 GHz frequency band in accordance with the regulation "Determination, measurement methods and inspection of limit values of electromagnetic field intensity originating from fixed telecommunication devices operating in the 10 kHz-60 GHz frequency band" (Official newspaper 12.07.2001). The data obtained were compared with the limit values announced by the international commission on non-ionizing radiation protection (ICNIRP).

2.2. Survey Study

Within the scope of our study, a questionnaire containing 25 questions was applied to 922 students studying at Aydın Adnan Menderes University Faculty of Medicine and Aydın Vocational School of Health. This application was carried out between May 2013 and March 2016. The age of the participants ranges between 19 and 25, with 57.5% female and 42.5% male. Before the study, the students were informed about the questionnaire. While no questions were asked about the identity of the students in the questionnaire, their personal information such as age, gender, which school they attended, which class they were in, were evaluated with 5 questions and their knowledge levels about ELF-EMF and energy transmission lines were evaluated with 20 questions. The study was approved by the Aydın Adnan Menderes University Ethics Committee at its meeting dated 22.05.2014 (Protocol no: 2014/370) and was carried out in accordance with the Declaration of Helsinki.

2.3. Statistical Analysis

All data obtained were analyzed using SPSS v.17.0. Survey data are expressed in percentiles of the participants. Measurements made at Adnan Menderes University Central Campus are given as arithmetic mean \pm standard error. $P \leq 0.05$ was considered statistically significant.

3. RESULTS AND DISCUSSION

3.1. ELF-EMF Measurement Results

Magnetic field and electric field measurements were made in 3 different areas (D1, D2, D3) where students are frequently found in Aydın Adnan Menderes University Central Campus (Figure 1). Accordingly, the magnetic field value was measured as 0.087 ± 0.015 mG on average, and the electric field strength value was measured as 0.037 ± 0.006 V/m on average. The magnetic field and electric field strength values measured at each point are given in Table 2 in detail. In addition, the average magnetic field value at 25 randomly selected points in the campus area was determined as 0.091 ± 0.011 mG and the electric field strength value as 0.461 ± 0.011 V/m. Table 2 shows the magnetic field and electric field strength values measured at these points.

In addition to these measurements, measurements were taken from 3 different points (Y1, Y2, Y3) under the energy transmission lines passing through the northern border of the Central Campus. Accordingly, the mean magnetic field values at the zero point are 5.56±0.12 mG in Y1, 8.90±0.14 mG in Y2 and 7.40±0.17 mG in Y3, 5.34±0.11 mG for Y1, 7.61±0.09 mG for Y2, 4.43±40 for Y3 at 5m right. 0.13 mG was determined as 6.44±0.11 mG for Y2 and 4.89±0.22 mG for Y3 (Figure 2).

The mean magnetic field values measured from the front of the transformers (from 0 meters) shown in Figure 1 as T1, T2 and T3 were determined as 7.34±1.12 mG at T1, 5.64±0.75 mG at T2 and 4.30±0.78 mG at T3. Similarly, the average magnetic field values measured from 5 meters away from the transformer building were determined as 5.90±0.99 mG at T1, 5.11±0.66 mG at T2 and 3.37±0.67 mG at T3 (Figure 3).

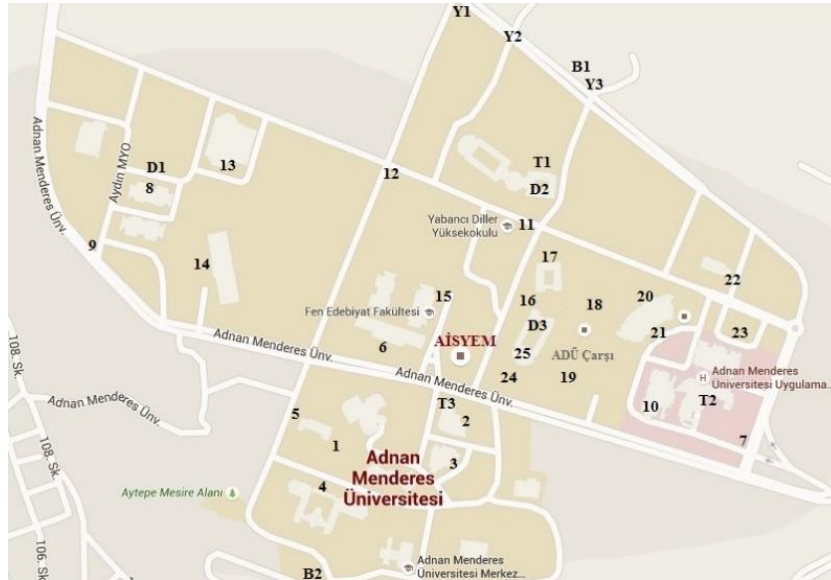


Figure 1. Measurement points in Adnan Menderes University Central Campus

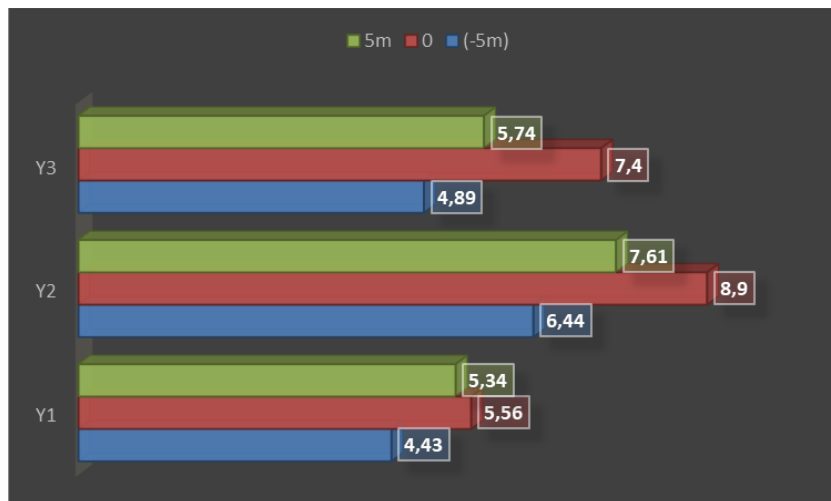


Figure 2. Magnetic field values (mG) measured at -5m, 0 and 5m distances from three different energy transmission line points

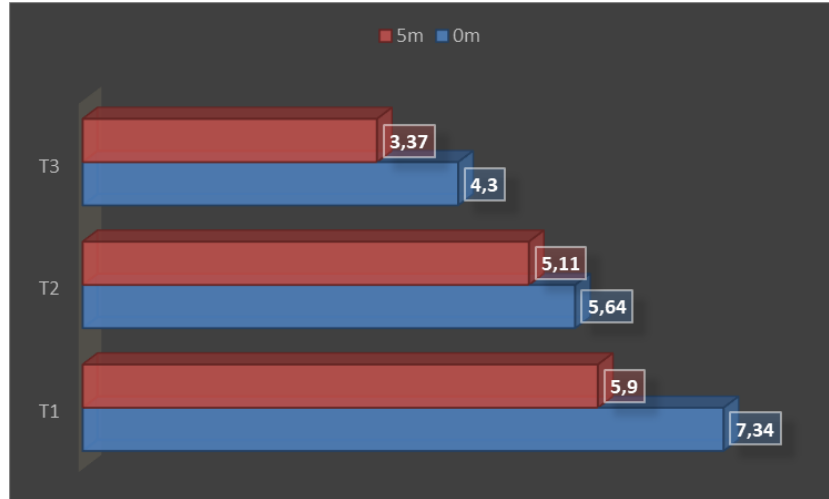


Figure 3. Magnetic field values (mG) measured at 0 and 5m distances from three different transformer points

Table 2. Magnetic field and electric field strength mean values

Measurement Point	E (V/m)	B (mG)
D1	0.08	0.26
D2	0.00	0.00
D3	0.03	0.00
1	0.11	0.17
2	0.12	0.13
3	0.14	0.23
4	0.07	0.14
5	0.14	0.09
6	0.15	0.10
7	0.15	0.14
8	0.20	0.16
9	0.17	0.20
10	0.13	0.30
11	0.27	0.00
12	1.08	0.00
13	0.27	0.00
14	0.33	0.00
15	0.08	0.03
16	0.23	0.03
17	2.41	0.07
18	1.34	0.00
19	1.53	0.00
20	1.16	0.00
21	0.21	0.13
22	0.23	0.13
23	0.48	0.13
24	0.18	0.03
25	0.35	0.07

3.2. Survey Study Results

21% of the medical faculty and Health Vocational School students correctly stated that X-rays are not an example of non-ionizing radiation, while the others gave different answers and this shows that the students do not fully comprehend the electromagnetic spectrum. While 75% of the students stated that electrical devices create both electric and magnetic fields, the percentage of students who have no idea about the subject was found to be 7 (Figure 4). In addition, 46% of the students have more than one electrical device (TV, radio, alarm clock, etc.) in their bedrooms, while 38% do not have any electrical devices (Figure 5).

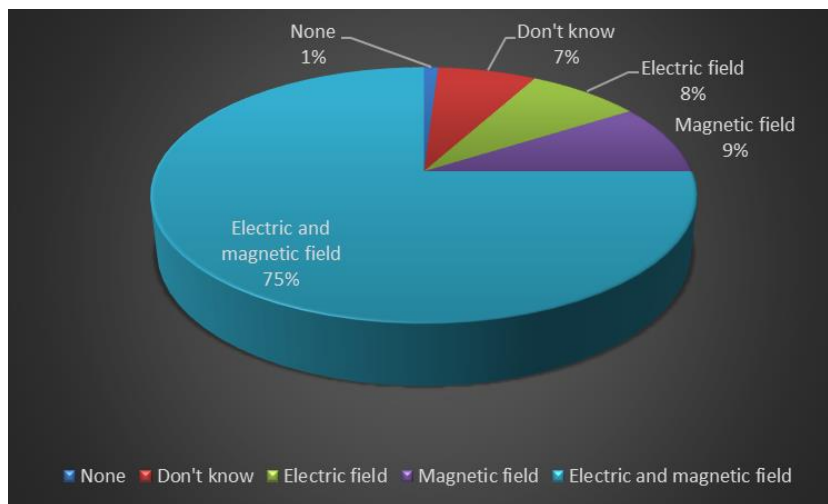


Figure 4. Participants' "What happens when appliances at home are working?" distribution of answers to the question

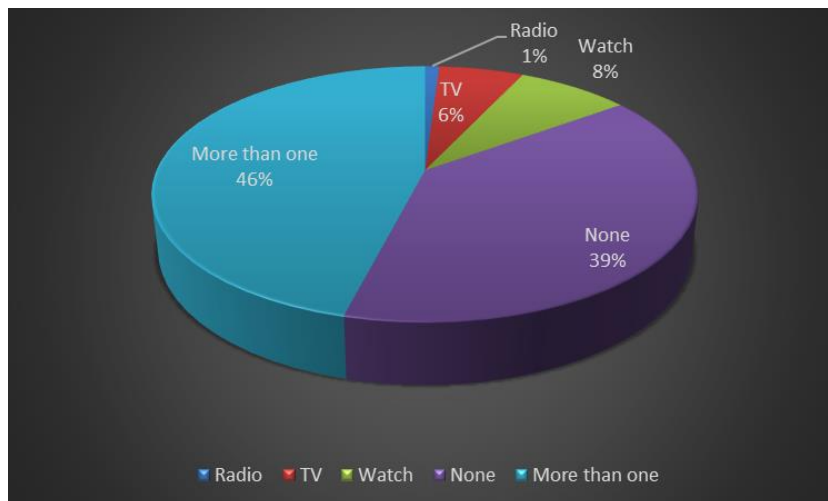


Figure 5. Percentage of electrical devices in the bedrooms of the participants

56.4% of the students stated that they spend 1-8 hours a day, 14% 8-12 hours a day, and 12% more than 12 hours a day in front of electrical devices such as computers, TVs and radios. In addition, 42% of these students spend 1-3 hours a day, 21% spend 3-8 hours, and 3% spend more than 8 hours a day just in front of the computer (Figure 6). While 61% of our students do not play computer games, 23% play computer games for a few hours every week, 9% for a few hours every day and 7% for more than 3 hours every day. While 35% of the students stated that they never used a hair dryer, 36% stated that they used a hair dryer at least twice a week, 22% at least 7 times a week, and 7.2% more than 7 times a week. The duration of using the hair dryer was 5 minutes or less in 36% of the students, between 5 and 10 minutes in 24% and more than 10 minutes in 7% of the students.

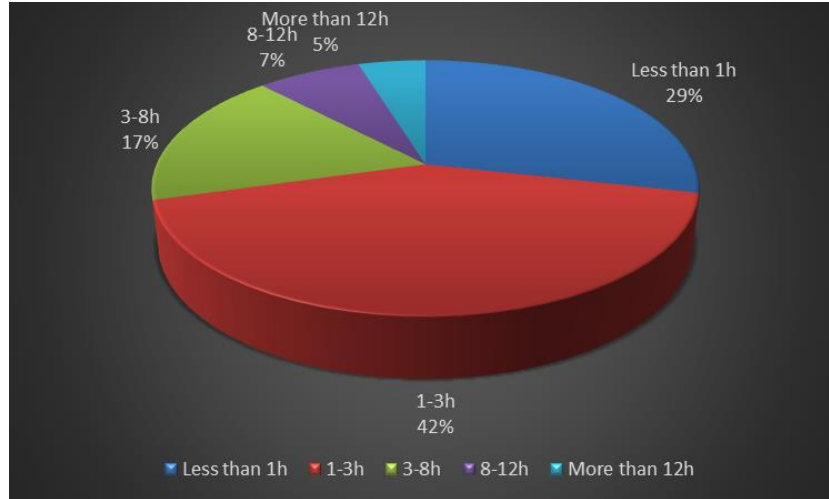


Figure 6. Percentages of time spent in front of the computer

While 64% of the students stated that they did not know how close they lived to the high voltage lines, 5% of them stated that they lived closer than 20m, 11% of them 20-100m away, and 22% more than 100m away (Figure 7). Similarly, 59% of the students stated that they did not know the distance of their houses to the transformers, while 7% reported that they were closer than 20m, 17% were 20 -100m away, and 18% were more than 100m away. 91% of the students stated that high voltage lines are associated with cancer.

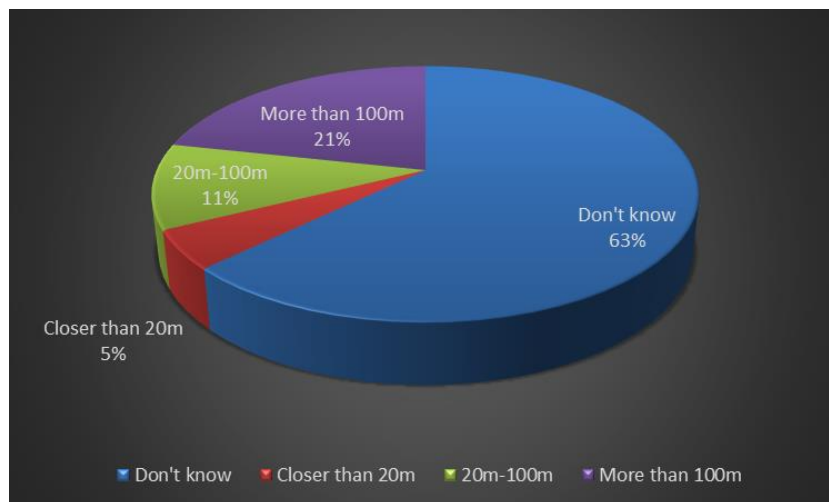


Figure 7. Distribution of students' answers to the question of how far they live from the high voltage line

4. CONCLUSION

Today, with the advancement of technology, there is an increasing demand for novel devices. EMF is created by several systems such that base stations, high voltage lines, radio/television broadcasts, wifi systems, etc. The signal strength and distance of electrical devices signify the intensity of EMFs. There is no information that ELF-EMF and RF-MF, which are non-ionizing radiation, directly damage DNA or cells (National Cancer Institute, 2019). However, although there is evidence that ELF-EMF has a negative effect on human health, the fact that the mechanism of action on living things has not been clearly revealed makes the results of laboratory studies open to discussion (Repacholi., 2012).

As seen in Figure 1 in Aydın Adnan Menderes University Central Campus, the magnetic field and electric field strength values measured from different points were found below the limit values. The magnetic field values measured under and around the energy transmission lines passing through the northern border of the campus were also within the ICNIRP limit values, and the distance of the power transmission lines (at least 25 m) from the settlements is important in reducing the possible effects. Similarly, the magnetic field values

measured around the transformers are within normal limits, and since the transformers are at least 10 meters away from the buildings, the degree of the possible impact on human health is significantly reduced. Therefore, Aydın Adnan Menderes University can be considered a relatively safe area since electromagnetic field exposure values are within the ICNIRP safe limit values.

As a result of the survey application, it is understood that our students are conscious to a certain extent about what ELF-EMF is and its effects, but they do not pay attention to protect themselves against the possible effects of ELF-EMF. According to the "precautionary principle" determined by the World Health Organization, since it is not yet known exactly what kind of problems it may cause in the future, the severity of ELF-EMF should be kept as low as possible. Therefore, it is necessary to develop behavioral awareness and attitude for students who will work in the field of health when they graduate from the university, to protect themselves against the effects of ELF-EMF. Health personnel who implement the measures to protect against the effects of ELF-EMF can play a role in raising the awareness of society against ELF-EMF appropriately.

ACKNOWLEDGEMENT

We would like to thank the students at Aydın Adnan Menderes University Faculty of Medicine and Aydın Health Vocational School who contributed to the realization of the study.

CONFLICT OF INTEREST

The authors declare no conflict of interest.

REFERENCES

- Alkayyali, T., Ochuba, O., Srivastava, K., Sandhu, J. K., Joseph, C., Ruo, S. W., Jain, A., Waqar, A., & Poudel, S. (2021). An Exploration of the Effects of Radiofrequency Radiation Emitted by Mobile Phones and Extremely Low Frequency Radiation on Thyroid Hormones and Thyroid Gland Histopathology. *Cureus*, 13(8), e17329. doi:[10.7759/cureus.17329](https://doi.org/10.7759/cureus.17329)
- Barati, M., Fahimi, H., Farahmand, L., & Madjid Ansari, A. (2020). 1Hz 100mT Electromagnetic Field Induces Apoptosis in Breast Cancer Cells Through Up-Regulation of P38 and P21. *Multidisciplinary Cancer Investigation*, 4(1), 23-29. doi:[10.30699/acadpub.mci.4.1.23](https://doi.org/10.30699/acadpub.mci.4.1.23)
- Bolte, J. F. B., Baliatsas, C., Eikelboom, T., & van Kamp, I. (2015). Everyday exposure to power frequency magnetic fields and associations with non-specific physical symptoms. *Environmental Pollution*, 196, 224-229. doi:[10.1016/j.envpol.2014.10.011](https://doi.org/10.1016/j.envpol.2014.10.011)
- Evci, E. D., Bilgin, M. D., Akgör, Ş., Zencirci, Ş. G., Ergin, F., & Beşer, E. (2007). Measurement of selected indoor physical environmental factors in hairdresser salons in a Turkish City. *Environmental Monitoring and Assessment*, 134(1-3), 471-477. doi:[10.1007/s10661-007-9637-y](https://doi.org/10.1007/s10661-007-9637-y)
- Franke, H., Ringelstein, E. B., & Stögbauer, F. (2005). Electromagnetic Fields (GSM 1800) Do Not Alter Blood-Brain Barrier Permeability to Sucrose in Models in Vitro with High Barrier Tightness. *Bioelectromagnetics*, 26(7), 529-535. doi:[10.1002/bem.20123](https://doi.org/10.1002/bem.20123)
- Gupta, S., Sharma, R. S., & Singh, R. (2022). Non-ionizing radiation as possible carcinogen. *International Journal of Environmental Health Research*, 32(4), 916-940. doi:[10.1080/09603123.2020.1806212](https://doi.org/10.1080/09603123.2020.1806212)
- IARC. Working Group on the Evaluation of Carcinogenic Risks to Humans (2002). *Non-Ionizing Radiation, Part 1: Static and Extremely Low-Frequency (ELF) Electric and Magnetic Fields*. Lyon (FR): International Agency for Research on Cancer. (IARC Monographs on the Evaluation of Carcinogenic Risks to Humans, No. 80) (Accessed:17/07/2022) [URL](https://www.iarc.fr/page.do?pid=117&tid=527&cid=12345)
- ICNIRP. International Commission on Non-Ionizing Radiation Protection. (2002). General approach to protection against non-ionizing radiation. *Health Physics*, 82(4), 540-548. doi:[10.1097/00004032-200204000-00017](https://doi.org/10.1097/00004032-200204000-00017)
- Kivrak, E. G., Altunkaynak, B. Z., Alkan, I., Yurt, K. K. Kocaman, A., & Onger, M. E. (2017). Effects of 900-MHz radiation on the hippocampus and cerebellum of adult rats and attenuation of such effects by folic acid

and *Boswellia sacra*. *Journal of Microscopy and Ultrastructure*, 5(4), 216-224. doi:[10.1016/j.jmau.2017.09.003](https://doi.org/10.1016/j.jmau.2017.09.003)

Kuribayashi, M., Wang, J., Fujiwara, O., Doi, Y., Nabaie, K., Tamano, S., Ogiso, T., Asamoto, M., & Shirai, T. (2005). Lack of Effects of 1439 MHz Electromagnetic Near Field Exposure on the Blood-Brain Barrier in Immature and Young Rats. *Bioelectromagnetics*, 26(7), 578-588. doi:[10.1002/bem.20138](https://doi.org/10.1002/bem.20138)

National Cancer Institute (2019). Electromagnetic Fields and Cancer, (Accessed:17/07/2022) [URL](#)

Raj, A. A., Ping Lee, C., & Sidek, M. F. (2020, December 07-08). *Protection against EMF at Transmission Line and Tower*. IEEE International Conference on Power and Energy (PECon), 376-381. doi:[10.1109/PECon48942.2020.9314453](https://doi.org/10.1109/PECon48942.2020.9314453)

Repacholi, M. (2012). Concern that EMF magnetic fields from power lines cause cancer. *Science of the Total Environment*, 426, 454-458. doi:[10.1016/j.scitotenv.2012.03.030](https://doi.org/10.1016/j.scitotenv.2012.03.030)

Umaç, B. (2019). *Aydın il merkezinde seçili bölgelerde biyofiziksel ölçümlerin karşılaştırılması*. MSc Thesis, Aydın Adnan Menderes University.



Gazi University

Journal of Science

PART A: ENGINEERING AND INNOVATION

<http://dergipark.org.tr/gujsa>

Detecting Turkish Fake News Via Text Mining to Protect Brand Integrity

Ozge DOGUC^{1*} ¹Istanbul Medipol University, Kavacik Guney Campus, Beykoz Istanbul

Keywords	Abstract
Text Mining Fake News Brand Management Data Management	Fake news has been in our lives as part of the media for years. With the recent spread of digital news platforms, it affects not only traditional media but also online media as well. Therefore, while companies seek to increase their own brand awareness, they should also protect their brands against fake news spread on social networks and traditional media. This study discusses a solution that accurately classifies the Turkish news published online as real and fake. For this purpose, a machine learning model is trained with tagged news. Initially, the headlines were analyzed within the scope of this study that are collected from Turkish online sources. As a next step, in addition to the headlines of these news, news contexts are also used in the analysis. Analysis are done with unigrams and bigrams. The results show 95% success for the headlines and 80% for the texts for correctly classifying the fake Turkish news articles. This is the first study in the literature that introduces an ML model that can accurately identify fake news in Turkish language.

Cite

Doguc, O. (2022). Detecting Turkish Fake News Via Text Mining to Protect Brand Integrity. *GU J Sci, Part A, 9(3)*, 323-333.

Author ID (ORCID Number)	Article Process
O. Doguc, 0000-0002-5971-9218	Submission Date 03.09.2022 Revision Date 20.09.2022 Accepted Date 22.09.2022 Published Date 30.09.2022

1. INTRODUCTION

Today, Internet users refer to online content for the decisions they make in their daily lives, the shopping they do, and the school they choose. In other words, many Internet users treat online sources as their main source of information. E-commerce customers use reviews and news about the products before making purchase decisions, and for this purpose companies use online content to impress customers (Ahmed et al., 2017). False or misleading news and comments are also used extensively to influence the decisions of internet users (Obadă, 2019). The biggest sources of spreading fake news or rumors are social media platforms such as Google, Facebook and Twitter (Becker, 2017). Given the lack of control people have over the spread of fake content along with misleading information, the issue of fake news has been around for years since the traditional media era (Lemann, 2016). Fake news has received more attention in the last few years, especially since the 2016 US elections.

In addition to advances in computer science, the dynamic nature of the web and social media, which can be updated with information from each user, helps people creating and spreading fake news. On the other hand, it is very difficult to identify institutions affected by fake news. According to the report of Trend Micro, a cyber security company, companies can easily purchase services from many fake news producers around the world. According to the same report, political parties also use these services to rig the election results by manipulating voters' views on certain issues (Levin, 2017). There are studies showing that detecting fake news is difficult and requires more sophisticated decision support systems than detecting fake products (Chu et al., 2021).

*Corresponding Author, e-mail: odoguc@medipol.edu.tr

Fake news targeting brands can negatively affect consumers' perceptions of them. It can even change consumers' behavior towards brands and cause them to leave bad reviews on the brand line. As the growing middle class in Turkey in recent years often conspicuously consumes premium brands as a form of self-identity and associates them with the class, the fake news about premium brands has begun to affect a wider audience (Bankole & Reyneke, 2020). Fake news can affect the Turkish named brands as well as the global ones (Mertoglu, 2020).

This paper presents an approach to detect Turkish fake news about e-commerce websites, using text analysis based on n-gram features and machine learning classification techniques. In this paper, using the Python programming language and machine learning tools in the literature, the data were created from Turkish news headlines and texts. This study introduces a trained ML model by using real and fake Turkish news. This is the first study in the literature that shows that Turkish fake news can be effectively and efficiently detected through analysis of headlines and body text.

1.1 Literature Survey

Machine learning, under the concept of AI, has emerged as the preferred method for applications such as computer vision, speech, recognition, natural language processing to process information quickly and learn correctly (Murphy, 2012). AI developers recognize that training can be done much easier by showing examples of desired input-output behavior, rather than programming (if-else) by predicting the expected response for all possible inputs. The impact of machine learning is evident in many data-intensive industrial areas such as computer science, consumer services, diagnostics of complex systems, and control of logistics chains (Mahoney, 2011). This section discusses studies that are in the literature that use ML techniques for detecting fake news.

1.1.1 Fake News

Conroy et al. (2015) lists the types of fake news as follows:

1. Image-based: Fake news posts use more graphics as content.
2. User-based: Most fake news is produced by fake accounts and is aimed at an audience that represents certain age groups, gender, and political affiliation.
3. Knowledge-based: Some fake news produces pseudo-scientific solutions to insoluble or difficult problems and make users believe it is real.
4. Genre-based: Mostly written by pseudo-authors who imitate and copy the style of some journalists and brands.
5. Postural-based: Presented in a way that changes the meaning and purpose of correct statements.

In the literature, many automatic detection techniques of fake news and spoofing posts have been discussed (Altunbey Özbay & Alataş, 2020; Toğaçar et al., 2021). These studies use semantic and frequency analysis of the Turkish language to detect fake news patterns. Fake news detection has many facets, ranging from the use of chatbots to spread false information to the use of clickbait to spread rumors. Many social media networks, including Facebook, have many click tricks that increase sharing and likes for posts and then spread fake information (Chen & Cheng, 2019). Significant amount of work has been done to date to detect fake information (Stahl, 2018). The following detection techniques were introduced by Parikh and Atrey (2018):

1. Modeling of deception
2. Clustering
3. Predictive modeling
4. Methods based on content markup
5. Methods not based on text sign

While certain level of success has been achieved in detecting fake news and posts using Machine Learning (ML) techniques, the ever-changing characteristics of fake news on social media networks pose challenges in accurate classification.

1.1.2 Detecting Fake News with Machine Learning

In recent years, detecting fraudulent online reviews and fake news has played an important role in business, and politics because of the potential impact of fake reviews on consumer behavior and purchasing decisions. Researchers used machine learning techniques with large datasets to enhance learning in intelligent mechanisms that can detect fake news so they can distinguish between words syntactically and semantically. It includes tasks such as detecting fake news, reviewing tags, keywords, text content and media used (image, video, etc.). There have been few studies in the literature that have done textual analysis of topics such as fake news, rumors or spam (Aytaç et al., 2020). There are two aspects to detecting fake news. First, it is based on linguistic and psychological reasons, in other words, features that can capture the meaning of the text. However, these features had trouble understanding text properly and did not perform well on long texts. The second approach, based on the neural network model, provides document-level representation to make sense of fake news text (Englmeier, 2021). In these studies, artificial neural network models were used to learn semantic representations in the field of Natural Language Processing (NLP) and achieved successful results (Spicer, 2018). In addition, Albahar (2021) and Zhao et al. (2020) use hybrid methods that combine text mining and statistical analysis. These studies examine propagation of the fake news over time and investigate how news articles are distributed over time through radial basis function (RBF). Similarly, de Souza et al. (2021) use iterative versions of Gaussian fields and harmonic functions for labeling the fake news. These studies are done for English and Chinese languages and focus on how fake news spread on Internet over time.

2. MATERIAL AND METHOD

In this paper, a machine learning model was created that can train the news and classify it as "real" or "not real" (fake) with the data obtained. Data was collected from online Turkish news sources. The sources are Turkish online media websites and articles that are published on social media. Web crawlers were used to find and collect article that had been published between January 2021 and December 2021. More than 1000 news articles, containing more than 50000 words were collected during this process. News articles about popular brand names (e.g. Nike, Prada, Gucci, Beymen, Apple, Vakko, etc.) were taken into consideration, and they were preprocessed to be used in ML algorithms. Table 1 shows an example fake news article collected through Turkish news sources. The words like *sızdırıldı* (leaked), *söylentiler* (rumors) are big hints about authenticity of the article.

Table 1. Example Turkish fake news article

	Turkish Original	English Translation
Title	<i>Apple iPhone 13 kamera özellikleri sızdırıldı</i>	<i>Apple iPhone 13 camera features leaked</i>
Text	<i>Sony, Apple iPhone ailesi için kamera sensörü tedarik etmeye devam edecek. Şirketin lens konusunda da Genius ve Largan ile çalışacağı belirtiliyor. Bu yılın başlarında yayımlanan raporlarda, iPhone 13 özellikleriyle ilgili bazı iddialar yer alıyordu. Analist Ming-Chi Kuo, iPhone 13 kamera özellikleri ile ilgili söylentileri doğruladı.</i>	<i>Sony will continue to supply camera sensors for the Apple iPhone family. It is stated that the company will also work with Genius and Largan on lenses. In the reports released earlier this year, there were some claims about iPhone 13 features. Analyst Ming-Chi Kuo has confirmed rumors about iPhone 13 camera features.</i>

An ML model was developed that can decide whether the news is real or fake by using the transformed data and various functions written, using Naïve Bayes statistical calculation. Collected data was split into two sets; majority of the data was used to train the model and the second set was used to validate the classification results.

In the light of previous academic studies on the subject, (Doguc et al., 2020) AI models for pattern-detection and sorting were designed for this research. Secondly, for efficiency the code needed for operations was written in Python language. After this stage, suitable news titles were searched for the dataset of the study. Data analyzed in the application are the headlines of the news published between 2020 and 2022. In addition, the texts of the news were also analyzed.

Naïve Bayes probability calculation was used for text data among artificial intelligence models. In Naive Bayes, the data was kept in separate lists and dictionaries according to whether they were real or fake, and how much of all the words passed as real and fake was analyzed.

2.1 Naïve Bayes

Naive Bayes (NB) is one of the best-known data mining algorithms for classification (Wu et al., 2008). It is a supervised learning algorithm, based on the Bayes' theorem. It is called as a 'Naive' classifier, as it assumes that all features in a class are independent (unrelated) of each other. For example, given that a fruit is apple, its three properties (being round, red and small) can be considered as dependent on each other, they are actually independent features of the fruit. In practice, most combinations of attribute values are either not available in the training data or are not available in sufficient numbers. NB circumvents this impasse by assuming conditional independence. Despite this independence assumption, Bayes is a competent classifier in many real-world applications (Zhang et al., 2016).

2.2 N-Gram

N-Gram is a n-character fragment taken from a string (Violos et al., 2018). N-Gram is used in the model building process by dividing a sentence into parts of words. In N-Gram, 'N' indicates the number of words to be grouped in a single section. There are three types of N-Gram (Drus & Khalid, 2019):

- Unigram: A token consisting of only one word.
- Bigram: A token consisting of two words.
- Trigram: A token consisting of three words.

2.3 Bag of Words

The bag of words, or BoW for short, is a way to extract features from text for use in modeling machine learning algorithms. A BoW is a representation of text that models the location, relationships, and interactions of words in a document. The reason why the model is called the word bag is that it provides summary information about the order or structure of the words in the document and can be used easily when necessary. The model checks if known words are found in the document. In this approach, the histogram of the words in the text is examined and each word is counted as a feature (Goldberg, 2017).

2.4 Text Classification

The text classification problem has been extensively studied in practice for the last decade. Recent developments in NLP and text mining techniques allowed researchers work in applications that use text classification methods efficiently. Most text classification and document classification systems are divided into four stages: feature extraction, size reduction, classifier selection, and evaluation (Jiang et al., 2018).

Feature extraction and preprocessing are crucial steps for text classification applications. Most text and document datasets have problems with words to block, misspellings, slang, etc. Contains many unnecessary words. Some text cleaning techniques are tokenization, stop words, capitalization, slang and abbreviation, noise removal, spelling correction, stemming and lemmatization.

3. RESULTS AND DISCUSSION

In this paper, detection of fake news is analyzed in 3 stages. In the first stage, it is discussed if a news article can be correctly identified as fake just by checking its headline, as headlines in the news usually contain the important summary. In addition, the words that most affect whether news is real, or fake is determined. Figure 1 shows the flowchart of the fake news analysis method.

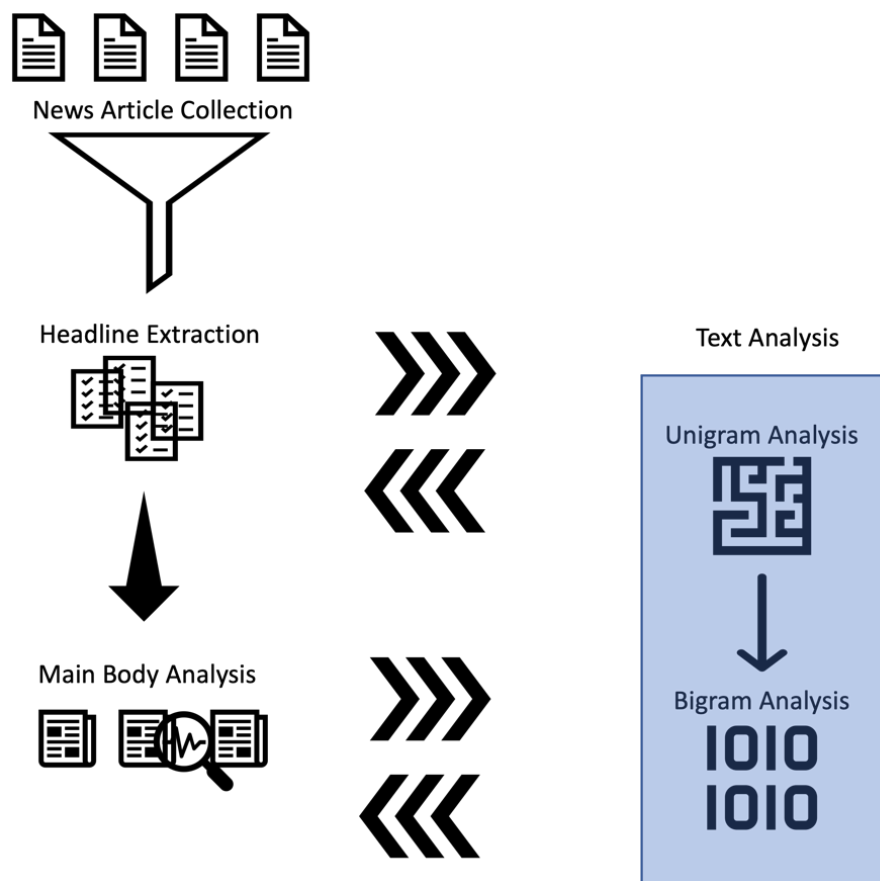


Figure 1. Flowchart of the fake news detection method

As shown in Figure 1, news articles are collected from Turkish online media, including articles from newspapers and tweets. Next, headlines are extracted from the articles, to be analyzed separately. The text analysis engine performs two-step analysis of the given text: unigram and bigram analysis. It determines if text is from a fake news or not, and a confidence score for the evaluation.

After eliminating the empty news headers, the detection application uses a tokenizer. The tokenizer serves to divide the text into tokens or words, and stopwords like *şey*. The stopwords, which are used in Turkish but have no direct meaning are excluded from analysis to prevent them from affecting classification. Then, using the *count vectorizer*, the given text is converted into a vector containing the frequencies of the words. In this way, words are converted into integer values that can be processed easily. Figure 2 shows the pseudocode.

```
dic = {}
y = 0
for x in vectorizer3.get_feature_names():
    dic[x] = y
    y = y + 1
```

Figure 2. Creating dictionary of words and their frequencies

In order to use the Naïve Bayes probabilities using the formula in Figure 3, the news articles are labeled as ‘Positive’ and ‘Negative’. The application counts the words in each article and prepares a learning bed based on the number of words and article’s sentiment. Next, the same is done with the bigrams, as shown in Figure 4. The purpose of doing this is to calculate probabilities among their own classes according to the Naive Bayes formula. All labels and probabilities are stored in dictionaries to improve efficient storage and fast lookup.

$$P(c|x) = \frac{P(x|c)P(c)}{P(x)}$$

Likelihood
Class Prior Probability

Posterior Probability
Predictor Prior Probability

$$P(c|X) = P(x_1|c) \times P(x_2|c) \times \dots \times P(x_n|c) \times P(c)$$

Figure 3. Naive Bayes Probability Calculation Formula

```
bigram_vectorizer3 = CountVectorizer(ngram_range=(2, 2), token_pattern=r'\b\w+\b', min_df=1)
bXY = bigram_vectorizer3.fit_transform(fixedTarget)
buniqCount = len(bigram_vectorizer3.get_feature_names())
bidic = {}
y = 0
for x in bigram_vectorizer3.get_feature_names():
    bidic[x] = y
    y += 1
biAllPos = 0
biAllNeg = 0
for x,y in zip(bXY,slabel):
    if(y == 0):
        biAllPos += np.sum(x)
    else:
        biAllNeg += np.sum(x)
```

Figure 4. Using Count Vectorizer for Double Words and Finding the Number of Positive and Negative Data

Next, the news data is split into 2 sets: training and test. During the training phase, the application calculates scoring for each news article; based on the formula below:

$$\frac{\text{number of repetitions of the word (negative, positive) + 1}}{\text{total number of words in positive or negative case + number of unique words in the file}}$$

The code snippet for the training algorithm is given in Figure 5.


```

testTitle = target
testLabel = label
|
posnoncount = 0
negnoncount = 0

unicount = 0
bicount = 0
stringcount = 0
for i,a in zip(testTitle,testLabel):
    if(type(i) != str):
        continue
    stringcount += 1
    i = re.sub(r'^[\w\s]', '', i)
    words = i.split()
    for ax in range(len(words)):
        words[ax] = words[ax].lower()
    x = positiveNaive(XY, words, uniqCount, vectorizer3, allPos, label, dic, posDic)
    x = x + (np.log(posCount/(posCount + negCount)))
    y = negativeNaive(XY, words, uniqCount, vectorizer3, allNeg, label, dic, negDic)
    y = y + (np.log(negCount/(posCount + negCount)))

    uniflag = 0
    if(x > y):
        uniflag = 0
    else:
        uniflag = 1

```

Figure 5. Code snippet for the training algorithm

The generated ML model has a success rate of 95% for single words and 99% for bigrams. The reason for high the success rates is that presence of some words or word groups in the headlines provide too much information about that classification of that news article. List in Figure 6 contains information about frequencies of the words which words have more impact on the classification results.

Real News Unigram				
Istanbul		moda		yaz
5362		5083		4936
Fake News Unigram				
dolar		Rusya		Ukrayna
3884		3368		3349
Real News Bigram				
Yaz modası		babalar günü		indirim kuponu
4030		3589		3309
Fake News Bigram				
Rusya Ukrayna		dolar kuru		hediye garantili
3608		2915		2318

Figure 6. Most frequent words without stopwords

Looking at the list above, it is seen that the content of some news, both real and fake, can be guessed from the title. In the second stage, the same methodology is used with news text context, not just the headlines. The functions mentioned above are reused for similar operations. In addition, the BoW method is used. Likewise, separate analyzes are made for unigrams and bigrams. Dictionaries are prepared for single words, the data is separated as positive / negative, and the calculation of the total number of words is carried out. Same is done for bigrams as well. The accuracy results are given below:

Accuracy with Unigrams: 81.44%

Accuracy with Bigrams: 62.63%

In news headlines, the result obtained as a result of the operation performed for bigrams was higher, while a higher result was obtained in the operation performed with single words using the entire news text. The reason for this may be that better words should be chosen in news headlines in order to express more with fewer words, and the words in succession should be in harmony.

Finally, this paper examines the impact of the strong words on the classification of fake news. For that purpose, 10 words whose presence strongly indicates that the news is real, 10 words whose absence strongly indicates that the news is real, 10 words whose presence strongly indicates that the news is fake, and 10 words whose absence strongly indicates that the news is fake were picked. In all cases, effect of the stopwords is also tested.

The data for 10 words whose presence strongly indicates that the news is real are as follows (Table 2):

Table 2. 10 Words that appear in the real news articles

<i>Term</i>	<i>Weight</i>
<i>Ve</i>	0.303
<i>Bir</i>	0.142
<i>Şey</i>	0.130
<i>Hangi</i>	0.118
<i>Ne</i>	0.106
<i>İle</i>	0.098
<i>Bu</i>	0.095
<i>Kadar</i>	0.091
<i>De/Da</i>	0.088
<i>Hep</i>	0.078

The list consists of mostly the stopwords, Table 3 shows the results without the stopwords:

Table 3. 10 Words that appear in the real news articles (without stopwords)

<i>Term</i>	<i>Weight</i>
<i>İstanbul</i>	0.102
<i>Moda</i>	0.091
<i>Hafta</i>	0.085
<i>İndirim</i>	0.083
<i>Baba</i>	0.081
<i>Yaz</i>	0.081
<i>Sipariş</i>	0.069
<i>Sezon</i>	0.069
<i>Garanti</i>	0.069
<i>Hediye</i>	0.067

Next, this paper analyzes if absence of words can be used to decide if a news article is real or fake. Table 4 shows the top the 10 words whose absence strongly separates a real news article from a fake one (appear in the fake news but not in the real ones):

Table 4. 10 words the absence of which strongly indicates the truth of the news

<i>Term</i>	<i>Weight</i>
<i>Iddia</i>	0.037
<i>Söylendi</i>	0.037
<i>Çarpıcı</i>	0.036
<i>Edildi</i>	0.035
<i>Bedava</i>	0.030
<i>Anında</i>	0.028
<i>iPhone</i>	0.028
<i>Hediye</i>	0.028
<i>Kazandınız</i>	0.025
<i>Hemen</i>	0.025

In other words, real news articles usually do not include words such as *iddia* and *söylendi*, while fake ones do. Similarly, Table 5 includes the top 10 words that appear in the fake news most frequently.

Table 5. 10 words whose existence strongly indicates that the news is fake

<i>Term</i>	<i>Weight</i>
<i>Dolar</i>	0.072
<i>Rusya</i>	0.061
<i>Ukrayna</i>	0.055
<i>İndirim</i>	0.023
<i>Faiz</i>	0.021
<i>Elektronik</i>	0.021
<i>Yaz</i>	0.019
<i>Telefon</i>	0.019
<i>Kupon</i>	0.019
<i>Ürün</i>	0.017

Trained with hundreds of news articles and their analysis results, this study creates an ML model for Turkish that can accurately detect fake news. Unlike the studies that are available in the literature (Obadā, 2019; Yalcin & Simsek, 2020; Zhao et al., 2020; Albahar, 2021; de Souza et al., 2021), this study doesn't rely on statistical analysis or temporal distribution of news articles. It combines NLP and ML techniques to analyze Turkish news articles and their headlines; and devise rules that can distinguish fake news through syntactic and semantic features.

4. CONCLUSION

This paper focused on how the news can be accurately classified as *real* or *fake* by using the news articles available in the online media. Fake news impact brand integrity and equity greatly (Chen & Cheng, 2019), and more than 80% of the online users come across with fake news every week (Belin, 2020). Turkish brands are not immune to the fake news, and this paper uses Turkish news articles to create an intelligent model that can successfully detect fake news.

Data used in the research are the news (texts) published in the past, these texts were first cleansed and preprocessed to be used in the AI models. Among the AI models, Naïve Bayes probability calculation was used for text data. While there are studies in the literature that achieve 91% success with natural language processing (NLP) (Toğaçar et al., 2021), in the established methodology, a success rate of over 95% was

achieved for headlines and around 80% for texts. As a result, it is shown that the news titles provide more important information than the article itself in the form of a summary. In addition to these, how the absence of words affects the reality of the news were examined. Naive Bayes gives more weight to the more frequent words and a classification can be done based on the frequencies. This is the first study that provides machine learning model that can accurately identify Turkish fake news.

CONFLICT OF INTEREST

The authors declare no conflict of interest.

REFERENCES

- Ahmed, H., Traore, I., & Saad, S. (2017, October 26-28). *Detection of Online Fake News Using N-Gram Analysis and Machine Learning Techniques*. In: I. Traore, I. Woungang & A. Awad (Eds.), *Intelligent, Secure, and Dependable Systems in Distributed and Cloud Environment, First International Conference, ISDDC 2017, Vancouver, BC, Canada*, (pp. 127–138). doi:[10.1007/978-3-319-69155-8_9](https://doi.org/10.1007/978-3-319-69155-8_9)
- Albahar, M. (2021). A hybrid model for fake news detection: Leveraging news content and user comments in fake news. *IET Information Security*, 15(2), 169–177. doi:[10.1049/ise2.12021](https://doi.org/10.1049/ise2.12021)
- Altunbey Özbay, F., & Alataş, B. (2020). Çevrimiçi sosyal medyada sahte haber tespiti. *DÜMF Mühendislik Dergisi*, 11(1), 91–103. doi:[10.24012/dumf.629368](https://doi.org/10.24012/dumf.629368)
- Aytaç, Ö. B., Silahtaroglu, G., & Doğuç, Ö. (2020). Analysis of Digital Marketing Strategies of Deposit Banks in Turkey via Text Mining Twitter Posts. In: H. Dincer & S. Yüksel (Eds.) *Strategic Outlook for Innovative Work Behaviours* (pp. 361–376). Springer. doi:[10.1007/978-3-030-50131-0_20](https://doi.org/10.1007/978-3-030-50131-0_20)
- Bankole, O., & Reyneke, M. (2020). The Effect of Fake News on the Relationship between Brand Equity and Consumer Responses to Premium Brands: An Abstract. In: S. Wu, F. Pantoja & N. Krey (Eds.), *Marketing Opportunities and Challenges in a Changing Global Marketplace* (pp. 461–462). Springer International Publishing. doi:[10.1007/978-3-030-39165-2_189](https://doi.org/10.1007/978-3-030-39165-2_189)
- Becker, R. (2017, June 26). Your short attention span could help fake news spread. [URL](#)
- Belin, A. (2020, June 25). How to Protect and Defend your Brand from Fake News. [URL](#)
- Chen, Z. F., & Cheng, Y. (2019). Consumer response to fake news about brands on social media: the effects of self-efficacy, media trust, and persuasion knowledge on brand trust. *Journal of Product & Brand Management*, 29(2), 188–198. doi:[10.1108/JPBM-12-2018-2145](https://doi.org/10.1108/JPBM-12-2018-2145)
- Chu, S. K. W., Xie, R., & Wang, Y. (2021). Cross-Language Fake News Detection. *Data and Information Management*, 5(1), 100–109. doi:[10.2478/dim-2020-0025](https://doi.org/10.2478/dim-2020-0025)
- Conroy, N. K., Rubin, V. L., & Chen, Y. (2015, November 6-10). Automatic deception detection: Methods for finding fake news. *Proceedings of the Association for Information Science and Technology (ASIS&T)*, 52(1), 1-4. doi:[10.1002/pr2.2015.145052010082](https://doi.org/10.1002/pr2.2015.145052010082)
- de Souza, M. C., Nogueira, B. M., Rossi, R. G., Marcacini, R. M., dos Santos, B. N., & Rezende, S. O. (2021). A network-based positive and unlabeled learning approach for fake news detection. *Machine Learning*. doi:[10.1007/s10994-021-06111-6](https://doi.org/10.1007/s10994-021-06111-6)
- Doguc, O., Aytac, O. B., & Silahtaroglu, G. (2020). Lemmatizer: Akıllı Türkçe kök bulma yöntemi. *Turkish Studies - Information Technologies and Applied Sciences*, 15(3), 289-299. doi:[10.47844/TurkishStudies.44220](https://doi.org/10.47844/TurkishStudies.44220)
- Drus, Z., & Khalid, H. (2019). Sentiment Analysis in Social Media and Its Application: Systematic Literature Review. *Procedia Computer Science*, 161, 707-714. doi:[10.1016/j.procs.2019.11.174](https://doi.org/10.1016/j.procs.2019.11.174)
- Englmeier, K. (2021). The Role of Text Mining in Mitigating the Threats from Fake News and Misinformation in Times of Corona. *Procedia Computer Science*, 181, 149-156. doi:[10.1016/j.procs.2021.01.115](https://doi.org/10.1016/j.procs.2021.01.115)
- Goldberg, Y. (2017). *Neural Network Methods in Natural Language Processing*. Morgan & Claypool Publishers. doi:[10.1007/978-3-031-02165-7](https://doi.org/10.1007/978-3-031-02165-7)

- Jiang, M., Liang, Y., Feng, X., Fan, X., Pei, Z., Xue, Y., & Guan, R. (2018). Text classification based on deep belief network and softmax regression. *Neural Computing and Applications*, 29(1), 61–70. doi:[10.1007/s00521-016-2401-x](https://doi.org/10.1007/s00521-016-2401-x)
- Lemann, N. (2016, November 30). Solving the Problem of Fake News. [URL](#)
- Levin, S. (2017, June 13). Pay to sway: report reveals how easy it is to manipulate elections with fake news. [URL](#)
- Mahoney, M. W. (2011). Randomized Algorithms for Matrices and Data. *Foundations and Trends in Machine Learning*, 3(2), 123–224. doi:[10.1561/22000000035](https://doi.org/10.1561/22000000035)
- Mertoglu, U. (2020). A Fake News Detection Model for Turkish Language (*Türkçe için Sahte Haber Tespit Modelinin Oluşturulması*). PhD Thesis. Hacettepe University.
- Murphy, K. (2012). *Machine Learning: A Probabilistic Perspective*. MIT Press.
- Obadă, D.-R. (2019). Sharing Fake News about Brands on Social Media: a New Conceptual Model Based on Flow Theory. *Argumentum. Journal of the Seminar of Discursive Logic, Argumentation Theory and Rhetoric*, 17(2), 144-166.
- Parikh, S. B., & Atrey, P. K. (2018, April 10-12). *Media-Rich Fake News Detection: A Survey*. In: 2018 IEEE Conference on Multimedia Information Processing and Retrieval (MIPR), (pp. 436–441). doi:[10.1109/MIPR.2018.00093](https://doi.org/10.1109/MIPR.2018.00093)
- Spicer, R. N. (2018). Lies, Damn Lies, Alternative Facts, Fake News, Propaganda, Pinocchios, Pants on Fire, Disinformation, Misinformation, Post-Truth, Data, and Statistics. In: *Free Speech and False Speech*, (pp 1-31). Springer International Publishing. doi:[10.1007/978-3-319-69820-5_1](https://doi.org/10.1007/978-3-319-69820-5_1)
- Stahl, K. (2018). Fake news detection in social media. California State University Stanislaus, 6.
- Toğaçar, M., Eşidir, K. A., & Ergen, B. (2021). Yapay Zekâ Tabanlı Doğal Dil İşleme Yaklaşımını Kullanarak İnternet Ortamında Yayınlanmış Sahte Haberlerin Tespiti. *Journal of Intelligent Systems: Theory and Applications*, 5(1), 1–8. doi:[10.38016/jista.950713](https://doi.org/10.38016/jista.950713)
- Violos, J., Tserpes, K., Varlamis, I., & Varvarigou, T. (2018). Text Classification Using the N-Gram Graph Representation Model Over High Frequency Data Streams. *Frontiers in Applied Mathematics and Statistics*, 4, 41. doi:[10.3389/fams.2018.00041](https://doi.org/10.3389/fams.2018.00041)
- Wu, X., Kumar, V., Ross Quinlan, J., Ghosh, J., Yang, Q., Motoda, H., McLachlan, G. J., Ng, A., Liu, B., Yu, P. S., Zhou, Z.-H., Steinbach, M., Hand, D. J., & Steinberg, D. (2008). Top 10 algorithms in data mining. *Knowledge and Information Systems*, 14(1), 1–37. doi:[10.1007/s10115-007-0114-2](https://doi.org/10.1007/s10115-007-0114-2)
- Yalcin, F., & Simsek, Y. (2020). A New Class of Symmetric Beta Type Distributions Constructed by Means of Symmetric Bernstein Type Basis Functions. *Symmetry*, 12(5), 779. doi:[10.3390/sym12050779](https://doi.org/10.3390/sym12050779)
- Zhang, L., Jiang, L., Li, C., & Kong, G. (2016). Two feature weighting approaches for naive bayes text classifiers. *Knowledge-Based Systems*, 100, 137–144.
- Zhao, Z., Zhao, J., Sano, Y., Levy, O., Takayasu, H., Takayasu, M., Li, D., Wu, J., & Havlin, S. (2020). Fake news propagates differently from real news even at early stages of spreading. *EPJ Data Science*, 9(1), 7. doi:[10.1140/epjds/s13688-020-00224-z](https://doi.org/10.1140/epjds/s13688-020-00224-z)



Gazi University

Journal of Science

PART A: ENGINEERING AND INNOVATION

<http://dergipark.org.tr/gujisa>

Adaptation of the Kantorovich Type Integral to the Dunkl Operator

Gürhan İÇÖZ¹ , Esmâ GÖKMEN² ¹Gazi University, Faculty of Science, Department of Mathematics²Gazi University, Graduate School of Natural and Applied Sciences

Keywords	Abstract
Dunkl Analogue	The purpose of this article is to show the adaptation of the Kantorovich type integral to the Dunkl operator. This article gives a sequence of operators to get an approximation result. The variant of the operator which is the Kantorovich type integral has been given and examined the approximation ratio by the first and second order modulus of continuity. The approximation order of the operators is shown by the first order modulus of continuity and the Lipschitz class functions.
Kantorovich-Type Integral	
First and Second Modulus of Continuity	
Lipschitz Class Function	

Cite

İçöz, G., & Gökmen, E. (2022). Adaptation of the Kantorovich Type Integral to the Dunkl Operator. *GU J Sci, Part A*, 9(3), 334-346.

Author ID (ORCID Number)	Article Process
G. İçöz, 0000-0003-1204-9517	Submission Date 25.07.2022
E. Gökmen, 0000-0003-4081-8766	Revision Date 10.08.2022
	Accepted Date 01.09.2022
	Published Date 30.09.2022

1. INTRODUCTION

The famous people in the approximation theory are defined the well-known operators and given the most important theorems as Bernstein, 1912; Szász, 1950; Korovkin, 1953; Lorentz, 1953; Gadzhiev, 1974; Altomare & Campiti, 1994; Jakimovski & Leviatan, 1969; DeVore & Lorentz, 1993.

In the recent years, many results about the generalization of the operators including Gamma function have been obtained by mathematicians (İçöz & Çekim, 2016; İçöz et al., 2016; Sucu et al., 2012; Mursaleen et al., 2016; Kanat & Sofyalıoğlu, 2018; 2019; Nasiruzzaman & Aljohani, 2020a, 2020b; Yazici et al., 2022). Sucu (2014) gave the Dunkl-analogue of Szász-Mirakyan operator as follows

$$E_m(\sigma, y) = \frac{1}{e_\mu(my)} \sum_{j=0}^{\infty} \frac{(my)^j}{\gamma_\mu(j)} \sigma\left(\frac{j + 2\mu\theta_j}{m}\right) \quad (1)$$

where $\mu > 0$, $m \in \mathbb{N}$, $y \geq 0$ and $\sigma \in C[0, \infty)$ whenever the aforementioned sum converges. Rosenblum (1994) gave the definition of $e_\mu(y)$ by

$$e_\mu(y) = \sum_{j=0}^{\infty} \frac{y^j}{\gamma_\mu(j)}$$

where the coefficients γ_μ are defined as follows for $k \in \mathbb{N}_0$ and $\mu > -\frac{1}{2}$

$$\gamma_\mu(2j) = \frac{2^{2j} j! \Gamma(j + \mu + 1/2)}{\Gamma(\mu + 1/2)}$$

and

$$\gamma_\mu(2j + 1) = \frac{2^{2j+1} j! \Gamma(j + \mu + 3/2)}{\Gamma(\mu + 1/2)}$$

where

$$\theta_j = \begin{cases} 0; j \in \{0, 2, 4, \dots, 2n, \dots\} \\ 1; j \in \{1, 3, \dots, 2n + 1, \dots\} \end{cases}$$

Sucu (2014) gave the following identities for E_m operators.

$$\begin{aligned} E_m\{1; y\} &= 1, \\ E_m\{t; y\} &= y, \\ E_m\{t^2; y\} &= y^2 + \left(1 + 2\mu \frac{e_\mu(-my)}{e_\mu(my)}\right) \frac{y}{m}. \end{aligned} \tag{2}$$

Now, the Kantorovich-type integral generalization of the operators T_m (İçöz & Çekim, 2016) is defined as

$$T_m(f; y) = \frac{m}{e_\mu(my)} \sum_{j=0}^{\infty} \frac{(my)^j}{\gamma_\mu(j)} \int_{\frac{j+2\mu\theta_j}{m}}^{\frac{j+1+2\mu\theta_j}{m}} f(t) dt. \tag{3}$$

T_m operators satisfy the following equalities

$$\begin{aligned} T_m(1, y) &= 1, \\ T_m(t, y) &= y + \frac{1}{2m}, \\ T_m(t^2, y) &= y^2 + 2 \left(1 + \mu \frac{e_\mu(-my)}{e_\mu(my)}\right) \frac{y}{m} + \frac{1}{3m^2}. \end{aligned} \tag{4}$$

The recursion relation is satisfied by

$$\gamma_\mu(j + 1) = (j + 1 + 2\mu\theta_{j+1})\gamma_\mu(j), \quad j \in \mathbb{N}_0 \tag{5}$$

The Dunkl derivation τ_μ has the form

$$(\tau_\mu v)(y) = \tau_\mu v(y) = \frac{dv}{dy} + \mu \frac{v(y) - v(-y)}{y}, \tag{6}$$

where μ is real number satisfying $\mu > -1/2$ and v is an entire function. Repeating this process we can have

$$(\tau_\mu^2 v)(y) = \tau_\mu^2 v(y) = \frac{d^2v}{dy^2} + \frac{2\mu}{y} \frac{dv}{dy} + \mu \frac{v(y) - v(-y)}{y} \tag{7}$$

Ben Cheikh and Gaied (2007) defined Dunkl-Appell polynomial set. (p_j) is called Dunkl-Appell polynomial set if and only if for $j \in \mathbb{N}_0$

$$\tau_\mu p_{j+1}(y) = \frac{\gamma_\mu(j+1)}{\gamma_\mu(j)} p_j(y). \quad (8)$$

The polynomials p_j can be written as

$$p_j(y) = \sum_{k=0}^j \binom{k}{j}_\mu b_{k-j} y^j, (b_0 \neq 0), \quad (9)$$

(p_j) is has the following generation function by

$$P(t)e_\mu(yt) = \sum_{j=0}^{\infty} \frac{p_j(y)}{\gamma_\mu(j)} t^j,$$

where

$$P(t) = \sum_{j=0}^{\infty} \frac{a_j}{\gamma_\mu(j)} t^j, (a_0 \neq 0).$$

In 2020, Sucu (2020) introduced a new generalization of the operator S_m with the Dunkl-Appell polynomials by

$$S_m(\varphi, y) = \frac{1}{P(1)e_\mu(my)} \sum_{j=0}^{\infty} \frac{p_j(my)}{\gamma_\mu(j)} \varphi\left(\frac{j+2\mu\theta_j}{m}\right). \quad (10)$$

Let $\{S_m\}_{m \geq 1}$ be the sequence of operators defined by (10). Then, in (İçöz & Çekim, 2016) there are following assertions:

$$\begin{aligned} S_m\{1; y\} &= 1, \\ S_m\{\psi; y\} &= y + \frac{(e_\mu(my) - e_\mu(-my))P'(1) + e_\mu(-my)(\tau_\mu P)(1)}{P(1)m e_\mu(my)}, \\ S_m(\psi^2; y) &= y^2 + \frac{e_\mu(my)(2P'(1)P(1) + 2\mu P(-1)e_\mu(-my))}{P(1)m e_\mu(my)} y \\ &\quad + \frac{(\tau_\mu P)(1)e_\mu(-my)}{P(1)m^2 e_\mu(my)} \\ &\quad + \frac{[2P''(1) - (\tau_\mu P)'(1) - (\tau_\mu P')(1) + P(1) - 2\mu P'(-1)](e_\mu(my) - e_\mu(-my))}{P(1)m^2 e_\mu(my)} \\ &\quad + \frac{(\tau_\mu^2 P)(1) + 2\mu(\tau_\mu P)(-1)}{P(1)m^2}. \end{aligned} \quad (11)$$

Now, we construct the Kantorovich type generalization of the operators S_m given by (10). For this purpose, we get $f \in C_{\mathbb{Z}}[0, \infty) = \{f \in C[0, \infty): f(\mathbb{Z}) = O(\lambda^{\mathbb{Z}})\}$ as $\mathbb{Z} \rightarrow \infty$. Then, for all $y \in [0, \infty)$, $\mathbb{Z} > m, m \in \mathbb{N}, P(1) \neq 0$ and $\mu \geq 0$. Our operators are given by

$$E_m(\varphi; y) = \frac{m}{P(1)e_\mu(my)} \sum_{j=0}^{\infty} \frac{p_j(my)}{\gamma_\mu(j)} \int_{\frac{j+2\mu\theta_j}{m}}^{\frac{j+1+2\mu\theta_j}{m}} \varphi(t) dt. \tag{12}$$

In here, we set up the operators E_m to the other operators in Nasiruzzaman & Aljohani (2020b), similary. But in the paper, we examine the operator E_m with the help of Dunkl derivation. In Nasiruzzaman & Aljohani (2020b), the authors use the classical derivation. Therefore, we have done a wider and more accurate study.

2. APPROXIMATION PROPERTIES OF E_m OPERATORS

Lemma 1. E_m operators are linear and positive operators. E_m operators satisfy the following equalities:

$$E_m\{1; y\} = 1, \tag{13}$$

$$E_m\{t; y\} = y + \frac{1}{P(1)m e_\mu(my)} \{e_\mu(-my)(\tau_\mu P)(1) + P'(1)[e_\mu(my) - e_\mu(-my)]\} + \frac{1}{2m}, \tag{14}$$

$$\begin{aligned} E_m\{t^2; y\} &= y^2 + \frac{e_\mu(my)(2P'(1)+P(1))+2\mu P(-1)e_\mu(-my)}{mP(1)e_\mu(my)} y + \frac{(\tau_\mu P)(1)e_\mu(-my)}{m^2P(1)e_\mu(my)} \\ &+ \frac{[2P''(1) - (\tau_\mu P)'(1) - (\tau_\mu P')(1) + P(1) - 2\mu P'(-1)](e_\mu(my) - e_\mu(-my))}{m^2P(1)e_\mu(my)} \\ &+ \frac{(\tau_\mu^2 P)(1) + 2\mu(\tau_\mu P)(-1)}{P(1)m^2} \\ &+ \frac{y}{m} + \frac{1}{m^2P(1)e_\mu(my)} \{e_\mu(-my)(\tau_\mu P)(1) + P'(1)[e_\mu(my) - e_\mu(-my)]\} + \frac{1}{3m^2}. \end{aligned} \tag{15}$$

Proof . For $\varphi(t) = 1$, from the generation function (9), we have

$$\begin{aligned} E_m(1; y) &= \frac{m}{P(1)e_\mu(my)} \sum_{j=0}^{\infty} \frac{p_j(my)}{\gamma_\mu(j)} \int_{\frac{j+2\mu\theta_j}{m}}^{\frac{j+1+2\mu\theta_j}{m}} dt \\ &= \frac{m}{P(1)e_\mu(my)} \sum_{j=0}^{\infty} \frac{p_j(my)}{\gamma_\mu(j)} \frac{1}{m} \\ &= \frac{1}{P(1)e_\mu(my)} \sum_{j=0}^{\infty} \frac{p_j(my)}{\gamma_\mu(j)} \end{aligned}$$

$$= \frac{e_\mu(my)}{e_\mu(my)} = 1.$$

For $\varphi(t) = t$, we obtain

$$\begin{aligned} E_m(t; y) &= \frac{m}{P(1)e_\mu(my)} \sum_{j=0}^{\infty} \frac{p_j(my)}{\gamma_\mu(j)} \int_{\frac{j+2\mu\theta_j}{m}}^{\frac{j+1+2\mu\theta_j}{m}} t dt \\ &= \frac{m}{P(1)e_\mu(my)} \sum_{j=0}^{\infty} \frac{p_j(my)}{\gamma_\mu(j)} \left[\frac{t^2}{2} \right]_{\frac{j+2\mu\theta_j}{m}}^{\frac{j+1+2\mu\theta_j}{m}} \\ &= \frac{1}{P(1)e_\mu(my)} \sum_{j=0}^{\infty} \frac{p_j(my)}{\gamma_\mu(j)} \frac{1}{2m} [2(j + 2\mu\theta_j) + 1] \\ &= \frac{1}{m} \frac{1}{P(1)e_\mu(my)} \sum_{j=0}^{\infty} \frac{p_j(my)}{\gamma_\mu(j)} (j + 2\mu\theta_j) \\ &\quad + \frac{1}{2m} \frac{1}{P(1)e_\mu(my)} \sum_{j=0}^{\infty} \frac{p_j(my)}{\gamma_\mu(j)}. \end{aligned} \tag{16}$$

If we use the equation

$$\gamma_\mu(j + 1) = (j + 1 + 2\mu\theta_{j+1})\gamma_\mu(j),$$

we can obtain

$$\gamma_\mu(j) = (j + 2\mu\theta_j)\gamma_\mu(j - 1).$$

Let's use the above equation in the operator, then we get

$$\begin{aligned} E_m(t; y) &= \frac{1}{m} \frac{1}{P(1)e_\mu(my)} \sum_{j=1}^{\infty} \frac{p_j(my)}{(j + 2\mu\theta_j) \gamma_\mu(j - 1)} (j + 2\mu\theta_j) + \frac{1}{2m} \\ &= \frac{1}{m} \frac{1}{P(1)e_\mu(my)} \sum_{j=1}^{\infty} \frac{p_j(my)}{\gamma_\mu(j - 1)} + \frac{1}{2m} \\ &= \frac{1}{m} \frac{1}{P(1)e_\mu(my)} \sum_{j=0}^{\infty} \frac{p_{j+1}(my)}{\gamma_\mu(j)} + \frac{1}{2m}. \end{aligned}$$

Taking the Dunkl derivative with respect to t of both sides of the equation

$$P(t)e_\mu(yt) = \sum_{j=0}^{\infty} \frac{p_j(y)}{\gamma_\mu(j)} t^j.$$

Then we obtain

$$\sum_{j=0}^{\infty} \frac{p_j(y)}{\gamma_{\mu}(j)} (j + 2\mu\theta_j) t^{j-1}$$

$$= yP(t)e_{\mu}(yt) + e_{\mu}(-yt)(\tau_{\mu}P)(t) + P'(t)[e_{\mu}(yt) - e_{\mu}(-yt)]. \tag{17}$$

In the above expression, if y is replaced by my and t is replaced by I then we can find

$$myP(1)e_{\mu}(my) + e_{\mu}(-my)(\tau_{\mu}P)(1) + P'(1)[e_{\mu}(my) - e_{\mu}(-my)]$$

$$= \sum_{j=1}^{\infty} \frac{p_j(my)}{\gamma_{\mu}(j)} (j + 2\mu\theta_j)$$

$$= \sum_{j=0}^{\infty} \frac{p_{j+1}(my)}{\gamma_{\mu}(j+1)\gamma_{\mu}(j)} (j + 1 + 2\mu\theta_{j+1})$$

$$= \sum_{j=0}^{\infty} \frac{p_{j+1}(my)}{\gamma_{\mu}(j)}.$$

Using the above equation in $E_m(t; y)$, we see that

$$E_m(t; y) = \frac{1}{m} \frac{1}{P(1)e_{\mu}(my)} \sum_{j=0}^{\infty} \frac{p_{j+1}(my)}{\gamma_{\mu}(j)} + \frac{1}{2m}$$

$$= \frac{1}{m} \frac{1}{P(1)e_{\mu}(my)} \{myP(1)e_{\mu}(my) + e_{\mu}(-my)(\tau_{\mu}P)(1) + P'(1)[e_{\mu}(my) - e_{\mu}(-my)]\}$$

$$+ \frac{1}{2m}$$

$$= y + \frac{1}{P(1)e_{\mu}(my)} \{e_{\mu}(-my)(\tau_{\mu}P)(1) + P'(1)[e_{\mu}(my) - e_{\mu}(-my)]\} + \frac{1}{2m}.$$

(18)

For $\varphi(t)=t^2$, we obtain

$$E_m(t^2; y) = \frac{m}{P(1)e_{\mu}(my)} \sum_{j=0}^{\infty} \frac{p_j(my)}{\gamma_{\mu}(j)} \int_{\frac{j+2\mu\theta_j}{m}}^{\frac{j+1+2\mu\theta_j}{m}} t^2 dt.$$

$$= \frac{m}{P(1)e_{\mu}(my)} \sum_{j=0}^{\infty} \frac{p_j(my)}{\gamma_{\mu}(j)} \left[\frac{t^3}{3} \right]_{\frac{j+2\mu\theta_j}{m}}^{\frac{j+1+2\mu\theta_j}{m}}$$

$$= \frac{m}{P(1)e_{\mu}(my)} \sum_{j=0}^{\infty} \frac{p_j(my)}{\gamma_{\mu}(j)} \frac{1}{3m^2} [3(j + 2\mu\theta_j)^2 + 3(j + 2\mu\theta_j) + 1]$$

$$\begin{aligned}
 &= \frac{1}{m^2} \frac{1}{P(1)e_\mu(my)} \sum_{j=0}^{\infty} \frac{p_j(my)}{\gamma_\mu(j)} (j + 2\mu\theta_j)^2 \\
 &+ \frac{1}{m^2} \frac{1}{P(1)e_\mu(my)} \sum_{j=0}^{\infty} \frac{p_j(my)}{\gamma_\mu(j)} (j + 2\mu\theta_j) \\
 &+ \frac{1}{3m^2} \frac{1}{P(1)e_\mu(my)} \sum_{j=0}^{\infty} \frac{p_j(my)}{\gamma_\mu(j)}. \tag{19}
 \end{aligned}$$

If we use the equation

$$\gamma_\mu(j + 1) = (j + 1 + 2\mu\theta_{j+1})\gamma_\mu(j),$$

we obtain

$$\gamma_\mu(j - 1) = (j - 1 + 2\mu\theta_{j-1})\gamma_\mu(j - 2).$$

Taking the Dunkl derivative with respect to t of both sides of the equation

$$P(t)e_\mu(yt) = \sum_{j=0}^{\infty} \frac{p_j(y)}{\gamma_\mu(j)} t^j,$$

we get

$$\begin{aligned}
 &\sum_{j=1}^{\infty} \frac{p_j(y)}{\gamma_\mu(j)} (j + 2\mu\theta_j) t^{j-1} \\
 &= yP(t)e_\mu(yt) + e_\mu(-yt)(\tau_\mu P)(t) + P'(t)[e_\mu(yt) - e_\mu(-yt)]. \tag{20}
 \end{aligned}$$

Again taking the derivative of both sides of the above equation with respect to t , we obtain

$$\begin{aligned}
 &\sum_{j=2}^{\infty} \frac{p_j(y)}{\gamma_\mu(j)} (j + 2\mu\theta_j)(j - 1 + 2\mu\theta_j) t^{j-2} \\
 &= y^2P(t)e_\mu(yt) + ye_\mu(-yt)(\tau_\mu P)(t) + yP'(t)[e_\mu(yt) - e_\mu(-yt)] \\
 &- ye_\mu(-yt)(\tau_\mu P)(t) + e_\mu(yt)(\tau_\mu^2 P)(t) + [e_\mu(-yt) - e_\mu(yt)](\tau_\mu P)'(t) \\
 &+ [ye_\mu(yt) + ye_\mu(-yt)]P'(t) + [e_\mu(-yt) - e_\mu(yt)](\tau_\mu P') \\
 &+ 2[e_\mu(yt) - e_\mu(-yt)]P''(t).
 \end{aligned}$$

In the above expression, if y is replaced by my and t is replaced by 1 we can find

$$\begin{aligned} & \frac{1}{m^2} \frac{1}{P(1)e_\mu(my)} \sum_{j=0}^{\infty} \frac{p_j(my)}{\gamma_\mu(j)} (j + 2\mu\theta_j)^2 \\ &= y^2 + \frac{e_\mu(my)(2P'(1) + P(1)) + 2\mu P(-1)e_\mu(-my)}{mP(1)e_\mu(my)} y + \frac{(\tau_\mu P)(1)e_\mu(-my)}{m^2 P(1)e_\mu(my)} \\ &+ \frac{[2P''(1) - (\tau_\mu P)'(1) - (\tau_\mu P')(1) + P(1) - 2\mu P'(-1)](e_\mu(my) - e_\mu(-my))}{m^2 P(1)e_\mu(my)} \\ &+ \frac{(\tau_\mu^2 P)(1) + 2\mu(\tau_\mu P)(-1)}{P(1)m^2} \end{aligned}$$

For

$$\frac{1}{m^2} \frac{1}{P(1)e_\mu(my)} \sum_{j=0}^{\infty} \frac{p_j(my)}{\gamma_\mu(j)} (j + 2\mu\theta_j)$$

if we use the equation (20), we have

$$\frac{y}{m} + \frac{1}{m^2 P(1)e_\mu(my)} \{e_\mu(-my)(\tau_\mu P)(1) + P'(1)[e_\mu(my) - e_\mu(-my)]\}.$$

Lastly, we get that

$$\begin{aligned} \frac{1}{3m^2} \frac{1}{P(1)e_\mu(my)} \sum_{j=0}^{\infty} \frac{p_j(my)}{\gamma_\mu(j)} &= \frac{1}{3m^2} \frac{1}{P(1)e_\mu(my)} \sum_{j=0}^{\infty} \frac{p_j(my)}{\gamma_\mu(j)} P(1)e_\mu(my) \\ &= \frac{1}{3m^2}. \end{aligned}$$

Here is the following result:

$$\begin{aligned} E_m(t^2; y) &= y^2 + \frac{e_\mu(my)(2P'(1) + P(1)) + 2\mu P(-1)e_\mu(-my)}{mP(1)e_\mu(my)} y + \frac{(\tau_\mu P)(1)e_\mu(-my)}{m^2 P(1)e_\mu(my)} \\ &+ \frac{[2P''(1) - (\tau_\mu P)'(1) - (\tau_\mu P')(1) + P(1) - 2\mu P'(-1)](e_\mu(my) - e_\mu(-my))}{m^2 P(1)e_\mu(my)} \\ &+ \frac{(\tau_\mu^2 P)(1) + 2\mu(\tau_\mu P)(-1)}{P(1)m^2} \end{aligned}$$

$$\begin{aligned}
 & + \frac{y}{m} + \frac{1}{m^2 P(1) e_\mu(my)} \{e_\mu(-my)(\tau_\mu P)(1) + P'(1)[e_\mu(my) - e_\mu(-my)]\} \\
 & + \frac{1}{3m^2}.
 \end{aligned}$$

So, the proof of the lemma is completed.

Let us denote, the first and second moments of operator E_m as follows $\nabla_1 = E_m(\mathfrak{S} - y; y)$ and $\nabla_2 = E_m((\mathfrak{S} - y)^2; y)$.

Lemma2: For E_m operators, the following relations are hold:

$$\nabla_1 = \frac{1}{mP(1)e_\mu(my)} \{e_\mu(-my)(\tau_\mu P)(1) + P'(1)[e_\mu(my) - e_\mu(-my)]\} + \frac{1}{2m} \tag{21}$$

$$\begin{aligned}
 \nabla_2 = & \frac{e_\mu(my)(2P'(1) + P(1)) + 2\mu P(-1)e_\mu(-my)}{mP(1)e_\mu(my)} y + \frac{(\tau_\mu P)(1)e_\mu(-my)}{m^2 P(1)e_\mu(my)} \\
 & + \frac{[2P''(1) - (\tau_\mu P)'(1) - (\tau_\mu P')(1) + P(1) - 2\mu P'(-1)](e_\mu(my) - e_\mu(-my))}{m^2 P(1)e_\mu(my)} \\
 & + \frac{(\tau_\mu^2 P)(1) + 2\mu(\tau_\mu P)(-1)}{P(1)m^2} - \frac{2y}{mP(1)e_\mu(my)} \{e_\mu(-my)(\tau_\mu P)(1) + P'(1)[e_\mu(my) - e_\mu(-my)]\} \\
 & + \frac{1}{m^2 P(1)e_\mu(my)} \{e_\mu(-my)(\tau_\mu P)(1) + P'(1)[e_\mu(my) - e_\mu(-my)]\} + \frac{1}{3m^2}. \tag{22}
 \end{aligned}$$

3. MAIN RESULTS

In this section, the rate of convergence is given with the help of the classical modulus continuity and Lipschitz class functions.

Lipschitz class of order α , $Lip_m(\alpha)$ ($0 < \alpha \leq 1, M > 0$) is defined as follows:

$$Lip_M(\alpha) = \{f: |f(q) - f(l)| \leq M|q - l|^\alpha, q, l \in [0, \infty)\}.$$

Theorem 1. Let $\varpi \in Lip_M(\beta)$. Then we have

$$|E_m(\varpi; y) - \varpi(y)| \leq M \cdot (\nabla_2(y))^{\beta/2},$$

Where ∇_2 is given as (22).

Proof. From the monotony property of E_m and Lemma 1, we obtain

$$\begin{aligned}
 |E_m(\varpi; y) - \varpi(y)| & = |E_m(\varpi(\mathfrak{S})) - \varpi(y); y| \\
 & \leq E_m(|\varpi(\mathfrak{S}) - \varpi(y)|; y) \\
 & \leq M \cdot E_m(|\mathfrak{S} - y|^\beta; y).
 \end{aligned}$$

From the Hölder inequality the following expression is deduced

$$\begin{aligned}
 |E_m(\varpi; y) - \varpi(y)| &\leq \frac{m}{P(1)e_\mu(my)} \sum_{j=0}^{\infty} \frac{p_j(my)}{\gamma_\mu(j)} \int_{\frac{j+2\mu\theta_j}{m}}^{\frac{j+1+2\mu\theta_j}{m}} |\varpi(t) - \varpi(y)| dt \\
 &\leq M \cdot \frac{1}{P(1)e_\mu(my)} \sum_{j=0}^{\infty} \frac{p_j(my)}{\gamma_\mu(j)} \int_{\frac{j+2\mu\theta_j}{m}}^{\frac{j+1+2\mu\theta_j}{m}} m^{\frac{\beta}{2}} |t - y|^{\beta} m^{\frac{2-\beta}{2}} dt \\
 &\leq M \cdot \frac{1}{P(1)e_\mu(my)} \sum_{j=0}^{\infty} \frac{p_j(my)}{\gamma_\mu(j)} \left(\int_{\frac{j+2\mu\theta_j}{m}}^{\frac{j+1+2\mu\theta_j}{m}} m(t - y)^2 dt \right)^{\frac{\beta}{2}} \\
 &\quad \times \left(\int_{\frac{j+2\mu\theta_j}{m}}^{\frac{j+1+2\mu\theta_j}{m}} m dt \right)^{\frac{2-\beta}{2}} \\
 &\leq M \sum_{j=0}^{\infty} \left(\frac{p_j(my)}{P(1)e_\mu(my)\gamma_\mu(j)} \int_{\frac{j+2\mu\theta_j}{m}}^{\frac{j+1+2\mu\theta_j}{m}} m \left(\frac{j + 2\mu\theta_j}{m} - y \right)^2 dt \right)^{\frac{\beta}{2}} \\
 &\quad \times \left(\frac{p_j(my)}{P(1)e_\mu(my)\gamma_\mu(j)} \right)^{\frac{2-\beta}{2}} \\
 &\leq M \cdot \left(\sum_{j=0}^{\infty} \frac{p_j(my)}{P(1)e_\mu(my)\gamma_\mu(j)} \int_{\frac{j+2\mu\theta_j}{m}}^{\frac{j+1+2\mu\theta_j}{m}} m \left(\frac{j + 2\mu\theta_j}{m} - y \right)^2 dt \right)^{\frac{\beta}{2}} \\
 &\quad \times \left(\sum_{j=0}^{\infty} \frac{p_j(my)}{P(1)e_\mu(my)\gamma_\mu(j)} \right)^{\frac{2-\beta}{2}} \\
 &= M \cdot (\nabla_2)^{\frac{\beta}{2}}.
 \end{aligned}$$

If ∇_2 is selected as (23), the desired result is obtained.

The modulus of continuity of function $\varphi \in C[0, \infty)$ is defined (DeVore & Lorentz, 1993) as follows

$$\omega(\varphi; \delta) = \sup_{y, h \in [0, \infty)} \{|\varphi(y) - \varphi(h)|, |y - h| \leq \delta\}.$$

Theorem 2. Let f be a uniformly continuous function on $[0, \infty)$. Then the following holds;

$$|E_m(\varphi; y) - \varphi(y)| \leq (1 + \partial_m(y))\omega\left(\varphi; \frac{1}{\sqrt{m}}\right),$$

where $\partial_m(y) = \sqrt{(m\nabla_2)}$.

Proof. According to Lemma 1, it follows that

$$\begin{aligned} |E_m(\varphi; y) - \varphi(y)| &\leq \frac{m}{P(1)e_\mu(my)} \sum_{j=0}^{\infty} \frac{p_j(my)}{\gamma_\mu(j)} \int_{\frac{j+2\mu\theta_j}{m}}^{\frac{j+1+2\mu\theta_j}{m}} |\varphi(t) - \varphi(y)| dt \\ &\leq \left\{ 1 + \frac{1}{\delta} \frac{m}{P(1)e_\mu(my)} \sum_{j=0}^{\infty} \frac{p_j(my)}{\gamma_\mu(j)} \int_{\frac{j+2\mu\theta_j}{m}}^{\frac{j+1+2\mu\theta_j}{m}} |(t) - y| dt \right\} \omega(\varphi; \delta). \end{aligned}$$

In the right hand side of above inequality, if we use Schwarz inequality we get

$$\begin{aligned} &\frac{1}{P(1)e_\mu(my)} \sum_{j=0}^{\infty} \frac{p_j(my)}{\gamma_\mu(j)} \int_{\frac{j+2\mu\theta_j}{m}}^{\frac{j+1+2\mu\theta_j}{m}} \sqrt{m}|t - y|\sqrt{m} dt \\ &\leq \frac{1}{P(1)e_\mu(my)} \sum_{j=0}^{\infty} \frac{p_j(my)}{\gamma_\mu(j)} \left(\int_{\frac{j+2\mu\theta_j}{m}}^{\frac{j+1+2\mu\theta_j}{m}} m(t - y)^2 dt \right)^{\frac{1}{2}} \\ &\times \left(\int_{\frac{j+2\mu\theta_j}{m}}^{\frac{j+1+2\mu\theta_j}{m}} m dt \right)^{\frac{1}{2}} \\ &\leq \left(\sum_{j=0}^{\infty} \frac{p_j(my)}{P(1)e_\mu(my)\gamma_\mu(j)} \int_{\frac{j+2\mu\theta_j}{m}}^{\frac{j+1+2\mu\theta_j}{m}} m(t - y)^2 dt \right)^{\frac{1}{2}} \\ &\times \left(\sum_{j=0}^{\infty} \frac{p_j(my)}{\gamma_\mu(j)P(1)e_\mu(my)} \right)^{\frac{1}{2}} \end{aligned}$$

$$= \sqrt{(\nabla_2)}.$$

From the above inequality and $\delta = \frac{1}{\sqrt{m}}$, we get

$$\begin{aligned} |E_m(\varphi; y) - \varphi(y)| &\leq \left\{1 + \frac{1}{\delta} \sqrt{(\nabla_2)}\right\} \omega(f; \delta) \\ &\leq (1 + \partial_m(y)) \omega\left(\varphi; \frac{1}{\sqrt{m}}\right). \end{aligned}$$

So, the proof is completed.

REFERENCES

- Altomare, F., & Campiti, M. (1994). Korovkin-type Approximation Theory and its Applications. Walter de Gruyter.
- Ben Cheikh, Y., & Gaied, M. (2007). Dunkl-Appell d-orthogonal polynomials. *Integral Transforms and Special Functions*, 18(8), 581-597. doi:[10.1080/10652460701445302](https://doi.org/10.1080/10652460701445302)
- Bernstein, S. N. (1912). Demonstration of the Weierstrass theorem based on the calculation of probabilities. *Common Soc. Math. Charkow Ser. 2t, 13*, 1-2.
- DeVore, R. A., & Lorentz, G. G. (1993). *Constructive approximation*. Springer Berlin, Heidelberg.
- Gadzhiev, A. D. (1974). The convergence problem for a sequence of positive linear operators on unbounded sets, and theorems analogous to that of PP Korovkin. *Dokl. Akad. Nauk SSSR*, 218(5), 1001-1004.
- İçöz, G., & Çekim, B. (2016). Stancu-type generalization of Dunkl analogue of Szász-Kantorovich operators. *Mathematical Methods in the Applied Sciences*, 39(7), 1803-1810. doi:[10.1002/mma.3602](https://doi.org/10.1002/mma.3602)
- İçöz, G., Varma, S., & Sucu, S. (2016). Approximation by operators including generalized Appell polynomials. *Filomat*, 30(2), 429-440. doi:[10.2298/FIL1602429I](https://doi.org/10.2298/FIL1602429I)
- Jakimovski, A., & Leviatan, D. (1969). Generalized Szász operators for the approximation in the infinite interval. *Mathematica (Cluj)*, 11(34), 97-103.
- Kanat, K., & Sofyaloğlu, M. (2018). Approximation by (p,q)-Lupaş-Schurer-Kantorovich operators. *Journal of Inequalities and Applications*, 263. doi:[10.1186/s13660-018-1858-9](https://doi.org/10.1186/s13660-018-1858-9)
- Kanat, K., & Sofyaloğlu, M. (2019). On Stancu type generalization of (p, q)-Baskakov-Kantorovich operators. *Communications Faculty of Sciences University of Ankara Series A1 Mathematics and Statistics*, 68(2), 1995-2013. doi:[10.31801/cfsuasmas.478852](https://doi.org/10.31801/cfsuasmas.478852)
- Korovkin, P. P. (1953). Convergence of linear positive operators in the spaces of continuous functions. *Dokl. Akad. Nauk. SSSR (N.S.)*, 90, 961-964.
- Lorentz, G. G. (1953). *Bernstein Polynomials*. University of Toronto Press.
- Mursaleen, M., Rahman, S., & Alotaibi, A. (2016). Dunkl generalization of q-Szász-Mirakjan Kantorovich operators which preserve some test functions. *Journal of Inequalities and Applications*, 317. doi:[10.1186/s13660-016-1257-z](https://doi.org/10.1186/s13660-016-1257-z)
- Nasiruzzaman, M., & Aljohani, A. F. (2020a). Approximation by Szász-Jakimovski-Leviatan-type operators via aid of Appell polynomials. *Journal of Function Spaces*, 9657489. doi:[10.1155/2020/9657489](https://doi.org/10.1155/2020/9657489)
- Nasiruzzaman, M., & Aljohani, A. F. (2020b). Approximation by parametric extension of Szász-Mirakjan-Kantorovich operators involving the Appell polynomials. *Journal of Function Spaces*, 8863664. doi:[10.1155/2020/8863664](https://doi.org/10.1155/2020/8863664)
- Rosenblum, M. (1994). Generalized Hermite polynomials and the Bose-like oscillator calculus. In: A. Feintuch & I. Gohberg (Eds.), *Nonselfadjoint Operators and Related Topics* (pp. 369-396). Birkhäuser, Basel. doi:[10.1007/978-3-0348-8522-5_15](https://doi.org/10.1007/978-3-0348-8522-5_15)

- Sucu, S. (2014). Dunkl analogue of Szász operators. *Applied Mathematics and Computation*, 244, 42-48. doi:[10.1016/j.amc.2014.06.088](https://doi.org/10.1016/j.amc.2014.06.088)
- Sucu, S. (2020). Approximation by sequence of operators including Dunkl-Appell polynomials. *Bulletin of the Malaysian Mathematical Sciences Society*, 43(3), 2455-2464. doi:[10.1007/s40840-019-00813-w](https://doi.org/10.1007/s40840-019-00813-w)
- Sucu, S., İçöz, G., & Varma, S. (2012). On some extensions of Szász operators including Boas-Buck-type polynomials. *Abstract and Applied Analysis*, 680340. doi:[10.1155/2012/680340](https://doi.org/10.1155/2012/680340)
- Szász, O. (1950). Generalization of S. Bernstein's polynomials to the infinite interval. *Journal of Research of the National Bureau of Standards*, 45(3), 239-245.
- Yazici, S., Yeşildal, F. T., & Çekim, B. (2022). On a generalization of Szász-Mirakyan operators including Dunkl-Appell polynomials. *Turkish Journal of Mathematics*, 46(6), 2353-2365. doi:[10.55730/1300-0098.3273](https://doi.org/10.55730/1300-0098.3273)



Gazi University

Journal of Science

PART A: ENGINEERING AND INNOVATION

<http://dergipark.org.tr/gujsa>

Investigation of Organic and Inorganic Contaminants in Water Sources around Elbistan Lignite Beds

Ayça DOĞRUL SELVER^{1*} , Yusuf URAS¹ ¹Kahramanmaraş Sütçü İmam University, Geological Engineering Department, Kahramanmaraş, Türkiye

Keywords	Abstract
Kahramanmaraş	The household and industrial use, as well as mining of coal, pose various environmental and health risks including lung and kidney diseases such as Balkan Endemic Nephropathy (BEN). BEN is a kidney disease and it is geographically confined to Balkan countries where extensive lignite deposits are located. The most accepted cause of BEN is the use of untreated waters contaminated by lignite-derived organic contaminants. Afşin-Elbistan basin contains approximately 50 % of the lignite reserves of Turkey which makes it an ideal location for the current study. In this work, water samples were taken from 10 different locations in the Afşin-Elbistan basin and they were analyzed for organic and inorganic contaminants. Results showed that none of the water samples were contaminated with inorganic contaminants and indeed met the Turkish drinking water standards. GC-MS analyses of the water samples revealed similar chromatograms. Briefly, all the water samples have similar organic compound types such as n-alkanes, chlorophyll-derived phytols, and plant- and animal-derived acids (i.e. palmitic acid). On the other hand, none of the samples were contaminated with carcinogenic and/or nephrotoxic organic compounds such as polyaromatic hydrocarbons and aromatic amines, which is contrary to many, but not all of the previous works conducted in Balkan countries. All these results may indicate that the influence of coal deposits on the groundwaters is minimal.
Lignite	
Organic Contaminants	
Inorganic Contaminants	
Groundwater	

Cite

Doğrul Selver, A., & Uras Y. (2022). Investigation of Organic and Inorganic Contaminants in Water Sources Around Elbistan Lignite Beds. *GU J Sci, Part A, 9(3)*, 347-358.

Author ID (ORCID Number)	Article Process
A. Doğrul Selver, 0000-0002-9003-5439	Submission Date 04.08.2022
Y. Uras, 0000-0001-5561-3275	Revision Date 24.08.2022
	Accepted Date 14.09.2022
	Published Date 30.09.2022

1. INTRODUCTION

Coal is still extensively used all over the world for electricity generation, industrial purposes, and heating. As it is well known, there are serious health problems and environmental issues associated with coal mining and use (Ding et al., 2001; Tiwary, 2001). Low-rank coals, such as lignites, contain various toxic organic and inorganic compounds such as polyaromatic hydrocarbons (PAHs), aromatic amines, lead, and cadmium. Groundwater and surface water leaches some of these organic compounds from the lignite beds and the use of these waters may lead to health problems like kidney diseases and cancer.

One of the health problems (possibly) related to the low-rank coals is a kidney disease named Balkan Endemic Nephropathy (BEN; Feder et al., 1991; Finkelman et al., 2002; Orem et al., 1999; 2002). BEN is geographically restricted to Balkan countries where Pliocene lignites are extensively found. On the other hand, studies are showing BEN-like diseases outside of Balkan countries (i.e. U.S.A) which is called Pan-endemic Nephropathy (PEN; Orem et al., 2007). There are numerous hypotheses for BEN aetiology such as exposure to toxins (Grollman & Jelaković, 2007; Lukinich-Gruia et al., 2022; Pfohl-Leszkowicz, et al., 2002; Stiborová et al., 2016, Stoev, 2017), to organic compounds leached from low-rank coal deposits (mainly lignites; Feder et al., 1991; Ojeda et al., 2019) and deficiency of some metals. However there are still some debates, the Pliocene lignite hypothesis is a plausible hypothesis mainly because of the high correlation between lignite deposit

*Corresponding Author, e-mail: aycaselve@ksu.edu.tr

locations and the BEN-endemic villages (Voice et al., 2006). The lignite hypothesis briefly suggests that organic contaminants leach into groundwater from lignite beds and the use of these untreated waters leads to acute exposure to low concentrations of nephrotoxic compounds which may lead to BEN (Orem et al., 1999).

Previous studies showed that untreated well waters taken from Balkan countries (mainly used for drinking) have numerous toxic and potentially toxic organic compounds such as PAHs (i.e. naphthalene, phenanthrene, anthracene, fluoranthene), phenolic compounds, heterocyclic compounds (N-, S-, O- containing cyclic compounds) and aliphatic compounds (Chakraborty et al., 2017; Orem et al., 1999; 2002). Leach experiments, indeed, indicated that water can leach many aromatic organic compounds from coal (Maharaj, 2014) therefore same compounds can be found both in the waters and in the coal samples (Maharaj et al., 2013; Maharaj, 2014; Orem et al., 2002). Concentrations of organic compounds in endemic area waters were found to be very low in concentration (usually $<0,1 \mu\text{g/L}$) however both concentrations and the number of compound types are higher compared to control group samples (Finkelman, 2007; Orem et al., 1999). On the other hand, the inorganic compounds such as lead and cadmium and anions like nitrate, sulfate are almost identical in both endemic and control group samples which leads to exclusion of metal deficiency hypothesis.

Although numerous studies were done in the Balkan countries and the lignite hypothesis is one of the accepted cause of BEN (Maharaj, 2014), new studies conducted on other lignite bearing areas from different parts of the world will surely help to understand (a) if untreated waters which are being in use show the similar contamination patterns and (b) if BEN-like diseases are common in these regions as well.

According to Ministry of Energy and Natural Sources (2017) data, approximately 50 % of the lignite reserves of Turkey, with a measured reserve amount of approximately 4 billion tonnes, are found in the Afşin – Elbistan basin. Considering the massive lignite reserves and water pollution being the secondary priority problem in Kahramanmaraş (Directorate General of Environmental Impact Assessment, 2018), this region is geographically ideal for the present study. The overarching aim of this study was to understand if untreated well waters taken from the Afşin-Elbistan basin are contaminated with (lignite-derived) organic and inorganic compounds and to see if the results are in line with the previous studies. In addition, although a BEN-like disease has not been reported in the study area yet, the results of this work may be a reference study for similar works and for the research on the kidney health of the residents of the area.

2. MATERIAL AND METHODS

2.1. Study Area and Sampling

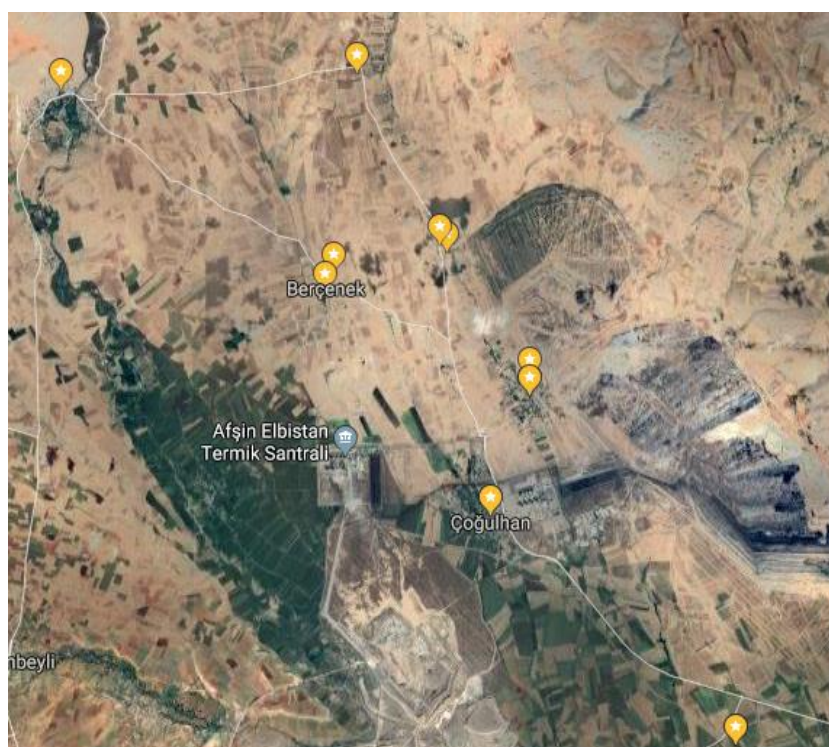
Water samples were collected from Berçenek, Alemdar, Çoğulhan, Kışlaköy and Çomudüz villages of Afşin-Kahramanmaraş (Table 1; Figure 1). All of the villages are near the Afşin-Elbistan thermal power plant and they are located on coal beds. 9 untreated well water samples and 1 surface water sample (sample number 7, as a control sample) were collected in the field. On every sampling location, in-situ measurements (i.e. pH and temperature) were conducted.

Different sampling methodologies were followed for different analyses types. For organic compounds sampling, all glasswares were solvent-cleaned (acetone) before use to avoid any organic contamination. On each location, on-site filtration was conducted by using a glass vacuum filtration apparatus with a manual pump and $0,45 \mu\text{m}$ glass fiber filters attached. 2 liters of water sample was filtered and collected in pre-cleaned glass bottles and 60 ml of methylene chloride (DCM) was added to each bottle to retard bacterial activity during storage. When sampling is done at one location, glass fiber is removed and all glass parts of the filtering apparatus was cleaned with acetone and DCM. Upon arrival to the laboratory, water samples were stored in the fridge until extraction.

For inorganic analyses, 100 ml water samples were filtered through cellulose syringe filters ($0,45\mu\text{m}$) and collected in polyethylene sampling bottles. Upon arrival to the laboratory, water samples were stored in the fridge. These samples were directly sent to KSU-USKİM (Kahramanmaraş Sütçü İmam University) and ACME Laboratories (Canada) for anion and cation analyses respectively.

Table 1. Coordinates of Sampling Locations

Sample No	Latitude	Longitude	Location	pH	Temperature
1	38°18'02.2"N	37°04'30.9"E	Kuşkayası	6,6	13.3
2	38°20'32.7"N	37°01'02.4"E	Çoğulhan	7.1	15
3	38°21'51.3"N	37°01'36.0"E	Alemdar	7.2	17.3
4	38°22'02.4"N	37°01'35.4"E	Alemdar	7.1	17.3
5	38°23'25.3"N	37°00'24.6"E	Çomudüz	7.3	13.6
6	38°23'30.5"N	37°00'18.5"E	Çomudüz	6.7	15.4
7	38°25'11.6"N	36°54'55.6"E	Tanır	7.3	11.1
8	38°23'11.4"N	36°58'49.1"E	Berçenek	7.4	14.8
9	38°22'58.9"N	36°58'41.6"E	Berçenek	7.2	14.1
10	38°25'22.9"N	36°59'08.3"E	Büget	7.1	14.0

**Figure 1.** Map of the Sampling Locations

2.2. Extractions and Instrumental Analyses for Organic Analyses

Extractions of the water samples were done in Geochemistry Laboratory, Kahramanmaraş Sütçü İmam University. The extraction methodology was adapted from Orem et al. (2007). Briefly, water samples were extracted by liquid/liquid extraction with four successive volumes of GC-MS grade DCM (60ml). The combined total lipid extract (240ml, TLE) was reduced to a volume of a few milliliters by rotary evaporation which was concentrated to 200 µl by evaporation under a nitrogen blow-down unit. A fraction of TLE was then used during gas chromatography/mass spectrometry (GC-MS) analyses.

GC-MS analyses were done on the TLE extracts (ULUTEM research facilities, Gaziantep University). Assignment of organic compounds was performed using a Shimadzu QP2020 GC-MS. A RESTEK Rxi-5ms column (30 m x 0,25 mm x 0.25 µm, 95 % dimethyl polysiloxane, 5 % diphenyl) was used for GC-MS analyses. The GC/MS operation settings were as described in Chakraborty et al. (2017).

Table 2. Concentrations of Anions

Sample No	Fluoride (ppm)	Chloride (ppm)	Sulfite (ppm)	Nitrite (ppm)	Nitrate (ppm)	Phosphate (ppm)
1	0,38	14,77	54,31	BDL	32,8	BDL
2	1,8	6,05	99,54	BDL	7	BDL
3	0,36	37,98	98,69	BDL	84,42	BDL
4	0,44	16,28	38,7	BDL	58,91	BDL
5	0,16	2,47	30,19	BDL	7,43	BDL
6	0,22	36,31	40,7	BDL	127,61	BDL
7	0,08	0,77	4,26	BDL	4,43	BDL
8	0,37	9,84	25,68	BDL	29,1	BDL
9	0,31	14,67	38,05	BDL	40,69	BDL
10	0,3	48,46	24,34	BDL	168,16	BDL
Mean	0,44	18,76	45,45	–	56,06	–

3. RESULTS AND DISCUSSION

3.1. Inorganic Analyses

Anion analyses showed that in all samples, nitrite and phosphate concentrations were below detection limits which are 0.054 ppm and 0.114 ppm respectively (Table 2; Figure 2). Fluoride concentrations ranged between 0.08–1.8 ppm (mean value of 0.44 ppm); chloride concentrations were between 0.77 – 48.5 ppm (mean value of 18.45 ppm); sulfate and nitrate concentrations ranged between 4.3–99.5 ppm and 7–168.2 ppm (mean values of 45.45 ppm and 56.06 ppm), respectively. Sample 2 showed the highest fluoride and sulfate concentrations with being 1.8 ppm and 99.54 ppm respectively. Sample 10 had the maximum chloride concentration (48.46 ppm) and nitrate concentration (168.16 ppm) while the control sample (sample 7) had the lowest concentrations of all anions.

These anion results showed that all well water samples, although they are mainly used for irrigation purposes, meet the Turkish regulations for drinking water criteria (Doğrul Selver & Uras, 2022). Considering the TS266 and WHO drinking water standards (Table 3), four of the samples exceed the acceptable limit for nitrate (sample number 3, 4, 6, and 10; 50 mg/L) on the other hand, all samples were below the acceptable limit for sulfate (250 mg/L), fluoride (1.5 mg/L) as well as chloride (250 mg/L; Table 2 and 3).

Orem et al. (2002) reported high nitrate concentrations (225 mg/l) in untreated well water samples taken from both BEN endemic and non-endemic sites which suggests that high nitrate concentrations can not be associated to BEN etiology. In this study, maximum nitrate concentration was measured in the water sample taken from the Büget region (sample number 10; 168.8 ppm) which is a large farmyard. On the other hand, in all the samples sulfate concentrations are much higher (4.2 - 99.5 mg/L) which is similar to what Orem et al. (2002) reported.

Cation results showed that none of the samples appear to be contaminated with heavy metals or with the metals suggested to have nephrotoxic effects. For instance, among toxic heavy metals, Hg, Cd, and Fe concentrations were below the detection limits in all water samples (Figure 3, Supplementary Table 1). All the other heavy metals (i.e. Cr, Co, Cu, Mn, Ni, and Zn) had concentrations below the minimum allowed limit for drinking water (Table 3). In addition, there was no major difference between the control group sample (sample 7) and

the other samples. Similarly, previous studies indicated that metal concentrations are similar in endemic and non-endemic sites (Batuman, 2006; Orem et al., 2002; 2004). Cd and Pb were suggested to have nephrotoxic effects and therefore it was suggested that these metals should be analyzed in well waters as well (Fowler et al., 2004; Orem et al., 1999; Weeden, 1991). In all the water samples analyzed in the present study, Pb and Cd concentrations are below detection limits (except for sample 8 and sample 10 for Pb concentration). In addition, As, B, Br, Cl, Cr, F, Li, Na, P, Rb, Se, Sr, and W are found to be statistically related to renal cancer rates in northwest Louisiana (Bunnell et al., 2006) however in the current study none of these elements are higher than allowed limits as well. Consequently, inorganic contaminants results are in line with the previous studies showing insignificant concentration values to be evaluated for environmental and health aspects.

Table 3. WHO and Turkish Drinking Water Standards

Element	WHO Standard (1993)	TS266 (2005)	Element	WHO Standard (1993)	TS266 (2005)
Al ($\mu\text{g/L}$)	200	200	Mn ($\mu\text{g/L}$)	100	50
As ($\mu\text{g/L}$)	10	10	Ni ($\mu\text{g/L}$)	70	20
B ($\mu\text{g/L}$)	2400	1000	Pb ($\mu\text{g/L}$)	10	10
Ba ($\mu\text{g/L}$)	700	–	Zn ($\mu\text{g/L}$)	3000	–
Cd ($\mu\text{g/L}$)	3	5	Flouride (mg/L)	1.5	1.5
Cr ($\mu\text{g/L}$)	50	50	Chloride (mg/L)	250	250
Cu ($\mu\text{g/L}$)	2000	2000	Nitrate (mg/L)	50	50
Fe ($\mu\text{g/L}$)	300	200	Sulfate (mg/L)	250	250
Hg ($\mu\text{g/L}$)	1	1	Nitrite (mg/L)	3	0,5

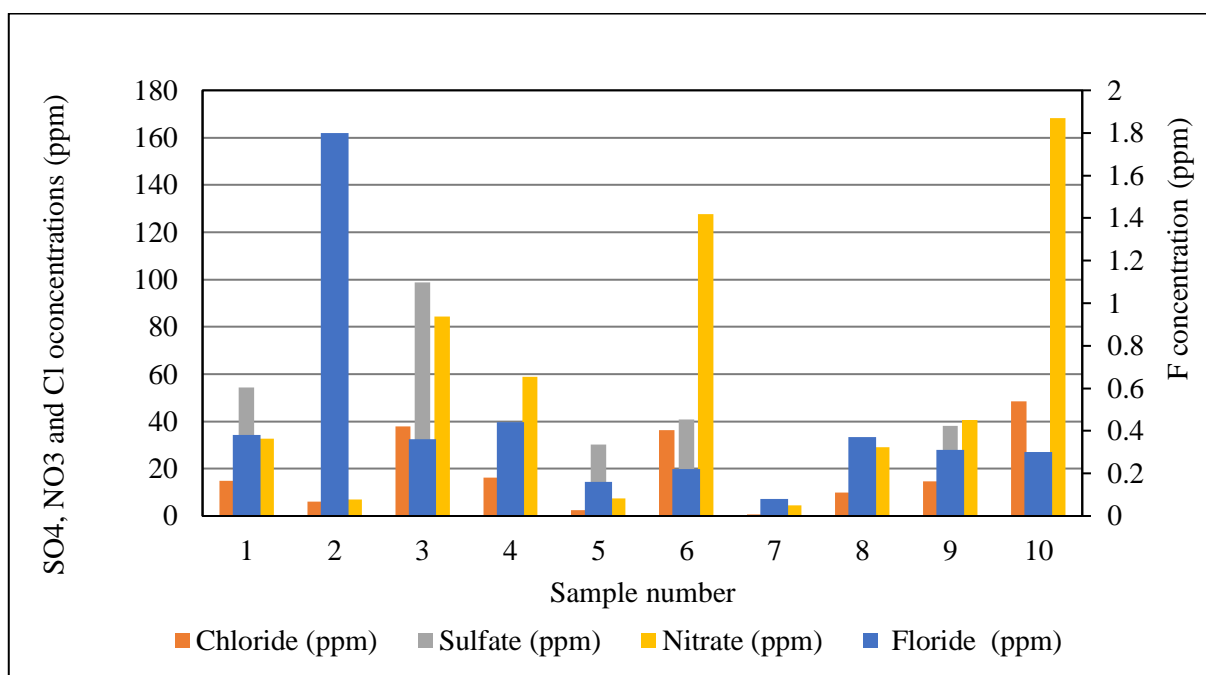


Figure 2. Histograms Showing Concentrations of Anions

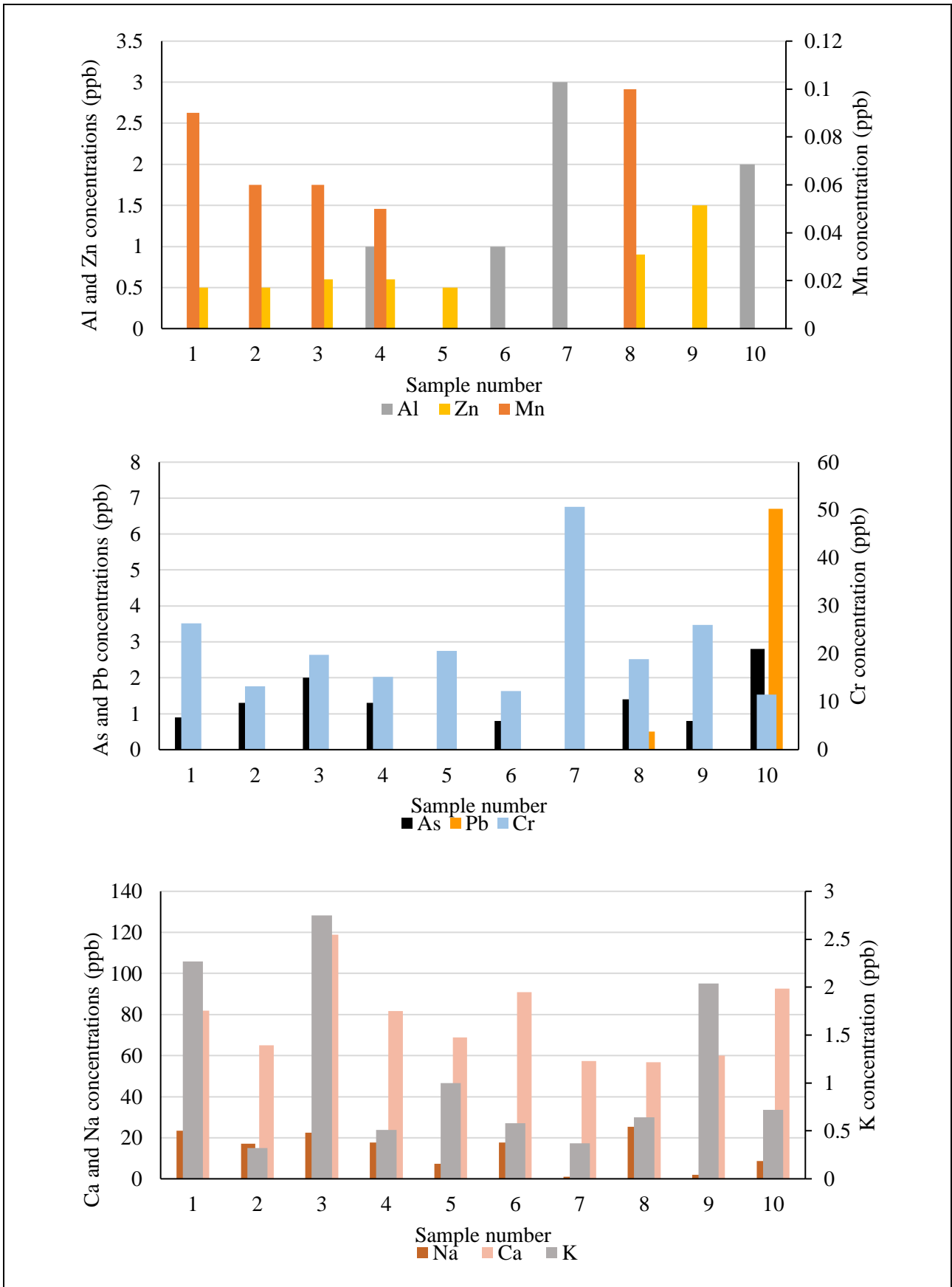


Figure 3. Histograms Showing Concentrations of Different Metals

3.2. Organic Analyses

A non-target screening methodology has been applied therefore the concentrations of compounds were not calculated. Similar chromatograms were obtained for all samples and major peaks in the chromatograms were identified. As a representative of all samples, labelled gas chromatogram of sample 9 was shown in Figure 4. Briefly, results showed that all water samples mainly contain n-alkanes, some animal and plant derived compounds (i.e. phytol and palmitic acid) and phthalates. None of the target compounds as being carcinogenic and nephrotoxic natures, such as PAHs and aromatic amines, were observed.

n-alkanes (C12-C34) are abundantly found in the samples which could indicate the addition of plant-derived compounds into the water sources. Palmitic acid which is a common compound found in plants and animals, and chlorophyll indicators such as phytol were also found in almost all the water samples.

Earlier studies indicated that, in well water samples taken from BEN endemic areas, the concentration and the number of organic compounds are higher than those of the non-endemic regions (Feder et al., 1991; Maharaj, 2014; Orem et al., 2002; 2007). On the other hand, the GC-MS results of the present study revealed that the organic compound composition of all the water samples is similar to each other. In almost all the water samples, phthalates, the most widespread man-made contaminants, were found. This finding is in line with the earlier studies where they found abundant and numerous phthalates (Bunnell et al., 2006; Maharaj, 2014). Bunnell et al. (2006) suggested that these phthalates are mainly originated from PVC well casings and plastic parts of the pump systems. Contamination during sample handling and extraction can be another explanation for phthalates in the water samples.

Most of the previous studies (Feder et al., 1991; Maharaj, 2014; Orem et al., 2002; 2007) showed that water samples taken from BEN-endemic areas contain coal- originated organic compounds such as PAHs, aliphatic & aromatic compounds, aromatic amines, some of which are known as nephrotoxic and/or carcinogenic compounds. In contrast, water samples taken from Afşin-Elbistan area are not contaminated with these abovementioned nephrotoxic and carcinogenic organic compounds, which may suggest a minimal influence of coal deposits on the groundwater quality. This outcome is parallel to the results of Iordanidis et al. (2016) and Kosateva et al. (2017a) reported. PAHs were not found in Amyneto lignites, Northern Greece and similarly coal derived PAHs were also not found in groundwater samples taken from Amyneto lignite basin which in turn indicates a minor influence of lignite deposits on groundwaters (Iordanidis et al., 2016). In other studies, Kosateva et al. (2017a) did leach experiments on Bulgarian lignites for 10 weeks by using different solvents and analytical equipments however did not find any harmful/ toxic organic compounds in the leachates (Kosateva et al., 2017a; 2017b). Considering all these, the absence of PAHs and other toxic and/or carcinogenic compounds in groundwaters related with lignites, as in the present study, and in leachates of lignites is not confounding.

4. CONCLUSIONS

In the current study, 10 water samples taken from the Afşin-Elbistan Basin were analyzed for organic and inorganic contaminants to understand whether these sources are contaminated and to evaluate the possible effects of coal beds on these water sources. Inorganic analyses showed that none of the toxic heavy metals including the ones that suggested to have nephrotoxic and/or carcinogenic effects (such as Cd, Pb, Fe and Al) are above the drinking water standards. This finding is in-line with most of the previous studies. In addition, organic analyses indicated that all water samples have similar organic matter compositions and have limited organic compound variation. To exemplify; while n-alkanes, phthalates, and some other common plant- & animal- derived organic compounds are present in almost all water samples, coal-derived compounds (such as PAHs and aromatic amines) are not found in any of the water samples. The lack of coal-derived organic molecules in well water samples may suggest that the effect of coal deposits on the groundwater quality is trivial. Surely, this work can be a reference study for similar prospective studies (on the research of the kidney health of the local people of the area as well) however, triplicate GC-MS runs for each sample and concentration measurements of the organic compounds would allow for more robust interpretations.

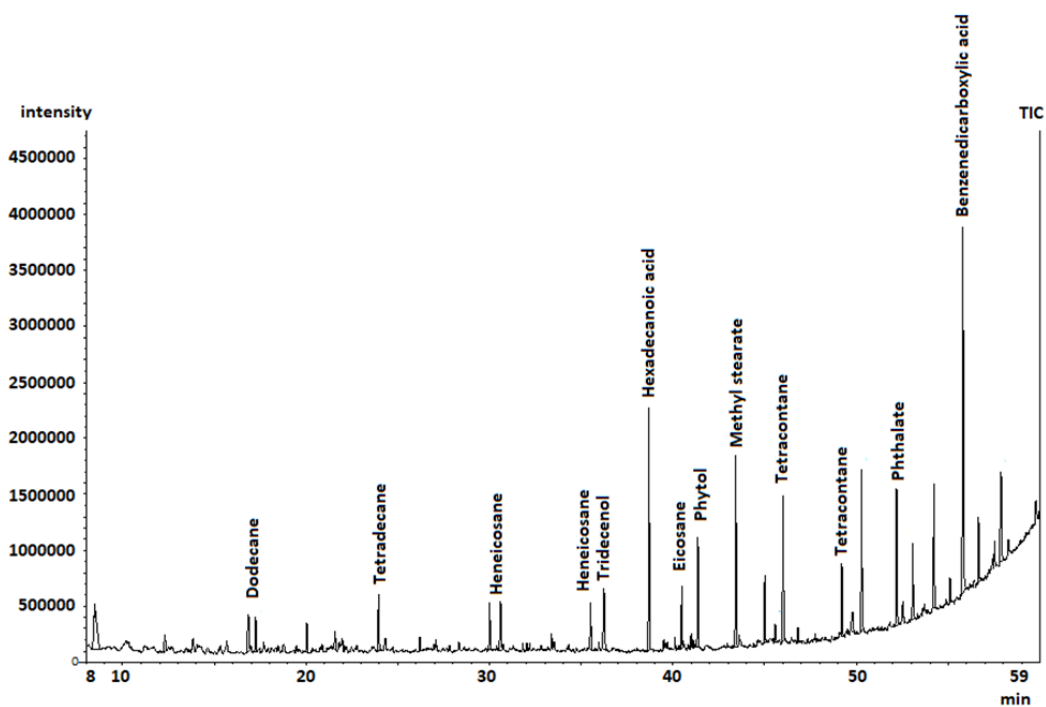


Figure 4. GC-MS chromatogram of sample 9

ACKNOWLEDGMENTS

We gratefully acknowledge the financial support by KSU-BAP (Project number:2018/7-36M). We thank Gelişim Laboratuvarı for designing a nitrogen blow-down set-up.

CONFLICT OF INTEREST

The authors declare no conflict of interest.

REFERENCES

- Batuman, V. (2006). Fifty years of Balkan endemic nephropathy: Daunting questions, elusive answers. *Kidney International*, 69(4), 644–646. doi:[10.1038/sj.ki.5000231](https://doi.org/10.1038/sj.ki.5000231)
- Bunnell, J. E., Tatu, C. A., Bushon, R. N., Stoeckel, D. M., Brady, A. M. G., Beck, M., Lerch, H. E., McGee, B., Hanson, B. C., Shi, R., & Orem, W. H. (2006). Possible linkages between lignite aquifers, pathogenic microbes, and renal pelvic cancer in northwestern Louisiana, USA. *Environmental Geochemistry and Health*, 28(6), 577–587. doi:[10.1007/s10653-006-9056-y](https://doi.org/10.1007/s10653-006-9056-y)
- Chakraborty, J., Varonka, M., Orem, W., Finkelman, R. B., & Manton, W. (2017). Geogenic organic contaminants in the low-rank coal-bearing Carrizo-Wilcox aquifer of East Texas, USA. *Hydrogeology Journal*, 25(4), 1219–1228. doi:[10.1007/s10040-016-1508-6](https://doi.org/10.1007/s10040-016-1508-6)
- Ding, Z., Zheng, B., Long, J., Belkin, H. E., Finkelman, R. B., Chen, C., Zhou, D., & Zhou, Y. (2001). Geological and geochemical characteristics of high arsenic coals from endemic arsenosis areas in southwestern Guizhou Province, China. *Applied Geochemistry*, 16(11–12), 1353–1360. doi:[10.1016/S0883-2927\(01\)00049-X](https://doi.org/10.1016/S0883-2927(01)00049-X)
- Directorate General of Environmental Impact Assessment, Permit and Inspection (2018). Türkiye Çevre Sorunları ve Öncelikleri Değerlendirme Raporu (2016 yılı verileriyle). [PDF](#)
- Doğrul Selver, A., & Uras, Y. (2022, June 16-18). *Organic and Inorganic Contaminants In Water Sources Around Elbistan Basin*. In: International Symposium on Advanced Engineering Technologies. Kahramanmaraş.

- Feder, G., Radovanovic, Z., & Finkelman, R. (1991). Relationship between weathered coal deposits and the etiology of Balkan endemic nephropathy. *Kidney International*, 40(34), S9–S11.
- Finkelman, R. B. (2007). Health impacts of coal: facts and fallacies. *Ambio*, 36(1), 103–106. doi:[10.1579/0044-7447\(2007\)36\[103:HIOCFA\]2.0.CO;2](https://doi.org/10.1579/0044-7447(2007)36[103:HIOCFA]2.0.CO;2)
- Finkelman, R. B., Orem, W., Castranova, V., Tatu, C. A., Belkin, H. E., Zheng, B., Lerch, H. E., Maharaj, S. V., & Bates, A. L. (2002). Health impacts of coal and coal use: Possible solutions. *International Journal of Coal Geology*, 50(1–4), 425–443. doi:[10.1016/S0166-5162\(02\)00125-8](https://doi.org/10.1016/S0166-5162(02)00125-8)
- Fowler, B. A., Whittaker, M. H., Lipsky, M., Wang, G., & Chen, X.-Q. (2004). Oxidative stress induced by lead, cadmium and arsenic mixtures: 30-Day, 90-day, and 180-day drinking water studies in rats: An overview. *BioMetals*, 17(5), 567–568. doi:[10.1023/B:BIOM.0000045740.52182.9d](https://doi.org/10.1023/B:BIOM.0000045740.52182.9d)
- Grollman, A. P., & Jelaković, B. (2007). Role of Environmental Toxins in Endemic (Balkan) Nephropathy. *Journal of the American Society of Nephrology*, 18(11), 2817–2823. doi:[10.1681/ASN.2007050537](https://doi.org/10.1681/ASN.2007050537)
- Iordanidis, A., Schwarzbauer, J., & Gudulas, K. (2016). Organic Pollutants in the Groundwaters Used for Irrigation Purpose Within a Coal-Bearing Basin of Northern Greece. *Bulletin of the Geological Society of Greece*, 50(4), 2155–2162. doi:[10.12681/bgsg.14268](https://doi.org/10.12681/bgsg.14268)
- Kosateva, A. D., Stefanova, M., Marinov, S. P., & Gonsalvesh, L. (2017a). Organic components in leachates from some Bulgarian lignites. *Bulgarian Chemical Communications*, 49(D), 25–29.
- Kosateva, A. D., Stefanova, M., Marinov, S., Czech, J., Carleer, R., & Yperman, J. (2017b). Characterization of organic components in leachables from Bulgarian lignites by spectroscopy, chromatography and reductive pyrolysis. *International Journal of Coal Geology*, 183(October), 100–109. doi:[10.1016/j.coal.2017.10.005](https://doi.org/10.1016/j.coal.2017.10.005)
- Lukinich-Gruia, A. T., Nortier, J., Pavlović, N. M., Milovanović, D., Popović, M., Drăghia, L. P., Păunescu, V., & Tatu, C. A. (2022). Aristolochic acid I as an emerging biogenic contaminant involved in chronic kidney diseases: A comprehensive review on exposure pathways, environmental health issues and future challenges. *Chemosphere*, 297(February). doi:[10.1016/j.chemosphere.2022.134111](https://doi.org/10.1016/j.chemosphere.2022.134111)
- Maharaj, S. V. M. (2014). Limitations and plausibility of the Pliocene lignite hypothesis in explaining the etiology of Balkan endemic nephropathy. *International Journal of Occupational and Environmental Health*, 20(1), 77–91. doi:[10.1179/2049396713Y.0000000046](https://doi.org/10.1179/2049396713Y.0000000046)
- Maharaj, S. V. M., Orem, W. H., Tatu, C. A., Lerch, H. E., 3rd, & Szilagyi, D. N. (2013). Organic compounds in water extracts of coal: Links to Balkan endemic nephropathy. *Environmental Geochemistry and Health*, 36(1), 1–17. doi:[10.1007/s10653-013-9515-1](https://doi.org/10.1007/s10653-013-9515-1)
- Ministry of Energy and Natural Resources. (2017). Kömür. (Accessed:01/01/2017) enerji.gov.tr/bilgimerkezi-tabiiikaynaklar-komur
- Ojeda, A. S., Ford, S. D., Gallucci, R. M., Ihnat, M. A., & Philp, R. P. (2019). Geochemical characterization and renal cell toxicity of water-soluble extracts from U.S. Gulf Coast lignite. *Environmental Geochemistry and Health*, 41(2), 1037–1053. doi:[10.1007/s10653-018-0196-7](https://doi.org/10.1007/s10653-018-0196-7)
- Orem, W. H., Feder, G. L., & Finkelman, R. B. (1999). A possible link between Balkan endemic nephropathy and the leaching of toxic organic compounds from Pliocene lignite by groundwater: Preliminary investigation. *International Journal of Coal Geology*, 40(2–3), 237–252. doi:[10.1016/S0166-5162\(98\)00071-8](https://doi.org/10.1016/S0166-5162(98)00071-8)
- Orem, W. H., Tatu, C. A., Feder, G. L., Finkelman, R. B., Lerch, H. E., Maharaj, S. V. M., Szilagyi, D., Dumitrascu, V., Paunescu, V., & Margineanu, F. (2002). Environment, geochemistry and the etiology of balkan endemic nephropathy: lessons from Romania. *Facta Universitatis, Medicine and Biology Series*, 9(1), 39–48.
- Orem, W. H., Tatu, C. A., Lerch, H. E., Susan V. M. Maharaj, N. P., Paunescu, V., & Dumitrascu, V. (2004). Identification and environmental significance of the organic compounds in water supplies associated with a Balkan endemic nephropathy region in Romania. *Journal of Environmental Health Research*, 3(2), 53–61.

- Orem, W., Tatu, C., Pavlovic, N., Bunnell, J., Lerch, H., Paunescu, V., Ordodi, V., Flores, D., Corum, M., & Bates, A. (2007). Health effects of toxic organic substances from coal: Toward “panendemic” nephropathy. *Ambio*, 36(1), 98–102. doi:[10.1579/0044-7447\(2007\)36\[98:heotos\]2.0.co;2](https://doi.org/10.1579/0044-7447(2007)36[98:heotos]2.0.co;2)
- Pfohl-Leszkowicz, A., Petkova-Bocharova, T., Chernozemsky, I. N., & Castegnaro, M. (2002). Balkan endemic nephropathy and associated urinary tract tumours: A review on aetiological causes and the potential role of mycotoxins. *Food Additives and Contaminants*, 19(3), 282–302. doi:[10.1080/02652030110079815](https://doi.org/10.1080/02652030110079815)
- Stiborová, M., Arlt, V. M., & Schmeiser, H. H. (2016). Balkan endemic nephropathy: an update on its aetiology. *Archives of Toxicology*, 90(11), 2595–2615. doi:[10.1007/s00204-016-1819-3](https://doi.org/10.1007/s00204-016-1819-3)
- Stoev, S. D. (2017). Balkan Endemic Nephropathy – Still continuing enigma, risk assessment and underestimated hazard of joint mycotoxin exposure of animals or humans. *Chemico-Biological Interactions*, 261, 63–79. doi:[10.1016/j.cbi.2016.11.018](https://doi.org/10.1016/j.cbi.2016.11.018)
- Tiwary, R. K. (2001). Environmental Impact of Coal Mining Onwater Regime and Its Management. *Water, Air, & Soil Pollution*, 132(1-2), 185-199. doi:[10.1023/A:1012083519667](https://doi.org/10.1023/A:1012083519667)
- Voice, T. C., McElmurry, S. P., Long, D. T., Dimitrov, P., Ganey, V. S., & Peptropoulos, E. A. (2006). Evaluation of the hypothesis that Balkan endemic nephropathy is caused by drinking water exposure to contaminants leaching from Pliocene coal deposits. *Journal of Exposure Science & Environmental Epidemiology*, 16, 515–524. doi:[10.1038/sj.jes.7500489](https://doi.org/10.1038/sj.jes.7500489)
- Weeden, R. P. (1991). Environmental renal disease: lead, cadmium and Balkan endemic nephropathy. *Kidney International Supplement*, 34.

Supplementary Table 1. Cation Concentrations of the Water Samples (in ppb ($\mu\text{g/L}$))

Sample No	Ag	Al	As	Au	B	Ba	Be	Bi	Br	Ca	Cd	Ce	Cl	Co
1	BDL	BDL	0.9	BDL	206	88.55	BDL	BDL	231	81.94	BDL	BDL	13	0.03
2	BDL	BDL	1.3	BDL	222	105.65	BDL	BDL	96	64.94	BDL	BDL	9	0.06
3	BDL	BDL	2	BDL	125	42.44	BDL	BDL	176	118.8	BDL	BDL	37	0.02
4	BDL	1	1.3	BDL	132	73.01	BDL	BDL	143	81.75	BDL	BDL	17	BDL
5	BDL	BDL	BDL	BDL	38	98.35	BDL	BDL	43	68.82	BDL	BDL	4	BDL
6	BDL	1	0.8	BDL	67	73.89	0.06	BDL	142	90.81	BDL	BDL	30	BDL
7	BDL	3	BDL	BDL	8	6.23	BDL	BDL	7	57.28	BDL	BDL	1	BDL
8	BDL	BDL	1.4	BDL	81	74.96	BDL	BDL	65	56.7	BDL	BDL	10	BDL
9	BDL	BDL	0.8	BDL	58	95.62	BDL	BDL	65	60.04	BDL	BDL	14	BDL
10	BDL	2	2.8	BDL	32	20.2	BDL	BDL	89	92.55	BDL	BDL	42	BDL
Sample No	Cr	Cs	Cu	Dy	Er	Eu	Fe	Ga	Gd	Ge	Hf	Hg	Ho	In
1	26.4	BDL	0.4	BDL	BDL	BDL	BDL	BDL	BDL	BDL	BDL	BDL	BDL	BDL
2	13.2	BDL	0.7	BDL	0.02	BDL	BDL	BDL	BDL	BDL	BDL	BDL	BDL	BDL
3	19.8	BDL	1.2	BDL	BDL	BDL	BDL	BDL	BDL	BDL	BDL	BDL	BDL	BDL
4	15.2	BDL	0.5	BDL	BDL	BDL	BDL	BDL	BDL	BDL	BDL	BDL	BDL	BDL
5	20.6	0.01	0.5	BDL	BDL	BDL	BDL	BDL	BDL	BDL	BDL	BDL	BDL	BDL
6	12.2	0.03	0.6	BDL	BDL	BDL	BDL	BDL	BDL	BDL	BDL	BDL	BDL	BDL
7	50.7	BDL	0.2	BDL	BDL	BDL	BDL	BDL	BDL	BDL	BDL	BDL	BDL	BDL
8	18.9	BDL	0.4	BDL	BDL	BDL	BDL	BDL	BDL	BDL	BDL	BDL	BDL	BDL
9	26	0.01	0.6	BDL	BDL	BDL	BDL	BDL	BDL	BDL	BDL	BDL	BDL	BDL
10	11.5	BDL	0.5	BDL	BDL	BDL	BDL	BDL	BDL	BDL	BDL	BDL	BDL	BDL
Sample No	K	La	Li	Lu	Mg	Mn	Mo	Na	Nb	Nd	Ni	P	Pb	Pd
1	2.27	BDL	9.5	BDL	12.4	0.09	1.6	23.34	BDL	BDL	BDL	13	BDL	BDL
2	0.32	BDL	15	BDL	24.63	0.06	5.4	17.11	BDL	BDL	2.3	BDL	BDL	BDL
3	2.75	BDL	11.2	BDL	25.01	0.06	1.1	22.39	BDL	BDL	0.7	BDL	BDL	BDL
4	0.51	BDL	11.4	BDL	21.52	0.05	0.8	17.69	BDL	BDL	0.5	BDL	BDL	0.03
5	1	BDL	11.9	BDL	15.34	BDL	0.6	7.33	BDL	BDL	BDL	14	BDL	0.02
6	0.58	BDL	8.6	BDL	13.17	BDL	0.5	17.76	BDL	BDL	0.6	BDL	BDL	0.02
7	0.37	BDL	0.6	BDL	4.18	BDL	0.2	0.97	BDL	BDL	BDL	BDL	BDL	BDL
8	0.64	BDL	9.6	BDL	12.59	0.1	1.3	25.4	BDL	BDL	BDL	BDL	0.5	0.02
9	2.04	BDL	15.5	BDL	18.11	BDL	0.8	2.033	BDL	BDL	0.3	23	BDL	BDL
10	0.72	BDL	2.2	BDL	14.8	BDL	0.6	8.57	BDL	BDL	BDL	BDL	6.7	BDL

Supplementary Table 1. (continued)

Sample No	Pr	Pt	Rb	Re	Rh	Ru	S	Sb	Sc	Se	Si	Sm	Sn	Sr
1	BDL	BDL	0.53	0.18	0.01	BDL	15	BDL	BDL	2.7	11404	BDL	BDL	517.11
2	BDL	BDL	0.31	0.03	0.03	BDL	25	0.1	3	1.6	13558	BDL	BDL	1147.04
3	BDL	0.02	0.49	0.27	0.03	BDL	24	BDL	4	0.9	16080	BDL	BDL	916.47
4	BDL	BDL	0.32	0.27	0.02	BDL	12	BDL	3	1.5	12841	BDL	0.18	878.35
5	BDL	BDL	0.94	0.01	0.01	BDL	9	BDL	2	BDL	10971	BDL	BDL	458.68
6	BDL	BDL	0.43	0.07	0.02	BDL	10	BDL	2	1.1	10524	BDL	BDL	556.98
7	BDL	BDL	0.18	0.01	0.01	BDL	2	BDL	BDL	BDL	3332	BDL	BDL	85.84
8	BDL	BDL	0.54	0.01	0.01	BDL	9	BDL	3	0.9	12297	BDL	BDL	486.56
9	BDL	0.02	0.87	0.02	0.02	BDL	10	BDL	3	0.5	11538	BDL	BDL	569.81
10	BDL	0.03	0.43	0.03	0.03	BDL	9	BDL	3	BDL	10705	BDL	BDL	628.74

Sample No	Ta	Tb	Te	Th	Ti	Tl	Tm	U	V	W	Y	Yb	Zn	Zr
1	BDL	BDL	BDL	BDL	BDL	BDL	BDL	1.99	4.3	BDL	BDL	BDL	0.5	BDL
2	BDL	BDL	BDL	BDL	BDL	BDL	BDL	11.32	8.1	BDL	BDL	BDL	0.5	BDL
3	BDL	BDL	0.13	BDL	BDL	BDL	BDL	1.04	9.7	BDL	BDL	BDL	0.6	BDL
4	BDL	BDL	BDL	BDL	BDL	BDL	BDL	3.93	5.7	BDL	BDL	BDL	0.6	BDL
5	BDL	BDL	BDL	BDL	BDL	BDL	BDL	0.36	2.6	BDL	BDL	BDL	0.5	BDL
6	BDL	BDL	BDL	BDL	BDL	BDL	BDL	0.99	2.2	BDL	BDL	BDL	BDL	BDL
7	BDL	BDL	BDL	BDL	BDL	BDL	BDL	0.14	BDL	BDL	BDL	BDL	BDL	BDL
8	BDL	BDL	0.11	BDL	BDL	BDL	BDL	1.16	6.6	BDL	BDL	BDL	0.9	BDL
9	BDL	BDL	BDL	BDL	BDL	BDL	BDL	1.11	5.6	BDL	BDL	BDL	1.5	BDL
10	BDL	BDL	BDL	BDL	BDL	BDL	BDL	0.51	2.9	BDL	BDL	BDL	BDL	BDL

JOURNAL OF SCIENCE

PART A: ENGINEERING AND INNOVATION



Correspondence Address

Gazi University
Graduate School of Natural and Applied Sciences
Emniyet Neighborhood, Bandırma Avenue
No:6/20B, 06560, Yenimahalle - ANKARA
B Block, Auxiliary Building

Yazışma Adresi

Gazi Üniversitesi
Fen Bilimleri Enstitüsü
Emniyet Mahallesi, Bandırma Caddesi
No:6/20B, 06560, Yenimahalle - ANKARA
B Blok, Ek Bina

e-mail | e-posta
gujsa06@gmail.com

web page | web sayfası
<https://dergipark.org.tr/tr/pub/gujisa>

e-ISSN 2147-9542